Synthetic Topological Quantum Matter and Nanostructures for Topological Quantum Computing

Mahan Ghafour Mohseni

Thesis submitted to the University of Ottawa
in partial fulfillment of the requirements for the
PhD degree in Physics

Department of Physics
Faculty of Science
University of Ottawa

Abstract

Quantum computers hold the promise of solving computational problems that are intractable for classical computers, by harnessing the principles of quantum mechanics. However, quantum computations are highly susceptible to noise and decoherence, which place strict limits on the size and depth of the circuits that can be reliably executed on current hardware. Topological quantum computing (TQC) has emerged as one of the promising approaches to building fault-tolerant quantum computers. The key idea is to store quantum information in the global properties of a physical system, making it naturally resilient to the local noise and errors that affect conventional qubits. This thesis focuses on synthetic topological quantum matter, the physical platform on which TQC is built, and investigates its electronic structure and topological properties. We study the conditions under which these systems enter a topological phase and host Majorana zero modes (MZMs), exotic zero-energy quasiparticles that appear at the boundaries of the system. MZMs are the key building block of TQC, as their quantum mechanical properties allow them to encode and process quantum information in a way that is protected from errors. We demonstrate the existence of MZMs in two canonical topological systems, the Kitaev chain and the semiconducting-superconducting nanowire. To address the experimental challenge of detecting MZMs, we develop an optical spectroscopy technique based on excitonic interactions, which provides clear and measurable signatures of the topological phase. We also explore the variational quantum eigensolver as a quantum algorithmic approach to approximating the ground-state energy of the many-body spectrum of topological systems. Furthermore, we discuss the practical setups for topological quantum matter and simulate them through numerical analysis. Altogether, we present several theoretical and numerical methods that can be used for numerical simulations and practical purposes of detecting MZMs in topological quantum matter.

Statement of Originality

This thesis presents original research carried out by the author under the supervision of Prof. Stefanie Czischek at the University of Ottawa. The research was performed in collaboration with co-authors, as detailed below. The results have been disseminated in the following publications.

1. M. Mohseni, H. Allami, D. Miravet, D. J. Gayowsky, M. Korkusinski, and P. Hawrylak, "*Majorana Excitons in a Kitaev Chain of Semiconductor Quantum Dots in a Nanowire*", *Nanomaterials* **13**, 2293 (2023). [Basis of Chapter 4, Section 4.3, and Chapter 6, Section 6.1.]

   I was the main contributor to this publication. I performed the analytical derivations, developed the exact diagonalization source code, generated and analyzed all presented data, participated in discussions on the direction of research, and wrote most of the manuscript. The co-authors proposed the initial research question, contributed to the interpretation of the results, and provided feedback on the written manuscript.

2. M. Mohseni, I. Cunha, D. Miravet, A. Wania Rodrigues, H. Allami, I. Assi, M. Korkusinski, and P. Hawrylak, "*Designing Majorana Quasiparticles in InAsP Quantum Dots in InP Nanowires with Variational Quantum Eigenvalue Solver*", *physica status solidi (b)* **262**, 2400552 (2025). [Basis of Chapter 6, Section 6.2.]

   I was the main contributor to this publication. I designed the symmetry-adapted variational ansätze, implemented the variational quantum eigensolver simulations, generated the presented data, carried out the benchmarking across the topological phase diagram, and wrote most of the manuscript. The co-authors contributed to the atomistic modeling of the InAsP/InP quantum dot platform, discussed the results and next steps, and provided feedback on the written manuscript.

3. M. Islam, M. Mohseni, I. Assi, D. Miravet, and P. Hawrylak, "*Spin Resolved Majorana Modes in Semiconductor Quantum Dot Arrays with Proximity Induced Superconductivity*", arXiv:2601.14527 (2026), currently under peer review. [Basis of Chapter 7.]

I contributed to this publication as second author. I participated in developing the bond fermion formulation, verified the analytical derivations and the exact diagonalization results, contributed to the evaluation and discussion of the results and next steps, and provided feedback on the written manuscript. The first author, M. Islam, led the project, performed the calculations, and wrote most of the manuscript.

Original contributions of this thesis. The following results, developed in publications [1] and [2] with the contributions described above, are presented in Chapters 4 and 6. First, the extension of the bond-fermion representation to the interacting excitonic problem and the resulting absorption spectrum valid for an arbitrary chain length N. Second, the identification of the edge-localized high-energy absorption peak as an optical signature of the Majorana zero mode, together with its extension to a mobile valence-band hole. Third, the design of the symmetry-adapted variational ansätze and the benchmarking of four ansätze across the topological phase diagram of the Kitaev chain. Chapter 7 presents the collaborative results of publication [3].

Background and review material. Chapters 1, 2, and 3, together with the model-defining portions of Chapters 4, 5, 6 and 7, present established results from the literature and contain no claim of originality. They are included to make the thesis self-contained, and all sources are cited where the corresponding material is introduced. The concluding Chapter 8 is an original synthesis of the above results and an outline of directions for future work.

Acknowledgements

I would like to express my sincere gratitude to my supervisor, Prof. Stefanie Czischek for allowing me to join her group. Her insights, patience, and continuous motivation have been invaluable in shaping this research and helping me grow as a scientist.

I would also like to thank Prof. Pawel Hawrylak for his guidance, help, and support throughout this work. I have learned a great deal from him, and I am deeply grateful for the knowledge and insight he has shared.

I would also like to thank Dr. Daniel Miravet, who has been present since the very beginning of my PhD journey. He has been not only an invaluable mentor but also a constant source of support and encouragement, much like an older brother to me. I am deeply grateful for all the guidance and help he has given me throughout these years.

I would also like to thank Dr. Logan Cooke for his support and helpful discussions throughout my PhD. His insights and encouragement were greatly appreciated and contributed positively to my research experience.

I would like to thank all the people in the Quantum Theory group, especially Dr. Marek Korkusinski, Dr. Iann Cunha, and Dr. Hassan Allami for having a bold part in my PhD study.

I would also like to thank all the members of the APRIQUOT group, including Riza, Faith, Edward, and Chris, for their friendship, support, and encouragement throughout my PhD. They have been more than just colleagues, and their motivation made this journey much more enjoyable.

Finally, I would like to thank my parents and my brother for their endless love and support, especially during the more challenging moments of this journey. Their encouragement and belief in me have always given me the strength to move forward.

Acronyms

QC	Quantum Computing
TQC	Topological Quantum Computing
CNOT	Controlled-NOT (gate)
VQE	Variational Quantum Eigensolver
HVA	Hamiltonian Variational Ansatz
ED	Exact Diagonalization
CI	Configuration Interaction
HF	Hartree–Fock
DMRG	Density Matrix Renormalization Group
MPS	Matrix Product States
SVD	Singular Value Decomposition
JW	Jordan–Wigner (transformation)
DOS	Density of States
TB	Tight-Binding
BCS	Bardeen–Cooper–Schrieffer
BdG	Bogoliubov–de Gennes
TSC	Topological Superconductor
SC	Superconductor
SOC	Spin–Orbit Coupling
TR	Time-Reversal

MZM	Majorana Zero Mode
SM	Semiconductor
SM-SC	Semiconducting-Superconducting
QD	Quantum Dot
CB	Conduction Band
VB	Valence Band
OBC	Open Boundary Conditions
1D	One-Dimensional

Contents

List of Figures

Chapter 1

Introduction

1.1 The Quantum Computing Landscape

The idea of using quantum mechanical systems to perform computation was first proposed by Feynman in 1982, who observed that classical computers face an exponential overhead when simulating quantum systems, and that a computer operating according to the laws of quantum mechanics could overcome this limitation [1]. This insight gave rise to the field of quantum computing (QC), which has since grown into one of the most active frontiers of modern physics and computer science [2].

A quantum computer operates on quantum bits, or qubits, which unlike their classical counterparts can exist in a coherent superposition of the basis states $|0\rangle$ and $|1\rangle$ [2]. More generally, a register of N qubits can simultaneously represent a superposition of all 2^N computational basis states, giving access to an exponentially large Hilbert space that a classical register of N bits can only traverse sequentially. A quantum computer harnesses three fundamental quantum mechanical resources: superposition, which enables parallel exploration of the state space; entanglement, which generates correlations between qubits that have no classical analogue; and unitary evolution, which manipulates these states through quantum gates, with the final result extracted via classical measurement [2, 3].

The potential of this paradigm was made concrete by a series of landmark algorithmic results. Shor's factoring algorithm [4] demonstrated that a quantum computer could break Rivest–Shamir–Adleman (RSA) encryption in polynomial time, a task believed to be classically intractable. Grover's search algorithm [5] provided a quadratic speedup for unstructured search problems. Perhaps most directly relevant to the physical sciences, quantum phase estimation and related algorithms provide the potential for substantial speedups in simulating quantum many-body systems, with transformative implications for quantum chemistry, materials design, and drug discovery [6, 7].

The pursuit of practical quantum advantage has driven rapid experimental progress across a wide variety of physical platforms. These include superconducting transmon

qubits [8], trapped ions [9], photonic circuits [10], spin qubits in semiconductor quantum dots [11], and neutral atoms in optical tweezer arrays [12]. Each platform offers a different balance between coherence time, gate fidelity, scalability, and connectivity. Recent demonstrations of quantum processors with hundreds of qubits have begun exploring computational regimes that challenge classical simulation [13].

Yet, the path from today's noisy devices to a large-scale, programmable quantum computers remain formidable. As quantum circuits scale to larger sizes, their performance is increasingly limited by quantum decoherence, the inevitable leakage of quantum information into environmental degrees of freedom, which collapses coherent superpositions into classical mixtures on a timescale set by the system's coherence time [14, 15]. Beyond decoherence, practical systems suffer from imperfect gate operations [16], leakage to non-computational states [17], and crosstalk between qubits [18]. Collectively, these noise processes impose a hard limit on the depth of quantum circuits that can be executed reliably, and therefore on the complexity of computations that can be performed. We are presently in the Noisy Intermediate-Scale Quantum (NISQ) era [13], a regime of devices with tens to hundreds of physical qubits that operate without full quantum error correction, powerful enough to explore near-term applications but not yet capable of running the deep circuits required by transformative algorithms such as Shor's.

Overcoming these limitations requires fault-tolerant quantum computation, the ability to perform arbitrarily long quantum computations in the presence of noise [19, 20]. Standard approaches to fault tolerance, such as the surface code [21], rely on encoding a single logical qubit in many physical qubits and performing error detection and correction at every step of the computation. While these schemes are in principle scalable, their overhead is enormous. Estimates for practically useful algorithms suggest the need for thousands of physical qubits per logical qubit at the error rates achievable today [20]. This resource burden motivates the search for an alternative paradigm, one in which qubits are intrinsically protected against local errors by the laws of physics rather than by active correction.

1.2 The Problem of Fault-Tolerance

The concept of fault-tolerant quantum computation addresses a fundamental question: can a quantum computer perform a reliable computation of arbitrary length, even when every physical component is noisy [19, 22]? The answer, established by the quantum threshold theorem [19, 22], is yes, provided that the noise affecting each physical

operation falls below a critical threshold value. Below this threshold, errors can be suppressed to arbitrarily low levels by encoding logical qubits redundantly across many physical qubits and by performing error correction continuously throughout the computation [2, 19, 22].

Classical computers have long employed error correction, a bit can be protected simply by tripling it and taking a majority vote [23]. Quantum error correction is considerably more subtle, for three reasons rooted in the laws of quantum mechanics [2]. First, quantum states cannot be copied: the no-cloning theorem forbids the duplication of an unknown quantum state, ruling out the straightforward classical strategy [24]. Second, quantum errors are continuous; unlike a classical bit-flip, a qubit can suffer an error of any magnitude and in any direction on the Bloch sphere [2]. Third, any attempt to measure the state of a qubit to diagnose its errors will in general disturb the very quantum information one is trying to protect [2]. The resolution to all three obstacles lies in encoding quantum information non-locally across an entangled register of physical qubits, measuring only collective stabilizer operators that reveal the syndrome of any error without exposing the encoded information [2, 25].

Among the many quantum error-correcting codes that have been developed, the surface code [21] stands out as the leading candidate for near-term fault-tolerant hardware, owing to its high-threshold error rate (approximately 1% per gate) and its requirement of only local, nearest-neighbour interactions on a two-dimensional qubit array. The surface code and related topological stabilizer codes [26] achieve their resilience by distributing logical information across the global topology of the code, so that any local error affects only a correctable syndrome. Here, the Clifford gates, generated by the Hadamard, phase, and CNOT gates, are those mapping the Pauli group to itself under conjugation; by the Gottesman-Knill theorem, circuits built solely from them can classically be simulated and hence not universal [2, 27]. A non-Clifford gate, such as the T gate $T = \mathrm{diag}(1, e^{i\pi/4})$, lies outside this group, and adding one to the Clifford set suffices for universal quantum computation [2].

Fault-tolerant implementations of non-Clifford gates, which are necessary for universal quantum computation [28], incur additional overhead through resource-intensive procedures such as magic state distillation [29], further multiplying the physical qubit count.

The combined effect of all these overheads is severe. The most recent resource estimates indicate that factoring a cryptographically relevant 2048-bit RSA integer with Shor's algorithm would require on the order of one million noisy physical qubits running for several days, and even this figure represents a roughly twenty-fold reduction

in the estimated qubit count achieved between 2019 and 2025 through algorithmic and error-correction improvements [30, 31]. Since current devices operate at the scale of hundreds to a few thousand noisy physical qubits, a fully fault-tolerant quantum computer capable of breaking real-world encryption remains far beyond the reach of current hardware [31]. This sobering assessment has stimulated intense interest in approaches that reduce or eliminate the need for active error correction by engineering qubits that are passively protected against noise at the physical level [26, 32, 33].

The central idea behind passive protection is to encode quantum information not in the fragile state of any single physical component, but in a global degree of freedom of a many-body quantum system, one that is invisible to any local perturbation. If the logical qubit is stored in a global property of the system that cannot be altered by any local perturbation, then the dominant source of errors in realistic devices is automatically suppressed, exponentially in the system size [26, 32]. This is the operating principle of topological quantum computing; rather than correcting errors after they occur, the encoding itself makes the logical qubit immune to them [26, 32, 34]. The physical systems capable of realizing this vision are topological phases of matter [35, 36], and the exotic quasiparticles they host, non-Abelian anyons, serve as the hardware for topologically protected qubits [26, 32, 34].

1.3 Topological Quantum Computing and Majorana Zero Modes

Topological Phases of Matter and the Role of Geometry

The notion that quantum information could be stored in the global, topological properties of a many-body system was placed on a firm theoretical footing by Kitaev [26], building on earlier ideas connecting topology and quantum statistics [37, 38]. The key insight is that the dimensionality of space has profound consequences for how quantum particles can behave. In two spatial dimensions, the topological properties of particles are fundamentally richer than in three dimensions, giving rise to an entirely new class of quantum particles called anyons, whose exchange properties have no three-dimensional analogue [32, 38].

The central property of a topological phase of matter is that it harbours a ground state degeneracy that is globally protected, meaning that the degenerate ground states cannot be distinguished by any local measurement, and no local perturbation can induce transitions between them [26, 32, 35]. This is in sharp contrast to conventional

ordered phases, where the ground state is selected by local order parameters and is readily perturbed by local noise. In a topological phase, quantum information encoded in the degenerate ground state manifold is therefore intrinsically protected against the local errors that plague conventional qubit architectures [26, 39].

Topological quantum computing exploits this structure directly [26, 34, 40]. Quantum information is encoded in the ground-state space of a topological system hosting a collection of exotic quasiparticles, and quantum gates are executed by adiabatically exchanging or "braiding" pairs of these quasiparticles. The outcome of such a braiding operation depends only on the topology of the exchange sequence. Gate errors due to environmental noise are therefore exponentially suppressed in the ratio of the bulk energy gap to the temperature [26, 32, 34]. The physical systems capable of realizing this vision support non-Abelian quasiparticles [41, 42] whose braiding implements non-trivial unitary operations on the ground-state manifold [32, 43], and these quasiparticles serve as the hardware for topologically protected qubits [26, 33, 34]. The most experimentally accessible and extensively studied candidates are Majorana zero modes [44–47]. A Majorana fermion is a particle that is its own antiparticle, first conceived by Ettore Majorana in 1937 as a real solution to the Dirac equation [48]. While fundamental Majorana fermions have not been observed in high-energy physics, their condensed-matter analogues Majorana zero modes (MZMs) emerge as zero-energy quasiparticle excitations localized at the boundaries of certain superconducting systems [44, 49, 50]. MZMs arise in pairs. Two spatially separated MZMs encode a single non-local conventional fermion. The two degenerate ground states corresponding to this fermion being empty or occupied differ in fermion parity but are otherwise identical in energy [32, 50]. This non-local encoding is the source of the topological protection. Any local perturbation couples only to one of the two MZMs at a time, and because a single Majorana operator cannot change the fermion parity of the state, it cannot induce transitions between the ground states [33, 50]. The energy splitting between the two ground states is exponentially small in the separation between the two MZMs divided by the superconducting coherence length, vanishing in the thermodynamic limit [46, 50]. This means that in a sufficiently long wire, the two ground states are effectively degenerate, and the topological qubit encoded in them is well protected against any local source of noise or decoherence. This degeneracy, however, is only one of the two ingredients required for protection. The ground-state manifold is separated from all excited states by a finite topological gap E_{gap}, defined as the minimum energy needed to create a bulk quasiparticle excitation above the manifold. The two requirements are complementary: the exponentially small ground-state splitting ensures

that local operators cannot mix the two qubit states, while the finite topological gap ensures that no local perturbation or thermal fluctuation with energy below E_{gap} can excite the system out of the ground-state manifold. The encoded qubit is therefore isolated both from itself, by the exponentially small splitting, and from the rest of the spectrum, by the topological gap with residual errors suppressed exponentially in the ratio E_{gap}/k_BT [26, 32, 34]. For the systems studied in this thesis, E_{gap} is of the order of the induced superconducting gap, typically ~ 0.1 meV (~ 1 K), so that at the millikelvin operating temperatures of dilution refrigerators this ratio is large.

Several properties make MZMs uniquely attractive as a platform for TQC. Their topological protection is intrinsic, i.e, the non-local fermionic qubit formed by a pair of MZMs is strongly protected against local perturbations, since no local operator can distinguish the two ground states [32, 50]. MZMs are predicted to arise in a variety of solid-state systems that can be engineered and controlled in the laboratory, providing a realistic experimental target. Their zero-energy pinning inside the bulk gap produces distinctive, detectable signatures in spectroscopic and transport measurements [51–53], giving a clear route to experimental verification. These properties have made the search for and manipulation of MZMs one of the most active areas in condensed matter physics over the past two decades [46, 47, 54], and they provide the central motivation for the theoretical and numerical investigations that constitute this thesis.

1.4 Physical Platforms for Majorana Zero Modes

The theoretical prediction of MZMs in condensed matter systems has motivated an extensive experimental effort to engineer and detect them in the laboratory [44–46, 49, 50]. The common ingredient across all platforms is topological superconductivity, a phase of matter in which the superconducting pairing has a non-trivial topological character, giving rise to a bulk energy gap and protected zero-energy modes at the boundaries [49, 50, 55]. While intrinsic topological superconductors are rare in nature, a key insight that has driven the field is that topological superconductivity can be engineered by combining conventional materials, ordinary superconductors, semiconductors, magnets, and topological insulators in carefully designed heterostructures [56–58].

The Kitaev Chain

The conceptual starting point for all MZM platforms is the Kitaev chain, a theoretical model proposed by Kitaev in 2001 [50]. It describes a one-dimensional wire of spinless electrons coupled by spinless p-wave superconducting pairing between neighbouring sites. In a certain regime of parameters, this simple model enters a topological phase in which an unpaired Majorana is localized at each end of the wire, while the bulk of the chain remains fully gapped. Despite its simplicity, the Kitaev chain captures the essential physics of topological superconductivity and serves as the theoretical benchmark against which all more realistic platforms are measured [33, 44, 45, 50].

The practical obstacle to directly realizing the Kitaev chain is that p-wave superconductivity does not occur naturally in most materials. For more than two decades, Sr_2RuO_4 was the leading candidate intrinsic chiral p-wave superconductor [59]. However, recent ^{17}O nuclear magnetic resonance measurements have observed a pronounced drop in the spin susceptibility below T_c [60], incompatible with the odd-parity (triplet) pairing required for a p-wave state, and subsequent work has placed constraints tight enough to exclude essentially all pure p-wave order parameters [61]. While the precise pairing symmetry of Sr_2RuO_4 remains unresolved, it is now widely regarded as unlikely to be a p-wave superconductor. The scarcity of robust intrinsic p-wave superconductivity, even in its most intensively studied candidate, motivates the engineered (synthetic) route to topological superconductivity described below.

Semiconductor-Superconductor Nanowires

The most extensively studied experimental platform is the semiconducting-superconducting (SM-SC) nanowire, proposed independently by Lutchyn et al. [57] and Oreg et al. [58] in 2010. In a conventional s-wave superconductor, the most common type, in which electrons with opposite spins pair up to form Cooper pairs, the pairing is topologically trivial and does not support MZMs [62]. What is needed instead is p-wave superconductivity, in which electrons of the same spin pair up, giving rise to a topologically non-trivial pairing that can host MZMs [49, 50]. While intrinsic p-wave superconductors are rare and difficult to work with, the key insight of Lutchyn et al. and Oreg et al. is that p-wave-like pairing can be engineered by placing an ordinary s-wave superconductor in close proximity to a semiconductor nanowire with strong spin-orbit coupling and subjecting it to a magnetic field [57, 58]. The spin-orbit coupling mixes spin-up and spin-down electrons, while the magnetic field lifts their degeneracy through the Zeeman effect. Together, these two ingredients effectively transform the s-wave

pairing of the superconductor into p-wave-like pairing in the nanowire through the superconducting proximity effect. When the magnetic field exceeds a critical value, the system undergoes a topological phase transition and MZMs appear at the two ends of the nanowire [44, 57, 58].

This proposal triggered a wave of experimental activity. The first reported signatures of MZMs came from the Kouwenhoven group at Delft in 2012, using InSb nanowires coupled to a NbTiN superconductor [52]. The experiment observed a zero-bias conductance peak in tunnelling spectroscopy, a hallmark of a zero-energy bound state at the wire's end that emerged when the magnetic field exceeded the predicted topological threshold. These early measurements reported zero-bias conductance peaks consistent with Majorana zero modes, but did not constitute unambiguous proof. Subsequent experiments on similar InAs and InSb nanowire devices reported increasingly robust zero-bias peaks [63], and more recently, near-quantized conductance values consistent with theoretical predictions for MZMs [47]. Proposals [64] and experimental realizations of minimal Kitaev chains assembled from just two quantum dots coupled by a superconductor have further advanced the field [64, 65]. However, a later claim of quantized Majorana conductance was retracted in 2021 after inconsistencies were identified in the data analysis [66], and it is now widely recognized that a zero-bias peak alone is not a definitive signature, since trivial Andreev bound states can produce strikingly similar features. This experience underscores the need for complementary and more discriminating detection strategies, which forms part of the motivation for the present thesis.

1.5 The Many-Body Problem and Zero Mode Detection

The theoretical and numerical study of topological systems hosting MZMs presents two fundamental challenges that run throughout this thesis. The first is computational in nature: topological superconductors are interacting quantum many-body systems, and simulating them exactly becomes rapidly intractable as the system size grows [67–69]. This intractability is a fundamental consequence of quantum mechanics; the dimension of the Hilbert space grows exponentially with the number of particles, making an exact description computationally expensive [2]. The second is experimental. Even once a topological phase has been identified theoretically, detecting its hallmark MZMs in a real device is far from straightforward [46, 47, 53, 70]. We discuss each challenge in

turn.

The Many-Body Problem

A quantum system of N interacting particles is described by a wave function that lives in a Hilbert space whose dimension grows exponentially with N [2, 69, 71]. For a chain of N fermionic sites, each of which can be occupied or empty, the number of independent quantum states is 2^N. Even for a modest chain of $N = 50$ sites, this already exceeds 10^{15} states, far beyond what can be stored or manipulated on any classical computer [2, 67]. This exponential wall is the central obstacle in the theoretical study of quantum many-body systems [67, 68], and it is not merely a limitation of current hardware, but it is a fundamental consequence of quantum mechanics itself [1, 2].

In the context of topological systems, this challenge manifests in several ways. Computing the energy spectrum of a topological chain, which is essential for identifying the topological phase and detecting the zero-energy regime requires diagonalizing a Hamiltonian matrix whose size grows exponentially with the chain length [67, 72, 73].

The system size and the visibility of topological features are among the factors that contribute to the choice of the numerical method throughout this thesis. A key message that emerges from our calculations is that the choice of numerical method must be carefully matched to the physical regime of interest.

The Detection of Majorana Zero Modes

A second and equally important problem is how to detect MZMs in an experiment. The difficulty stems from the property that makes MZMs attractive for quantum computing, which is their non-local character [32, 33, 50]. Because the quantum information stored in a pair of MZMs is distributed across the entire system, no single local measurement can directly reveal it [32, 50]. Instead, one must rely on indirect signatures such as observable quantities that are sensitive to the presence of zero-energy boundary modes, and which can be calculated theoretically and then compared with experiment [45, 46, 53, 74].

The most widely used experimental probe to date is tunnelling spectroscopy. It is based on measuring the differential conductance at the end of a nanowire as a function of bias voltage. A MZM localized at the wire ends produces a sharp peak in the conductance at zero bias voltage, the so-called zero-bias peak, because it provides a resonant channel for electrons to tunnel into the superconductor via

Andreev reflection [51, 52]. In the ideal limit of a perfectly separated MZM, this peak is predicted to be quantized [51]. This signature has been observed in numerous experiments [47, 52, 63], and has been widely interpreted as evidence for MZMs.

However, as discussed in the previous section, a zero-bias peak is not uniquely diagnostic of a topological MZM. Trivial subgap states such as Andreev bound states, which can form near the wire ends due to disorder or smooth confinement potentials, produce strikingly similar conductance features [46, 53]. Distinguishing between the two cases is experimentally demanding and has been the source of considerable controversy in the field [47, 70]. What is needed are additional theoretical tools that go beyond the zero-bias peak and provide complementary, more discriminating signatures of the topological phase [33, 46, 47, 53, 70].

This thesis contributes to this effort in two directions. The first is the development of an optical detection scheme based on excitonic spectroscopy. It works by adding an electron-hole pair to the topological system and studying the resulting absorption spectrum. We show that MZMs created by photon absorption leave distinctive fingerprints in the optical response of the system, including characteristic peak splittings and edge-localized intensity patterns that are directly accessible in optical measurements on InAsP quantum dot nanowires [75]. The second is the calculation of the local spectral function of the semiconducting-superconducting nanowire, which provides a spatially resolved map of the low-energy quasiparticle excitations and reveals the edge localization of the zero-energy mode in a manner directly analogous to the zero-bias conductance peaks sought in tunnelling experiments [76].

1.6 Thesis Contributions and Outline

The contents of this thesis are based on research published in peer-reviewed journals and a manuscript currently under peer review. A list of manuscripts related to this thesis is:

1. **M. Mohseni**, H. Allami, D. Miravet, D. J. Gayowsky, M. Korkusinski, and P. Hawrylak, "Majorana Excitons in a Kitaev Chain of Semiconductor Quantum Dots in a Nanowire," *Nanomaterials*, vol. 13, no. 16, p. 2293, 2023. [75]

2. **M. Mohseni**, I. Cunha, D. Miravet, A. Wania Rodrigues, H. Allami, I. Assi, M. Korkusinski, and P. Hawrylak, "Designing Majorana Quasiparticles in InAsP Quantum Dots in InP Nanowires with Variational Quantum Eigenvalue Solver," *physica status solidi (b)*, vol. 262, no. 7, p. 2400552, 2025. [77]

3. M. Islam, **M. Mohseni**, I. Assi, D. Miravet, and P. Hawrylak, "Majorana Fermions in Spin Up and Down Electronic Complexes in Spin-Orbit Coupled Array of Semiconductor Quantum Dots in Proximity to s-type Superconductor and in Magnetic Field," *arXiv preprint*, arXiv:2601.14527, 2026. [76]

Figures 4.3, 4.4, 6.1, 6.3, 6.4, 6.5, 6.6, 6.7, 6.12, 6.13, 6.14, 7.1, 7.3, 7.4, and 7.8 are reused from the publications.

After reviewing the basics of topological quantum computing in Chapter 2, we provide a self-contained development of the methods employed throughout the thesis in Chapter 3. We introduce the configuration interaction approach, illustrated on spinless and spinful tight-binding chains. We develop the Hartree-Fock mean-field approximation as a computationally efficient complement to exact methods. We then present the variational quantum eigensolver in detail, including the Jordan-Wigner transformation that maps fermionic Hamiltonians onto spin operators, the construction of physically motivated variational ansätze, and the classical optimization strategies used to minimize the energy. Finally, we introduce the density matrix renormalization group and its formulation in terms of matrix product states, which underpins our treatment of longer chains in later chapters.

Our first main contribution concerns the Kitaev chain and its topological properties. In Chapter 4, we establish an exact analytical and numerical characterization of the Kitaev model by working in the Majorana and bond fermion representations. We show that a bond fermion transformation diagonalizes the Kitaev Hamiltonian exactly in the topological regime, making the non-local character of the zero modes transparent and providing an analytical benchmark for all subsequent numerical work. Through exact diagonalization, we compute the full energy spectrum of the chain as a function of the Hamiltonian parameters and demonstrate the emergence of zero-energy states as the system is tuned across the topological phase transition. We complement this with a probability density analysis that directly visualizes the spatial localization of the MZMs at the chain ends in the topological phase. This exact solution identifies the topological phase, and explains why MZMs are robust against local perturbations.

Chapter 5 extends the analysis to the semiconducting-superconducting nanowire. Starting from the Bogoliubov-de-Gennes (BdG) Hamiltonian for a semiconductor nanowire with spin-orbit coupling and Zeeman splitting in proximity to an s-wave superconductor, we carry out a systematic study of the band structure of this system. We examine the effects of each physical ingredient, the Zeeman field, spin-orbit coupling, and superconducting pairing on the band structure and spin texture of the nanowire, and show how their interplay drives the system through a topological phase transition.

We identify the precise condition on the Hamiltonian parameters under which the gap closes and reopens in a topologically non-trivial fashion, and demonstrate the emergence of MZMs in the open-boundary spectrum. This analysis establishes a clear and quantitative connection between the microscopic parameters of the device and the topological phase diagram, which is essential for guiding experimental efforts.

In the first part of Chapter 6, we introduce the optical detection scheme based on optical spectroscopy [75]. We model an InAsP quantum dot nanowire in proximity to a p-wave superconductor and add an excitonic interaction to the Kitaev chain by coupling a mobile or localized hole to the electronic degrees of freedom. Using exact diagonalization in the bond fermion representation, we calculate the absorption spectrum of this interacting system. We show the characteristic peak splittings and edge-localized intensity patterns that are qualitatively distinct from the response of the trivial phase and are related to MZMs. For the case of a localized hole we derive an analytical solution for the absorption spectrum that is valid for chains of arbitrary length, enabling the results to be directly compared with optical measurements without requiring large-scale numerical simulations. This work introduces optical spectroscopy as a new tool in the MZM detection toolkit.

The second part of Chapter 6 addresses the question of whether near-term quantum computers can be used to simulate topological phases of matter. We apply the variational quantum eigensolver to the Kitaev chain, constructing symmetry-adapted variational ansätze that respect the parity structure of the Hamiltonian and are therefore capable of correctly capturing the ground-state degeneracy of the topological phase [77]. We benchmark four ansätze including physically motivated and hardware-efficient designs against the exact solution, demonstrating that a suitably constructed VQE reliably reproduces the ground-state energy throughout the topological phase. We further map out the performance of each ansatz across the topological phase diagram, identifying the parameter regimes where each approach is most effective. This work establishes a concrete framework for quantum simulation of topological matter on near-term quantum hardware, and points toward a route for extending quantum algorithmic methods to experimentally relevant topological platforms.

Chapter 7 returns to the SM-SC nanowire and develops a comprehensive numerical analysis of its many-body spectrum [76]. We begin with exact diagonalization of short chains and demonstrate the emergence of near-degenerate even and odd parity ground states in the topological regime, a direct signature of the MZMs. We then address the finite-size limitation of exact diagonalization by employing density matrix renormalization group (DMRG) to study longer chains, and perform a finite-size

scaling analysis of the parity splitting that reveals the minimum chain length required for the topological features to become clearly visible. We introduce an exact analytical mapping between the SM-SC model and a pair of coupled Kitaev chains, which makes the connection between the two topological platforms explicit and provides an analytical handle on the conditions required for MZMs to form. Using this mapping, we calculate the local spectral function of the system by exact diagonalization, and show that it displays a sharp low-energy peak exclusively at the chain boundaries, which is a direct numerical counterpart of the zero-bias conductance peaks sought in tunnelling experiments, and a spatially resolved confirmation of the edge localization of the MZMs.

Taken together, the contributions of this thesis advance the field of topological quantum matter in three interconnected directions. First, we provide exact analytical and numerical benchmarks for two canonical MZM platforms, the Kitaev chain and the SM-SC nanowire that clarify the conditions for topological behaviour and establish reliable reference points for future theoretical and experimental work. Second, we introduce and develop two new detection strategies for MZMs, optical excitonic spectroscopy and the local spectral function that go beyond the standard zero-bias peak and bring the theoretical analysis into direct contact with experiment. Third, we demonstrate that hybrid quantum-classical algorithms are capable of correctly capturing the topological ground state of the Kitaev chain, opening a concrete path toward quantum simulation of topological phases on near-term quantum hardware. Together, these results lower the barrier between theoretical models of topological matter and the experimental and computational tools available to probe them.

Chapter 2

Topological Quantum Computing

In this chapter, we introduce topological quantum computing (TQC) with non-abelian anyons, quasiparticles that are generalizations of bosons and fermions [26, 32]. TQC is considered as a promising fault-tolerant version of quantum computing (QC) [34]. This is done through storing the information in the geometrical features of the system, which are robust against local errors. We begin by discussing the limitations of QC, then defining the basics of anyons and their statistics [32, 34]. We then show how non-Abelian anyons are used for TQC. Next, we introduce a promising candidate for realizing non-Abelian anyons: Majorana zero modes (MZM)s [54, 78]. We conclude the chapter by giving examples of systems that host MZMs [32, 79]. These will serve as motivation for all the work that follows.

2.1 Motivation and Limitations of Quantum Computing

The ultimate goal of QC is to build a real-world quantum computer with, for example, a few million logical quantum bits (qubits) to provide us with capabilities to solve computationally challenging tasks, such as simulating quantum systems for chemistry and material science [26, 80]. A quantum computer, in principle, uses the quantum mechanical resources of linear superposition, unitary evolution, and the exponentially large Hilbert space of the entangled and non-entangled states; however the final read-out process is still a classical measurement [3, 20].

When scaling up to larger scales, many problems appear, such as interconnectivity, leaking, and most importantly, quantum decoherence: a physical system will remain in a coherent superposition of states only for a finite and short coherence time (compared to the quantum gates operation time) [14, 81]. Any interaction with the rest of the world or any measurement that leads phenomena such as wavefunction collapse will decohere the system [2, 15, 82]. Apart from decoherence, there are also

coherent sources of error such as leakage error [17] and crosstalk error [18], to name a few. This leads to the concept of **quantum error correction**, or **fault-tolerant quantum computation**. Error correction looks to detect and correct both coherent and decoherent sources of error [19]. In other words, quantum decoherence is the noise in quantum computation and error correction minimizes or eliminates the noise in the computer [19, 83–85] . On the other hand, there exists other alternatives, which do not try to make the system noiseless, but instead, they make it immune to the usual sources of quantum decoherence. One of these approaches is **topological quantum computation** [32, 86, 87] . In TQC, quantum decoherence becomes irrelevant due to the globally robust topological nature of the computation.

As proposed by Alexi Kitaev in 2003, if a physical system has topological degrees of freedom that are insensitive to local perturbations, then information contained in those degrees of freedom would be intrinsically protected against errors caused by local interactions with the environment [26]. The topological degrees of freedom refer to the fundamental, irreducible components of a system that cannot be continuously altered or eliminated while preserving the system's essential topological structure [39] . Most physical systems have local degrees of freedom that react to local perturbations [88] . Take the famous 2-level spin quantum system used to represent the so-called qubit [11] , in particular, the spin-up $|\uparrow\rangle$ and spin-down $|\downarrow\rangle$ states of an electron in a magnetic field. Any variation in the local magnetic field $\mathbf{B}(t)$ alters the Zeeman energy splitting between these two states, thereby changing the relative phase between them.

The qubit is defined as:

$$|0\rangle \equiv |\uparrow\rangle\,, \qquad |1\rangle \equiv |\downarrow\rangle\,. \tag{2.1}$$

The Hamiltonian for a spin-$\frac{1}{2}$ particle in a magnetic field is given by

$$H = -\gamma\, \mathbf{S} \cdot \mathbf{B}, \tag{2.2}$$

where γ is the gyromagnetic ratio and $\mathbf{S}$ is the vector of spin operators. Fluctuations or inhomogeneities in the magnetic field lead to changes in the Zeeman splitting, which will be given by $\Delta E = \hbar\gamma B_z$ if we take the magnetic field along z-axis. This in turn modifies the relative phase between the two spin states in the superposition

$$|\psi(t)\rangle = c_\uparrow e^{-i\omega_\uparrow t}\,|\uparrow\rangle + c_\downarrow e^{-i\omega_\downarrow t}\,|\downarrow\rangle\,, \tag{2.3}$$

with $\omega_\uparrow - \omega_\downarrow = \gamma B_z$. Such variations cause dephasing in the qubit's superposition,

representing a key source of decoherence in spin-based quantum systems [11]. So at first sight the TQC solution does not sound too realistic until we recall that condensed phases of matter do exist that are insensitive to local perturbations that are called "topological phases" that are topologically invariant at low temperatures. A topological phase is a gapped quantum phase of matter whose long wavelength, low-energy properties are invariant under any smooth local deformation that does not close the bulk gap [35] . Illustratively, topological phases are special quantum states of matter whose global properties remain unchanged even if you gently distort the system, as long as you don't cause a phase transition (i.e., close the energy gap between the ground and excited states). "Gapped" means there's a finite energy gap between the ground state and the first excited state:

$$E_{\text{gap}} = E_1 - E_0 > 0 \tag{2.4}$$

Because of this gap, low-energy excitations (with energy $E \ll E_{\text{gap}}$) cannot easily excite the system, so the system is stable. Moreover, long wavelength means the system is being probed over large distances, much larger than the atomic spacing a of your system. For a wavevector k,

$$\lambda = \frac{2\pi}{k} \gg a. \tag{2.5}$$

Low energy excitations correspond to slow, collective modes of the system (not atomic vibrations or microscopic fluctuations). At these scales, as the distance between two particles (say fermions for instance) is changed by stretching the system, the other fermions in the system will rearrange themselves so as to keep the energy unchanged.

2.2 Basics of Anyons and Braiding Statistics

2.2.1 Topology of 3+1 and 2+1 dimensional Spaces

In quantum mechanics, the statistical properties of identical particles are determined by how their many-body wavefunction transforms under particle exchange [37] . Particles in (3+1) spatial+time dimensional systems are categorized into two groups, namely bosons and fermions. This essentially describes the two possible symmetries of a many-body system wave function. Under the exchange of any two particles, the

bosonic wave function remains symmetric,

$$\psi(\mathbf{r}_1, \mathbf{r}_2) = \psi(\mathbf{r}_2, \mathbf{r}_1), \tag{2.6}$$

while that of fermions is anti-symmetric,

$$\psi(\mathbf{r}_1, \mathbf{r}_2) = -\psi(\mathbf{r}_2, \mathbf{r}_1). \tag{2.7}$$

The symmetry of the wave function leads to many prominent features, such as the Pauli principle, superfluidity, the metallic state, and Bose-Einstein condensation, to name a few [89] . For bosons and fermions in three dimensions (3D), interchanging twice corresponds to a 2π rotation of one particle around the other, since rotations in 3D are topologically trivial (one can continuously deform a loop to a point). If we denote each interchange by $e^{i\theta}$ for θ being an arbitrary angle, the acquired phase after interchanging twice becomes $e^{i2\theta} = 1$. This is topologically equivalent to the case where none of the particles move at all, and the wave function remains unaltered by two such interchanges of particles.

In the language of path integral, we consider all possible trajectories in (3+1) dimensions that take N particles from initial positions $R_1, R_2, ..., R_N$ at time t_i to final positions $R'_1, R'_2, \ldots, R'_N$ at time t_f. When the particles are distinguishable, all trajectories can be continuously deformed into the trajectory in which the particles do not move at all. However, when the particles are indistinguishable, the permutation group S_N will classify each trajectory [90]. The group S_N contains all $N!$ possible permutations of N identical particles, and each element of S_N represents a distinct way of exchanging particle positions, specifying how the initial positions are permuted to obtain the final positions. In quantum mechanics, the representation of S_N under which the many-body wavefunction transforms determines the quantum statistics of the particles: symmetric representations correspond to bosons, antisymmetric ones to fermions [37, 38].

Now we focus on (2+1) dimensional systems. A particle loop that encircles another particle in 2d cannot be deformed to a point without cutting through the other particle. As a result, the trajectory of double interchange is nontrivial, and the system does not necessarily come back to the same initial state. This is the basis of the (2+1)d statistics, which is called "braiding statistics", and the particles that obey these statistics are called "anyons" [32] . Let us denote the operation of exchanging particles i and $i+1$ with the operator σ_i, illustrated in Fig. 2.1.. By convention we choose the exchange to be counterclockwise through the operator σ_i. These exchanges form

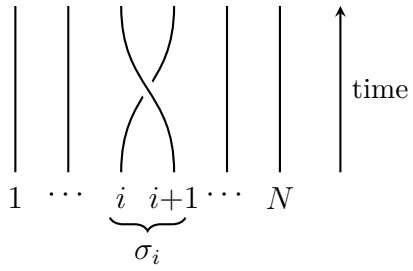

Figure 2.1: The braid generator σ_i exchanges neighbouring particles i and $i+1$. Time flows upward, so each line is the worldline of a particle. By convention σ_i denotes the counterclockwise exchange; here strand $i{+}1$ passes over strand i. The inverse σ_i^{-1} corresponds to the opposite (clockwise) crossing, in which strand $i{+}1$ passes under. In contrast to a transposition in the permutation group, a double exchange σ_i^2 leaves both particles in their original positions but is a non-trivial braid that cannot be undone in the plane, i.e. $\sigma_i^2 \neq 1$.

the braid group B_N, which differs fundamentally from the permutation group. For N particles, the braid group is generated by $\sigma_1, \sigma_2, \ldots, \sigma_{N-1}$ and obeys the relations

$$\begin{aligned} \sigma_i\sigma_j &= \sigma_j\sigma_i \quad \text{for } |i-j|>1 \\ \sigma_i\sigma_{i+1}\sigma_i &= \sigma_{i+1}\sigma_i\sigma_{i+1}. \end{aligned} \tag{2.8}$$

Unlike the permutation group, $\sigma_i^2 \neq 1$, allowing more general representations [80, 91].

2.2.2 Abelian and non-Abelian Anyons

There are two categories of anyons, Abelian and non-Abelian. For Abelian anyons, the effect of an exchange is a global phase θ [32]. When two anyons are exchanged, the wavefunction transforms as

$$\psi(\mathbf{r}_1, \mathbf{r}_2) \to e^{i\theta}\psi(\mathbf{r}_2, \mathbf{r}_1). \tag{2.9}$$

Performing the exchange twice gives

$$\psi(\mathbf{r}_1, \mathbf{r}_2) \to e^{2i\theta}\psi(\mathbf{r}_1, \mathbf{r}_2). \tag{2.10}$$

Bosons correspond to $\theta = 0$, fermions to $\theta = \pi$, and anyons have $0 < \theta < \pi$ [38] . In general, the topological interaction between anyons of different types a and b is encoded by mutual statistics θ_{ab}, the phase acquired when anyon of type a encircles anyon of type b. These phases define the statistics and can be fractional, which

underpins phenomena like the fractional quantum Hall effect [92].

In addition to Abelian anyons, there exist non-Abelian anyons whose exchange operations correspond to non-commuting unitary transformations acting on a degenerate ground-state manifold. In such systems, the many-body wavefunction does not simply pick up a scalar phase $e^{i\theta}$ upon particle exchange; instead, the system's state vector is rotated within a multidimensional Hilbert space that depends on the braiding history of the particles. Consequently, successive exchanges of non-Abelian anyons do not, in general, commute, giving rise to rich topological quantum statistics distinct from both bosons, fermions, and Abelian anyons.

The presence of non-Abelian anyons implies that the ground state of the system is degenerate. This degeneracy arises because different exchanges of anyons, known as fusion channels, correspond to orthogonal ground states with identical energy, as long as the particles remain spatially well separated and the bulk energy gap remains open. Since no local operator can distinguish between these globally different fusion outcomes, the degeneracy is intrinsically robust against local perturbations. The collection of these degenerate ground states forms a finite-dimensional Hilbert space in which the braiding operations are represented by unitary matrices and act as unitary transformations [32, 41, 93].

Suppose there are g-fold degenerate ground states $\{\psi_\alpha\}_{\alpha=1}^{g}$ associated with a fixed configuration of non-Abelian anyons. When the two neighbouring anyons at positions i and $i+1$ are exchanged, the system remains in the degenerate ground-state manifold, but the wavefunction undergoes a nontrivial unitary transformation described by

$$\psi_\alpha \longrightarrow \sum_{\beta=1}^{g} \rho(\sigma_i)_{\alpha\beta}\, \psi_\beta, \tag{2.11}$$

where σ_i is the braid generator introduced above, which exchanges the anyons in positions i and $i+1$ (with $i = 1, \ldots, N-1$ for N anyons), and $\rho(\sigma_i) \in U(g)$ is its unitary representation. It is important to distinguish the two index families appearing here: the positional index i specifies which adjacent pair of anyons is braided, whereas the indices $\alpha, \beta = 1, \ldots, g$ label the basis states of the g-fold degenerate ground-state manifold on which the matrix $\rho(\sigma_i)$ acts. The matrices $\rho(\sigma_i)$ act on the g-dimensional Hilbert space spanned by the degenerate ground states. Since ρ is a representation (a group homomorphism) of the braid group B_N, these matrices inherit the braid

relations,

$$\begin{aligned} \rho(\sigma_i)\,\rho(\sigma_j) &= \rho(\sigma_j)\,\rho(\sigma_i) \qquad\qquad \text{for } |i-j|>1, \\ \rho(\sigma_i)\,\rho(\sigma_{i+1})\,\rho(\sigma_i) &= \rho(\sigma_{i+1})\,\rho(\sigma_i)\,\rho(\sigma_{i+1}). \end{aligned} \tag{2.12}$$

Physically, the set of all unitary operations that can be realised by adiabatically braiding the N anyons is the image of the representation ρ, i.e. the subgroup of $U(g)$ generated by the braid matrices $\rho(\sigma_i)$:

$$\rho(B_N) \;=\; \Big\langle\, \rho(\sigma_1),\, \rho(\sigma_2),\, \ldots,\, \rho(\sigma_{N-1}) \,\Big\rangle \;\subseteq\; U(g), \tag{2.13}$$

that is, all unitary transformations obtainable by composing the elementary braids. The explicit form of $\rho(\sigma_i)$ (and hence $U(g)$) depends on the underlying topological field theory that describes the anyons, such as $\mathrm{SU}(2)_k$ Chern–Simons theory, the Ising anyon model, or the Moore–Read state in the fractional quantum Hall effect [32, 41, 42]. In practice, these matrices are obtained by solving the consistency relations of the braiding rules of the anyons, as we will illustrate in our examples.

Braiding operations do not commute in general

$$[\rho(\sigma_i), \rho(\sigma_j)] \neq 0 \quad \text{for some } i, j \tag{2.14}$$

This non-commutativity is the signature of non-Abelian statistics and underlies their potential use for topological quantum computing, where quantum gates are implemented by physically braiding particles. Unlike Abelian anyons, whose braiding results only in an overall phase factor and therefore cannot transform quantum states within a degenerate manifold [13, 26, 32], non-Abelian anyons act as non-commuting unitary operators on a topologically protected ground-state subspace. This property allows braiding to implement robust quantum gates, with information encoded nonlocally and thus intrinsically protected against local sources of decoherence [26, 32, 39].

2.2.3 Fusion Channels and Topological Charges

In systems hosting anyons, not only can particles be braided around one another, but they can also be fused together. Fusion describes the process of adiabatically bringing two anyons to within a separation much smaller than their distance to all other anyons, so that the pair appears from outside as a single composite excitation

with a definite total topological charge. The fusion rules describe the possible values c of this combined charge when anyons of types a and b are fused. The outcome is unique for Abelian anyons and generally multi-valued for non-Abelian anyons. This behaviour is governed by fusion rules [32, 94, 95]. Fusion rules describe the possible outcomes when two anyons of types a and b are brought together. Mathematically, this is written as

$$a \times b = \sum_c N_{ab}^c \, c, \tag{2.15}$$

where:

- c labels all the possible resulting particle types,
- $N_{ab}^c \in \mathbb{Z}_{\geq 0}$ counts how many times type c appears in the fusion of a and b.

If $N_{ab}^c = 0$, then fusion into c is forbidden. If $N_{ab}^c > 1$, the fusion space is degenerate and spans multiple orthogonal states. A prototypical example of non-Abelian anyons is the Ising anyon model, relevant to Majorana zero modes [32, 44, 50] (we will discuss this in 2.4). This model includes three types of particles:

- 1: the vacuum (trivial particle),
- σ: the non-Abelian anyon (associated with Majorana zero modes),
- ψ: a fermionic excitation.

The fusion rules are

$$\begin{aligned} \sigma \times \sigma &= 1 + \psi \\ \sigma \times \psi &= \sigma \\ \psi \times \psi &= 1 \end{aligned} \tag{2.16}$$

These rules imply that fusing two σ-anyons may result in either the vacuum or a fermion ψ. In section 2.2.4 we will illustrate the basics of topological quantum computing with this model. It is important to note that these fusion rules are axioms of the effective topological quantum field theory defining the Ising anyon model, rather than properties derived from a microscopic system.

2.2.4 Fusion Spaces

When multiple anyons are present, the total fusion space becomes a high-dimensional Hilbert space [32, 40]. The Ising fusion rules in Eq. (2.16) imply that each pair of σ anyons can fuse either into the vacuum (1) or into the fermion (ψ) channel. When

multiple anyons are present, the number of possible consistent fusion outcomes grows exponentially with n, but the total topological charge constraint reduces the count by one binary factor, yielding a Hilbert space of dimension 2^{n-1} [32, 43, 95]. Therefore, for a system of $2n$ Ising anyons with their topological charged being constrained to the vacuum sector 1, the dimension of the corresponding fusion space (or degenerate ground-state manifold) is 2^{n-1}. Each allowed fusion path defines a state in this space, often visualized using fusion trees, where branching represents intermediate fusion outcomes. A schematic representation of this process is shown below

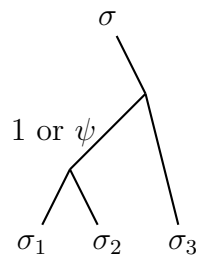

Figure 2.2: Fusion tree for three Ising anyons. The figure is read from bottom to top. The intermediate fusion channel between σ_1 and σ_2 can be either the vacuum 1 or the fermion ψ, leading to a two-dimensional fusion space [94, 95].

Each anyon carries a topological charge, a label that defines the superselection sector it belongs to. A superselection rule means that the topological charge commutes with every local observable, so that all local operators are block-diagonal with respect to these sectors [32, 42]. The statement that states of different topological charge "cannot be coherently superposed" is thus an in-principle one rather than a practical limitation: although such a superposition can be written down formally, no local operator possesses matrix elements between the two sectors, so the relative phase between them is unobservable by any local measurement, and the superposition is physically indistinguishable from an incoherent (classical) mixture. What singles out topological charge is its non-locality, meaning that it cannot be created, altered, or detected by any operator acting within a bounded region, but only by a non-local process such as bringing in another anyon or braiding a test anyon around it. It is precisely this requirement of non-locality that protects the quantum information encoded in the topological charge from local noise, while still permitting its manipulation through controlled non-local (braiding) operations. In systems with topological order, each distinct type of anyon then defines a separate superselection sector, and the possible charge combinations obey the system's fusion rules.

The set of all topological charges in a theory forms a fusion algebra, which includes

the vacuum as identity and is associative under fusion. Each topological charge a is associated with a quantum dimension d_a, which characterizes how the dimension of the fusion space grows as more anyons of type a are added to the system. Mathematically, the quantum dimensions satisfy the fusion algebra constraint

$$d_a d_b = \sum_c N_{ab}^{\ c}\, d_c, \tag{2.17}$$

where $N_{ab}^{\ c}$ are the fusion coefficients appearing in the rules $a \times b = \sum_c N_{ab}^{\ c}\, c$. Formally, if n identical anyons of type a are fused together, the total dimension of the resulting Hilbert space scales asymptotically as d_a^n for large n. For Abelian anyons, the fusion outcome is unique, so $d_a = 1$. In contrast, non-Abelian anyons can fuse in multiple distinct ways, leading to $d_a > 1$. The quantum dimension thus quantifies the internal degrees of freedom associated with each anyon type and determines the system's total topological ground-state degeneracy on nontrivial manifolds For Abelian anyons, $d_a = 1$. Applying this relation to the Ising fusion rules gives

$$d_\sigma^2 = d_1 + d_\psi, \qquad d_\sigma d_\psi = d_\sigma, \qquad d_\psi^2 = d_1.$$

Since the vacuum 1 always has dimension $d_1 = 1$, the second and third equations imply $d_\psi = 1$. Substituting into the first equation yields

$$d_\sigma^2 = 1 + 1 = 2 \quad \Rightarrow \quad d_\sigma = \sqrt{2}.$$

Therefore, the quantum dimensions for the Ising theory are

$$d_1 = 1, \qquad d_\psi = 1, \qquad d_\sigma = \sqrt{2}. \tag{2.18}$$

These values indicate that the vacuum and the fermion ψ are Abelian particles (since $d = 1$), while the non-Abelian anyon σ has a quantum dimension $d_\sigma = \sqrt{2}$, reflecting its two possible fusion outcomes and the resulting internal fusion-space degeneracy. A non-integer quantum dimension may at first appear puzzling, since the Hilbert space of any finite collection of anyons is necessarily of integer dimension. The resolution is that d_a is not the dimension of a single anyon's state space, but rather the asymptotic rate at which the collective fusion-space dimension grows as anyons of type a are added. For N such anyons, the dimension scales as d_a^N. For Abelian particles ($d = 1$) this rate is unity, so no additional states are generated and no quantum information can be stored. For the non-Abelian σ anyon, $d_\sigma = \sqrt{2}$ means that each additional

σ multiplies the available Hilbert space by $\sqrt{2}$ asymptotically, so that a pair of σ anyons contributes a two-dimensional space (one qubit). The non-integer value reflects the fundamentally non-local character of this degeneracy: a single σ anyon does not possess a well-defined state space of its own, and only collections of anyons do.

2.3 Topological Quantum Computing with Non-Abelian Anyons

Topological quantum computing (TQC) leverages the exotic properties of non-Abelian anyons to encode and manipulate quantum information in a way that is intrinsically protected from local sources of noise, including local fluctuations in electric and magnetic fields, lattice vibrations (phonons), charge impurities, or other forms of environmental coupling that induce unwanted transitions or dephasing of the qubit states [26, 32, 96]. This protection arises from the non-local nature of the topological degrees of freedom associated with anyons. In TQC, qubits are encoded in the fusion space of non-Abelian anyons. Consider the Ising anyons (σ) with their first fusion rule

$$\sigma \times \sigma = 1 + \psi. \tag{2.19}$$

A qubit can be encoded using four σ-anyons with total topological charge fixed to the vacuum [26, 32] . The two basis states correspond to two distinct fusion paths, that is, two possible sequences of intermediate fusion outcomes consistent with the overall constraint of total topological charge being the vacuum. In a system of four Ising anyons $(\sigma_1, \sigma_2, \sigma_3, \sigma_4)$, one convenient choice of fusion path is to first fuse the pair (σ_1, σ_2), and then combine the result with the remaining two anyons. The two possible fusion outcomes of the first pair define the logical basis states:

$$|0\rangle \equiv (\sigma_1 \times \sigma_2 \to 1), \qquad |1\rangle \equiv (\sigma_1 \times \sigma_2 \to \psi),$$

where the total fusion outcome of all four anyons is constrained to the vacuum. This choice of fusion order defines one particular fusion basis [32, 94, 95].

Braiding anyons around each other implements unitary operations on the degenerate fusion-space manifold. In the Ising anyon model, exchanging two σ anyons corresponds to applying a braid operator $\rho(\sigma_i)$ that acts nontrivially on the qubit basis. For

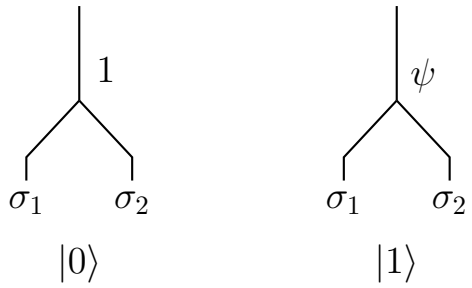

Figure 2.3: Fusion-tree basis for an Ising-anyon qubit with total topological charge fixed to the vacuum: $|0\rangle \equiv (\sigma_1 \times \sigma_2 \to 1)$ and $|1\rangle \equiv (\sigma_1 \times \sigma_2 \to \psi)$ (see, e.g., [32, 95]).

example, exchanging σ_1 and σ_2 performs the unitary transformation

$$\rho(\sigma_1) = e^{-i\frac{\pi}{8}} \begin{pmatrix} 1 & 0 \\ 0 & i \end{pmatrix},$$

which acts as a phase gate (also known as the $\pi/4$ or T-gate up to an overall phase) on the computational basis $\{\, |0\rangle, |1\rangle \,\}$ defined earlier. Because these braiding operations do not depend on the microscopic details of the trajectories of particles, they are intrinsically fault-tolerant and robust to local sources of noise [32, 43, 95]. This robustness can be made precise at the level of the computational basis. Because the states $|0\rangle$ and $|1\rangle$ are distinguished only by the non-local fusion channel of well-separated anyons, they are locally indistinguishable, meaning that any operator O_{loc} supported in a bounded region acts within the computational subspace as a multiple of the identity, up to corrections exponentially small in the anyon separation L,

$$\langle i|\, O_{\text{loc}}\, |j\rangle = c\, \delta_{ij} + \mathcal{O}\Big(e^{-L/\xi}\Big), \tag{2.20}$$

where ξ is the correlation length. A local perturbation can therefore neither connect the two basis states, so there is no bit-flip error, since $\langle 0|\, O_{\text{loc}}\, |1\rangle \approx 0$ nor distinguish them, so there is no dephasing, since $\langle 0|\, O_{\text{loc}}\, |0\rangle \approx \langle 1|\, O_{\text{loc}}\, |1\rangle$. The encoded information is thus invisible to local noise.

To determine how the braid operator $\rho(\sigma_1)$ acts on the qubit encoded in four Ising anyons, we start from the algebraic structure of the Ising anyon model

$$\sigma \times \sigma = 1 + \psi, \qquad \sigma \times \psi = \sigma, \qquad \psi \times \psi = 1.$$

For four σ anyons $(\sigma_1, \sigma_2, \sigma_3, \sigma_4)$ with total topological charge fixed to the vacuum 1, the Hilbert space is two-dimensional, spanned by the basis $|0\rangle, |1\rangle$. It is worth

clarifying why four σ anyons (two pairs), where each is able to fuse to 1 or ψ, encode a two-dimensional space rather than a four-dimensional one. Without any constraint on the total charge, the two pairwise fusion outcomes a (for $\sigma_1 \times \sigma_2$) and b (for $\sigma_3 \times \sigma_4$) would indeed give $2 \times 2 = 4$ states. However, the total topological charge of all four anyons is the fusion $a \times b$, and fixing it to the vacuum requires $a \times b = 1$. By the Ising fusion rules this holds only when $a = b$ (since $1 \times 1 = \psi \times \psi = 1$, whereas $1 \times \psi = \psi$), so the two pairs are forced to fuse into the same channel. The outcome of the second pair is locked to that of the first and is not an independent degree of freedom. Only one binary label therefore remains, which is the common fusion channel of the pairs, and it gives the two basis states

$$|0\rangle = |(\sigma_1\sigma_2)_1, (\sigma_3\sigma_4)_1\rangle\,, \qquad |1\rangle = |(\sigma_1\sigma_2)_\psi, (\sigma_3\sigma_4)_\psi\rangle\,, \tag{2.21}$$

in agreement with the dimension $2^{n-1} = 2^{2-1} = 2$ established above. Figure 2.2 accordingly labels the qubit by the fusion channel of a single pair, the channel of the remaining pair being fixed by the total-charge constraint. This also explains why four anyons, rather than two, are required to encode one qubit: for a single pair, fixing the total charge to the vacuum forces the unique outcome $\sigma_1 \times \sigma_2 = 1$, leaving no free label and hence no qubit.

The operator $\rho(\sigma_i)$ represents the effect of exchanging the i-th and $(i+1)$-th anyons counterclockwise. For the Ising theory, these operators form a non-Abelian representation of the braid group B_n. The elementary exchange of two anyons is governed by the R-matrix

$$R_c^{ab} : V_c^{ab} \to V_c^{ba}, \tag{2.22}$$

which introduces a phase factor depending on the fusion channel c. For two σ anyons,

$$R_1^{\sigma\sigma} = e^{-i\pi/8}, \qquad R_\psi^{\sigma\sigma} = e^{i3\pi/8}.$$

These phases are derived from the conformal spins of the Ising primary fields $h_1 = 0$, $h_\sigma = 1/16$, and $h_\psi = 1/2$, through

$$R_c^{\sigma\sigma} = e^{-i\pi(h_c - 2h_\sigma)}.$$

The exchange of σ_1 and σ_2 acts within a fixed fusion channel, since both anyons are

fused first in our chosen basis. Therefore, $\rho(\sigma_1)$ is diagonal in the $\{|0\rangle, |1\rangle\}$ basis:

$$\rho(\sigma_1) = \begin{pmatrix} R_1^{\sigma\sigma} & 0 \\ 0 & R_\psi^{\sigma\sigma} \end{pmatrix} = e^{-i\pi/8} \begin{pmatrix} 1 & 0 \\ 0 & i \end{pmatrix}.$$

This unitary operation multiplies the two basis states by different topological phases, implementing a relative $\pi/2$ phase rotation between $|0\rangle$ and $|1\rangle$. Up to a global phase, this corresponds to the phase gate $S = \mathrm{diag}(1, i)$, a Clifford gate (in some conventions called the $\pi/4$ phase gate). Note that this is *distinct* from the non-Clifford T (or $\pi/8$) gate $\mathrm{diag}(1, e^{i\pi/4})$:

$$\rho(\sigma_1) \sim \begin{pmatrix} 1 & 0 \\ 0 & i \end{pmatrix}.$$

This operator acts on the encoded qubit purely through the topological exchange of σ_1 and σ_2 and it depends only on the braid topology, not on microscopic details of motion [32, 43, 95].

The single-qubit construction generalizes directly. Since $2n$ Ising anyons with total topological charge fixed to the vacuum span a fusion space of dimension 2^{n-1}, encoding two logical qubits (a four-dimensional space) requires $2^{n-1} = 4$, i.e. $n = 3$, or six σ anyons $(\sigma_1, \ldots, \sigma_6)$ with total charge 1. Grouping them into three pairs $(\sigma_1\sigma_2)$, $(\sigma_3\sigma_4)$, $(\sigma_5\sigma_6)$, each pair fuses to a channel $a, b, c \in \{1, \psi\}$. The total-charge constraint $a \times b \times c = 1$ fixes the third channel in terms of the first two, $c = a \times b$ (each Ising charge being its own inverse), leaving two free binary labels that are precisely the two logical qubits. Identifying the channel 1 with $|0\rangle$ and ψ with $|1\rangle$, and assigning the first qubit to $(\sigma_1\sigma_2)$ and the second to $(\sigma_3\sigma_4)$, the computational basis is

$$\begin{aligned} |00\rangle &= |(\sigma_1\sigma_2)_1,\, (\sigma_3\sigma_4)_1,\, (\sigma_5\sigma_6)_1\rangle\,, \\ |01\rangle &= |(\sigma_1\sigma_2)_1,\, (\sigma_3\sigma_4)_\psi,\, (\sigma_5\sigma_6)_\psi\rangle\,, \\ |10\rangle &= |(\sigma_1\sigma_2)_\psi,\, (\sigma_3\sigma_4)_1,\, (\sigma_5\sigma_6)_\psi\rangle\,, \\ |11\rangle &= |(\sigma_1\sigma_2)_\psi,\, (\sigma_3\sigma_4)_\psi,\, (\sigma_5\sigma_6)_1\rangle\,, \end{aligned} \tag{2.23}$$

where the third pair $(\sigma_5\sigma_6)$ is kept to the first two so as to keep the total charge in the vacuum sector. The four states are those containing an even number of ψ pairs, consistent with $\dim \mathcal{H} = 2^{n-1} = 4$. In practice a "sparse" encoding using eight anyons (two independent groups of four), $(\sigma_1 \ldots \sigma_4)$ and $(\sigma_5 \ldots \sigma_8)$, each with its own sub-charge fixed to the vacuum is often preferred, since it keeps the two qubits in separate fusion subspaces and reduces leakage out of the computational space during

braiding. The six-anyon encoding above is the minimal one; both are consistent with the rule that $2n$ anyons of fixed total charge encode $n-1$ logical qubits.

For Ising anyons, braiding alone is not computationally universal [32, 97]. The reason can be read directly from the braid relations of Eq. (2.2.2): the generators $\rho(\sigma_i)$ they constrain generate only a finite subgroup of the unitary group, which for the Ising theory is (a subgroup of) the Clifford group. The single-pair exchange computed above gives the phase gate $S = \mathrm{diag}(1, i)$, while braiding within and between groups of four anyons generates the Hadamard gate and an entangling two-qubit gate; together these are the Clifford operations. By the Gottesman–Knill theorem, any circuit composed solely of Clifford gates can be simulated efficiently on a classical computer [27, 98], so the Clifford group is not universal. What braiding cannot produce is a non-Clifford gate such as the T (or $\pi/8$) gate $T = \mathrm{diag}(1, e^{i\pi/4})$, which lies outside the finite image $\rho(B_N)$. Universality is recovered only by supplementing braiding with such a gate, for instance through magic-state distillation [29] or a non-topologically protected operation. This limitation motivates the search for richer anyon models whose braiding is computationally universal, which we turn to next. The operators $\rho(\sigma_i)$ represent the elementary exchanges (or braids) of the i-th and $(i+1)$-th anyons. These exchanges are not simple swaps, but rather topologically distinct operations corresponding to one particle moving counterclockwise around another in two dimensions. The set of all possible braids of N anyons forms a group, known as the braid group B_N, whose generators $\{\sigma_1, \sigma_2, \ldots, \sigma_{N-1}\}$ obey the relations in Eq. 2.2.2. These relations are known as the Yang-Baxter equation [32, 99, 100]. It encodes the associativity of three consecutive exchanges: braiding particles i and $i+1$ first, then $(i+1)$ and $(i+2)$, produces the same overall braid as doing them in the opposite order. Geometrically, this ensures that different smooth deformations of the same braid correspond to the same topological operation.

The second relation,

$$\rho(\sigma_i)\rho(\sigma_j) = \rho(\sigma_j)\rho(\sigma_i) \quad \text{for } |i-j| \geq 2,$$

means that exchanges of well-separated pairs of anyons commute: braiding disjoint pairs in either order yields the same final state.

Together, these relations define a non-Abelian group when the $\rho(\sigma_i)$ are represented by non-commuting unitary matrices, as in the case of non-Abelian anyons. Thus, the exchange (braiding) operations generate a non-trivial representation of B_N on the degenerate fusion Hilbert space, forming the foundation of topological quantum

computation [26, 32, 95].

Another anyonic model is the Fibonacci anyons. Fibonacci anyons can achieve universality through braiding alone [29, 32, 101]. The Fibonacci theory has a single nontrivial anyon τ (besides the vacuum 1) with fusion

$$\tau \times \tau = 1 + \tau. \tag{2.24}$$

It is the minimal non-Abelian model whose braiding is computationally universal. The quantum dimensions $\{d_a\}$ satisfy the fusion–algebra constraint

$$d_a\, d_b = \sum_c N_{ab}^{\ c}\, d_c, \tag{2.25}$$

where $N_{ab}^{\ c}$ are the fusion coefficients [32, 42, 95]. For the Fibonacci theory,

$$d_\tau^2 = d_1 + d_\tau = 1 + d_\tau. \tag{2.26}$$

Thus d_τ satisfies the quadratic

$$d_\tau^2 - d_\tau - 1 = 0, \tag{2.27}$$

whose positive root is the golden ratio φ

$$d_\tau = \frac{1+\sqrt{5}}{2} = \varphi. \tag{2.28}$$

The non-Abelian fusion rule of this model implies that the Hilbert-space dimension grows non-trivially with the number of anyons. The dimension of the fusion space for n τ-anyons with total topological charge fixed to 1 or τ is given by the $(n-1)$-th Fibonacci number F_{n-1}

$$\dim \mathcal{H}_n^{(a)} = F_{n-1}, \tag{2.29}$$

where a denotes the total topological charge [32, 94, 95].

(i) Three-τ encoding. For three τ anyons, the possible fusion channels can be found recursively:

$$(\tau_1 \times \tau_2) \times \tau_3.$$

The first pair $\tau_1 \times \tau_2$ can fuse into either 1 or τ. If the total charge of all three anyons is constrained to τ, only the following two fusion paths are consistent:

$$|0\rangle \equiv ((\tau_1 \times \tau_2 \to 1) \times \tau_3 \to \tau), \tag{2.30}$$

$$|1\rangle \equiv ((\tau_1 \times \tau_2 \to \tau) \times \tau_3 \to \tau). \tag{2.31}$$

These two independent fusion channels form a two-dimensional fusion space, which can be used to encode a single logical qubit. The total charge being τ ensures the system remains within a nontrivial topological sector.

(ii) Four-τ encoding. Similarly, for four anyons,

$$((\tau_1 \times \tau_2) \times \tau_3) \times \tau_4,$$

and the total charge is now fixed to 1 (the vacuum). The allowed intermediate fusion outcomes yield again two consistent paths:

$$|0\rangle \equiv ((\tau_1 \times \tau_2 \to 1) \times (\tau_3 \times \tau_4 \to 1) \to 1), \tag{2.32}$$

$$|1\rangle \equiv ((\tau_1 \times \tau_2 \to \tau) \times (\tau_3 \times \tau_4 \to \tau) \to 1). \tag{2.33}$$

Thus, the logical subspace spanned by $|0\rangle$ and $|1\rangle$ is two-dimensional. This encoding is topologically equivalent to the three-τ construction, but with total charge 1 instead of τ.The four-anyon scheme is often preferred for two related reasons. First, fixing the total topological charge (equivalently, the total fermion parity) of the group of four anyons confines all braiding operations to a single charge-conserving subspace. Braids permute the basis states within this subspace without leaking the qubit into a sector of different total charge, so the encoded information remains protected. Second, this encoding is naturally compatible with measurement-only topological quantum computation [94], in which logical gates are realized not by physically transporting anyons but by an adaptive sequence of joint topological-charge (parity) measurements of anyon pairs. Since the qubit is defined through the fusion channels (pair parities) of the four anyons, the same measurements that define the qubit can be used to manipulate and read it out, making the four-anyon unit the natural building block for measurement-based architectures [33]. It should be emphasized that Fibonacci anyons have not yet been unambiguously realized in any physical system. The leading candidate is the $\nu = 12/5$ fractional quantum Hall plateau, proposed to be described by the $k = 3$ Read–Rezayi state, whose quasiparticles include Fibonacci

anyons [102, 103]; numerical density-matrix renormalization-group studies support this identification, but the non-Abelian nature of the state remains experimentally unconfirmed and the plateau is fragile. Engineered platforms have also been proposed, for example coupled networks of parafermion modes in superconductor-quantum-Hall heterostructures [86]. More recently, the non-Abelian braiding of Fibonacci anyons has been emulated digitally on a superconducting quantum processor [104], demonstrating the braiding rules in a synthetic setting, though this is a programmable simulation rather than a solid-state realization. Fibonacci anyons therefore remain, at present, primarily a theoretical model, albeit one of great interest, since their braiding alone is computationally universal.

In both cases, the two possible fusion channels form a logical qubit:

$$\mathcal{H}_{\text{logical}} = \text{span}\{\,|0\rangle, |1\rangle\,\}. \tag{2.34}$$

Because braiding of τ anyons corresponds to unitary transformations that depend only on the topology of the exchange, this qubit enjoys intrinsic protection from local sources of noise. Furthermore, Fibonacci anyons are computationally universal: their braiding matrices densely generate the full unitary group $SU(2)$ on this two-dimensional logical space [32, 95, 105].

We use $\rho(\sigma_i)$ for the braid representation on the fusion space of three τ anyons τ_1, τ_2, τ_3, consistent with earlier notation. To write $\rho(\sigma_i)$ explicitly we first define the F-matrix, which encodes the associativity of anyon fusion at the level of Hilbert spaces.

For three anyons of types a, b, c fusing to a total charge d, the fusion can be carried out in two natural orders: either by fusing a and b first into an intermediate charge e and then fusing the result with c, or by fusing b and c first into an intermediate charge f and then fusing with a. Each order provides a basis of the same fusion space, indexed by the allowed intermediate charge. The F-matrix F_d^{abc} is the unitary transformation between these two bases,

$$\Big|(ab)_e\, c \to d\Big\rangle \;=\; \sum_f \Big[F_d^{abc}\Big]_{ef} \Big|a\,(bc)_f \to d\Big\rangle, \tag{2.35}$$

with e running over the allowed channels of $a \times b$ and f over those of $b \times c$. The F-symbols are not free. They are constrained, up to gauge, by the pentagon equation, which requires that the different sequences of F-moves on any fusion tree of four anyons commute [32, 42, 95]. Together with the R-matrix encoding pairwise exchange

(constrained by an analogous hexagon equation, the F- and R-symbols specify the modular category that defines a given anyon model.

Specializing to Fibonacci, the only non-trivial F-matrix in the theory is $F_\tau^{\tau\tau\tau}$, since this is the unique choice of external charges (a, b, c, d) for which both intermediate channels can take more than one value ($e, f \in \{1, \tau\}$). The pentagon equation then determines this 2×2 unitary uniquely (up to gauge), as follows. Both fusion orders span the same two-dimensional Hilbert space with total charge τ. The matrix $F^\tau_{\tau\tau\tau}$ is obtained by demanding consistency with the Fibonacci fusion rule $\tau \times \tau = 1 + \tau$ and by solving the pentagon equation, the fundamental associativity condition of anyon fusion [32, 42, 94]. For the Fibonacci theory, this equation uniquely fixes the absolute values of the F-matrix elements (up to overall phases), leading to the simple real orthogonal form expressed in terms of the golden ratio

$$F \equiv F^\tau_{\tau\tau\tau} = \begin{pmatrix} \varphi^{-1} & \varphi^{-1/2} \\ \varphi^{-1/2} & -\varphi^{-1} \end{pmatrix}, \qquad F^{-1} = F^{\mathsf{T}} = F. \tag{2.36}$$

The R-matrix describes the phase accumulated when two anyons are exchanged (braided) within a given fusion channel, given in EQ. (2.22). For Fibonacci anyons, the only nontrivial fusion channel is $\tau \times \tau = 1 + \tau$, so the exchange operator is diagonal in the channel basis:

$$R \equiv R^{\cdot}_{\tau\tau} = \begin{pmatrix} R^1_{\tau\tau} & 0 \\ 0 & R^\tau_{\tau\tau} \end{pmatrix} = \begin{pmatrix} e^{-4\pi i/5} & 0 \\ 0 & e^{+3\pi i/5} \end{pmatrix}. \tag{2.37}$$

The specific phases $e^{-4\pi i/5}$ and $e^{3\pi i/5}$ are determined by the topological spins $h_1 = 0$ and $h_\tau = 2/5$ of the Fibonacci conformal field theory via

$$R^{\tau\tau}_c = e^{-2\pi i(h_c - 2h_\tau)}. \tag{2.38}$$

These values ensure consistency with the hexagon equations, which enforce compatibility between fusion and braiding operations. Conventions differing by overall phases are physically equivalent; the choice above follows the standard unitary normalization used in Refs. [32, 80, 94, 95].

For three anyons in the order (τ_1, τ_2, τ_3),

$$\rho(\sigma_1) = R = \begin{pmatrix} e^{-4\pi i/5} & 0 \\ 0 & e^{+3\pi i/5} \end{pmatrix}, \qquad \rho(\sigma_2) = F^{-1}RF \;=\; FRF. \tag{2.39}$$

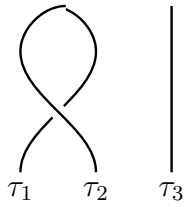

Figure 2.4: Schematic braid on three Fibonacci anyons (exchange of strands 1 and 2). Adapted from [32].

These two unitaries satisfy the braid relation $\rho(\sigma_1)\rho(\sigma_2)\rho(\sigma_1) = \rho(\sigma_2)\rho(\sigma_1)\rho(\sigma_2)$ and, under repeated products, generate a set that is dense in SU(2) on the encoded qubit, as shown in Fig. 2.4. Thus braiding Fibonacci anyons alone implements universal gate set [32, 101, 105].

The topological nature of the encoding provides protection against local perturbations. Errors that do not involve braiding or fusion of anyons cannot affect the stored quantum information. This makes TQC inherently fault-tolerant. Topological charge measurements can be performed by fusing anyons and detecting the resulting particle type [26, 32, 94]. We next show a promising candidate for non-Abelian anyons that could be used for TQC.

2.4 Majorana Zero Modes as Non-Abelian Anyons

In this section we introduce Majorana zero modes (MZMs) and how they can be considered as Non-Abelian anyons. MZMs are quasiparticle excitations that emerge at zero energy in certain topological superconductors. We discuss their difference with bosons and fermions and why their topological protection makes them one of the most promising platforms for TQC [32, 43, 50].

2.4.1 From the Dirac equation to Majorana Fermions

The Dirac equation is the fundamental wave equation describing spin-$\frac{1}{2}$ particles such as electrons. It was introduced by Paul Dirac in 1928 [106] in order to combine two key principles of physics: quantum mechanics, which describes the wave-like behavior of particles, and special relativity, which requires that all physical laws take the same form in every inertial reference frame [106].

In natural units we take $\hbar$ and c (speed of light) to be one ($\hbar = c = 1$), the Dirac equation reads

$$(i\gamma^\mu \partial_\mu - m)\,\psi = 0. \tag{2.40}$$

Here each symbol has a clear physical meaning: ψ is the Dirac spinor, a four-component complex wavefunction describing the quantum state of a spin-$\frac{1}{2}$ particle. Two components represent spin-up and spin-down states of a particle, and the other two represent those of its antiparticle [107, 108]. m is the rest mass of the particle, usually expressed in units of energy (for example, electron mass $m_e = 0.511$ MeV). ∂_μ denotes differentiation with respect to spacetime coordinates: $\partial_\mu = (\partial_t, -\nabla)$, where $\partial_t = \frac{\partial}{\partial t}$ and $\nabla = (\partial_x, \partial_y, \partial_z)$. The indices μ and ν label the four spacetime directions $(0, 1, 2, 3)$, corresponding to time and the three spatial dimensions. These indices are summed over whenever repeated (Einstein summation convention).

The γ^μ operators appearing in the Dirac equation are 4×4 matrices that generalize the Pauli matrices to relativistic four-component spinors. They satisfy

$$\{\gamma^\mu, \gamma^\nu\} = 2\,\eta^{\mu\nu}, \qquad \eta^{\mu\nu} = \mathrm{diag}(1, -1, -1, -1), \tag{2.41}$$

which ensures the Lorentz invariance of the Dirac equation [107–109].

A convenient representation for explicit calculations is the chiral (or Weyl) basis, in which the gamma matrices take the block form

$$\gamma^0 = \begin{pmatrix} 0 & I \\ I & 0 \end{pmatrix}, \qquad \gamma^i = \begin{pmatrix} 0 & \sigma^i \\ -\sigma^i & 0 \end{pmatrix}, \qquad (i = 1, 2, 3), \tag{2.42}$$

where the σ^i are the 2×2 Pauli matrices,

$$\sigma^1 = \begin{pmatrix} 0 & 1 \\ 1 & 0 \end{pmatrix}, \quad \sigma^2 = \begin{pmatrix} 0 & -i \\ i & 0 \end{pmatrix}, \quad \sigma^3 = \begin{pmatrix} 1 & 0 \\ 0 & -1 \end{pmatrix}. \tag{2.43}$$

Here, I denotes the 2×2 identity matrix. It is also useful to define the fifth gamma matrix,

$$\gamma^5 = i\,\gamma^0\gamma^1\gamma^2\gamma^3 = \begin{pmatrix} -I & 0 \\ 0 & I \end{pmatrix}. \tag{2.44}$$

In the Dirac representation (often used in relativistic quantum mechanics), the gamma matrices take the form

$$\gamma^0 = \begin{pmatrix} I & 0 \\ 0 & -I \end{pmatrix}, \qquad \gamma^i = \begin{pmatrix} 0 & \sigma^i \\ -\sigma^i & 0 \end{pmatrix}. \tag{2.45}$$

The Dirac and Weyl representations are related by a unitary transformation, so

physical predictions are identical in either basis [109].

Majorana fermions emerge as a special solution to the Dirac equation, obtained by imposing a reality condition on the Dirac field. To understand this, it is helpful to look at how a Dirac spinor can be decomposed and what its components represent physically. A Dirac spinor ψ has four complex components, which can be organized into two two-component spinors:

$$\psi = \begin{pmatrix} \chi_L \\ \chi_R \end{pmatrix}, \tag{2.46}$$

where χ_L and χ_R are known as the left-handed and right-handed components (or chiral components) of the field. This decomposition is most naturally expressed in the Weyl or chiral basis of the Dirac matrices [107, 109].

The labels "left" and "right" refer to the particle's chirality, a property related to how the particle's intrinsic spin is oriented relative to its momentum. For a left-handed (right-handed) particle, the spin points in the opposite (same) direction as its momentum. In the massless limit, chirality coincides with helicity, the direction of spin relative to motion. When mass is introduced, the two components χ_L and χ_R become coupled by the Dirac mass term, allowing a left-handed particle to transform into a right-handed one and vice versa.

In the standard (Dirac or Weyl) representation, one convenient choice is the charge-conjugation matrix $C = -i\gamma^2$, which satisfies $C^{-1}\gamma^\mu C = -(\gamma^\mu)^*$. A Majorana fermion is obtained by requiring $\psi = \psi^c$.

To see the resulting reality condition explicitly, the Dirac spinor decomposes into its left- and right-handed Weyl components, $\psi = (\chi_L, \chi_R)^T$ with $\gamma^5\chi_L = -\chi_L$ and $\gamma^5\chi_R = +\chi_R$. Writing $\gamma^2 = \begin{pmatrix} 0 & \sigma^2 \\ -\sigma^2 & 0 \end{pmatrix}$, the charge-conjugation matrix is block off-diagonal,

$$C = -i\gamma^2 = \begin{pmatrix} 0 & -i\sigma^2 \\ i\sigma^2 & 0 \end{pmatrix}. \tag{2.47}$$

Acting on $\psi^* = (\chi_L^*, \chi_R^*)^T$ gives

$$\psi^c = C\psi^* = \begin{pmatrix} 0 & -i\sigma^2 \\ i\sigma^2 & 0 \end{pmatrix} \begin{pmatrix} \chi_L^* \\ \chi_R^* \end{pmatrix} = \begin{pmatrix} -i\sigma^2\,\chi_R^* \\ i\sigma^2\,\chi_L^* \end{pmatrix}. \tag{2.48}$$

Imposing the Majorana condition $\psi = \psi^c$ and equating components yields

$$\chi_L = -i\sigma^2\,\chi_R^*, \qquad \chi_R = i\sigma^2\,\chi_L^*. \tag{2.49}$$

The two relations are not independent: conjugating the second and using $(\sigma^2)^* = -\sigma^2$ together with $(\sigma^2)^2 = \mathbb{1}$ returns the first, so the Majorana condition expresses χ_R entirely in terms of χ_L. This precisely halves the number of independent components of the field (from two complex Weyl spinors to one). This relation shows that the right-handed part χ_R is not independent but completely determined by the complex conjugate of χ_L. As a result, a Majorana fermion contains only two real degrees of freedom, half that of a Dirac fermion.

The Majorana condition eliminates any distinction between particle and antiparticle states. Because the field equals its own conjugate, it cannot carry an electric charge or any conserved $U(1)$ quantum number. Such a fermion is therefore neutral by definition. This property underlies the concept of Majorana zero modes in condensed-matter systems: localized, charge-neutral quasiparticle excitations that are their own antiparticles and emerge as zero-energy solutions of the effective Dirac equation [33, 74].

2.4.2 Majorana Zero Modes

Having introduced the concept of Majorana fermions as self-conjugate particles, we now turn to their physical realization in condensed-matter systems: Majorana zero modes (MZMs). These are quasiparticle excitations that appear at zero energy in certain superconductors, typically localized at the edges, ends, or topological defects of the system [33, 44, 50, 74].

To describe such a mode at the operator level, an ordinary fermion is described by creation and annihilation operators $c^\dagger$ and c obeying $\{c, c^\dagger\} = 1$ and $c^2 = 0$. A pair of Majorana operators is obtained by taking the Hermitian and anti-Hermitian combinations of these,

$$\gamma_1 = c + c^\dagger, \qquad \gamma_2 = -i\,(c - c^\dagger), \tag{2.50}$$

which invert to reconstruct the fermion,

$$c = \tfrac{1}{2}(\gamma_1 + i\gamma_2), \qquad c^\dagger = \tfrac{1}{2}(\gamma_1 - i\gamma_2). \tag{2.51}$$

By construction, each Majorana operator is its own Hermitian conjugate,

$$\gamma_i = \gamma_i^\dagger, \tag{2.52}$$

which is the operator analogue of the reality condition $\psi = \psi^c$ introduced earlier and expresses that a Majorana mode is its own antiparticle. Using $\{c, c^\dagger\} = 1$ and $c^2 = 0$, the operators in Eq. (2.50) satisfy

$$\{\gamma_i, \gamma_j\} = 2\delta_{ij}, \qquad \gamma_i^2 = 1, \tag{2.53}$$

in contrast to ordinary fermions, for which $c^2 = 0$.

Equations (2.50)–(2.51) make explicit that a single ordinary (Dirac) fermion mode is equivalent to two Majorana modes, and conversely that two Majorana operators combine into one fermion. In this sense a Majorana zero mode represents half of a conventional fermion. The occupation number of the reconstructed fermion is

$$n = c^\dagger c = \tfrac{1}{2}\,(1 + i\gamma_1\gamma_2), \tag{2.54}$$

so its two eigenvalues $n = 0, 1$ are encoded jointly in the pair (γ_1, γ_2) rather than in either operator alone.

MZMs typically arise in systems that combine superconductivity, spin-orbit coupling, and time-reversal-symmetry breaking (for instance, due to a magnetic field) [33, 44, 57, 58]; two such systems are introduced in Chapters 4 and 5. Because they are neither ordinary fermions nor bosons but emergent zero-energy quasiparticles, MZMs are natural candidates to realize the non-Abelian anyons discussed earlier in this chapter. Establishing this connection is what would make the systems that host MZMs useful for topological quantum computation, and it is the central theme pursued in the remainder of this thesis.

2.4.3 Ising Anyons from Majorana Zero Modes

Majorana zero modes (MZMs) provide a concrete physical realization of non-Abelian anyons, specifically of the Ising type [32, 43, 44, 50, 110].

The combined state of the two Majoranas is characterized by their fermion parity, defined as

$$P_{12} = i\gamma_1\gamma_2 = 2n - 1 = \begin{cases} -1, & n = 0 \text{ (even parity)}, \\ +1, & n = 1 \text{ (odd parity)}. \end{cases} \tag{2.55}$$

The parity operator P_{12} distinguishes whether the joint fermionic mode formed by γ_1 and γ_2 is in an even (no unpaired electron) or odd (one unpaired electron) state. Because γ_1 and γ_2 can be localized far apart, the encoded information stored in the parity $P_{12} = \pm 1$ is nonlocal and hence robust against any local perturbations [33, 50].

This structure is precisely that of the Ising anyon model introduced in Section 2.2.2. The name refers to the fact that the three superselection sectors of this anyon theory (the vacuum 1, the non-Abelian anyon σ, and the fermion ψ) coincide with the three primary fields of the two-dimensional critical Ising conformal field theory, with conformal weights $h_1 = 0$, $h_\sigma = 1/16$, and $h_\psi = 1/2$ (the same fields whose conformal spins fixed the R-matrix). Majorana zero modes realize this model under the following identifications: a single MZM carries the non-Abelian charge σ, while the complex fermion

$$f = \tfrac{1}{2}(\gamma_1 + i\gamma_2), \qquad f^\dagger = \tfrac{1}{2}(\gamma_1 - i\gamma_2) \tag{2.56}$$

built from two MZMs carries the fermion charge ψ in its odd-parity (occupied) state and the vacuum charge 1 in its even-parity (empty) state. Combining two Majoranas into one complex fermion therefore corresponds to fusing two σ anyons, $\sigma \times \sigma = 1 + \psi$, with the outcome (1 or ψ) selected by the fermion parity $P_{12} = \pm 1$. In this sense the Majorana system is a physical realization of the fusion and braiding rules of the Ising anyon model [32, 43, 50].

Based on the fermionic parity, when the occupation is even ($n = 0$), the pair fuses to the vacuum (1); when it is odd ($n = 1$), the pair fuses to the fermion (ψ). Therefore, the parity P_{12} distinguishes between the two possible fusion channels of $\sigma_1 \times \sigma_2$, directly linking fermion parity in the Majorana picture to the Ising anyon fusion outcomes [32, 44].

Exchanging two neighbouring Majoranas γ_i and γ_j can be represented via a unitary braid operator

$$U_{ij} = \exp\!\left(\frac{\pi}{4}\,\gamma_i\gamma_j\right). \tag{2.57}$$

To see this, note that the product $\gamma_i\gamma_j$ is anti-Hermitian:

$$(\gamma_i\gamma_j)^\dagger = -\,\gamma_i\gamma_j,$$

so that $\gamma_i\gamma_j$ acts as a generator of infinitesimal unitary rotations. And because $(\gamma_i\gamma_j)^2 = -1$, the exponential of this operator produces a unitary rotation, just as the exponential of Pauli matrices generates rotations in spin space

$$e^{\theta\gamma_i\gamma_j} = \cos\theta + \gamma_i\gamma_j \sin\theta. \tag{2.58}$$

This unitary can be viewed as a rotation by angle 2θ in the two-dimensional plane spanned by (γ_i, γ_j).

Applying this unitary rotation to γ_i and γ_j gives

$$\begin{aligned} e^{\theta\gamma_i\gamma_j}\,\gamma_i\,e^{-\theta\gamma_i\gamma_j} &= \gamma_i\cos(2\theta) + \gamma_j\sin(2\theta), \\ e^{\theta\gamma_i\gamma_j}\,\gamma_j\,e^{-\theta\gamma_i\gamma_j} &= \gamma_j\cos(2\theta) - \gamma_i\sin(2\theta). \end{aligned} \tag{2.59}$$

Setting $\theta = \pi/4$ produces a rotation by 90°:

$$\gamma_i \;\longrightarrow\; \gamma_j, \qquad \gamma_j \;\longrightarrow\; -\gamma_i,$$

which exactly corresponds to the counterclockwise exchange (braiding) of the two Majorana modes.

The operator U_{ij} therefore represents the process of physically exchanging (or winding) the Majorana γ_i around γ_j. Because such an exchange acts nontrivially, U_{ij} performs a non-Abelian unitary transformation that depends only on the topology of the braid, not on microscopic details of the path [32, 43, 44]. These operators form a non-Abelian representation of the braid group, satisfying

$$U_jU_{j+1}U_j = U_{j+1}U_jU_{j+1}, \qquad [U_j, U_k] = 0 \quad (|j-k| \geq 2). \tag{2.60}$$

This non-commutative algebra is what endows Majorana zero modes with non-Abelian exchange statistics, central to topological quantum computation.

Using the Majorana algebra, one can verify that

$$U_{ij}\gamma_iU_{ij}^\dagger = \gamma_j, \qquad U_{ij}\gamma_jU_{ij}^\dagger = -\gamma_i, \qquad U_{ij}\gamma_kU_{ij}^\dagger = \gamma_k \;(k \neq i, j). \tag{2.61}$$

This transformation corresponds to a counterclockwise exchange of γ_i and γ_j. Because the operations for successive exchanges do not generally commute,

$$U_{12}U_{23} \neq U_{23}U_{12},$$

the set of braid operators $\{U_{ij}\}$ provides a non-Abelian representation of the braid group, as was expected for Ising anyons [32, 43].

Four-Majorana Qubit and Braiding Gates. A system containing four Majorana modes $(\gamma_1, \gamma_2, \gamma_3, \gamma_4)$ with fixed total parity $(i\gamma_1\gamma_2)(i\gamma_3\gamma_4) = +1$ defines a two-dimensional Hilbert space, i.e. one logical qubit. Introducing the two pair parities

$P_{12} = i\gamma_1\gamma_2$ and $P_{34} = i\gamma_3\gamma_4$, the total-parity constraint $P_{12}P_{34} = +1$ fixes $P_{34} = P_{12}$. The two parities are not independent, and specifying P_{12} determines P_{34}. We encode one logical qubit (the subscript L denoting the encoded or logical qubit) in this fixed total-parity sector, with logical basis states

$$|0_L\rangle : P_{12} = +1,\ P_{34} = +1, \qquad |1_L\rangle : P_{12} = -1,\ P_{34} = -1. \tag{2.62}$$

The logical information is therefore stored in the shared parity of the two Majorana pairs which is a nonlocal quantity rather than in any single Majorana mode. In the anyonic language, $|0_L\rangle$ corresponds to both pairs fusing to the vacuum channel and $|1_L\rangle$ to both fusing to the fermion channel ψ, consistent with the total charge being fixed to the vacuum.

Within this space, the braid operators act as single-qubit gates:

$$U_{12} = e^{i\frac{\pi}{4}Z}, \qquad U_{23} = e^{i\frac{\pi}{4}X}, \qquad U_{34} = e^{i\frac{\pi}{4}Z}, \tag{2.63}$$

where X and Z are Pauli matrices acting on the encoded qubit subspace. Explicitly, in the computational basis $\{|0_L\rangle, |1_L\rangle\}$, these operators have the matrix forms

$$U_{12} = \begin{pmatrix} e^{i\pi/4} & 0 \\ 0 & e^{-i\pi/4} \end{pmatrix}, \qquad U_{23} = \frac{1}{\sqrt{2}} \begin{pmatrix} 1 & i \\ i & 1 \end{pmatrix}, \qquad U_{34} = \begin{pmatrix} e^{i\pi/4} & 0 \\ 0 & e^{-i\pi/4} \end{pmatrix}. \tag{2.64}$$

The action of these gates on the logical states is then

$$U_{12}|0_L\rangle = e^{\,i\pi/4}|0_L\rangle, \qquad U_{12}|1_L\rangle = e^{-i\pi/4}|1_L\rangle, \tag{2.65}$$

$$U_{23}|0_L\rangle = \tfrac{1}{\sqrt{2}}(|0_L\rangle + i|1_L\rangle), \qquad U_{23}|1_L\rangle = \tfrac{1}{\sqrt{2}}(i|0_L\rangle + |1_L\rangle). \tag{2.66}$$

The operator U_{23} thus performs a $\pi/2$ rotation about the X axis on the Bloch sphere, while U_{12} and U_{34} implement $\pi/2$ rotations about the Z axis.

Since these unitaries do not commute,

$$U_{12}U_{23} \neq U_{23}U_{12},$$

their composition yields a nontrivial rotation in Hilbert space, illustrating the non-Abelian nature of Majorana braiding.

Scaling to Multiple Qubits and Two-Qubit Gates. Each logical qubit uses four Majorana modes with their total parity fixed, as constructed above. This four-Majorana unit is often called a tetron [111]. A register of N logical qubits is built from N such groups, that is $4N$ Majorana modes in total. The total parity of each group is fixed separately, and each group stores one qubit in its own protected parity sector. This per-group scheme is the sparse encoding introduced earlier for anyons. It keeps every qubit in a separate fusion subspace, which reduces leakage out of the computational space during braiding [33, 110]. Adding qubits in a physical device therefore means adding more such groups of Majorana modes, for example more wire segments or more tetrons in a scalable array [111].

Single-qubit gates act inside one group. They are exactly the braids U_{12}, U_{23}, and U_{34} written above, which rotate the encoded qubit about the Z and X axes. Two-qubit gates act between groups. They are obtained by braiding a Majorana of one group with a Majorana of a neighbouring group. The operator has the same form as before,

$$U_{jk} = \exp\Big(\tfrac{\pi}{4}\,\gamma_j\gamma_k\Big), \tag{2.67}$$

now with γ_j belonging to the first qubit and γ_k to the second. This braid does not factorize into separate operations on the two qubits. It therefore entangles them and realizes a two-qubit Clifford gate, equivalent to a controlled-Z gate up to single-qubit gates [32, 44]. In many Majorana platforms these gates are realized without physically moving the Majorana modes. Instead one performs an adaptive sequence of joint fermion-parity measurements of Majorana pairs. The entangling gate uses a pair taken from two different qubits. This measurement-based route is the basis of measurement-only topological quantum computation [94, 111].

Although these braiding rotations are not by themselves sufficient for universal quantum computation, they form the fundamental building blocks of topological quantum gates in Majorana-based qubits [32, 43, 110]. As discussed for Ising anyons, braiding Majorana zero modes generates only the Clifford group, comprising the single-qubit Clifford gates from braids within a four-Majorana qubit together with an entangling two-qubit gate from braids between qubits. By the Gottesman-Knill theorem, this gate set is efficiently classically simulable and therefore not universal [27, 98]. Universality requires supplementing these protected braiding operations with a single non-Clifford gate, the canonical choice being the T (or $\pi/8$) gate. This gate cannot be realized by braiding and must instead be implemented by an unprotected operation. For example, by bringing two Majoranas close together for a controlled

time so that their finite energy splitting accumulates the required dynamical phase, or by coupling the qubit to an ancillary system [110, 111]. Because such operations lack topological protection, they introduce errors. The non-Clifford gate they provide can nonetheless be made fault-tolerant. A noisy auxiliary state prepared by the unprotected operation is purified to arbitrarily high fidelity using only the protected Clifford operations, and then used to apply the T gate by gate teleportation [29]. In this hybrid scheme the bulk of the computation remains topologically protected, and only the comparatively rare non-Clifford gates carry this additional, non-topological cost.

2.5 Physical Realizations of MZMs

While Majorana fermions were originally introduced as mathematical solutions of the Dirac equation by Ettore Majorana in 1937 [48], condensed-matter systems can realize them as emergent quasiparticle excitations in topological superconductors. Over the past two decades, several promising platforms have been theoretically proposed and experimentally explored as hosts for MZMs. These implementations share the key ingredients of superconductivity, spin–orbit coupling, and time-reversal symmetry breaking, which together enable the formation of topological superconducting phases supporting localized zero-energy modes at defects or boundaries [32, 44, 45, 50, 112].

The explicit construction of how these ingredients combine to produce a topological superconducting phase and its localized Majorana zero modes is developed in the following two chapters, which present the two systems studied in this thesis. Chapter 4 introduces the one-dimensional Kitaev chain, the abstract model of a spinless p-wave topological superconductor, in which the Majorana end modes appear most transparently. Chapter 5 then presents the semiconductor-superconductor nanowire of Lutchyn and Oreg [57, 58], in which proximity-induced superconductivity, Rashba spin-orbit coupling, and a Zeeman field that breaks time-reversal symmetry combine to realize an effective spinless p-wave superconductor hosting Majorana zero modes at the wire ends. Each system provides a distinct pathway to realize, manipulate, and potentially braid MZMs, forming the foundation for topological quantum computing. Our overarching goal is to introduce and implement analytical and numerical methods for detecting MZMs, so as to better characterize the topological systems that could serve as a basis for topological quantum computing.

Chapter 3

Methodology

In this chapter, we dive into the theoretical and numerical methods used throughout the rest of the work. The focus is on four different subjects: Exact Diagonalization (ED) sometimes known as Configuration Interaction (CI), Hartree Fock mean field, Variational Quantum Eigensolver (VQE), and Density Matrix Renormalization Group (DMRG). We begin by introducing the many-body problem, first and second quantization notation followed by ED. Spinless and spinful tight-binding (TB) models are provided as examples of ED. We then continue with the mean-field approximations, in particular Hartree Fock method. VQE is then introduced to show how we can formulate the problem of finding the ground state of a many-body system by using a quantum algorithm. Finally we conclude the chapter by presenting the DMRG method, along with Matrix Product States (MPS) and the computational benefits that will be of great use in the many-body problem.

3.1 Many-body Problem

We begin by defining the many-body system. Let us consider N interacting electrons subject to the potential of nuclei [69, 71, 113]. Our Hamiltonian is given by

$$\hat{H} = \sum_{i=1}^{N} \left[-\frac{\hbar^2}{2m^*} \nabla_i^2 + V_{\text{ext}}(\vec{r}_i) \right] + \frac{1}{2} \sum_{i \neq j}^{N} \frac{e^2}{|\vec{r}_i - \vec{r}_j|}. \tag{3.1}$$

The first term in the Hamiltonian corresponds to the kinetic energy of electrons with effective mass m^*. The second term $V_{\text{ext}}(\vec{r}_i)$ is the Coulomb interaction between electrons and ions. If we have M ionic positive charges, $V_{\text{ext}}(\vec{r}_i)$ is given by

$$V_{\text{ext}}(\vec{r}_i) = -\sum_{\alpha=1}^{M} \frac{Z_\alpha e^2}{|\vec{r}_i - \vec{R}_\alpha|}, \tag{3.2}$$

with $\vec{r}_i$ being the electron position, $\vec{R}_\alpha$ the ion position, Z_α the atomic number and e

the electron charge. The final term in Eq. (3.1) describes the Coulomb interaction among pairs of electrons.

We can rewrite the Hamiltonian in terms of one and two-body operators [69, 71, 113]. We introduce a one-body Hamiltonian term $\hat{H}_0$ and a two-body interaction term $\hat{V}_{ee}$,

$$\hat{H} = \hat{H}_0 + \hat{V}_{ee}. \tag{3.3}$$

The one-body part is a sum over the N electrons of a single-particle Hamiltonian h_0,

$$\hat{H}_0 = \sum_{i=1}^{N} h_0(\vec{r}_i), \qquad h_0(\vec{r}) = -\frac{\hbar^2}{2m^*}\nabla^2 + V_{\text{ext}}(\vec{r}). \tag{3.4}$$

Here $\vec{r}_i$ is the position of the i-th electron, and ∇_i differentiates with respect to $\vec{r}_i$. The symbol $\vec{r}$ denotes the position of a single electron. We focus on the single-particle part first. In first quantization, the Hamiltonian acts on a many-electron wavefunction

$$\Psi(\vec{r}_1, \sigma_1; \ldots; \vec{r}_N, \sigma_N), \tag{3.5}$$

where σ_i labels the spin degree of freedom of the i-th electron. This wavefunction contains explicit sums over particle coordinates as well as spin indices.

Second quantization provides a more compact and powerful representation by expressing the Hamiltonian in terms of field operators that create and annihilate particles with a given spin at position $\vec{r}$ [69, 71, 113]. To move from first to second quantization, we introduce the fermionic field operators $\hat{\Psi}_\sigma(\vec{r})$ and $\hat{\Psi}^\dagger_\sigma(\vec{r})$, which annihilate and create, respectively, an electron with spin σ at position $\vec{r}$. These operators satisfy the canonical anticommutation relations

$$\{\hat{\Psi}_\sigma(\vec{r}), \hat{\Psi}^\dagger_{\sigma'}(\vec{r}')\} = \delta_{\sigma\sigma'}\,\delta(\vec{r} - \vec{r}'), \qquad \{\hat{\Psi}_\sigma(\vec{r}), \hat{\Psi}_{\sigma'}(\vec{r}')\} = 0. \tag{3.6}$$

These operators allow us to write the Hamiltonian in a basis-independent way, where both particle labels and spin labels are absorbed into the algebra of the field operators.

In second quantization, a general one-body operator $\hat{O}_1$ that may act on both spatial and spin degrees of freedom is written in the form [69, 71]

$$\hat{O}_1 = \sum_{\sigma,\sigma'} \int d\vec{r}\; \hat{\Psi}^\dagger_\sigma(\vec{r})\, \hat{O}_{\sigma\sigma'}(\vec{r})\, \hat{\Psi}_{\sigma'}(\vec{r}). \tag{3.7}$$

This expression follows from the fact that $\hat{\Psi}^\dagger_\sigma(\vec{r})\hat{\Psi}_{\sigma'}(\vec{r})$ acts on the spin-resolved fermionic density at position $\vec{r}$, while $\hat{O}_{\sigma\sigma'}(\vec{r})$ operates in spin space and may include

spin-independent terms.

Applying this general rule to the single-particle Hamiltonian $\hat{H}_0$, we obtain

$$\hat{H}_0 = \sum_{\sigma,\sigma'} \int d\vec{r}\, \hat{\Psi}^\dagger_\sigma(\vec{r})\, \hat{H}_{0,\sigma\sigma'}(\vec{r})\, \hat{\Psi}_{\sigma'}(\vec{r}). \tag{3.8}$$

This formula expresses the kinetic energy and external one-body potentials, including possible spin-dependent terms, in terms of field operators. The dependence on the spin indices σ and σ' arises from the fact that the single-particle Hamiltonian acts not only in real space but also in spin space [69, 71, 113]. In first quantization, the one-body operator is generally written as

$$\hat{H}_0 = \hat{H}_0(\vec{r}, \vec{p}) \otimes \hat{S}, \tag{3.9}$$

where $\hat{S}$ is a spin operator that acts on the internal spin degree of freedom. If the Hamiltonian is spin-independent (e.g., purely kinetic energy and scalar external potential), then it is proportional to the identity in spin space,

$$\hat{H}_{0,\sigma\sigma'}(\vec{r}) = \left[-\frac{\hbar^2}{2m^*} \nabla^2 + V_{\text{ext}}(\vec{r}) \right] \delta_{\sigma\sigma'}. \tag{3.10}$$

In this case, the operator is diagonal in the spin basis. The advantage is that the particle and spin labels no longer appear explicitly in the many-body wavefunction; instead, fermionic statistics and spin structure are automatically encoded in the anticommutation relations of $\hat{\Psi}_\sigma$ and $\hat{\Psi}^\dagger_\sigma$.

Similarly, a two-body operator of the form

$$\hat{O}_2 = \frac{1}{2} \sum_{\substack{i,j=1 \\ i \neq j}}^{N} \hat{W}(\vec{r}_i, \sigma_i; \vec{r}_j, \sigma_j) \tag{3.11}$$

is written in second quantization as

$$\hat{O}_2 = \frac{1}{2} \sum_{\sigma,\sigma'} \iint d\vec{r}\, d\vec{r}\,'\ \hat{\Psi}^\dagger(\vec{r}, \sigma) \hat{\Psi}^\dagger(\vec{r}\,', \sigma') \hat{W}(\vec{r}, \sigma; \vec{r}\,', \sigma') \hat{\Psi}(\vec{r}\,', \sigma') \hat{\Psi}(\vec{r}, \sigma). \tag{3.12}$$

To proceed further, we expand the field operators in a complete orthonormal set of single-particle orbitals $\{\phi_i(\vec{r})\}$, for example Wannier functions localized at lattice

sites [114, 115]:

$$\hat{\Psi}(\vec{r},\sigma) = \sum_i \phi_i(\vec{r})\,\hat{c}_{i\sigma}, \tag{3.13}$$

$$\hat{\Psi}^\dagger(\vec{r},\sigma) = \sum_i \phi_i^*(\vec{r})\,\hat{c}_{i\sigma}^\dagger. \tag{3.14}$$

Here $\hat{c}_{i\sigma}$ annihilates an electron in orbital i with spin σ, and $\hat{c}_{i\sigma}^\dagger$ creates one electron in orbital i with spin σ. They obey the anti-commutation relations

$$\{\hat{c}_{i\sigma}, \hat{c}_{j\sigma'}^\dagger\} = \delta_{ij}\delta_{\sigma\sigma'}, \qquad \{\hat{c}_{i\sigma}, \hat{c}_{j\sigma'}\} = 0, \qquad \{\hat{c}_{i\sigma}^\dagger, \hat{c}_{j\sigma'}^\dagger\} = 0. \tag{3.15}$$

Substituting the expansion of the field operators gives

$$\begin{aligned}\hat{H}_0 &= \sum_\sigma \int d\vec{r} \left(\sum_i \phi_i^*(\vec{r})\,\hat{c}_{i\sigma}^\dagger\right) H_0(\vec{r}) \left(\sum_j \phi_j(\vec{r})\,\hat{c}_{j\sigma}\right) \\ &= \sum_\sigma \sum_{i,j} \hat{c}_{i\sigma}^\dagger \hat{c}_{j\sigma} \int d\vec{r}\,\phi_i^*(\vec{r})\,H_0(\vec{r})\,\phi_j(\vec{r}).\end{aligned} \tag{3.16}$$

We define the one-body matrix elements

$$t_{ij} = \int d\vec{r}\,\phi_i^*(\vec{r})\,H_0(\vec{r})\,\phi_j(\vec{r}), \tag{3.17}$$

so that the one-body Hamiltonian becomes

$$\hat{H}_0 = \sum_\sigma \sum_{i,j} t_{ij}\,\hat{c}_{i\sigma}^\dagger \hat{c}_{j\sigma}. \tag{3.18}$$

The choice of single-particle orbitals $\{\phi_i(\vec{r})\}$ is not unique. In general, they only need to form a complete orthonormal basis. They are eigenstates of H_0 only if we deliberately choose the single-particle energy eigenbasis [69, 113].

If we select ϕ_i to be eigenfunctions of the one-body Hamiltonian,

$$H_0(\vec{r})\phi_i(\vec{r}) = \varepsilon_i \phi_i(\vec{r}), \tag{3.19}$$

then the matrix elements t_{ij} become diagonal due to orthonormality,

$$t_{ij} = \varepsilon_i \delta_{ij}, \tag{3.20}$$

and the Hamiltonian is diagonal in the orbital index,

$$\hat{H}_0 = \sum_{i,\sigma} \varepsilon_i \hat{c}^\dagger_{i\sigma} \hat{c}_{i\sigma}. \tag{3.21}$$

This situation corresponds to working in the energy (or band) basis.

However, in lattice models it is often advantageous to use localized orbitals, such as Wannier functions centered at lattice sites [114, 115]. A Wannier function is a localized orbital built from the extended Bloch eigenstates of a periodic single-particle Hamiltonian. In a crystal the eigenstates of H_0 are Bloch functions $\psi_{n\vec{k}}(\vec{r})$, labelled by a band index n and a crystal momentum $\vec{k}$, and each one is spread over the whole crystal. The Wannier function for band n tied to lattice site $\vec{R}$ is defined as their Fourier transform over the Brillouin zone,

$$w_{n\vec{R}}(\vec{r}) = \frac{1}{\sqrt{N_k}} \sum_{\vec{k}} e^{-i\vec{k}\cdot\vec{R}}\, \psi_{n\vec{k}}(\vec{r}), \tag{3.22}$$

where N_k is the number of $\vec{k}$ points. These functions are localized around $\vec{R}$, form an orthonormal set, and are translates of one another, $w_{n\vec{R}}(\vec{r}) = w_{n\mathbf{0}}(\vec{r} - \vec{R})$. They are not unique. The Bloch states carry a gauge freedom, namely an arbitrary $\vec{k}$ dependent phase, or for several bands a unitary mixing $U_{mn}(\vec{k})$, and different choices give Wannier functions with different localization. A common way to fix this freedom is to choose the gauge that minimizes the spatial spread of the orbitals. This defines the maximally localized Wannier functions [116, 117], which are obtained numerically from a band-structure calculation, for example with the Wannier90 package [118]. With the orbitals ϕ_i taken to be such Wannier functions, the matrix elements t_{ij} defined above become the onsite energies and hopping amplitudes of the lattice model. Wannier functions are generally not eigenstates of H_0. In this case the matrix t_{ij} is not diagonal, and the Hamiltonian naturally separates into onsite and hopping terms,

$$\hat{H}_0 = \sum_{i,\sigma} \varepsilon_i \hat{c}^\dagger_{i\sigma} \hat{c}_{i\sigma} + \sum_{i \neq j,\sigma} t_{ij} \hat{c}^\dagger_{i\sigma} \hat{c}_{j\sigma}, \tag{3.23}$$

where

$$\varepsilon_i \equiv t_{ii} \tag{3.24}$$

are the onsite energies and t_{ij} $(i \neq j)$ are hopping amplitudes. This is the most general form of a second-quantized Hamiltonian in terms of creation and annihilation operators of the single-particle.

We now treat the electron-electron interaction term. In first quantization it is

$$\hat{V}_{ee} = \frac{1}{2} \sum_{\substack{i,j=1 \\ i \neq j}}^{N} V(\vec{r}_i - \vec{r}_j). \tag{3.25}$$

Using Eq. (3.12), the corresponding second-quantized form is

$$\hat{V}_{ee} = \frac{1}{2} \sum_{\sigma,\sigma'} \iint d\vec{r}\, d\vec{r}\,' \; \hat{\Psi}^\dagger(\vec{r},\sigma) \hat{\Psi}^\dagger(\vec{r}\,',\sigma') V(\vec{r} - \vec{r}\,') \hat{\Psi}(\vec{r}\,',\sigma') \hat{\Psi}(\vec{r},\sigma). \tag{3.26}$$

We again expand the field operators in the orbital basis:

$$\hat{\Psi}(\vec{r},\sigma) = \sum_i \phi_i(\vec{r})\, \hat{c}_{i\sigma}, \tag{3.27}$$

$$\hat{\Psi}^\dagger(\vec{r},\sigma) = \sum_i \phi_i^*(\vec{r})\, \hat{c}_{i\sigma}^\dagger. \tag{3.28}$$

Substituting these into Eq. (3.26) yields

$$\begin{aligned} \hat{V}_{ee} = \frac{1}{2} \sum_{\sigma,\sigma'} \iint d\vec{r}\, d\vec{r}\,' \; & \left(\sum_i \phi_i^*(\vec{r}) \hat{c}_{i\sigma}^\dagger \right) \left(\sum_j \phi_j^*(\vec{r}\,') \hat{c}_{j\sigma'}^\dagger \right) \\ & \times V(\vec{r} - \vec{r}\,') \left(\sum_k \phi_k(\vec{r}\,') \hat{c}_{k\sigma'} \right) \left(\sum_l \phi_l(\vec{r}) \hat{c}_{l\sigma} \right) \\ = \frac{1}{2} \sum_{\sigma,\sigma'} \sum_{i,j,k,l} & \hat{c}_{i\sigma}^\dagger \hat{c}_{j\sigma'}^\dagger \hat{c}_{k\sigma'} \hat{c}_{l\sigma} \iint d\vec{r}\, d\vec{r}\,' \; \phi_i^*(\vec{r}) \phi_j^*(\vec{r}\,') V(\vec{r} - \vec{r}\,') \phi_k(\vec{r}\,') \phi_l(\vec{r}). \end{aligned} \tag{3.29}$$

We define the two-body Coulomb elements

$$V_{ijkl} = \iint d\vec{r}\, d\vec{r}\,' \; \phi_i^*(\vec{r}) \phi_j^*(\vec{r}\,') V(\vec{r} - \vec{r}\,') \phi_k(\vec{r}\,') \phi_l(\vec{r}), \tag{3.30}$$

so the interaction term becomes

$$\hat{V}_{ee} = \frac{1}{2} \sum_{\sigma,\sigma'} \sum_{i,j,k,l} V_{ijkl}\, \hat{c}_{i\sigma}^\dagger \hat{c}_{j\sigma'}^\dagger \hat{c}_{k\sigma'} \hat{c}_{l\sigma}. \tag{3.31}$$

If the interaction does not depend explicitly on spin (as is the case for the Coulomb interaction), the spin indices only appear in the creation and annihilation operators, and the matrix elements V_{ijkl} are spin-independent.

Combining the one-body and two-body parts, Eqs. (3.18) and (3.31), the full

many-body Hamiltonian in second quantization reads

$$\hat{H} = \sum_{\sigma} \sum_{i,j} t_{ij}\, \hat{c}^{\dagger}_{i\sigma} \hat{c}_{j\sigma} + \frac{1}{2} \sum_{\sigma,\sigma'} \sum_{i,j,k,l} V_{ijkl}\, \hat{c}^{\dagger}_{i\sigma} \hat{c}^{\dagger}_{j\sigma'} \hat{c}_{k\sigma'} \hat{c}_{l\sigma}. \tag{3.32}$$

which is the standard second-quantized form of the interacting tight-binding Hamiltonian. This completes the formulation of a many-body problem. In the subsequent sections, we introduce various approaches to solve a many-body problem.

3.2 Configuration Interaction

The configuration interaction (CI) method, also known as exact diagonalization (ED), takes the many-body Hamiltonian and finds its energy spectrum by representing the Hamiltonian as a matrix in a chosen many-body basis and then diagonalizing this matrix [69, 119, 120]. In this way, the ground state and all excited states within the chosen Hilbert space are obtained in a numerically exact manner.

The starting point of the CI method is a set of single-particle orbitals $\{\phi_i(\vec{r}, \sigma)\}$, where i labels the orbital quantum numbers and σ denotes the spin degree of freedom. These orbitals may be atomic, molecular, or lattice Wannier orbitals, or any other convenient orthonormal basis [119–121]. Associated to each orbital we introduce fermionic creation and annihilation operators $\hat{c}^{\dagger}_{i\sigma}$ and $\hat{c}_{i\sigma}$, satisfying

$$\{\hat{c}_{i\sigma}, \hat{c}^{\dagger}_{j\sigma'}\} = \delta_{ij}\, \delta_{\sigma\sigma'}, \qquad \{\hat{c}_{i\sigma}, \hat{c}_{j\sigma'}\} = \{\hat{c}^{\dagger}_{i\sigma}, \hat{c}^{\dagger}_{j\sigma'}\} = 0. \tag{3.33}$$

We then construct the many-body Fock space by acting with the creation operators on the vacuum state $|0\rangle$:

$$|\Phi_\alpha\rangle = \prod_{(i,\sigma)\in\alpha} \hat{c}^{\dagger}_{i\sigma} |0\rangle\,, \tag{3.34}$$

where α denotes a configuration, i.e. a specific pattern of occupied single-particle orbitals. In most cases such as the many-body Hamiltonian shown before, one usually restricts to a sector with fixed particle number N (and often fixed spin projection), so that the basis states $\{|\Phi_\alpha\rangle\}$ form an orthonormal basis of this N-particle subspace.

The dimension D of this Hilbert space grows combinatorially with the number of available single-particle orbitals [69]. For example, if there are M distinct single-particle spin-orbitals and the particle number is fixed to N, then

$$D = \binom{M}{N}. \tag{3.35}$$

The growth becomes most severe near half filling, $N = M/2$. Using Stirling's approximation $n! \approx \sqrt{2\pi n}\,(n/e)^n$ for large n, one finds

$$\binom{M}{M/2} = \frac{M!}{\left(\frac{M}{2}!\right)^2} \;\approx\; \frac{2^M}{\sqrt{\pi M/2}}, \tag{3.36}$$

which scales asymptotically as

$$D \sim \frac{2^M}{\sqrt{M}}. \tag{3.37}$$

Thus, at half filling the Hilbert space dimension grows exponentially with M, up to a subleading algebraic prefactor. This exponential scaling of the Hilbert space is the fundamental limitation of exact diagonalization methods for interacting many-body systems.

Second-quantized Hamiltonian and matrix elements

We now demonstrate the application of ED on the many-body Hamiltonian in Eq. 3.32. The coefficients are assumed to be known from the underlying microscopic model or from ab initio calculations.

The CI method proceeds by computing all matrix elements of $\hat{H}$ in the basis $\{|\Phi_\alpha\rangle\}$:

$$H_{\alpha\beta} = \langle\Phi_\alpha|\,\hat{H}\,|\Phi_\beta\rangle\,. \tag{3.38}$$

Using the fermionic anticommutation relations, these matrix elements can be evaluated analytically in terms of t_{ij} and V_{ijkl} and the occupation patterns defining $|\Phi_\alpha\rangle$ and $|\Phi_\beta\rangle$. The resulting matrix H is a $D \times D$ Hermitian matrix that fully encodes the many-body Hamiltonian within the chosen Hilbert space.

To reduce computational cost, it is advantageous to exploit all symmetries of the Hamiltonian. If $\hat{H}$ commutes with a set of conserved quantities $\{\hat{Q}_\mu\}$,

$$[\hat{H}, \hat{Q}_\mu] = 0, \tag{3.39}$$

then $\hat{H}$ and all $\hat{Q}_\mu$ can be simultaneously diagonalized [69, 122]. This implies that the Hilbert space decomposes into invariant subspaces characterized by definite eigenvalues (quantum numbers) of the conserved operators.

Let Γ denote the collection of quantum numbers associated with $\{\hat{Q}_\mu\}$. The full

Hilbert space $\mathcal{H}$ can then be written as a direct sum of orthogonal symmetry sectors,

$$\mathcal{H} = \bigoplus_{\Gamma} \mathcal{H}^{(\Gamma)}, \tag{3.40}$$

where each subspace $\mathcal{H}^{(\Gamma)}$ consists of states satisfying

$$\hat{Q}_\mu \left|\psi^{(\Gamma)}\right\rangle = q_\mu^{(\Gamma)} \left|\psi^{(\Gamma)}\right\rangle . \tag{3.41}$$

Because $\hat{H}$ preserves these quantum numbers, it maps each symmetry sector onto itself,

$$\hat{H}\,\mathcal{H}^{(\Gamma)} \subseteq \mathcal{H}^{(\Gamma)}. \tag{3.42}$$

As a result, in a basis ordered according to symmetry sectors, the Hamiltonian matrix takes block-diagonal form,

$$\hat{H} = \bigoplus_{\Gamma} \hat{H}^{(\Gamma)}, \tag{3.43}$$

where $\hat{H}^{(\Gamma)}$ denotes the restriction of $\hat{H}$ to the subspace $\mathcal{H}^{(\Gamma)}$. The symbol $\bigoplus$ denotes a direct sum. It indicates that the full operator acts independently on mutually orthogonal subspaces, so that matrix elements connecting different symmetry sectors vanish:

$$\langle\psi^{(\Gamma)}|\,\hat{H}\,|\psi^{(\Gamma')}\rangle = 0 \quad \text{for } \Gamma \neq \Gamma'. \tag{3.44}$$

Thus, diagonalizing $\hat{H}$ reduces to diagonalizing each block $\hat{H}^{(\Gamma)}$ separately. The CI procedure can then be applied independently in each block, which significantly reduces the effective matrix dimension in comparison to considering the full Hilbert space at once. In particular, when one is interested in the ground state, it is often sufficient to focus on the sector containing the physical ground-state quantum numbers.

Numerical diagonalization

After constructing the Hamiltonian matrix in a given symmetry sector, the next step is to obtain its eigenvalues and eigenvectors. In principle, one can perform a full diagonalization,

$$H^{(\Gamma)}\mathbf{v}_n^{(\Gamma)} = E_n^{(\Gamma)}\mathbf{v}_n^{(\Gamma)}, \tag{3.45}$$

which yields the complete spectrum $\{E_n^{(\Gamma)}\}$ and the corresponding eigenstates $\{|\Psi_n^{(\Gamma)}\rangle\}$, with

$$|\Psi_n^{(\Gamma)}\rangle = \sum_{\alpha\in\Gamma} v_{n,\alpha}^{(\Gamma)} \left|\Phi_\alpha\right\rangle . \tag{3.46}$$

For moderate matrix dimensions $D = \dim \mathcal{H}^{(\Gamma)}$, full dense diagonalization can be performed using standard $O(D^3)$ algorithms such as QR or divide-and-conquer methods implemented in LAPACK [73, 123, 124]. Here, "moderate" typically refers to matrix sizes $D \lesssim 10^4$–10^5, for which storing the full dense matrix (requiring $O(D^2)$ memory) and performing cubic-time diagonalization remain computationally feasible. Since dense diagonalization scales as $O(D^3)$ in time and $O(D^2)$ in memory, the computational cost rapidly becomes prohibitive beyond this regime.

Once the eigenstates have been obtained for a given symmetry sector, any observable represented by an operator $\hat{O}$ can be evaluated straightforwardly. For an eigenstate $|\Psi_n\rangle$, the expectation value is

$$\langle \hat{O} \rangle_n = \langle \Psi_n | \hat{O} | \Psi_n \rangle = \sum_{\alpha,\beta} (v_{n,\alpha})^* v_{n,\beta} \langle \Phi_\alpha | \hat{O} | \Phi_\beta \rangle . \tag{3.47}$$

For operators that are expressed in second quantization (e.g. densities, currents, spin operators, or correlation functions), the matrix elements $\langle \Phi_\alpha | \hat{O} | \Phi_\beta \rangle$ are again evaluated using the algebra of creation and annihilation operators.

In this way, the CI/ED method provides access not only to the full many-body spectrum but also to a wide range of static and dynamical observables, limited only by the size of the Hilbert space that can be handled numerically [67, 69, 125].

Computational Limitations

Despite its simplicity and numerical exactness within the chosen Hilbert space, the CI method suffers from an exponential growth of the Hilbert space dimension with system size [67, 68, 72]. For example, a one-dimensional spinless chain of L sites has a Hilbert-space dimension $D = 2^L$. Here each of the L sites is either empty or occupied by a single spinless fermion, so there are two states per site. The dimension 2^L is therefore that of the full Fock space, and it sums over all particle numbers from 0 to L.

The computational cost is directly determined by this dimension. If the Hamiltonian is stored as a dense matrix, the memory requirement scales as $O(D^2)$, while full diagonalization scales as $O(D^3)$ in time using standard eigensolvers [73, 123]. Even for sparse representations, iterative methods such as the Lanczos algorithm do not form the full matrix. They keep only a small, fixed number of vectors of length D, together with the sparse Hamiltonian. For example, the Lanczos three-term recurrence retains only about three such vectors at a time. The memory therefore scales linearly with D,

as $O(D)$, rather than as the $O(D^2)$ of a dense matrix [126].

To illustrate the hardware limitation, consider $L = 16$, for which $D = 2^{16} = 65{,}536$. These estimates assume real double-precision numbers, which occupy 8 bytes each. A single state vector then requires $8D \approx 0.5$ MB of memory, while a dense Hamiltonian requires $8D^2 \approx 34$ GB, already approaching the limits of typical workstation hardware. If the Hamiltonian is complex, each entry occupies 16 bytes and these figures roughly double, to about 1 MB per vector and 69 GB for the dense matrix. Since dense diagonalization scales as D^3, the computational time rapidly becomes prohibitive beyond this range.

As a consequence, ED is restricted to systems with a modest number of degrees of freedom, typically one-dimensional spinless chains with $L \sim 10$–16 sites on present-day hardware [67, 72, 126]. To reach such system sizes in practice, careful use of symmetries and optimized numerical techniques (e.g., sparse-matrix representations, Krylov or Lanczos eigensolvers, and parallelization) is essential [68, 126].

In practice, ED is therefore most powerful as a benchmarking tool and for gaining detailed insight into the many-body physics of small clusters, which can then guide the development and validation of more scalable approximate methods [67, 68, 126].

3.2.1 Spinless Tight-binding Chain

To illustrate the CI procedure, we now consider a spinless tight-binding Hamiltonian with nearest-neighbour hopping and onsite energy ε. In second quantization, for a chain of L sites with open boundary conditions, the Hamiltonian reads

$$\hat{H} = \varepsilon \sum_{i=1}^{L} \hat{n}_i - t \sum_{i=1}^{L-1} \left(\hat{c}_i^\dagger \hat{c}_{i+1} + \hat{c}_{i+1}^\dagger \hat{c}_i \right), \tag{3.48}$$

where $\hat{c}_i^\dagger$ and $\hat{c}_i$ create and annihilate a spinless fermion on site i, and

$$\hat{n}_i = \hat{c}_i^\dagger \hat{c}_i \tag{3.49}$$

is the local number operator. The first term in Eq. (3.48) assigns an energy ε to each occupied site, while the second term allows particles to hop between neighbouring sites with amplitude t.

For spinless fermions there are only two possible local states at each site, empty or occupied

- $|0\rangle_i$: site i empty,

- $|1\rangle_i = \hat{c}_i^\dagger |0\rangle_i$: one fermion at site i.

As an example, we take a chain of $L = 3$ sites. The full Fock space is obtained by taking tensor products of these local states. A convenient notation is to write a basis state as a binary occupation string

$$|n_1 n_2 n_3\rangle \equiv (\hat{c}_1^\dagger)^{n_1} (\hat{c}_2^\dagger)^{n_2} (\hat{c}_3^\dagger)^{n_3} |0\rangle , \tag{3.50}$$

where $n_i \in \{0, 1\}$ and $|0\rangle$ is the vacuum with all sites empty. For 3 sites, we will have $2^3 = 8$ configurations. The eight many-body basis states are

$$\begin{aligned}
&|0\rangle = |000\rangle, && \hat{c}_1^\dagger |0\rangle = |100\rangle, \\
&\hat{c}_2^\dagger |0\rangle = |010\rangle, && \hat{c}_3^\dagger |0\rangle = |001\rangle, \\
&\hat{c}_1^\dagger \hat{c}_2^\dagger |0\rangle = |110\rangle, && \hat{c}_1^\dagger \hat{c}_3^\dagger |0\rangle = |101\rangle, \\
&\hat{c}_2^\dagger \hat{c}_3^\dagger |0\rangle = |011\rangle, && \hat{c}_1^\dagger \hat{c}_2^\dagger \hat{c}_3^\dagger |0\rangle = |111\rangle.
\end{aligned}$$

In CI, we use these states as a basis in which to represent the Hamiltonian. In numerical implementations it is convenient to associate each binary string with the corresponding integer obtained by interpreting it as a bit pattern, e.g.

$$|n_1 n_2 n_3\rangle \leftrightarrow n = n_1 2^2 + n_2 2^1 + n_3 2^0, \tag{3.51}$$

so that

$$\begin{aligned}
&|000\rangle \to 0, \quad |001\rangle \to 1, \quad |010\rangle \to 2, \quad |011\rangle \to 3, \\
&|100\rangle \to 4, \quad |101\rangle \to 5, \quad |110\rangle \to 6, \quad |111\rangle \to 7.
\end{aligned} \tag{3.52}$$

This indexing allows us to store state coefficients in arrays and to use bit operations to implement the action of $\hat{H}$. For efficient implementation on a computer, we store these binary strings in objects such as dictionaries.

Action of the Hamiltonian on basis states. We now compute the action of $\hat{H}$ on some basis states to illustrate how matrix elements are obtained.

Onsite term. The onsite part is diagonal in the occupation basis:

$$\hat{H}_\varepsilon = \varepsilon \sum_{i=1}^{3} \hat{n}_i. \tag{3.53}$$

For a given basis state $|n_1 n_2 n_3\rangle$, we count the number of occupied sites:

$$\hat{H}_\varepsilon |n_1 n_2 n_3\rangle = \varepsilon (n_1 + n_2 + n_3) |n_1 n_2 n_3\rangle . \tag{3.54}$$

For example,

$$\hat{H}_\varepsilon \,|100\rangle = \varepsilon \,|100\rangle\,, \tag{3.55}$$

$$\hat{H}_\varepsilon \,|110\rangle = 2\varepsilon \,|110\rangle\,. \tag{3.56}$$

Hopping term. The hopping part for $L = 3$ is

$$\hat{H}_t = -t\Big(\hat{c}_1^\dagger \hat{c}_2 + \hat{c}_2^\dagger \hat{c}_1 + \hat{c}_2^\dagger \hat{c}_3 + \hat{c}_3^\dagger \hat{c}_2\Big). \tag{3.57}$$

Each term moves a particle between neighbouring sites provided that the departure site is occupied and the arrival site is empty. Fermi statistics enter through possible sign factors, but for spinless fermions with the standard ordering $1 < 2 < 3$ the examples below are straightforward.

Consider first the one-particle state $|100\rangle$:

$$\hat{H}_t \,|100\rangle = -t\Big(\hat{c}_1^\dagger \hat{c}_2 + \hat{c}_2^\dagger \hat{c}_1 + \hat{c}_2^\dagger \hat{c}_3 + \hat{c}_3^\dagger \hat{c}_2\Big)\,|100\rangle\,. \tag{3.58}$$

Only the term $\hat{c}_2^\dagger \hat{c}_1$ gives a non-zero contribution:

$$\hat{c}_1 \,|100\rangle = |000\rangle\,, \tag{3.59}$$

$$\hat{c}_2^\dagger \,|000\rangle = |010\rangle\,, \tag{3.60}$$

so that

$$\hat{H}_t \,|100\rangle = -t \,|010\rangle\,. \tag{3.61}$$

All other terms annihilate the state because either the departure site is empty or the arrival site is already occupied.

Similarly, for $|010\rangle$ we obtain

$$\hat{c}_1^\dagger \hat{c}_2 \,|010\rangle = \hat{c}_1^\dagger \,|000\rangle = |100\rangle\,, \tag{3.62}$$

$$\hat{c}_3^\dagger \hat{c}_2 \,|010\rangle = \hat{c}_3^\dagger \,|000\rangle = |001\rangle\,, \tag{3.63}$$

while the other two terms give zero, so

$$\hat{H}_t \,|010\rangle = -t\Big(|100\rangle + |001\rangle\Big). \tag{3.64}$$

Finally,

$$\hat{H}_t \,|001\rangle = -t \,|010\rangle\,. \tag{3.65}$$

The CI method often exploits particle-number conservation to work within a fixed-N sector. For $L = 3$ and $N = 1$ the basis states are

$$|\phi_1\rangle = |100\rangle\,, \quad |\phi_2\rangle = |010\rangle\,, \quad |\phi_3\rangle = |001\rangle\,. \tag{3.66}$$

Using the results above, we can read off the 3×3 Hamiltonian matrix $H^{(N=1)}$ defined by

$$\hat{H}\,|\phi_j\rangle = \sum_{i=1}^{3} H_{ij}^{(N=1)}\,|\phi_i\rangle\,. \tag{3.67}$$

We find

$$\hat{H}\,|\phi_1\rangle = (\varepsilon\,|100\rangle) - t\;|010\rangle = \varepsilon\,|\phi_1\rangle - t\;|\phi_2\rangle\,, \tag{3.68}$$

$$\hat{H}\,|\phi_2\rangle = (\varepsilon\,|010\rangle) - t(|100\rangle + |001\rangle) = -t\;|\phi_1\rangle + \varepsilon\,|\phi_2\rangle - t\;|\phi_3\rangle\,, \tag{3.69}$$

$$\hat{H}\,|\phi_3\rangle = (\varepsilon\,|001\rangle) - t\;|010\rangle = -t\;|\phi_2\rangle + \varepsilon\,|\phi_3\rangle\,. \tag{3.70}$$

Therefore,

$$H^{(N=1)} = \begin{pmatrix} \varepsilon & -t & 0 \\ -t & \varepsilon & -t \\ 0 & -t & \varepsilon \end{pmatrix}. \tag{3.71}$$

Diagonalizing this small matrix yields the exact one-particle energy spectrum for the three-site chain. The entire 8×8 Hamiltonian is shown in table (3.1), and the energy levels are displayed in Fig. 3.1.

Growth of the Hilbert space with system size. For a spinless fermionic chain with L sites, each site can be either empty or occupied. The dimension of the full Fock space is therefore

$$\dim \mathcal{H}_{\text{full}} = 2^L. \tag{3.72}$$

If we restrict ourselves to a fixed particle number N, the relevant Hilbert space is the N-particle sector, whose dimension is given by the binomial coefficient

$$\dim \mathcal{H}_N = \binom{L}{N}, \tag{3.73}$$

corresponding to the number of ways to distribute N indistinguishable fermions over L sites with at most one fermion per site. Summing over all possible particle numbers

recovers the full Fock-space dimension:

$$\sum_{N=0}^{L} \binom{L}{N} = 2^L. \tag{3.74}$$

This exponential growth with L is the fundamental limitation of the CI approach: although the method is conceptually straightforward and numerically exact within the chosen Hilbert space, the size of the Hamiltonian matrix increases so rapidly that only relatively small systems can be treated in practice.

	$\|000\rangle$	$\|100\rangle$	$\|010\rangle$	$\|001\rangle$	$\|110\rangle$	$\|101\rangle$	$\|011\rangle$	$\|111\rangle$
$\langle 000\|$	0	0	0	0	0	0	0	0
$\langle 100\|$	0	ε	$-t$	0	0	0	0	0
$\langle 010\|$	0	$-t$	ε	$-t$	0	0	0	0
$\langle 001\|$	0	0	$-t$	ε	0	0	0	0
$\langle 110\|$	0	0	0	0	2ε	$-t$	0	0
$\langle 101\|$	0	0	0	0	$-t$	2ε	$-t$	0
$\langle 011\|$	0	0	0	0	0	$-t$	2ε	0
$\langle 111\|$	0	0	0	0	0	0	0	3ε

Table 3.1: Hamiltonian matrix for the spinless three-site tight-binding chain in the Fock basis $\{|000\rangle, |100\rangle, |010\rangle, |001\rangle, |110\rangle, |101\rangle, |011\rangle, |111\rangle\}$. The diagonal elements count the number of occupied sites and thus carry factors of ε, while the off-diagonal elements $-t$ connect configurations that differ by a single hop of a fermion between neighbouring sites. The matrix is block diagonal in the particle-number sectors $N = 0, 1, 2, 3$.

3.2.2 Spinful Tight-binding Chain

We now extend the CI construction to a spinful tight-binding Hamiltonian with onsite energy. In contrast to the spinless case, each lattice site can now host up to two electrons, distinguished by their spin projection $\sigma = \uparrow, \downarrow$. This increases the size of the local Hilbert space and leads to a faster growth of the many-body Hilbert space with system size.

We consider a one-dimensional chain of L sites with nearest-neighbour hopping and a spin-independent onsite energy ε. In second quantization the Hamiltonian reads

$$\hat{H} = \varepsilon \sum_{i=1}^{L} \sum_{\sigma=\uparrow,\downarrow} \hat{n}_{i\sigma} - t \sum_{i=1}^{L-1} \sum_{\sigma=\uparrow,\downarrow} \left(\hat{c}^\dagger_{i\sigma} \hat{c}_{i+1,\sigma} + \hat{c}^\dagger_{i+1,\sigma} \hat{c}_{i\sigma} \right), \tag{3.75}$$

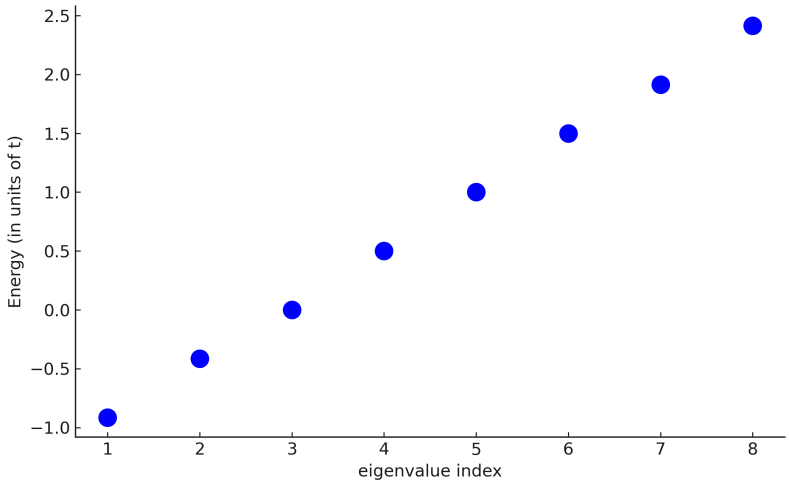

Figure 3.1: Full energy spectrum of the 3-sites spinless tight-binding Hamiltonian with $t = 1$ and $\epsilon = 0.5$ using CI.

where $\hat{c}^\dagger_{i\sigma}$ ($\hat{c}_{i\sigma}$) creates (annihilates) an electron with spin σ on site i, and

$$\hat{n}_{i\sigma} = \hat{c}^\dagger_{i\sigma}\hat{c}_{i\sigma} \tag{3.76}$$

is the corresponding number operator. The first term in Eq. (3.75) assigns an energy ε to each electron, independent of its spin, while the second term allows spin-conserving hopping between neighbouring sites with amplitude t.

The Hamiltonian conserves both the total particle number

$$\hat{N} = \sum_{i,\sigma} \hat{n}_{i\sigma} \tag{3.77}$$

and the spin projection

$$\hat{S}_z = \frac{1}{2}\sum_i \big(\hat{n}_{i\uparrow} - \hat{n}_{i\downarrow}\big). \tag{3.78}$$

Therefore, the Hilbert space naturally decomposes into sectors labelled by N, $N_\uparrow$ and $N_\downarrow$ (or equivalently N and S_z).

For each site i there are now four possible local configurations:

- $|0\rangle_i$: site i is empty;
- $|\uparrow\rangle_i = \hat{c}^\dagger_{i\uparrow}|0\rangle_i$: one electron with spin up;
- $|\downarrow\rangle_i = \hat{c}^\dagger_{i\downarrow}|0\rangle_i$: one electron with spin down;
- $|\uparrow\downarrow\rangle_i = \hat{c}^\dagger_{i\uparrow}\hat{c}^\dagger_{i\downarrow}|0\rangle_i$: a doubly occupied site.

Thus the local Hilbert space on a single site has dimension 4.

The full Fock space for the chain is obtained as the tensor product of the local spaces. A generic basis state can be written as

$$|\Phi_\alpha\rangle = \prod_{(i,\sigma)\in\alpha} \hat{c}^\dagger_{i\sigma} |0\rangle \,, \tag{3.79}$$

where we can order the product according to a fixed convention (for example, increasing site index and, for each site, spin-up before spin-down), and α denotes a particular configuration specifying which spin-orbitals (i, σ) are occupied. In an equivalent occupation-number notation we can write

$$|\{n_{i\uparrow}, n_{i\downarrow}\}\rangle = \prod_{i=1}^{L} (\hat{c}^\dagger_{i\uparrow})^{n_{i\uparrow}} (\hat{c}^\dagger_{i\downarrow})^{n_{i\downarrow}} |0\rangle \,, \qquad n_{i\sigma} \in \{0, 1\}. \tag{3.80}$$

Since there are $2L$ spin-orbitals (i, σ) and each can be either empty or occupied, the dimension of the full Fock space is

$$\dim \mathcal{H}_{\text{full}} = 2^{2L} = 4^L, \tag{3.81}$$

reflecting the four local states per site.

To use the symmetries of the spinful chain, we typically fix the total number of electrons N and often also the spin projection S_z, or equivalently the numbers $N_\uparrow$ and $N_\downarrow$. These are related by

$$N = N_\uparrow + N_\downarrow, \qquad S_z = \frac{1}{2}(N_\uparrow - N_\downarrow). \tag{3.82}$$

The dimension of the Hilbert space in a fixed $(N_\uparrow, N_\downarrow)$ sector is obtained by a simple combinatorial argument: there are L possible sites for spin-up electrons and L independent sites for spin-down electrons. Choosing $N_\uparrow$ spin-up electrons and $N_\downarrow$ spin-down electrons gives

$$\dim \mathcal{H}_{N_\uparrow, N_\downarrow} = \binom{L}{N_\uparrow}\binom{L}{N_\downarrow}. \tag{3.83}$$

Summing over all $N_\uparrow, N_\downarrow$ reproduces the full Fock-space dimension:

$$\sum_{N_\uparrow=0}^{L} \sum_{N_\downarrow=0}^{L} \binom{L}{N_\uparrow}\binom{L}{N_\downarrow} = \left(\sum_{N_\uparrow=0}^{L} \binom{L}{N_\uparrow}\right)\left(\sum_{N_\downarrow=0}^{L} \binom{L}{N_\downarrow}\right) = 2^L \cdot 2^L = 4^L. \tag{3.84}$$

In practice, the CI basis is constructed explicitly in the desired sector by enumerating all configurations with the given values of $N_\uparrow$ and $N_\downarrow$ and assigning each of them a unique index.

To illustrate these general considerations, we now work out explicitly the Hamiltonian matrices for a short chain with $L = 3$ sites in several $(N_\uparrow, N_\downarrow)$ sectors. In the one-particle sector $N = 1$ the Hamiltonian matrix in the basis $\{|1\uparrow\rangle, |2\uparrow\rangle, |3\uparrow\rangle, |1\downarrow\rangle, |2\downarrow\rangle, |3\downarrow\rangle\}$ is shown in Table 3.2.The two-particle sectors with parallel spins, $(N_\uparrow, N_\downarrow) = (2, 0)$ and $(0, 2)$, are summarized in Tables 3.3 and 3.4, respectively, while the fully polarized three-particle sectors $(3, 0)$ and $(0, 3)$, which each contain a single basis state, are shown in Tables 3.5 and 3.6. Finally, the mixed-spin three-particle sector $(N_\uparrow, N_\downarrow) = (2, 1)$ is represented in Table 3.7. The full many-body energy spectrum for $L = 3$ is plotted in Fig. 3.2.

Now we proceed to construct the Hamiltonian matrix. Once the basis $\{|\Phi_\alpha\rangle\}$ in a fixed sector is constructed, the CI method requires the matrix elements

$$H_{\alpha\beta} = \langle\Phi_\alpha| \hat{H} |\Phi_\beta\rangle . \tag{3.85}$$

The diagonal matrix element is

$$H_{\alpha\alpha} = \varepsilon N_\alpha, \tag{3.86}$$

where N_α is the total number of electrons in configuration α.

The hopping part of the Hamiltonian is

$$\hat{H}_t = -t \sum_{i=1}^{L-1} \sum_{\sigma} \Big(\hat{c}^\dagger_{i\sigma} \hat{c}_{i+1,\sigma} + \hat{c}^\dagger_{i+1,\sigma} \hat{c}_{i\sigma} \Big). \tag{3.87}$$

Each term $\hat{c}^\dagger_{i\sigma} \hat{c}_{j\sigma}$ moves an electron with spin σ from site j to site $j + 1$. Acting on a basis state $|\{n_{k\sigma'}\}\rangle$, such a term yields a non-zero result only if

$$n_{j\sigma} = 1, \qquad n_{i\sigma} = 0, \tag{3.88}$$

i.e. there is an electron at (j, σ) and the target (i, σ) is empty. The resulting state is another basis configuration in which the occupations at (i, σ) and (j, σ) have been exchanged:

$$\hat{c}^\dagger_{i\sigma} \hat{c}_{j\sigma} |\ldots, n_{i\sigma} = 0, \ldots, n_{j\sigma} = 1, \ldots\rangle = \pm |\ldots, n_{i\sigma} = 1, \ldots, n_{j\sigma} = 0, \ldots\rangle . \tag{3.89}$$

The overall sign $\pm$ arises from commuting the fermionic operators through the string

of creation operators defining the basis state; it is given by $(-1)^P$, where P is the number of occupied spin-orbitals between (i, σ) and (j, σ) in the chosen ordering. In an actual implementation, this sign is computed efficiently using bit operations.

Thus, for two basis states $|\Phi_\alpha\rangle$ and $|\Phi_\beta\rangle$ that differ by the motion of exactly one electron with spin σ from site j to $i = j \pm 1$, the hopping term generates an off-diagonal matrix element

$$H_{\alpha\beta} = -t \times (\pm 1), \tag{3.90}$$

with the sign determined as above. If the two configurations differ by more than one single-particle occupation, the hopping term does not connect them directly and $H_{\alpha\beta} = 0$.

Because $\hat{H}$ commutes with both $\hat{N}$ and $\hat{S}_z$, the Hamiltonian matrix constructed in this way is block diagonal in sectors labeled by $(N_\uparrow, N_\downarrow)$. The CI method proceeds by:

1. Enumerating all configurations in the chosen $(N_\uparrow, N_\downarrow)$ sector and assigning them indices to form the basis $\{|\Phi_\alpha\rangle\}$.

2. Computing the diagonal onsite energies from $\hat{H}_\varepsilon$, which depend only on the total particle number in each configuration.

3. Applying the hopping operator $\hat{H}_t$ to each basis state to find the connected configurations and their associated matrix elements $\pm t$.

4. Assembling the resulting sparse Hermitian matrix $H_{\alpha\beta}$ and diagonalizing it (typically using iterative eigensolvers such as Lanczos) to obtain the many-body spectrum in that sector [125, 126].

Growth of the Hilbert space. The spinful tight-binding model already exhibits a rapid growth of the Hilbert space. For L sites the full Fock space has dimension 4^L, and even restricted sectors such as half filling ($N = L$) with $S_z = 0$ still have dimensions of order

$$\dim \mathcal{H}_{N_\uparrow = N_\downarrow = L/2} = \binom{L}{L/2}^2. \tag{3.91}$$

For example, for $L = 3$ sites,

$$\dim \mathcal{H}_{\text{full}} = 4^3 = 64, \tag{3.92}$$

which already exceeds the $2^3 = 8$ states of a spinless chain of the same length. This combinatorial growth ultimately limits the CI/ED approach to relatively small system

sizes, despite the conceptual simplicity of the method and the absence of interactions in the present example. Nonetheless, for small L the CI method yields the numerically exact many-body eigenstates, which makes it a valuable benchmark for more advanced and scalable techniques discussed later in this chapter. An explicit example of the full spectrum for $L = 3$ is shown in Fig. 3.2.

	$\|1;0\rangle$	$\|2;0\rangle$	$\|3;0\rangle$	$\|0;1\rangle$	$\|0;2\rangle$	$\|0;3\rangle$
$\langle 1;0\|$	ε	$-t$	0	0	0	0
$\langle 2\ 0\|$	$-t$	ε	$-t$	0	0	0
$\langle 3\ 0\|$	0	$-t$	ε	0	0	0
$\langle 0;1\|$	0	0	0	ε	$-t$	0
$\langle 0;2\|$	0	0	0	$-t$	ε	$-t$
$\langle 0;3\|$	0	0	0	0	$-t$	ε

Table 3.2: Hamiltonian matrix for a spinful three-site tight-binding chain in the one-particle sector $N = 1$. The matrix is block diagonal in spin due to spin-conserving hopping. Each block is identical to the spinless tight-binding Hamiltonian, with onsite energy ε and nearest-neighbour hopping $-t$.

	$\|12;0\rangle$	$\|13;0\rangle$	$\|23;0\rangle$
$\langle 12;0\|$	2ε	$-t$	0
$\langle 13;0\|$	$-t$	2ε	$-t$
$\langle 23;0\|$	0	$-t$	2ε

Table 3.3: $L = 3$ spinful tight-binding Hamiltonian in the $(N_\uparrow, N_\downarrow) = (2, 0)$ sector.

	$\|0;12\rangle$	$\|0;13\rangle$	$\|0;23\rangle$
$\langle 0;12\|$	2ε	$-t$	0
$\langle 0;13\|$	$-t$	2ε	$-t$
$\langle 0;23\|$	0	$-t$	2ε

Table 3.4: $L = 3$ spinful tight-binding Hamiltonian in the $(N_\uparrow, N_\downarrow) = (0, 2)$ sector.

	$\lvert 123;0\rangle$
$\langle 123;0\rvert$	3ε

Table 3.5: $L = 3$ spinful tight-binding Hamiltonian in the $(N_\uparrow, N_\downarrow) = (3, 0)$ sector.

	$\lvert 0;123\rangle$
$\langle 0;123\rvert$	3ε

Table 3.6: $L = 3$ spinful tight-binding Hamiltonian in the $(N_\uparrow, N_\downarrow) = (0, 3)$ sector.

	$\lvert 12;1\rangle$	$\lvert 12;2\rangle$	$\lvert 12;3\rangle$	$\lvert 13;1\rangle$	$\lvert 13;2\rangle$	$\lvert 13;3\rangle$	$\lvert 23;1\rangle$	$\lvert 23;2\rangle$	$\lvert 23;3\rangle$
$\langle 12;1\rvert$	3ε	$-t$	0	$-t$	0	0	0	0	0
$\langle 12;2\rvert$	$-t$	3ε	$-t$	0	$-t$	0	0	0	0
$\langle 12;3\rvert$	0	$-t$	3ε	0	0	$-t$	0	0	0
$\langle 13;1\rvert$	$-t$	0	0	3ε	$-t$	0	$-t$	0	0
$\langle 13;2\rvert$	0	$-t$	0	$-t$	3ε	$-t$	0	$-t$	0
$\langle 13;3\rvert$	0	0	$-t$	0	$-t$	3ε	0	0	$-t$
$\langle 23;1\rvert$	0	0	0	$-t$	0	0	3ε	$-t$	0
$\langle 23;2\rvert$	0	0	0	0	$-t$	0	$-t$	3ε	$-t$
$\langle 23;3\rvert$	0	0	0	0	0	$-t$	0	$-t$	3ε

Table 3.7: $L = 3$ spinful tight-binding Hamiltonian in the $(N_\uparrow, N_\downarrow) = (2, 1)$ sector, basis $\lvert ij_\uparrow; k_\downarrow\rangle$.

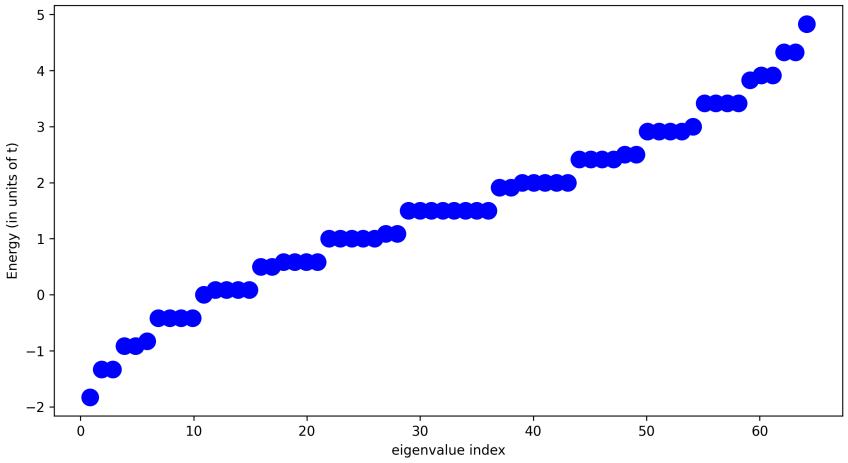

Figure 3.2: Full energy spectrum of the $L = 3$ spinful tight-binding Hamiltonian with $t = 1$ and $\epsilon = 0.5$ using CI.

3.3 Mean-field approximations

So far we have discussed both non-interacting systems (single-particle Hamiltonians) and fully interacting many-body systems treated by exact diagonalization in a restricted Hilbert space. While configuration interaction or exact diagonalization provide numerically exact results within the chosen basis, their computational cost grows exponentially with system size [67, 68, 72]. This makes them impractical for larger systems, or for systematic scans over many parameters.

In this section we describe the mean-field approaches employed in this work to treat electron–electron interactions at reduced cost. The central idea of mean-field theory is to replace the full interacting many-body problem by an effective single-particle problem, in which each electron moves in a self-consistent potential generated by the average distribution of all the other electrons [69, 113].

We focus on the Hartree–Fock (HF) approximation, which explicitly treats both direct (Hartree) and exchange (Fock) contributions at the mean-field level [69, 71, 119].

3.3.1 Hartree–Fock approximation

We start from the general many-body Hamiltonian written in second quantization in an orthonormal single-particle basis $\{\varphi_p(\vec{r})\}$, with fermionic operators $c_{i\sigma}^\dagger$ and $c_{i\sigma}$ creating and annihilating an electron in orbital i with spin σ [69, 71, 113]:

$$H = \sum_{i,j,\sigma} \epsilon_{ij}\, c_{i\sigma}^\dagger c_{j\sigma} + \frac{1}{2} \sum_{i,j,k,l} \sum_{\sigma,\sigma'} \langle i,j|V|k,l\rangle\, c_{i\sigma}^\dagger c_{j\sigma'}^\dagger c_{k\sigma'} c_{l\sigma}. \tag{3.93}$$

Here ϵ_{ij} contains all one-body contributions such as onsite energy or hopping, and

$$\langle i,j|V|k,l\rangle = \int d\vec{r}\, d\tilde{\vec{r}}\, \varphi_i^*(\vec{r})\, \varphi_j^*(\tilde{\vec{r}})\, V(\vec{r}-\tilde{\vec{r}})\, \varphi_k(\tilde{\vec{r}})\, \varphi_l(\vec{r}) \tag{3.94}$$

are the two-body Coulomb matrix elements [69, 119]. They satisfy the symmetry properties

$$\langle i,j|V|k,l\rangle = \langle j,i|V|l,k\rangle = \langle k,l|V|i,j\rangle^*. \tag{3.95}$$

The first term in Eq. (3.93) is quadratic in the fermionic operators and can be diagonalized straightforwardly. The second term is quartic and is responsible for the complexity of the interacting many-body problem.

In the Hartree–Fock approximation we assume that the many-body ground state

can be approximated by

$$|\mathrm{HF}\rangle = \prod_{\lambda,\sigma}^{\mathrm{occ}} b^\dagger_{\lambda\sigma}|0\rangle, \tag{3.96}$$

where $b^\dagger_{\lambda\sigma}$ creates an electron in a Hartree–Fock orbital labelled by λ and spin σ. The symbol "occ" indicates that the product runs over all occupied single-particle orbitals in the Hartree–Fock ground state. That is, for a system with N electrons, exactly N orbitals $\{\lambda\}$ are filled, and the remaining orbitals are empty. These orbitals are linear combinations of the original basis states:

$$b^\dagger_{\lambda\sigma} = \sum_p a^\sigma_{\lambda p} c^\dagger_{p\sigma}, \qquad c^\dagger_{p\sigma} = \sum_\lambda a^{\sigma *}_{\lambda p} b^\dagger_{\lambda\sigma}. \tag{3.97}$$

Because $|\mathrm{HF}\rangle$ is a Slater determinant, Wick's theorem applies: any expectation value of a product of fermionic operators can be expressed as a sum of products of two-operator contractions [69, 71, 127].

It is convenient to introduce the one-body density matrix in the original basis

$$\rho^\sigma_{ij} = \langle \mathrm{HF}|c^\dagger_{i\sigma} c_{j\sigma}|\mathrm{HF}\rangle. \tag{3.98}$$

Since the Hartree–Fock Hamiltonian conserves the spin projection S_z, the up- and down-spin sectors remain independent [69, 113]. Consequently, the Hartree–Fock ground state factorizes into a tensor product of two independent Slater determinants,

$$|\mathrm{HF}\rangle = |\mathrm{HF}_\uparrow\rangle \otimes |\mathrm{HF}_\downarrow\rangle. \tag{3.99}$$

Because of this factorization, operators that mix different spin projections connect orthogonal Fock sectors and therefore have vanishing expectation values. In particular, the one-body density matrix becomes diagonal in spin space,

$$\langle c^\dagger_{i\sigma} c_{j\sigma'}\rangle = \delta_{\sigma\sigma'}\, \rho^\sigma_{ij}, \tag{3.100}$$

where

$$\rho^\sigma_{ij} = \langle c^\dagger_{i\sigma} c_{j\sigma}\rangle \tag{3.101}$$

is the spin-resolved density matrix. This case is known as a collinear Hartree–Fock solution. Collinear means that the spin moments everywhere point along a single common axis, taken here as the spin quantization axis z. Equivalently, the single-particle states are eigenstates of S_z, and the mean-field Hamiltonian contains no

spin-flip terms connecting $\uparrow$ and $\downarrow$. The spin structure therefore remains block diagonal, and each spin sector can be treated independently. A non-collinear solution, by contrast, allows the spin moments to point in different directions. The two spin sectors then mix, S_z is no longer conserved, and the block-diagonal structure is lost. Such solutions are required when spin-flip terms are present.

We now focus on the interaction part of the Hamiltonian,

$$\hat{V}_{ee} = \frac{1}{2} \sum_{i,j,k,l} \sum_{\sigma,\sigma'} \langle i,j|V|k,l\rangle \, c^\dagger_{i\sigma} c^\dagger_{j\sigma'} c_{k\sigma'} c_{l\sigma}. \tag{3.102}$$

As noted above, because $|\mathrm{HF}\rangle$ is a Slater determinant, Wick's theorem applies, and it is exact. Written out for a product of four fermion operators, it expresses the expectation value as a sum of two-operator contractions,

$$\langle c^\dagger_{i\sigma} c^\dagger_{j\sigma'} c_{k\sigma'} c_{l\sigma}\rangle = \langle c^\dagger_{i\sigma} c_{l\sigma}\rangle \langle c^\dagger_{j\sigma'} c_{k\sigma'}\rangle - \langle c^\dagger_{i\sigma} c_{k\sigma'}\rangle \langle c^\dagger_{j\sigma'} c_{l\sigma}\rangle. \tag{3.103}$$

This is an identity and involves no approximation.

The approximation enters at a separate step, as the mean-field decoupling of the operator. We write each fermion bilinear as its average plus a fluctuation, $\delta\hat{A} = \hat{A} - \langle\hat{A}\rangle$. For any two bilinears this gives the exact relation

$$\hat{A}\hat{B} = \langle\hat{A}\rangle\hat{B} + \hat{A}\langle\hat{B}\rangle - \langle\hat{A}\rangle\langle\hat{B}\rangle + \delta\hat{A}\,\delta\hat{B}. \tag{3.104}$$

The Hartree–Fock approximation neglects the last term, $\delta\hat{A}\,\delta\hat{B}$, which carries the correlations beyond mean field. Applying this to the four-operator product, in both the direct (Hartree) and exchange (Fock) channels, and absorbing the resulting constant into an overall energy shift, we obtain

$$\begin{aligned} c^\dagger_{i\sigma} c^\dagger_{j\sigma'} c_{k\sigma'} c_{l\sigma} \approx\ & \underbrace{\langle c^\dagger_{j\sigma'} c_{k\sigma'}\rangle c^\dagger_{i\sigma} c_{l\sigma}}_{\text{direct (Hartree)}} + \underbrace{\langle c^\dagger_{i\sigma} c_{l\sigma}\rangle c^\dagger_{j\sigma'} c_{k\sigma'}}_{\text{direct (Hartree)}} \\ & - \underbrace{\langle c^\dagger_{j\sigma'} c_{l\sigma}\rangle c^\dagger_{i\sigma} c_{k\sigma'}}_{\text{exchange (Fock)}} - \underbrace{\langle c^\dagger_{i\sigma} c_{k\sigma'}\rangle c^\dagger_{j\sigma'} c_{l\sigma}}_{\text{exchange (Fock)}}. \end{aligned} \tag{3.105}$$

The symbol $\approx$ here denotes the mean-field neglect of the fluctuation term in Eq. (3.104), not Wick's theorem, which is exact. Using Eq. (3.100), the expectation

values are written in terms of the density matrix:

$$\langle c^\dagger_{j\sigma'} c_{k\sigma'} \rangle = \rho^{\sigma'}_{jk}, \qquad \langle c^\dagger_{i\sigma} c_{l\sigma} \rangle = \rho^{\sigma}_{il}, \tag{3.106}$$

$$\langle c^\dagger_{j\sigma'} c_{l\sigma} \rangle = \delta_{\sigma\sigma'} \rho^{\sigma}_{jl}, \qquad \langle c^\dagger_{i\sigma} c_{k\sigma'} \rangle = \delta_{\sigma\sigma'} \rho^{\sigma}_{ik}. \tag{3.107}$$

Substituting Eq. (3.105) into Eq. (3.102) we obtain

$$\hat{V}_{ee} \approx \frac{1}{2} \sum_{i,j,k,l} \sum_{\sigma,\sigma'} \langle i,j|V|k,l\rangle \Big[\rho^{\sigma'}_{kj} c^\dagger_{i\sigma} c_{l\sigma} + \rho^{\sigma}_{li} c^\dagger_{j\sigma'} c_{k\sigma'} - \delta_{\sigma\sigma'} \rho^{\sigma}_{lj} c^\dagger_{i\sigma} c_{k\sigma} - \delta_{\sigma\sigma'} \rho^{\sigma}_{ki} c^\dagger_{j\sigma} c_{l\sigma} \Big]. \tag{3.108}$$

We now simplify term by term.

Direct (Hartree) contribution. Consider the first two terms in the square brackets. The first one reads

$$\hat{V}^{(1)}_{\mathrm{H}} = \frac{1}{2} \sum_{i,l,\sigma} \left[\sum_{j,k,\sigma'} \langle i,j|V|k,l\rangle \, \rho^{\sigma'}_{kj} \right] c^\dagger_{i\sigma} c_{l\sigma}. \tag{3.109}$$

The second Hartree term has operator structure $c^\dagger_{j\sigma'} c_{k\sigma'}$; by relabelling dummy indices $(i,\sigma) \leftrightarrow (j,\sigma')$ and $(l,k) \leftrightarrow (k,l)$ and using the symmetry of the Coulomb matrix elements, we obtain an identical contribution. Therefore the factor of $1/2$ cancels and the full Hartree term is

$$\hat{V}_{\mathrm{H}} = \sum_{i,l,\sigma} \left[\sum_{j,k,\sigma'} \langle i,j|V|k,l\rangle \, \rho^{\sigma'}_{kj} \right] c^\dagger_{i\sigma} c_{l\sigma}. \tag{3.110}$$

Exchange (Fock) contribution. The third term in Eq. (3.108) reads

$$\hat{V}^{(1)}_{\mathrm{F}} = -\frac{1}{2} \sum_{i,k,\sigma} \left[\sum_{j,l} \langle i,j|V|k,l\rangle \, \rho^{\sigma}_{lj} \right] c^\dagger_{i\sigma} c_{k\sigma}, \tag{3.111}$$

where the Kronecker delta $\delta_{\sigma\sigma'}$ has been used to perform the spin sum σ'. The fourth term in Eq. (3.108) can be treated in exactly the same way by relabelling dummy indices, leading to an identical contribution. Again, the factor $1/2$ cancels and we obtain

$$\hat{V}_{\mathrm{F}} = -\sum_{i,k,\sigma} \left[\sum_{j,l} \langle i,j|V|k,l\rangle \, \rho^{\sigma}_{lj} \right] c^\dagger_{i\sigma} c_{k\sigma}. \tag{3.112}$$

Quadratic Hartree–Fock Hamiltonian. Collecting the Hartree and Fock contributions, the interaction part in the Hartree–Fock approximation becomes

$$\hat{V}_{ee}^{\mathrm{HF}} = \sum_{i,l,\sigma} \left[\sum_{j,k,\sigma'} \left(\langle i,j|V|k,l\rangle \, \rho_{kj}^{\sigma'} - \langle i,j|V|k,l\rangle \, \rho_{kj}^{\sigma} \delta_{\sigma\sigma'} \right) \right] c_{i\sigma}^{\dagger} c_{l\sigma}. \tag{3.113}$$

It is convenient to define the Hartree–Fock self-energy (or effective mean-field potential)

$$\Sigma_{il}^{\sigma}[\rho] = \sum_{j,k,\sigma'} \left(\langle i,j|V|k,l\rangle \, \rho_{kj}^{\sigma'} - \langle i,j|V|l,k\rangle \, \rho_{kj}^{\sigma} \delta_{\sigma\sigma'} \right), \tag{3.114}$$

so that

$$\hat{V}_{ee}^{\mathrm{HF}} = \sum_{i,l,\sigma} \Sigma_{il}^{\sigma}[\rho] \; c_{i\sigma}^{\dagger} c_{l\sigma}. \tag{3.115}$$

Adding the one-body part of the Hamiltonian, the full HF Hamiltonian is purely quadratic:

$$H_{\mathrm{HF}} = \sum_{i,l,\sigma} h_{il,\sigma}^{\mathrm{HF}} \; c_{i\sigma}^{\dagger} c_{l\sigma}, \qquad h_{il,\sigma}^{\mathrm{HF}} = \epsilon_{il} + \Sigma_{il}^{\sigma}[\rho]. \tag{3.116}$$

This is of the same form as the non-interacting Hamiltonian, but with an effective single-particle matrix $h^{\mathrm{HF}}[\rho]$ that depends on the density matrix itself.

The Hartree–Fock ground-state energy is obtained by taking the expectation value of the full Hamiltonian with respect to $|\mathrm{HF}\rangle$:

$$\begin{aligned} E_{\mathrm{HF}} &= \langle \mathrm{HF}|H|\mathrm{HF}\rangle \\ &= \sum_{i,j,\sigma} \epsilon_{ij} \, \rho_{ij}^{\sigma} + \frac{1}{2} \sum_{i,j,k,l} \sum_{\sigma,\sigma'} \langle i,j|V|k,l\rangle \left(\langle c_{i\sigma}^{\dagger} c_{j\sigma'}^{\dagger} c_{k\sigma'} c_{l\sigma} \rangle_{\mathrm{HF}} \right). \end{aligned} \tag{3.117}$$

Evaluating the four-operator expectation value by Wick's theorem and using the same contractions as in Eq. (3.105), we find

$$E_{\mathrm{HF}} = \sum_{i,j,\sigma} \epsilon_{ij} \, \rho_{ij}^{\sigma} + \frac{1}{2} \sum_{i,j,k,l} \sum_{\sigma,\sigma'} \langle i,j|V|k,l\rangle \Big(\rho_{il}^{\sigma} \rho_{jk}^{\sigma'} - \delta_{\sigma\sigma'} \rho_{ik}^{\sigma} \rho_{jl}^{\sigma} \Big). \tag{3.118}$$

The first term inside the parentheses is the Hartree (direct) energy, while the second term is the Fock (exchange) contribution. The prefactor $1/2$ ensures that each pair interaction is counted only once, avoiding double counting when summing over all indices.

Using the effective single-particle matrix h^{HF} defined in Eq. (3.116), one can

equivalently write

$$E_{\mathrm{HF}} = \sum_{i,j,\sigma} h^{\mathrm{HF}}_{ij,\sigma}\, \rho^{\sigma}_{ij} - \frac{1}{2} \sum_{i,j,k,l} \sum_{\sigma,\sigma'} \langle i,j|V|k,l\rangle \Big(\rho^{\sigma}_{il}\rho^{\sigma'}_{jk} - \delta_{\sigma\sigma'}\rho^{\sigma}_{ik}\rho^{\sigma}_{jl} \Big), \tag{3.119}$$

which makes explicit that, although h^{HF} already contains mean-field interaction effects, a separate interaction energy must be subtracted to avoid double counting.

Since the Hartree–Fock Hamiltonian H_{HF} depends on the density matrix ρ through Eq. (3.114), the HF equations must be solved self-consistently. The practical algorithm proceeds as follows:

1. **Initial guess.** Choose an initial density matrix $\rho^{(0)}$, e.g., from the non-interacting ground state or a simple trial configuration.

2. **Build HF Hamiltonian.** Construct $h^{\mathrm{HF}}[\rho^{(n)}]$ via Eq. (3.116).

3. **Diagonalize.** Solve the single-particle eigenvalue problem

$$\sum_{s} h^{\mathrm{HF}}_{il,\sigma}[\rho^{(n)}]\, \psi^{(n)}_{\lambda l\sigma} = \varepsilon^{(n)}_{\lambda\sigma} \psi^{(n)}_{\lambda i\sigma} \tag{3.120}$$

   and fill the lowest-energy orbitals according to the required particle number and spin sector.

4. **Update density matrix.** Construct a new density matrix

$$\rho^{\sigma,(n+1)}_{ij} = \sum_{\lambda\,\in\,\mathrm{occ}} \psi^{(n)*}_{\lambda i\sigma} \psi^{(n)}_{\lambda j\sigma}. \tag{3.121}$$

5. **Convergence check.** Compare $\rho^{(n+1)}$ (or $E^{(n+1)}_{\mathrm{HF}}$) with $\rho^{(n)}$; if the change is smaller than a chosen tolerance, the self-consistent solution has been found. Otherwise, set $n \to n+1$ and repeat.

Compared to exact diagonalization, HF replaces the exponential growth of the many-body Hilbert space by a polynomial-cost sequence of single-particle diagonalizations. The price is that correlations beyond a single Slater determinant are neglected [119–121].

3.4 Variational Quantum Eigensolver

In this section we introduce the variational quantum eigensolver (VQE), a hybrid quantum–classical algorithm designed to approximate ground-state properties of

interacting quantum many-body systems. VQE was first demonstrated by Peruzzo [128] and has since become one of the most widely studied approaches for exploiting near-term quantum devices for electronic structure and other many-body problems [129, 130]. The exact diagonalization method scales exponentially with system size because it requires explicit storage and manipulation of the full many-body wavefunction. VQE instead represents the wavefunction implicitly as a parametrized quantum circuit acting on a register of qubits and uses measurements on the quantum device, combined with a classical optimizer, to minimize the energy expectation value, thus providing an approximation of the ground state energy [128–131].

3.4.1 Variational principle and cost function

The starting point of the variational quantum eigensolver (VQE) is the Rayleigh–Ritz variational principle [69, 122]. We consider a Hamiltonian $\hat{H}$ with (unknown) ground-state energy E_0 and choose a family of normalized trial states $|\psi(\boldsymbol{\theta})\rangle$, parametrized by a set of real parameters $\boldsymbol{\theta} = (\theta_1, \theta_2, \ldots, \theta_{N_\theta})$. The corresponding energy functional,

$$E(\boldsymbol{\theta}) = \langle\psi(\boldsymbol{\theta})|\, \hat{H}\, |\psi(\boldsymbol{\theta})\rangle\,, \tag{3.122}$$

satisfies the variational bound

$$E(\boldsymbol{\theta}) \geq E_0 \quad \text{for all } \boldsymbol{\theta}, \tag{3.123}$$

with equality only when $|\psi(\boldsymbol{\theta})\rangle$ coincides with the exact ground state (up to a global phase). The variational bound follows directly from the Rayleigh–Ritz variational principle [69, 122]. Let $\{|E_n\rangle\}$ be the complete orthonormal set of eigenstates of $\hat{H}$,

$$\hat{H}\,|E_n\rangle = E_n\,|E_n\rangle\,, \qquad E_0 \leq E_1 \leq E_2 \leq \ldots. \tag{3.124}$$

Any normalized trial state $|\psi\rangle$ can be expanded in this basis,

$$|\psi\rangle = \sum_n c_n\,|E_n\rangle\,, \qquad \sum_n |c_n|^2 = 1. \tag{3.125}$$

The expectation value of the Hamiltonian is therefore

$$\langle\psi|\, \hat{H}\, |\psi\rangle = \sum_n |c_n|^2 E_n. \tag{3.126}$$

Since $E_n \geq E_0$ for all n, we obtain

$$\langle\psi|\,\hat{H}\,|\psi\rangle = E_0 \sum_n |c_n|^2 + \sum_{n>0} |c_n|^2 (E_n - E_0) \;\geq\; E_0. \tag{3.127}$$

The inequality becomes an equality only if $|c_n|^2 = 0$ for all $n > 0$, i.e., when $|\psi\rangle$ coincides with the exact ground state $|E_0\rangle$.

The VQE algorithm aims to solve the optimization problem

$$E_{\mathrm{VQE}} = \min_{\boldsymbol{\theta}} \langle\psi(\boldsymbol{\theta})|\,\hat{H}\,|\psi(\boldsymbol{\theta})\rangle\,. \tag{3.128}$$

In practice, $\hat{H}$ could be an interacting many-body Hamiltonian acting on a high-dimensional Hilbert space, and the trial state $|\psi(\boldsymbol{\theta})\rangle$ is generated by a parametrized quantum circuit (ansatz) on a qubit register.

VQE is a hybrid algorithm: state preparation and measurement are carried out on a quantum device, while the optimization over $\boldsymbol{\theta}$ is performed on a classical computer. The algorithm proceeds iteratively as follows:

1. **Hamiltonian of the problem.** One first specifies the quantum many-body system of interest (for instance, an interacting electronic system or a lattice spin model) and writes down the target Hamiltonian $\hat{H}$ in a form suitable for implementation on a quantum computer, which will be clarified. For VQE to be efficient, $\hat{H}$ must decompose into a sum of a polynomial number of terms whose expectation values can be measured separately (e.g. a sum of few-body interaction terms). Details of the Hamiltonian representation and fermion-to-qubit mapping are discussed in later sections.

2. **Definition of the ansatz.** One chooses a parametrized quantum circuit $\hat{U}(\boldsymbol{\theta})$ acting on n qubits, and defines the trial state as

$$|\psi(\boldsymbol{\theta})\rangle = \hat{U}(\boldsymbol{\theta})\,|\psi_{\mathrm{ref}}\rangle\,, \tag{3.129}$$

   where $|\psi_{\mathrm{ref}}\rangle$ is a fixed reference state. The circuit is built from a sequence of one and two-qubit gates, some of which depend explicitly on the parameters $\boldsymbol{\theta} = (\theta_1, \ldots, \theta_{N_\theta})$. Typically, these parameters enter as rotation angles in single-qubit gates,

$$R_\alpha(\theta) = e^{-i\theta\sigma_\alpha/2}, \tag{3.130}$$

   where $\sigma_\alpha \in \{\sigma_x, \sigma_y, \sigma_z\}$ are Pauli matrices, or as continuous parameters in

entangling gates such as controlled rotations or parametrized two-qubit evolutions. In this way, each θ_k controls the strength of a unitary transformation generated by a chosen Hermitian operator, and the full unitary takes the structured form

$$\hat{U}(\boldsymbol{\theta}) = \prod_k e^{-i\theta_k \hat{G}_k}, \tag{3.131}$$

where $\{\hat{G}_k\}$ are Hermitian generators determined by the ansatz design.

The depth and structure of the circuit determine the expressiveness of the ansatz and its sensitivity to hardware noise [129, 132, 133].

3. **State preparation on the quantum device.** For a given parameter vector $\boldsymbol{\theta}$, the circuit $\hat{U}(\boldsymbol{\theta})$ is executed on the quantum hardware, preparing the corresponding n-qubit state $|\psi(\boldsymbol{\theta})\rangle$.

4. **Measurement of observables.** The expectation value $E(\boldsymbol{\theta})$ is estimated by repeated projective measurements of $\hat{H}$ on $|\psi(\boldsymbol{\theta})\rangle$.The Hamiltonian is decomposed into a sum of measurement-friendly terms (e.g. tensor products of Pauli operators), and each group of mutually commuting terms is measured separately. The resulting bit strings are collected over many repetitions (shots) and used to estimate $E(\boldsymbol{\theta})$ as a statistical average. The number of required measurements grows with the number of Hamiltonian terms and with the inverse square of the desired statistical precision (error).

5. **Classical optimization.** The estimated energy $E(\boldsymbol{\theta})$ is passed to a classical optimizer which proposes an updated parameter set $\boldsymbol{\theta}'$, attempting to reduce the cost function. Gradient-free (Nelder–Mead, COBYLA, SPSA) and gradient-based (stochastic gradient, L-BFGS) optimizers are both commonly used [129, 131, 134–137]. Because measurements are noisy and each evaluation of $E(\boldsymbol{\theta})$ is stochastic, the choice of optimizer matters, and the methods listed above are not equally robust to this noise [129, 138]. Stochastic optimizers such as SPSA and stochastic gradient descent are built for noisy function and gradient estimates, and they tolerate sampling noise comparatively well [129, 136]. Methods that fit local models or curvature approximations to the sampled values, such as Nelder-Mead, COBYLA, and L-BFGS, are more sensitive to noise. They tend to perform well only when $E(\boldsymbol{\theta})$ is estimated with many measurement shots or in noiseless simulation [134, 135, 137]. On present-day hardware, noise-robust optimizers together with error-mitigation techniques are therefore often required

[131, 139, 140].

6. **Convergence and post-processing.** Steps 3–5 are repeated until a convergence criterion is satisfied, for example when the change in the energy estimate between successive iterations falls below a given threshold or after a fixed maximum number of iterations. Once converged, the final parameter set $\boldsymbol{\theta}_\star$ provides an approximation to the ground state, from which other observables can be measured straightforwardly on the quantum device.

3.4.2 VQE for quantum many-body systems

The VQE framework can be used for quantum many-body problems, where the size of the Hilbert space grows exponentially with the number of degrees of freedom. By encoding the relevant many-body degrees of freedom into a register of qubits, VQE can represent states using a number of parameters and gate operations that scale only polynomially with system size, provided a suitable ansatz is chosen [128–132].

From the perspective of many-body methods, it is useful to compare VQE, CI, and mean-field approaches:

- **Compared to CI**, VQE does not require explicit construction and full diagonalization of the many-body Hamiltonian matrix: the Hilbert-space dimension appears only implicitly through the number of qubits and the structure of the ansatz and Hamiltonian decomposition. In practice, however, this advantage is offset by several serious challenges on current noisy devices. For small systems, CI/ED is routinely used to benchmark VQE: even for modest problem sizes, classical diagonalization (possibly with symmetry reduction or sparse methods) always remains more accurate and more predictable in cost, whereas VQE can suffer from noise, barren plateaus, ansatz expressibility issues, and difficult classical optimization landscapes.[6, 128, 129, 133] For larger systems where CI becomes intractable, VQE is in principle a candidate route to capturing correlation effects beyond mean-field on quantum hardware, but recent studies indicate that achieving a practical quantum advantage will likely require substantial error mitigation, problem-specific ansätze, and improved optimization strategies, and remains an open challenge on near-term devices.[130, 141, 142]

- **Compared to mean-field methods**, VQE can represent entangled many-body states that go far beyond a single Slater determinant or product state [128, 129, 131, 143, 144]. While mean-field approaches replace the full interaction with

an effective one-body potential, VQE keeps the full interacting Hamiltonian and uses the variational freedom of the ansatz to approximate its ground state within the accessible variational manifold.

Whether VQE provides an actual computational advantage over classical many-body methods depends on several factors: the expressiveness and trainability of the chosen ansatz, the scaling of measurement requirements, the performance of the classical optimizer, and the noise characteristics of the underlying hardware. [130] discusses in detail how these aspects affect the overall resources needed and formulates conditions under which VQE could achieve a genuine quantum advantage for many-body problems [129, 133].

To summarize the VQE approach:

1. Choose the many-body Hamiltonian $\hat{H}$.
2. Select a parametrized ansatz circuit $\hat{U}(\boldsymbol{\theta})$ acting on qubits and a reference state $|\psi_{\text{ref}}\rangle$.
3. Prepare $|\psi(\boldsymbol{\theta})\rangle = \hat{U}(\boldsymbol{\theta})\,|\psi_{\text{ref}}\rangle$ on the quantum device.
4. Estimate $E(\boldsymbol{\theta})$ by repeated measurements of $\hat{H}$ on $|\psi(\boldsymbol{\theta})\rangle$.
5. Use a classical optimizer to update $\boldsymbol{\theta}$ so as to reduce $E(\boldsymbol{\theta})$.
6. Iterate steps 3–6 until convergence, and then extract ground-state properties from the optimized state $|\psi(\boldsymbol{\theta}_\star)\rangle$.

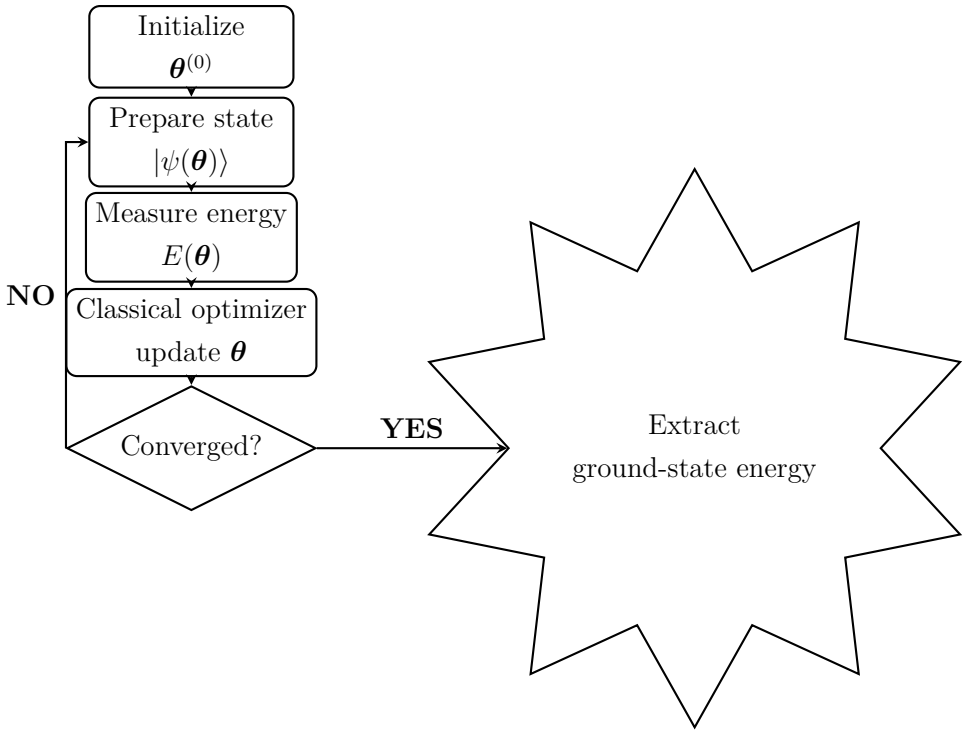

Figure 3.3: Schematic flowchart of the VQE optimization loop.

It is graphically shown in Fig. 3.3. In the remainder of this section we will specify how we can represent a many-body Hamiltonian in a suitable form to be used for VQE, through applying the Jordan-Wigner transformation.

3.4.3 Jordan–Wigner Transformation

In the previous sections we have formulated our many-body problem in second quantization using fermionic creation and annihilation operators $c_j^\dagger$ and c_j (or $c_{j\sigma}^\dagger$ and $c_{j\sigma}$ for spinful systems). To implement these Hamiltonians on a quantum computer, or to recast them as spin models, it is convenient to map fermionic operators to operators acting on spin-1/2 degrees of freedom. The main difficulty is that fermionic operators satisfy non-local anti-commutation relations,

$$\{c_p, c_q\} = 0, \qquad \{c_p^\dagger, c_q^\dagger\} = 0, \qquad \{c_p, c_q^\dagger\} = \delta_{pq}, \tag{3.132}$$

whereas local spin operators acting on different sites commute. The Jordan–Wigner (JW) transformation provides an explicit, invertible mapping between fermionic operators and tensor products of spin-1/2 operators such that the anti-commutation relations in Eq.(3.132) are exactly preserved [145–147]. In this way an interacting

fermionic Hamiltonian can be rewritten as a sum of spin (Pauli) strings, which is the form required by VQE and other quantum-algorithmic approaches.

We consider a one-dimensional ordering of the fermionic modes, labelled by $j = 1, \ldots, M$. On each site j we introduce a spin-1/2 degree of freedom with spin operators $\hat{S}_j^x, \hat{S}_j^y, \hat{S}_j^z$ (equivalently Pauli matrices $\hat{\sigma}_j^\alpha = 2\hat{S}_j^\alpha$, $\alpha = x, y, z$). We also define the spin raising and lowering operators

$$\hat{S}_j^+ = \hat{S}_j^x + i\hat{S}_j^y, \qquad \hat{S}_j^- = \hat{S}_j^x - i\hat{S}_j^y, \tag{3.133}$$

which satisfy the usual $\mathfrak{su}(2)$ algebra together with $\hat{S}_j^z$. Operators acting on different sites commute:

$$[S_p^\alpha, S_q^\beta] = 0 \qquad \text{for } p \neq q, \tag{3.134}$$

for any $\alpha, \beta \in \{x, y, z, +, -\}$. If we naively tried to identify $c_j \sim \hat{S}_j^-$, operators on different sites would commute instead of anti-commute, in contradiction with (3.132). The key idea of the JW transformation is therefore to attach to each fermionic mode a phase string that keeps track of the fermion parity of all sites to the "left" of j in the chosen ordering.

For each site j we introduce the phase operator

$$\Phi_j = \pi \sum_{m=1}^{j-1} \left(\tfrac{1}{2} + \hat{S}_m^z \right), \tag{3.135}$$

and its exponential

$$\mathrm{e}^{i\Phi_j} = \prod_{m=1}^{j-1} (-2\hat{S}_m^z), \tag{3.136}$$

which plays the role of the Jordan–Wigner string. Because $(2S_m^z)^2 = 1$ and S_m^z commutes with $\hat{S}_j^\pm$ for $m \neq j$, this operator simply keeps track of whether the number of fermions on sites $1, \ldots, j-1$ is even or odd. The JW map for spinless fermions is then defined as

$$c_j^\dagger = \mathrm{e}^{-i\Phi_j} \hat{S}_j^+, \qquad c_j = \hat{S}_j^- \, \mathrm{e}^{i\Phi_j}. \tag{3.137}$$

One can verify explicitly that Eq.(3.137) satisfies the canonical fermionic anti-commutation relations Eq.(3.132). The non-local phase string $\mathrm{e}^{i\Phi_j}$ ensures that exchanging the order of c_p and c_q (with $p \neq q$) produces the required minus sign.

In this convention the local fermionic number operator becomes

$$n_j = c_j^\dagger c_j = \hat{S}_j^+ \hat{S}_j^- = \frac{1}{2} + \hat{S}_j^z, \tag{3.138}$$

so that an empty fermionic mode corresponds to the spin-down state $|\downarrow\rangle_j$ with eigenvalue $-\frac{1}{2}$ and $n_j = 0$, while an occupied mode corresponds to the spin-up state $|\uparrow\rangle_j$ with eigenvalue $\frac{1}{2}$ and $n_j = 1$. This establishes a direct correspondence between the fermionic basis $\{|0\rangle, |1\rangle\}$ and the spin basis $\{|\downarrow\rangle, |\uparrow\rangle\}$ on each site.

In the following we apply this JW construction to a spinless tight-binding model, expressing the basic second-quantized operators in terms of products of spin operators $\hat{S}_j^x, \hat{S}_j^y, \hat{S}_j^z$ (or equivalently Pauli matrices), as required for implementation on a quantum computer.

Nearest-neighbour hopping. Consider a generic hopping term between sites i and j (with $i < j$ for definiteness),

$$T_{ij} = c_i^\dagger c_j + c_j^\dagger c_i. \tag{3.139}$$

Using the commutation relations between $\hat{S}^\pm$ and $\hat{S}^z$, one finds

$$c_i^\dagger c_j = \mathrm{e}^{-i\Phi_i} \hat{S}_i^+ \hat{S}_j^- \mathrm{e}^{i\Phi_j} = \hat{S}_i^+ \left[\prod_{k=i}^{j-1} \left(2\hat{S}_k^z \right) \right] \hat{S}_j^-, \tag{3.140}$$

and similarly for $c_j^\dagger c_i$. It is convenient to write

$$T_{ij} = \left(\hat{S}_i^+ \hat{S}_j^- + \hat{S}_j^+ \hat{S}_i^- \right) \prod_{k=i+1}^{j-1} \left(2\hat{S}_k^z \right). \tag{3.141}$$

Expressing $\hat{S}^\pm$ in terms of $\hat{S}^x$ and $\hat{S}^y$ via Eq.(3.133) yields

$$T_{ij} = 2 \left[\hat{S}_i^x \hat{S}_j^x + \hat{S}_i^y \hat{S}_j^y \right] \prod_{k=i+1}^{j-1} \left(2\hat{S}_k^z \right). \tag{3.142}$$

For nearest neighbours ($j = i+1$) the string between i and j is empty and the product reduces to the identity, so the hopping term reduces to a purely local $XX + YY$ coupling,

$$T_{i,i+1} = 2 \left(\hat{S}_i^x \hat{S}_{i+1}^x + \hat{S}_i^y \hat{S}_{i+1}^y \right). \tag{3.143}$$

Example: spinless tight-binding chain with on-site energy For the one-dimensional spinless tight-binding Hamiltonian with a uniform on-site energy ϵ and

nearest-neighbour hopping t on a chain of N sites,

$$H = \epsilon \sum_{j=1}^{N} c_j^\dagger c_j - t \sum_{j=1}^{N-1} \left(c_j^\dagger c_{j+1} + c_{j+1}^\dagger c_j \right). \tag{3.144}$$

The on-site term becomes

$$\epsilon \sum_{j=1}^{N} c_j^\dagger c_j = \epsilon \sum_{j=1}^{N} n_j = \epsilon \sum_{j=1}^{N} \left(\frac{1}{2} + \hat{S}_j^z \right). \tag{3.145}$$

For nearest neighbours j and $j+1$ we start from the Jordan–Wigner map for spinless fermions

$$c_j^\dagger = e^{-i\Phi_j} \hat{S}_j^+, \qquad c_{j+1} = \hat{S}_{j+1}^- e^{i\Phi_{j+1}}, \tag{3.146}$$

with

$$\Phi_j = \pi \sum_{m=1}^{j-1} \left(\tfrac{1}{2} + \hat{S}_m^z \right), \qquad \Phi_{j+1} = \pi \sum_{m=1}^{j} \left(\tfrac{1}{2} + \hat{S}_m^z \right) = \Phi_j + \pi \left(\tfrac{1}{2} \hat{S}_j^z \right). \tag{3.147}$$

Then

$$\begin{aligned} c_j^\dagger c_{j+1} &= e^{-i\Phi_j} \hat{S}_j^+ \hat{S}_{j+1}^- e^{i\Phi_{j+1}} \\ &= e^{-i\Phi_j} \hat{S}_j^+ \hat{S}_{j+1}^- e^{i\Phi_j} e^{i\pi(\frac{1}{2} + \hat{S}_j^z)}. \end{aligned} \tag{3.148}$$

The operators $e^{\pm i\Phi_j}$ depend only on $\hat{S}_m^z$ with $m < j$, so they commute with both $\hat{S}_j^+$ and $\hat{S}_{j+1}^-$. Thus, we can move them together and cancel them:

$$c_j^\dagger c_{j+1} = \hat{S}_j^+ \hat{S}_{j+1}^- e^{i\pi(\frac{1}{2} + \hat{S}_j^z)}. \tag{3.149}$$

Next we simplify the exponential. Since $\hat{S}_j^z$ has eigenvalues $\pm\frac{1}{2}$, we have

$$e^{i\pi(\frac{1}{2} + \hat{S}_j^z)} = \begin{cases} e^{i\pi(1)} = -1, \\ e^{i\pi(0)} = +1, \end{cases} \tag{3.150}$$

so as an operator identity

$$e^{i\pi(\frac{1}{2} + \hat{S}_j^z)} = -2\hat{S}_j^z. \tag{3.151}$$

Hence

$$c_j^\dagger c_{j+1} = -2\hat{S}_j^+ \hat{S}_{j+1}^- \hat{S}_j^z. \tag{3.152}$$

Because $\hat{S}^-_{j+1}$ acts on site $j+1$, it commutes with $\hat{S}^z_j$, so we can rewrite

$$c_j^\dagger c_{j+1} = -2\hat{S}^+_j \hat{S}^z_j \hat{S}^-_{j+1}. \tag{3.153}$$

Using the spin-$\frac{1}{2}$ identity

$$\hat{S}^+_j \hat{S}^z_j = -\tfrac{1}{2}\hat{S}^+_j \quad \Rightarrow \quad \hat{S}^+_j(-2\hat{S}^z_j) = \hat{S}^+_j, \tag{3.154}$$

we obtain

$$c_j^\dagger c_{j+1} = \hat{S}^+_j \hat{S}^-_{j+1}. \tag{3.155}$$

Similarly, starting from

$$c_{j+1}^\dagger = e^{-i\Phi_{j+1}}\hat{S}^+_{j+1}, \qquad c_j = \hat{S}^-_j e^{i\Phi_j}, \tag{3.156}$$

one finds, by analogous steps (or by taking the Hermitian conjugate of the previous result),

$$c_{j+1}^\dagger c_j = \hat{S}^+_{j+1}\hat{S}^-_j. \tag{3.157}$$

Therefore, for nearest neighbours the Jordan–Wigner strings cancel, and we arrive at

$$c_j^\dagger c_{j+1} + c_{j+1}^\dagger c_j = \hat{S}^+_j \hat{S}^-_{j+1} + \hat{S}^+_{j+1}\hat{S}^-_j. \tag{3.158}$$

We now express this in terms of $\hat{S}^x$ and $\hat{S}^y$ using

$$\hat{S}^+_j = \hat{S}^x_j + i\hat{S}^y_j, \qquad \hat{S}^-_j = \hat{S}^x_j - i\hat{S}^y_j. \tag{3.159}$$

First,

$$\begin{aligned}
\hat{S}^+_j \hat{S}^-_{j+1} &= (\hat{S}^x_j + i\hat{S}^y_j)(\hat{S}^x_{j+1} - i\hat{S}^y_{j+1}) \\
&= \hat{S}^x_j \hat{S}^x_{j+1} - i\hat{S}^x_j \hat{S}^y_{j+1} + i\hat{S}^y_j \hat{S}^x_{j+1} + \hat{S}^y_j \hat{S}^y_{j+1}, \qquad (3.160)\\
\hat{S}^+_{j+1}\hat{S}^-_j &= (\hat{S}^x_{j+1} + i\hat{S}^y_{j+1})(\hat{S}^x_j - i\hat{S}^y_j) \\
&= \hat{S}^x_{j+1}\hat{S}^x_j - i\hat{S}^x_{j+1}\hat{S}^y_j + i\hat{S}^y_{j+1}\hat{S}^x_j + \hat{S}^y_{j+1}\hat{S}^y_j. \qquad (3.161)
\end{aligned}$$

Using the fact that spin operators on different sites commute, $\hat{S}^\alpha_j \hat{S}^\beta_{j+1} = \hat{S}^\beta_{j+1}\hat{S}^\alpha_j$, we can rewrite the second expression with the same ordering of sites:

$$\hat{S}^+_{j+1}\hat{S}^-_j = \hat{S}^x_j \hat{S}^x_{j+1} + i\hat{S}^y_j \hat{S}^x_{j+1} - i\hat{S}^x_j \hat{S}^y_{j+1} + \hat{S}^y_j \hat{S}^y_{j+1}. \tag{3.162}$$

Adding the two,

$$\begin{aligned}\hat{S}_j^+\hat{S}_{j+1}^- + \hat{S}_{j+1}^+\hat{S}_j^- &= \left[\hat{S}_j^x\hat{S}_{j+1}^x + \hat{S}_j^x\hat{S}_{j+1}^x\right] \\ &\quad + \left[-i\hat{S}_j^x\hat{S}_{j+1}^y - i\hat{S}_j^x\hat{S}_{j+1}^y\right] \\ &\quad + \left[i\hat{S}_j^y\hat{S}_{j+1}^x + i\hat{S}_j^y\hat{S}_{j+1}^x\right] \\ &\quad + \left[\hat{S}_j^y\hat{S}_{j+1}^y + \hat{S}_j^y\hat{S}_{j+1}^y\right] \\ &= 2\Big(\hat{S}_j^x\hat{S}_{j+1}^x + \hat{S}_j^y\hat{S}_{j+1}^y\Big), \end{aligned} \tag{3.163}$$

because the mixed terms $\propto \hat{S}_j^x\hat{S}_{j+1}^y$ and $\hat{S}_j^y\hat{S}_{j+1}^x$ cancel pairwise.

Therefore the hopping term in Eq. (3.144) becomes

$$-t\sum_{j=1}^{N-1}\left(c_j^\dagger c_{j+1} + c_{j+1}^\dagger c_j\right) = -2t\sum_{j=1}^{N-1}\left(\hat{S}_j^x\hat{S}_{j+1}^x + \hat{S}_j^y\hat{S}_{j+1}^y\right). \tag{3.164}$$

Equation (3.164) expresses the original fermionic tight-binding model entirely in terms of spin operators (or, equivalently, Pauli matrices via $\sigma_j^\alpha = 2\hat{S}_j^\alpha$), and serves as the starting point for the VQE simulations.

3.4.4 Pauli–string Representation of Many-body Hamiltonians

Combining the above ingredients, any second–quantized fermionic Hamiltonian with one and two–body operators can be mapped to a qubit Hamiltonian of the form

$$\hat{H} = \sum_\alpha h_\alpha\,\hat{P}_\alpha, \qquad \hat{P}_\alpha = \bigotimes_{p=1}^{M}\hat{\sigma}_p^{\alpha_p}, \quad \alpha_p \in \{0, x, y, z\}, \tag{3.165}$$

where $\hat{\sigma}^0 = \hat{I}$ is the identity operator on a single qubit and M is the total number of qubits introduced by the Jordan–Wigner mapping (equal to the number of fermionic modes) [145–147]. Each operator $\hat{P}_\alpha$ is thus a tensor product ("Pauli string") of single–qubit operators, and the real coefficients h_α encode the microscopic parameters of the original many–body model: on–site energies, hopping amplitudes, interaction strengths, and pairing amplitudes [2, 131].

From the point of view of many–body physics, the transformation Eq.(3.165) replaces the original Fock–space problem (whose dimension grows combinatorially with particle number and system size) by an equivalent spin–1/2 model acting on M

qubits [147]. The nonlocal fermionic statistics are carried entirely by the structure of the Pauli strings, while the spectrum and eigenstates of $\hat{H}$ are identical to those of the original interacting fermionic Hamiltonian [145, 146]. In particular, all many–body properties of interest—ground–state energy, excitation spectrum, correlation functions, and entanglement measures—can be recovered from Eq.(3.165).

In the VQE framework, Eq. (3.165) is the natural endpoint of the mapping stage and the starting point of the variational optimization [128, 129, 131]. Given a parametrized many–body trial state $|\psi(\boldsymbol{\theta})\rangle$ prepared on M qubits, the energy expectation value can be written as

$$E(\boldsymbol{\theta}) = \langle\psi(\boldsymbol{\theta})|\,\hat{H}\,|\psi(\boldsymbol{\theta})\rangle = \sum_{\alpha} h_\alpha\ \langle\psi(\boldsymbol{\theta})|\,\hat{P}_\alpha\,|\psi(\boldsymbol{\theta})\rangle\,. \tag{3.166}$$

Hence the interacting many–body energy is obtained as a weighted sum of expectation values of Pauli strings, each of which corresponds to a measurable observable on the quantum device [128, 131]. In practice, the strings $\hat{P}_\alpha$ are grouped into mutually commuting sets so that the corresponding many–body observables can be measured in a common basis, reducing the total measurement overhead [130, 140].

This Pauli–string representation plays the same role for VQE that the matrix representation of the Hamiltonian plays for exact diagonalization: it provides the complete description of the interacting many–body problem in a fixed basis. The key difference is that, instead of constructing and diagonalizing the full Hamiltonian matrix in classical memory, VQE evaluates Eq.(3.166) by sampling the expectation values of Pauli strings on a quantum processor and uses a classical optimizer to variationally approach the ground state [128–130]. We will later specify the particular many–body Hamiltonians and ansätze used in this work, always starting from their Pauli–string representation Eq.(3.165).

3.5 Density Matrix Renormalization Group

We return to the exponential growth of the Hilbert space of many-body systems. For a chain of L spin-1/2 degrees of freedom the Hilbert-space dimension is 2^L. Even for modest system sizes, configuration interaction becomes impractical. The ground states and low-lying excitations of local Hamiltonians, however, occupy only a small and structured corner of this large space. Tensor-network methods exploit this structure. The Density Matrix Renormalization Group (DMRG) is the most important of these methods in one dimension [68, 148–150]. In short, DMRG is an

algorithm that optimizes a matrix-product-state (MPS) ansatz for the ground state of a local Hamiltonian on a chain [148–151].

In this section we introduce the tensor-network notation that underlies DMRG. The goal is a compact graphical language for many-body tensors. In this language the structure of a state and the cost of manipulating it are both easy to see.

We build up to the algorithm in four steps. First we introduce tensors and the few operations that DMRG needs. These are products, traces, contractions, and the singular value decomposition. Second we use the singular value decomposition to define the matrix product state, which is the variational form that DMRG optimizes. Third we explain why this form is so efficient in one dimension, using the area law for entanglement. Finally we describe the DMRG algorithm itself on a concrete spinless chain.

3.5.1 Tensors and Tensor Operations

A pure state of L local degrees of freedom, each with on-site Hilbert-space dimension d, can be written in a local basis as

$$|\psi\rangle = \sum_{j_1,\ldots,j_L=0}^{d-1} C_{j_1 j_2 \ldots j_L} \; |j_1\rangle \otimes |j_2\rangle \otimes \cdots \otimes |j_L\rangle \,, \tag{3.167}$$

The coefficients $C_{j_1 j_2 \ldots j_L}$ form a rank-L tensor [69, 71]. More generally, a rank-r tensor is an array of complex numbers

$$T_{i_1 i_2 \ldots i_r} \in \mathbb{C}^{d_1 \times d_2 \times \cdots \times d_r}, \tag{3.168}$$

with one index i_k for each factor space of dimension d_k. Scalars, vectors, and matrices are the rank-0, rank-1, and rank-2 cases.

In tensor-network notation, a tensor is drawn as a node (a geometric shape) with one leg for each index [150–152]. For instance, a rank-four tensor $R_{\rho\sigma\mu\nu}$ is drawn as

$R_{\rho\sigma\mu\nu} \longleftrightarrow$ 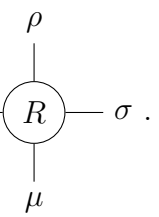 . (3.169)

In many-body applications it is convenient to distinguish two kinds of index.

Physical indices label the local basis states $|j\rangle$ on each site. Virtual or bond indices connect tensors and encode the entanglement between subsystems [150, 153]. In diagrams we keep track only of which legs are connected. The choice of node shape or leg orientation carries no extra meaning.

DMRG manipulates tensors through a small set of operations. These are tensor products, traces, contractions, and singular value decompositions. Each has a simple graphical rule. The rules mirror Einstein summation, but without writing the indices explicitly.

The tensor (outer) product of a rank-r tensor A and a rank-s tensor B is the rank-$(r+s)$ tensor shown below.

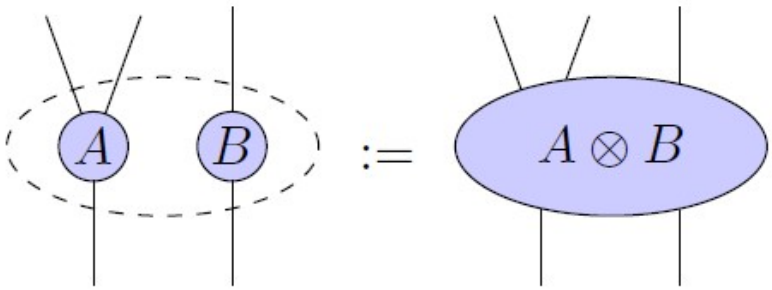

The value of a disconnected network is the product of the values of its connected components.

Given a tensor $T_{i_1 \ldots i_r}$ whose x-th and y-th indices have the same dimension, the partial trace over these indices is

$$[\mathrm{Tr}_{x,y} T]_{i_1 \ldots i_{x-1} i_{x+1} \ldots i_{y-1} i_{y+1} \ldots i_r} = \sum_{\alpha=1}^{d_x} T_{i_1 \ldots i_{x-1}\, \alpha\, i_{x+1} \ldots i_{y-1}\, \alpha\, i_{y+1} \ldots i_r}. \tag{3.170}$$

In the diagram, summation over a shared index is shown by connecting the corresponding legs.

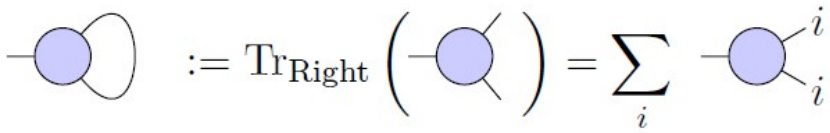

The usual trace of a matrix and the partial trace of a density matrix over a subsystem are special cases of this operation.

The most common operation in a tensor network is contraction. To contract two tensors, we take their tensor product and then trace over a shared set of indices. For instance, contracting the last index of $A_{i\alpha}$ with the first index of $B_{\alpha j}$ gives

$$C_{ij} = \sum_{\alpha} A_{i\alpha} B_{\alpha j}, \tag{3.171}$$

which is ordinary matrix multiplication. We draw this contraction below.

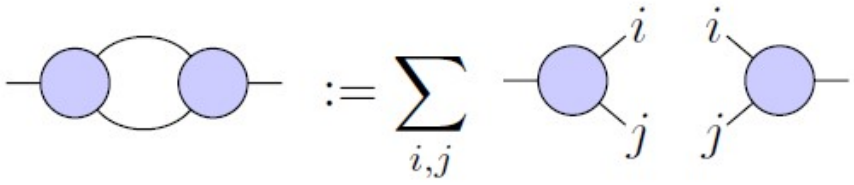

In DMRG, inner products, expectation values, correlation functions, and effective Hamiltonians are all expressed as such contractions of the state with the local operators.

3.5.2 Grouping, splitting and the singular-value decomposition

A central idea behind tensor-network methods is that a high-rank tensor can be treated as a matrix. We do this by grouping several indices into a single combined index. For a tensor $T_{i_1 \ldots i_n j_1 \ldots j_m}$, we define

$$T_{I,J} := T_{i_1 \ldots i_n j_1 \ldots j_m}, \tag{3.172}$$

where I runs over all combined values of $(i_1, \ldots, i_n)$ and J over all combined values of $(j_1, \ldots, j_m)$. We can now apply standard matrix operations to T. The most important is the singular value decomposition (SVD),

$$T_{I,J} = \sum_{\alpha} U_{I\alpha} S_{\alpha} V^{\dagger}_{\alpha J}, \tag{3.173}$$

shown in graphical form below.

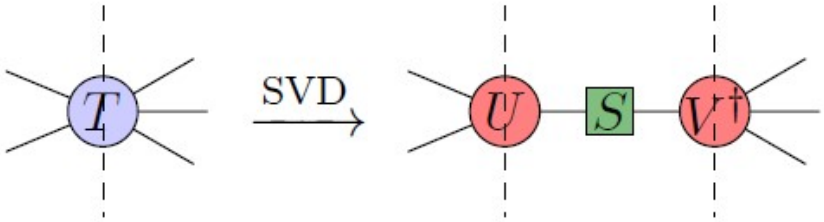

Here U and V are isometric tensors. Their legs across the decomposition satisfy $U^\dagger U = I$ and $V^\dagger V = I$. The matrix S is diagonal, with non-negative singular values S_α.

In many-body physics the singular values are the Schmidt coefficients of a bipartition of the chain. Their distribution measures the entanglement across the cut. It also guides truncation. By discarding the small singular values, we obtain the best low-rank approximation of the state. DMRG uses this property directly. After optimizing the local tensors, it applies an SVD to compress the state back to a fixed bond dimension, keeping only the largest Schmidt modes.

3.5.3 Tensor Networks for Quantum Many-body States and Matrix Product States

With these ingredients we can define a tensor network. It is a set of tensors together with a pattern of contracted legs. The uncontracted legs are the external indices, and they fix the rank of the overall object. To evaluate the network for a fixed assignment of the external indices, we multiply all tensor entries and sum over all internal indices allowed by the connections.

We saw that the wave function of a one-dimensional many-body system of length L can be written in a local basis as

$$|\Psi\rangle = \sum_{j_1,\ldots,j_L=1}^{d} C_{j_1 j_2 \ldots j_L} \, |j_1\rangle \otimes |j_2\rangle \otimes \cdots \otimes |j_L\rangle \,, \tag{3.174}$$

Here d is the on-site Hilbert-space dimension. The coefficient $C_{j_1 j_2 \ldots j_L}$ is a rank-L tensor with d components along each physical index. The Hilbert space has dimension d^L, which grows exponentially with system size. This growth is the source of the difficulty of exact diagonalization.

A matrix product state (MPS) parametrizes a many-body state $|\Psi\rangle$ as a product of local tensors with bounded internal dimension. The idea is to factorize the coefficient

tensor into a product of low-rank objects,

$$C_{j_1 j_2 \ldots j_L} = \sum_{\{\alpha_i\}} A^{[1]\,j_1}_{\alpha_0 \alpha_1} A^{[2]\,j_2}_{\alpha_1 \alpha_2} \cdots A^{[L]\,j_L}_{\alpha_{L-1} \alpha_L}, \tag{3.175}$$

The indices α_i with $i = 0, \ldots, L$ are auxiliary bond indices of dimension D_i. For open boundary conditions we set $D_0 = D_L = 1$, so the first and last tensors are row and column vectors. The maximum bond dimension

$$D = \max_i D_i \tag{3.176}$$

controls how much the ansatz can express. It is the main variational parameter of the DMRG calculations below.

Equation (3.175) defines an MPS with open boundary conditions. Inserting it into Eq. (3.174) gives the standard MPS form

$$|\Psi\rangle = \sum_{j_1, \ldots, j_L} A^{[1]\,j_1} A^{[2]\,j_2} \cdots A^{[L]\,j_L} \, |j_1 j_2 \ldots j_L\rangle \,, \tag{3.177}$$

For each configuration $(j_1, \ldots, j_L)$ the product of matrices $A^{[1]\,j_1} A^{[2]\,j_2} \cdots A^{[L]\,j_L}$ is a scalar, because $D_0 = D_L = 1$.

In the tensor-network language, each tensor $A^{[i]}$ is a node with three legs. One leg is physical, of dimension d. The other two are bond legs, of dimensions D_{i-1} and D_i. The MPS in Eq. (3.177) is then a chain of such nodes with their bond legs contracted, as drawn below.

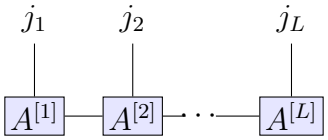

Each horizontal line is a contracted bond index. Each vertical line is an uncontracted physical index.

The power of the MPS form comes from the entanglement structure of low-energy states of local Hamiltonians. Consider a bipartition of the chain into a left block $\mathcal{L} = \{1, \ldots, \ell\}$ and a right block $\mathcal{R} = \{\ell+1, \ldots, L\}$. Any pure state $|\Psi\rangle$ has a Schmidt decomposition across this cut,

$$|\Psi\rangle = \sum_{\alpha=1}^{\chi} \lambda_\alpha \, |\phi^{[\mathcal{L}]}_\alpha\rangle \otimes |\phi^{[\mathcal{R}]}_\alpha\rangle \,, \tag{3.178}$$

The Schmidt coefficients satisfy $\lambda_\alpha \geq 0$ and $\sum_\alpha \lambda_\alpha^2 = 1$. The Schmidt rank χ is at

most $d^{\min(\ell, L-\ell)}$. The entanglement entropy across the cut is

$$S_{\mathrm{vN}} = -\sum_{\alpha=1}^{\chi} \lambda_\alpha^2 \log \lambda_\alpha^2. \tag{3.179}$$

The MPS form encodes this structure directly. The bond dimension D_ℓ across the cut between sites ℓ and $\ell+1$ bounds the Schmidt rank, $\chi \leq D_\ell$. It therefore bounds the entanglement entropy as well,

$$S_{\mathrm{vN}} \leq \log D_\ell. \tag{3.180}$$

Ground states of gapped local one-dimensional Hamiltonians obey an area law for entanglement. That is, S_{vN} saturates to a constant in the thermodynamic limit. The entropy therefore does not grow with system size. This is why a modest bond dimension suffices, and why MPS and DMRG work so well for one-dimensional systems [150, 151].

It is convenient to bring an MPS into a canonical form [150, 151, 153]. In this form the tensors to the left of a chosen bond build an orthonormal basis for the left block. The tensors to the right build an orthonormal basis for the right block. One reaches this form by a sequence of singular value decompositions along the chain. This is equivalent to a sequence of Schmidt decompositions. Each site tensor then factorizes as

$$A^{[i]\,j_i} = \Gamma^{[i]\,j_i} \Lambda^{[i]}, \tag{3.181}$$

where $\Lambda^{[i]}$ is a diagonal matrix of singular values, which are the Schmidt coefficients, and $\Gamma^{[i]\,j_i}$ is an isometric tensor obeying the orthonormality conditions of the canonical form.

The number of variational parameters in an open-boundary MPS is of order

$$N_{\mathrm{MPS}} \sim L\, d\, D^2, \tag{3.182}$$

This scales only linearly with the system size L. A generic many-body state needs d^L parameters, which is exponential. For moderate D the MPS therefore explores only a small slice of the Hilbert space. That slice is the important one, because it matches the entanglement structure of low-energy states in one dimension.

Local observables and correlation functions are computed by contracting the matching tensor network. For a nearest-neighbour Hamiltonian, the cost of evaluating $\langle \Psi | \hat{H} | \Psi \rangle$ scales as $\mathcal{O}(L d^2 D^3)$. This is polynomial in L, not exponential. DMRG is

then a variational energy minimization over the manifold of MPS with fixed bond dimension D.

3.5.4 DMRG for a spinless tight-binding chain

To illustrate how DMRG operates in practice, we consider again the one-dimensional spinless tight-binding model with on-site energies and nearest-neighbour hopping introduced earlier.

Before the details, here is the idea of the algorithm. DMRG searches for the ground state within the set of matrix product states of a fixed bond dimension D. It does not vary all the tensors at once. It works on two neighbouring tensors at a time and holds the rest of the chain fixed. For that small local problem it solves a standard eigenvalue problem and keeps the lowest eigenvector. It then splits this result back into two tensors with a singular value decomposition, and it truncates the bond back to dimension D. Moving this active pair along the chain, and sweeping back and forth, lowers the energy until it converges. The rest of this section makes each step precise.

For a chain of L sites with open boundary conditions, the second-quantized Hamiltonian reads

$$\hat{H} = \epsilon \sum_{j=1}^{L} \hat{n}_j - t \sum_{j=1}^{L-1} \left(\hat{c}_j^\dagger \hat{c}_{j+1} + \hat{c}_{j+1}^\dagger \hat{c}_j \right), \tag{3.183}$$

where $\hat{c}_j^\dagger$ ($\hat{c}_j$) creates (annihilates) a spinless fermion on site j, and $\hat{n}_j = \hat{c}_j^\dagger \hat{c}_j$ is the number operator.

Each lattice site has a local Hilbert space spanned by the occupation number basis

$$|0\rangle_j = (1,\, 0)^T \equiv \text{empty}, \qquad |1\rangle_j = (0,\, 1)^T \equiv \text{one fermion}, \tag{3.184}$$

so the local dimension is $d = 2$. In this basis the local operators are the 2×2 matrices

$$\hat{c}_j = \begin{pmatrix} 0 & 1 \\ 0 & 0 \end{pmatrix}, \quad \hat{c}_j^\dagger = \begin{pmatrix} 0 & 0 \\ 1 & 0 \end{pmatrix}, \quad \hat{n}_j = \begin{pmatrix} 0 & 0 \\ 0 & 1 \end{pmatrix}, \quad I_j = \begin{pmatrix} 1 & 0 \\ 0 & 1 \end{pmatrix}. \tag{3.185}$$

An arbitrary many-body state is written in the occupation basis as

$$|\Psi\rangle = \sum_{j_1,\ldots,j_L=0,1} C_{j_1 j_2 \ldots j_L} \, |j_1 j_2 \ldots j_L\rangle \,. \tag{3.186}$$

Rather than store the full coefficient tensor $C_{j_1 \ldots j_L}$, we represent $|\Psi\rangle$ as a matrix

product state with open boundary conditions,

$$|\Psi\rangle = \sum_{j_1,\ldots,j_L} A^{[1]\,j_1} A^{[2]\,j_2} \cdots A^{[L]\,j_L} \, |j_1 j_2 \ldots j_L\rangle \,, \tag{3.187}$$

Here $A^{[1]\,j_1}$ is a $1 \times D_1$ row vector and $A^{[L]\,j_L}$ is a $D_{L-1} \times 1$ column vector. For $2 \leq i \leq L-1$, each $A^{[i]\,j_i}$ is a $D_{i-1} \times D_i$ matrix. The maximum bond dimension $D = \max_i D_i$ sets how much entanglement the state can hold. It is the main variational parameter of DMRG.

To evaluate expectation values efficiently, we bring the MPS into a mixed canonical form. The purpose of this form is simple. It makes the left and right block bases orthonormal, which turns the local energy minimization into a small standard eigenvalue problem. We reach it by performing successive singular value decompositions along the chain, so that the tensors obey orthonormality conditions on their bond indices [150–152].

A tensor $A^{[k]j_k}$ is left-orthonormal if it satisfies

$$\sum_{j_k,\alpha_{k-1}} A^{[k]j_k}_{\alpha_{k-1}\alpha_k} \left(A^{[k]j_k}_{\alpha_{k-1}\alpha'_k}\right)^* = \delta_{\alpha_k\alpha'_k}. \tag{3.188}$$

View this tensor as a matrix with row index (α_{k-1}, j_k) and column index α_k. The condition says that its columns are orthonormal. Equivalently, contracting the tensor with its conjugate over the physical index j_k and the left bond index α_{k-1} gives the identity on the right bond space.

Similarly, a tensor is right-orthonormal if

$$\sum_{j_k,\alpha_k} \left(A^{[k]j_k}_{\alpha_{k-1}\alpha_k}\right)^* A^{[k]j_k}_{\alpha'_{k-1}\alpha_k} = \delta_{\alpha_{k-1}\alpha'_{k-1}}. \tag{3.189}$$

Now view it as a matrix with row index α_{k-1} and column index (j_k, α_k). The condition says that its rows are orthonormal.

These conditions have a simple meaning. They make the block states built from the tensors orthonormal. If all tensors to the left of bond $(\ell, \ell+1)$ are left-orthonormal, then the left block states form an orthonormal basis,

$$\langle \Phi^{[\mathcal{L}]}_\alpha | \Phi^{[\mathcal{L}]}_\beta \rangle = \delta_{\alpha\beta}. \tag{3.190}$$

If all tensors to the right are right-orthonormal, the right block states do as well,

$$\langle \Phi_{\alpha}^{[\mathcal{R}]} | \Phi_{\beta}^{[\mathcal{R}]} \rangle = \delta_{\alpha\beta}. \tag{3.191}$$

In this mixed canonical form, the full state reads

$$|\Psi\rangle = \sum_{\alpha_{\ell-1}, j_\ell, j_{\ell+1}, \alpha_{\ell+1}} \Theta_{\alpha_{\ell-1} j_\ell j_{\ell+1} \alpha_{\ell+1}} \, |\Phi_{\alpha_{\ell-1}}^{[\mathcal{L}]}\rangle \otimes |j_\ell\rangle \otimes |j_{\ell+1}\rangle \otimes |\Phi_{\alpha_{\ell+1}}^{[\mathcal{R}]}\rangle \,, \tag{3.192}$$

where the left and right block bases are orthonormal, as above. The central tensor

$$\Theta_{\alpha_{\ell-1} j_\ell j_{\ell+1} \alpha_{\ell+1}} = \sum_{\alpha_\ell} \Lambda_{\alpha_{\ell-1}}^{[\ell-1]} \Gamma_{\alpha_{\ell-1}\alpha_\ell}^{[\ell]\, j_\ell} \Gamma_{\alpha_\ell \alpha_{\ell+1}}^{[\ell+1]\, j_{\ell+1}} \Lambda_{\alpha_{\ell+1}}^{[\ell+1]} \tag{3.193}$$

collects the two active site tensors and the neighbouring Schmidt coefficients $\Lambda^{[\ell-1]}$ and $\Lambda^{[\ell+1]}$. The objects $\Gamma_{\alpha_{\ell-1}\alpha_\ell}^{[\ell]\, j_\ell}$ are the site tensors of the canonical MPS. Each $\Gamma^{[\ell]}$ is a rank-three tensor with three indices.

- one physical index $j_\ell = 0, \ldots, d-1$,
- one left bond index $\alpha_{\ell-1} = 1, \ldots, D_{\ell-1}$,
- one right bond index $\alpha_\ell = 1, \ldots, D_\ell$.

For each fixed physical index j_ℓ, the object $\Gamma^{[\ell]\, j_\ell}$ is a $D_{\ell-1} \times D_\ell$ matrix. The bond indices $\alpha_{\ell-1}$ and α_ℓ connect neighbouring sites and carry the entanglement. The physical index j_ℓ selects the local state $|j_\ell\rangle$ at site ℓ [150–152].

In canonical form, the Γ tensors are separated from the Schmidt coefficients Λ. The MPS then takes the structured form

$$A^{[\ell]\, j_\ell} = \Lambda^{[\ell-1]} \Gamma^{[\ell]\, j_\ell} \Lambda^{[\ell]}. \tag{3.194}$$

The diagonal matrices $\Lambda^{[\ell]}$ hold the Schmidt values for the bipartition at bond ℓ. The Γ tensors give the change of basis between neighbouring Schmidt spaces.

In the product

$$\Gamma_{\alpha_{\ell-1}\alpha_\ell}^{[\ell]\, j_\ell} \Gamma_{\alpha_\ell \alpha_{\ell+1}}^{[\ell+1]\, j_{\ell+1}}, \tag{3.195}$$

the shared bond index α_ℓ is summed over. This is the contraction between adjacent sites. It propagates entanglement along the chain. The Λ tensors control the magnitude of that entanglement through the Schmidt spectrum.

The Hamiltonian in Eq. (3.183) is a sum of on-site and nearest-neighbour terms,

$$\hat{H} = \sum_{i=1}^{L} \hat{h}_i + \sum_{i=1}^{L-1} \hat{h}_{i,i+1}, \tag{3.196}$$

with

$$\hat{h}_i = \epsilon_i \hat{n}_i, \qquad \hat{h}_{i,i+1} = -t\Big(\hat{c}_i^\dagger \hat{c}_{i+1} + \hat{c}_{i+1}^\dagger \hat{c}_i\Big). \tag{3.197}$$

On two neighbouring sites $(\ell, \ell+1)$, the Hamiltonian restricted to those sites is

$$\hat{H}_{\mathrm{loc}}^{[\ell,\ell+1]} = \hat{h}_\ell + \hat{h}_{\ell+1} + \hat{h}_{\ell,\ell+1}. \tag{3.198}$$

We build its matrix in the local basis $\{|00\rangle, |01\rangle, |10\rangle, |11\rangle\} = \{|0_\ell 0_{\ell+1}\rangle, \dots\}$ from tensor products of the local operators,

$$\hat{h}_\ell = \epsilon_\ell \, \hat{n} \otimes I, \tag{3.199}$$

$$\hat{h}_{\ell+1} = \epsilon_{\ell+1} \, I \otimes \hat{n}, \tag{3.200}$$

$$\hat{h}_{\ell,\ell+1} = -t\Big(\hat{c}^\dagger \otimes \hat{c} + \hat{c} \otimes \hat{c}^\dagger\Big). \tag{3.201}$$

Using the explicit matrices for $\hat{c}$, $\hat{c}^\dagger$, and $\hat{n}$, we find

$$\hat{H}_{\mathrm{loc}}^{[\ell,\ell+1]} = \begin{pmatrix} 0 & 0 & 0 & 0 \\ 0 & \epsilon_{\ell+1} & -t & 0 \\ 0 & -t & \epsilon_\ell & 0 \\ 0 & 0 & 0 & \epsilon_\ell + \epsilon_{\ell+1} \end{pmatrix}. \tag{3.202}$$

This 4×4 matrix enters the effective Hamiltonian used in the DMRG update.

DMRG minimizes the energy over the MPS manifold of fixed bond dimension D,

$$E[\Psi] = \frac{\langle \Psi | \, \hat{H} \, | \Psi \rangle}{\langle \Psi | \Psi \rangle}. \tag{3.203}$$

It does so by optimizing two neighbouring tensors at a time. We take the two central tensors, collected in Θ of Eq. (3.192), as the variational object. The left and right block states are held fixed. These block states are orthonormal, so the norm of the state reduces to the norm of Θ alone,

$$\langle \Psi | \Psi \rangle = \sum_{\alpha_{\ell-1}, j_\ell, j_{\ell+1}, \alpha_{\ell+1}} \Big| \Theta_{\alpha_{\ell-1} j_\ell j_{\ell+1} \alpha_{\ell+1}} \Big|^2. \tag{3.204}$$

Thus Θ is a normalized vector in a small effective space. Its dimension is $D_{\ell-1} \times d^2 \times D_{\ell+1}$, which is far smaller than the full Hilbert space.

The energy of the full state can then be written as an expectation value of Θ alone,

$$\langle \Psi | \, \hat{H} \, | \Psi \rangle = \langle \Theta | \, \hat{H}_{\text{eff}}^{[\ell,\ell+1]} \, | \Theta \rangle \, . \tag{3.205}$$

Here $\hat{H}_{\text{eff}}^{[\ell,\ell+1]}$ is an effective Hamiltonian that acts only on Θ. It collects the following pieces.

- the local Hamiltonian terms acting on the active bond $(\ell, \ell+1)$, denoted $\hat{H}_{\text{loc}}^{[\ell,\ell+1]}$ in Eq. (3.202),
- all contributions that lie entirely within the left block, summarized by a left environment tensor $L^{[\ell-1]}$,
- all contributions that lie entirely within the right block, summarized by a right environment tensor $R^{[\ell+1]}$,
- the remaining terms that couple the active bond to its neighbouring blocks.

In the tensor-network language, we obtain $\hat{H}_{\text{eff}}^{[\ell,\ell+1]}$ by contracting all tensors of the MPS and of the (matrix-product) Hamiltonian except those at sites ℓ and $\ell+1$. We then solve the eigenvalue problem

$$\hat{H}_{\text{eff}}^{[\ell,\ell+1]} \, | \Theta \rangle = E \, | \Theta \rangle \tag{3.206}$$

for its lowest eigenvector, using an iterative sparse-matrix method such as Lanczos or Davidson. The resulting eigenvector Θ_{GS} minimizes the energy while the rest of the MPS is held fixed.

Once we have the optimal two-site tensor Θ_{GS}, we reshape it into a matrix by grouping indices,

$$\Theta_{\alpha_{\ell-1} j_\ell j_{\ell+1} \alpha_{\ell+1}} \;\longrightarrow\; \Theta_{(\alpha_{\ell-1} j_\ell),(j_{\ell+1} \alpha_{\ell+1})}, \tag{3.207}$$

and perform a singular value decomposition,

$$\Theta_{(\alpha_{\ell-1} j_\ell),(j_{\ell+1} \alpha_{\ell+1})} = \sum_{\tilde{\alpha}_\ell} U_{(\alpha_{\ell-1} j_\ell),\tilde{\alpha}_\ell} S_{\tilde{\alpha}_\ell} V^\dagger_{\tilde{\alpha}_\ell,(j_{\ell+1} \alpha_{\ell+1})}. \tag{3.208}$$

Here S is diagonal, with the singular values in non-increasing order. DMRG truncates the bond by keeping only the largest D singular values, that is $\tilde{\alpha}_\ell = 1, \ldots, D$. The

discarded weight

$$\epsilon_{\text{disc}} = \sum_{\tilde{\alpha}_\ell > D} S^2_{\tilde{\alpha}_\ell} \tag{3.209}$$

measures the truncation error at this bond.

We then define the new MPS tensors as

$$\Gamma^{[\ell]\, j_\ell}_{\alpha_{\ell-1}\tilde{\alpha}_\ell} = U_{(\alpha_{\ell-1} j_\ell),\tilde{\alpha}_\ell}, \tag{3.210}$$

$$\Lambda^{[\ell]}_{\tilde{\alpha}_\ell} = S_{\tilde{\alpha}_\ell}, \tag{3.211}$$

$$\Gamma^{[\ell+1]\, j_{\ell+1}}_{\tilde{\alpha}_\ell \alpha_{\ell+1}} = \left(S^{-1} V^\dagger\right)_{\tilde{\alpha}_\ell,(j_{\ell+1}\alpha_{\ell+1})}. \tag{3.212}$$

This restores the canonical form, with the orthonormality conditions now imposed on the updated tensors. Finally we update the environments $L^{[\ell]}$ and $R^{[\ell]}$ by contracting the new tensors with the local Hamiltonian terms.

The full DMRG algorithm is a sequence of sweeps through the chain.

1. **Initialization.** Start from an initial MPS, for example a product state such as all sites empty or a half-filled configuration, with bond dimension D. Build the initial left and right environments for Eq. (3.183).

2. **Left-to-right sweep.** For $\ell = 1, 2, \ldots, L-1$, carry out the following steps.

   (a) Bring the MPS into mixed canonical form around bond $(\ell, \ell+1)$.

   (b) Construct the effective Hamiltonian $\hat{H}^{[\ell,\ell+1]}_{\text{eff}}$ by contracting all tensors except those on sites ℓ and $\ell+1$.

   (c) Solve the eigenproblem in Eq. (3.206) for its lowest eigenvector Θ_{GS}.

   (d) Perform the SVD, truncate to bond dimension D, and update the tensors $A^{[\ell]}$ and $A^{[\ell+1]}$.

   (e) Update the left environment $L^{[\ell]}$.

3. **Right-to-left sweep.** Repeat the same steps for $\ell = L-1, L-2, \ldots, 1$, now updating the right environments $R^{[\ell]}$.

4. **Convergence check.** After each full sweep, compute the ground-state energy E_{GS} and the discarded weight. Repeat the sweeps until the change in energy and the discarded weight fall below set thresholds.

In the non-interacting case treated here, the exact ground state can also be found by diagonalizing the single-particle hopping matrix and filling the lowest orbitals. The

value of the DMRG formulation is that it carries over directly to interacting versions of Eq. (3.183), where no simple single-particle picture exists. The spinless tight-binding chain therefore serves as a convenient benchmark for the MPS and DMRG machinery used later in this thesis for more complex many-body Hamiltonians.

Chapter 4

Majorana Zero Modes in the Kitaev Model

Parts of this chapter including the numerical diagonalization of the Hamiltonian are based on Ref. [75], with more derivations and detail shown. I have done all calculations in this paper.

In this chapter we introduce the Kitaev model and how it describes a system with topological degrees of freedom, making it a candidate for topological quantum computing. We show the existence of MZMs through Majorana and bond mathematical transformations of the Hamiltonian. Finally we discuss why this model is not suitable for experimental purposes due to the nature of the superconductivity.

4.1 Topological Superconductors

A superconductor is a phase of matter that, below a critical temperature T_c, shows two hallmark properties [154, 155]. The first is zero electrical resistance, meaning that an electric current can flow indefinitely without energy dissipation. The second is the Meissner effect, the expulsion of magnetic flux from the bulk of the material. These properties arise from the formation of Cooper pairs, which are bound states of two electrons with opposite momenta and spins. The Cooper pairs condense into a macroscopic quantum state described by a complex order parameter

$$\Delta(\mathbf{r}) = |\Delta(\mathbf{r})|e^{i\phi(\mathbf{r})}. \tag{4.1}$$

where $|\Delta|$ is the magnitude of the so-called superconducting gap and ϕ is the macroscopic phase and $\mathbf{r}$ denotes the position in real space, i.e., the spatial coordinate where the superconducting order parameter (or pair potential) is defined. It represents the energy required to break a Cooper pair and create two quasiparticle excitations. In the normal metallic state, electronic excitations can occur with arbitrarily small

energy near the Fermi surface. In contrast, in the superconducting phase there exists an energy window of width $2|\Delta|$ around the Fermi level in which no single-particle states are available. This energy gap is a direct consequence of Cooper pairing and is responsible for the stability of the superconducting state. The order parameter $\Delta(\mathbf{r})$ is defined at each point in real space. It describes the local strength and phase of the Cooper pair condensate. Here $\mathbf{r}$ is the position of the pair in the material, which we take to be the center of mass of its two electrons. The dependence of Δ on $\mathbf{r}$ therefore tells us how the condensate varies from place to place, for example near a vortex or close to a sample boundary.

The pairing symmetry is set by a separate coordinate. The two electrons of a pair sit at positions $\mathbf{r}_1$ and $\mathbf{r}_2$, and their relative separation is

$$\mathbf{r}_{12} = \mathbf{r}_1 - \mathbf{r}_2. \tag{4.2}$$

This separation is the distance of one electron from the other. It is not a position in the material. The way the pair amplitude depends on $\mathbf{r}_{12}$, or equivalently on the relative momentum after a Fourier transform, fixes the type of superconductivity. This dependence is what distinguishes s-wave, p-wave, and d-wave pairing [156]).

A topological superconductor (TSC) is a superconducting phase that is distinguished not only by the presence of a finite pairing gap in the bulk, but also by a nontrivial topological invariant defined for its quasiparticle band structure [55, 157]. Unlike a conventional superconductor, whose properties are fully described by spontaneous symmetry breaking and the magnitude of the order parameter, a TSC possesses a global topological property that cannot change unless the bulk energy gap closes [36, 158].

In the Bogoliubov–de Gennes (BdG) description, the superconducting state is described in terms of quasiparticle excitations, which are coherent superpositions of electrons and holes [159–161]. The corresponding quasiparticle spectrum forms energy bands in momentum space. If these bands are separated by a finite bulk gap, one can define a topological invariant from the structure of the occupied BdG bands [36, 158]. For a one-dimensional superconductor with particle-hole symmetry, this invariant is a $\mathbb{Z}_2$ number. It takes only two values, which label the trivial phase and the topological phase. This invariant is the Majorana number [50].

We start with a simple metal with spin degeneracy given by the single-particle Hamiltonian

$$H = \left(\frac{p^2}{2m} - \mu\right) I_{2\times 2}, \tag{4.3}$$

where μ is the chemical potential that defines the Fermi surface, m is the electron mass, and $I_{2\times 2}$ is the identity matrix in the spin variables. The total momentum is the vector $\mathbf{p} = (p_1, \ldots, p_d)$ in d spatial dimensions, and $p = |\mathbf{p}|$ is its magnitude. Assuming isotropy, the Hamiltonian depends on the momentum only through $p^2 = \sum_{i=1}^{d} p_i^2$, which is the square of this magnitude. If we include many electrons, the system must be described by a many-body Hamiltonian written in second quantization. It takes the form

$$H = \sum_{\mathbf{p},\sigma} c_{\mathbf{p}\sigma}^\dagger \left(\frac{\mathbf{p}^2}{2m} - \mu \right) c_{\mathbf{p}\sigma} = \sum_{\mathbf{p},\sigma} \epsilon(\mathbf{p})\, c_{\mathbf{p}\sigma}^\dagger c_{\mathbf{p}\sigma}, \tag{4.4}$$

where $c_{\mathbf{p}\sigma}^\dagger$ creates a fermion with momentum $\mathbf{p}$ and spin σ, and

$$\epsilon(\mathbf{p}) = \frac{\mathbf{p}^2}{2m} - \mu. \tag{4.5}$$

Here μ is the chemical potential. At zero temperature, the chemical potential coincides with the Fermi energy E_F, which is defined as the energy of the highest occupied single-particle state in the ground state. The set of momenta satisfying $\epsilon(\mathbf{p}) = 0$ defines the Fermi surface. States with $\epsilon(\mathbf{p}) < 0$ lie below the Fermi level and are occupied in the ground state, while states with $\epsilon(\mathbf{p}) > 0$ are empty.

The many-body ground state is therefore obtained by filling all single-particle states with energies below the Fermi level. It can be written as

$$|\mathrm{FS}\rangle = \prod_{\mathbf{p},\sigma}^{\epsilon(\mathbf{p})<0} c_{\mathbf{p}\sigma}^\dagger \, |0\rangle, \tag{4.6}$$

where $|0\rangle$ is the vacuum state defined by $c_{\mathbf{p}\sigma}|0\rangle = 0$ for all $\mathbf{p}, \sigma$.

The notation $|\mathrm{FS}\rangle$ emphasizes that this state is the Fermi sea: all momentum states inside the Fermi surface are filled, and all states outside are empty. This state minimizes the total energy of the Hamiltonian in Eq. (4.4).

The operators $c_{\mathbf{p}\sigma}^\dagger, c_{\mathbf{p}'\sigma'}$ obey the anti-commutation relation

$$\{c_{\mathbf{p}\sigma}^\dagger, c_{\mathbf{p}'\sigma'}\} = \delta_{\sigma\sigma'}\delta_{\mathbf{p}\mathbf{p}'}, \tag{4.7}$$

which implies

$$c_{\mathbf{p}\sigma} c_{\mathbf{p}\sigma}^\dagger = 1 - c_{\mathbf{p}\sigma}^\dagger c_{\mathbf{p}\sigma}. \tag{4.8}$$

Using Eq. (4.8), we can rewrite the number operator as

$$c_{\mathbf{p}\sigma}^\dagger c_{\mathbf{p}\sigma} = \frac{1}{2}\left(c_{\mathbf{p}\sigma}^\dagger c_{\mathbf{p}\sigma} - c_{\mathbf{p}\sigma} c_{\mathbf{p}\sigma}^\dagger \right) + \frac{1}{2}. \tag{4.9}$$

Substituting this into the Hamiltonian gives

$$\begin{aligned} H &= \sum_{\mathbf{p},\sigma} \epsilon(\mathbf{p}) \left[\frac{1}{2} \left(c^\dagger_{\mathbf{p}\sigma} c_{\mathbf{p}\sigma} - c_{\mathbf{p}\sigma} c^\dagger_{\mathbf{p}\sigma} \right) + \frac{1}{2} \right] \\ &= \frac{1}{2} \sum_{\mathbf{p},\sigma} \epsilon(\mathbf{p}) \left(c^\dagger_{\mathbf{p}\sigma} c_{\mathbf{p}\sigma} - c_{\mathbf{p}\sigma} c^\dagger_{\mathbf{p}\sigma} \right) + \frac{1}{2} \sum_{\mathbf{p},\sigma} \epsilon(\mathbf{p}). \end{aligned} \tag{4.10}$$

The last term is a constant energy shift. The summand $\epsilon(\mathbf{p})$ does not depend on σ. The sum over the two spin values $\sigma = \uparrow, \downarrow$ therefore gives a factor of 2. This factor cancels the prefactor $\frac{1}{2}$, so the constant becomes

$$\frac{1}{2} \sum_{\mathbf{p},\sigma} \epsilon(\mathbf{p}) = \frac{1}{2} \sum_{\mathbf{p}} 2\, \epsilon(\mathbf{p}) = \sum_{\mathbf{p}} \epsilon(\mathbf{p}). \tag{4.11}$$

Therefore, we can rewrite the Hamiltonian as

$$\begin{aligned} H &= \frac{1}{2} \sum_{\mathbf{p},\sigma} \left[c^\dagger_{\mathbf{p}\sigma}\, \epsilon(\mathbf{p})\, c_{\mathbf{p}\sigma} - c_{\mathbf{p}\sigma}\, \epsilon(\mathbf{p})\, c^\dagger_{\mathbf{p}\sigma} \right] + \sum_{\mathbf{p}} \epsilon(\mathbf{p}) \\ &= \frac{1}{2} \sum_{\mathbf{p},\sigma} \left[c^\dagger_{\mathbf{p}\sigma}\, \epsilon(\mathbf{p})\, c_{\mathbf{p}\sigma} - c_{-\mathbf{p}\sigma}\, \epsilon(-\mathbf{p})\, c^\dagger_{-\mathbf{p}\sigma} \right] + \sum_{\mathbf{p}} \epsilon(\mathbf{p}), \end{aligned} \tag{4.12}$$

where we also relabeled the sum index $\mathbf{p}$ in the second term to $-\mathbf{p}$. Because the sum runs over the full momentum space, this relabeling does not change the value of the sum. For a free particle dispersion $\epsilon(\mathbf{p}) = \epsilon(-\mathbf{p})$, the spectrum is even in momentum, which makes the expression explicitly symmetric between $\mathbf{p}$ and $-\mathbf{p}$.

In order to write the Hamiltonian in a more compact form, we introduce the Nambu spinor

$$\Psi_{\mathbf{p}} = \begin{pmatrix} c_{\mathbf{p}\uparrow} \\ c_{\mathbf{p}\downarrow} \\ c^\dagger_{-\mathbf{p}\uparrow} \\ c^\dagger_{-\mathbf{p}\downarrow} \end{pmatrix}, \tag{4.13}$$

The reason for introducing the Nambu spinor is that superconductivity mixes particle and hole degrees of freedom. In a superconducting state, the pairing term creates or annihilates pairs of electrons with opposite momenta and spins. As a result, the Hamiltonian no longer conserves the particle number. Writing them together in the Nambu spinor allows us to treat particle and hole operators on equal footing. The Hamiltonian then becomes

$$H = \sum_{\mathbf{p}} \Psi^\dagger_{\mathbf{p}} H_{\mathrm{BdG}}(\mathbf{p}) \Psi_{\mathbf{p}} + \text{constant}, \tag{4.14}$$

with

$$H_{\mathrm{BdG}}(\mathbf{p}) = \frac{1}{2}\begin{pmatrix} \epsilon(p) & 0 & 0 & 0 \\ 0 & \epsilon(p) & 0 & 0 \\ 0 & 0 & -\epsilon(-p) & 0 \\ 0 & 0 & 0 & -\epsilon(-p) \end{pmatrix}. \tag{4.15}$$

The matrix $H_{\mathrm{BdG}}(\mathbf{p})$ is called the Bogoliubov–de Gennes (BdG) Hamiltonian. It describes the dynamics of Bogoliubov quasiparticles, which are coherent superpositions of electrons and holes. The eigenvalues of this matrix give the quasiparticle excitation spectrum of the superconductor. In this way, the many-body problem is reduced to considering an effective single-particle matrix in the enlarged Nambu space. The additional constant term originates from rewriting the Hamiltonian in symmetric form using fermionic anticommutation relations. This term is proportional to $\sum_{\mathbf{p}} \epsilon(\mathbf{p})$ and represents a uniform shift of the total energy. Since physical observables such as excitation energies depend only on energy differences, adding a constant does not modify the spectrum of excitations or the eigenstates of the system. Therefore, dropping this constant does not change the physical properties of the model.

It can be seen that the block Hamiltonian $H_{\mathrm{BdG}}(\mathbf{p})$ is invariant under

$$H_{\mathrm{BdG}}(\mathbf{p}) = -CH^*_{\mathrm{BdG}}(-\mathbf{p})C^{-1}, \tag{4.16}$$

where $C = \tau^x \otimes I_{2\times 2}$ and

$$\tau^x = \begin{pmatrix} 0 & 1 \\ 1 & 0 \end{pmatrix}. \tag{4.17}$$

This represents the particle–hole (or charge-conjugation) symmetry of the BdG Hamiltonian. It becomes more important when we consider superconducting pairing. Note that instead of having two degrees of freedom (one band and two spins), the BdG Hamiltonian has four. These four energy eigenvalues of H_{BdG} are two copies of $\epsilon(p)$ and two copies of $-\epsilon(-p)$. The point of this formalism becomes clear once we introduce superconducting pairing.

4.2 p-Wave Superconductors in One Dimension

One of the topological superconductor models is mean-field BdG Hamiltonian of spinless fermions in one and two dimensions [50, 162]. Spinless fermions can be viewed as fermions that are fully spin-polarized due to a source of time-reversal (TR) breaking such as a magnetic field [44, 55]. We consider a one-dimensional wire with

p-wave superconductivity as an illustration for the topological superconductor model. This was first introduced by Kitaev [50]. We begin with a non-superconducting one-dimensional metal of spinless (or spin-polarized) fermions:

$$H = \sum_p c_p^\dagger \left(\frac{p^2}{2m} - \mu \right) c_p, \tag{4.18}$$

where μ is the chemical potential and m is the fermion mass, and the operator $c_p^\dagger$ (c_p) creates (annihilates) a fermion with momentum p. We will use a momentum-dependent p-wave potential:

$$H_\Delta = \frac{1}{2} \sum_p \left(\Delta\, p\, c_p^\dagger c_{-p}^\dagger + \Delta^*\, p\, c_{-p} c_p \right). \tag{4.19}$$

The p-wave potential pairs the electrons with the same spin but opposite momenta with strength Δ, and as it can be seen from its form, it does not conserve the number of fermions. The name p-wave refers to the momentum dependence of the pairing. The gap function is $\Delta(p) = \Delta\, p$, which is odd under $p \to -p$. This odd form is required by the Pauli principle. The two paired fermions carry the same spin, so the orbital part of the pair must be antisymmetric. In the classification of Cooper pairs by their orbital angular momentum ℓ, the channels $\ell = 0, 1, 2$ are named s-wave, p-wave, and d-wave, after the atomic orbitals. An even gap belongs to the $\ell = 0$ channel. A gap that is odd and linear in momentum belongs to the $\ell = 1$ channel. The form $\Delta(p) \propto p$ is therefore a p-wave gap.

It is useful to compare this with conventional Bardeen-Cooper-Schrieffer (BCS) superconductivity [154]. The BCS pairing term is

$$H_\Delta^{\mathrm{BCS}} = \sum_p \left(\Delta\, c_{p\uparrow}^\dagger c_{-p\downarrow}^\dagger + \Delta^*\, c_{-p\downarrow} c_{p\uparrow} \right), \tag{4.20}$$

where the gap Δ is constant in momentum. It pairs electrons of opposite spin at opposite momenta, forming a spin singlet. The singlet is antisymmetric in spin, so the orbital part is allowed to be symmetric, which is why a constant gap is permitted. The p-wave case is the mirror of this. The spins are aligned, so the orbital part must be antisymmetric, and the gap must be odd in momentum. One consequence is a difference in the gap structure. The BCS gap is finite everywhere on the Fermi surface, while the p-wave gap $\Delta(p) \propto p$ vanishes at $p = 0$. Throughout this work, we only take discrete lattices, but for the sake of generality the continuous version of the above

Hamiltonian is [44]

$$H = \int dx \left[\Psi^\dagger(x) \left(\frac{p_x^2}{2m} - \mu \right) \Psi(x) + \Psi(x) |\Delta| e^{i\phi} p_x \Psi(x) + \text{h.c.} \right], \tag{4.21}$$

where $\Psi^\dagger(x)$ ($\Psi(x)$) is the real-space creation (annihilation) operator, m is the effective electron mass, and $p_x = -i\hbar\,\partial_x$ is the momentum operator along the wire. In contrast to the momentum-space form in Eq. (4.63), where p is a momentum eigenvalue, here p_x is a differential operator that acts on $\Psi(x)$.

We now combine the normal-state Hamiltonian in Eq. (4.18) with the pairing term in Eq. (4.63). The total Hamiltonian becomes

$$H = \sum_p \epsilon(p)\, c_p^\dagger c_p + \frac{1}{2} \sum_p \left(\Delta\, p\, c_p^\dagger c_{-p}^\dagger + \Delta^*\, p\, c_{-p} c_p \right), \tag{4.22}$$

where

$$\epsilon(p) = \frac{p^2}{2m} - \mu. \tag{4.23}$$

Because of the pairing terms, the Hamiltonian no longer conserves particle number. Instead, it mixes states with different fermion numbers. To diagonalize the Hamiltonian, we group the operators c_p and $c_{-p}^\dagger$ into a Nambu spinor,

$$\Psi_p = \begin{pmatrix} c_p \\ c_{-p}^\dagger \end{pmatrix}. \tag{4.24}$$

In this basis, the Hamiltonian can be written in matrix form as

$$H = \sum_p \frac{1}{2} \Psi_p^\dagger \begin{pmatrix} \epsilon(p) & \Delta p \\ \Delta^* p & -\epsilon(p) \end{pmatrix} \Psi_p + \text{constant}. \tag{4.25}$$

The off-diagonal entries Δp and $\Delta^* p$ are linear in the momentum p. A momentum that enters linearly is the hallmark of a Dirac Hamiltonian. The 2×2 matrix appearing above is the BdG Hamiltonian for a one-dimensional p-wave superconductor. The negative sign in the lower diagonal element reflects the particle–hole structure.

The quasiparticle energy bands are obtained by diagonalizing this matrix. They are given by the eigenvalues of

$$H_{\text{BdG}}(p) = \begin{pmatrix} \epsilon(p) & \Delta p \\ \Delta^* p & -\epsilon(p) \end{pmatrix}. \tag{4.26}$$

Solving the characteristic equation

$$\det(H_{\mathrm{BdG}}(p) - E\mathbb{I}) = 0 \tag{4.27}$$

gives

$$E_{\pm}(p) = \pm\sqrt{\epsilon(p)^2 + |\Delta|^2 p^2}. \tag{4.28}$$

The spectrum consists of two symmetric bands, $E_+(p)$ and $E_-(p)$, which reflect the particle–hole symmetry of the BdG Hamiltonian. It is shown in Fig. 4.1. The system remains gapped for all $\mu \neq 0$, while the gap closes at the critical point $\mu = 0$.

This critical point separates two distinct physical regimes: the weak-pairing phase ($\mu > 0$) and the strong-pairing phase ($\mu < 0$).

To understand the difference between these two phases, it is useful to first consider the system in the absence of pairing, i.e., when $\Delta = 0$. In that case, the dispersion reduces to the following spectrum

$$\epsilon(p) = \frac{p^2}{2m} - \mu. \tag{4.29}$$

For $\mu > 0$, the system has a Fermi surface defined by $\epsilon(p) = 0$. Low-energy fermionic states exist near the Fermi momentum $\pm p_F$. When a small pairing term Δ is introduced, it couples states close to the Fermi surface and opens a gap there. This is the usual BCS mechanism: pairing occurs between fermions near the Fermi level, and the superconducting state can be viewed as a weak instability of a metal. In this regime, the system is called the weak-pairing phase. Although the pairing is p-wave and momentum-dependent, the basic picture remains similar to conventional BCS theory.

In contrast, for $\mu < 0$, the normal-state dispersion has no Fermi surface. All single-particle states lie above zero energy, meaning the system is already gapped even before pairing is introduced. Adding the pairing term does not open a gap at a Fermi surface, since no such surface exists. Instead, the system forms tightly bound pairs, and the resulting superconducting state does not arise from a weak instability of a metal. For this reason, this regime is called the strong-pairing phase.

Although both phases are superconducting and gapped, they are topologically distinct. The gap closing at $\mu = 0$ marks a topological phase transition between them.

To decide which phase is topological, it is useful to rewrite the BdG Hamiltonian in a form where its direction in Pauli-matrix space is explicit. The phase transition occurs when the bulk gap closes. In this model the gap closes at $p = 0$ when $\mu = 0$.

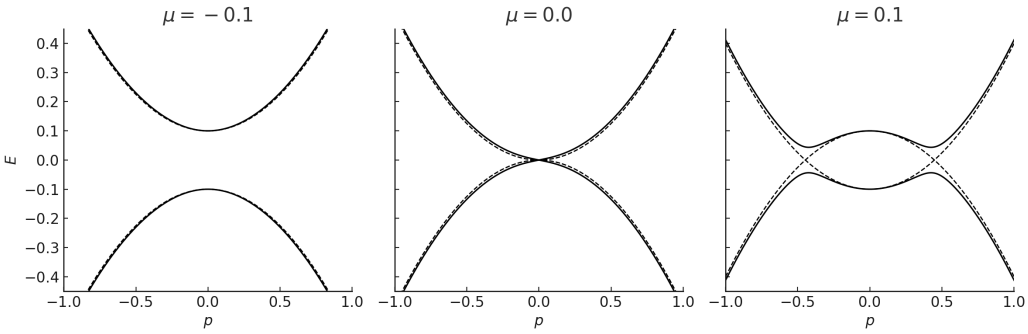

Figure 4.1: Plot of the dispersion relation for a 1D p-wave superconductor. The solid lines correspond to $E_{\pm}(p) = \pm\sqrt{\epsilon(p)^2 + |\Delta|^2 p^2}$ with $m = 1.0$, $\mu = \pm 0.1$, $|\Delta| = 0.1$. The dashed line shows the normal metal case $\Delta = 0$. The left figure shows the "strong-pairing phase" where $\mu < 0$. The middle figure is the critical $\mu = 0$ case, and the right figure is the "weak-pairing" phase.

Therefore, to study the structure near the transition, we expand around small p and keep the leading terms. Since $\epsilon(p) = p^2/2m - \mu$, for sufficiently small $|p|$ we may approximate

$$\epsilon(p) \approx -\mu, \tag{4.30}$$

so that

$$H_{\mathrm{BdG}}(p) \approx \begin{pmatrix} -\mu & \Delta\, p \\ \Delta^*\, p & \mu \end{pmatrix}. \tag{4.31}$$

Any 2×2 Hermitian matrix can be expanded as

$$H = d_0\, \mathbb{I} + d_x \sigma^x + d_y \sigma^y + d_z \sigma^z, \tag{4.32}$$

with the Pauli matrices

$$\sigma^x = \begin{pmatrix} 0 & 1 \\ 1 & 0 \end{pmatrix}, \quad \sigma^y = \begin{pmatrix} 0 & -i \\ i & 0 \end{pmatrix}, \quad \sigma^z = \begin{pmatrix} 1 & 0 \\ 0 & -1 \end{pmatrix}, \tag{4.33}$$

and d_is being coefficients. Now write the pairing amplitude as $\Delta = \Delta_R + i\Delta_I$, where $\Delta_R = \mathrm{Re}\,\Delta$ and $\Delta_I = \mathrm{Im}\,\Delta$. Then the off-diagonal term becomes

$$\Delta\, p = (\Delta_R + i\Delta_I)p. \tag{4.34}$$

Using Eq. (4.31), we can separate the real and imaginary parts in the off-diagonal

entries:

$$\begin{pmatrix} -\mu & (\Delta_R + i\Delta_I)p \\ (\Delta_R - i\Delta_I)p & \mu \end{pmatrix} = -\mu \begin{pmatrix} 1 & 0 \\ 0 & -1 \end{pmatrix} + \Delta_R p \begin{pmatrix} 0 & 1 \\ 1 & 0 \end{pmatrix} - \Delta_I p \begin{pmatrix} 0 & -i \\ i & 0 \end{pmatrix}. \tag{4.35}$$

Therefore,

$$H_{\mathrm{BdG}}(p) = (\mathrm{Re}\,\Delta)\, p\, \sigma^x - (\mathrm{Im}\,\Delta)\, p\, \sigma^y - \mu\, \sigma^z. \tag{4.36}$$

For a single uniform superconductor, the overall phase of Δ is not physical, it can be removed by a global $U(1)$ redefinition of the fermion operators (the usual gauge freedom of the mean-field description) [154, 159]. If we write $\Delta = |\Delta| e^{i\phi}$, then under

$$c_p \to e^{i\phi/2} c_p, \qquad c_{-p}^\dagger \to e^{-i\phi/2} c_{-p}^\dagger, \tag{4.37}$$

the pairing term $\Delta p\, c_p^\dagger c_{-p}^\dagger + \mathrm{h.c.}$ becomes real. We may therefore take Δ to be real and positive, and Eq. (4.36) reduces to

$$H_{\mathrm{BdG}}(p) = \Delta\, p\, \sigma^x - \mu\, \sigma^z. \tag{4.38}$$

Equation (4.38) has the same structure as a one-dimensional massive Dirac Hamiltonian written in a 2×2 representation,

$$H_{\mathrm{Dirac}}(p) = v\, p\, \sigma^x + m\, \sigma^z, \tag{4.39}$$

where v plays the role of a velocity and m is the Dirac mass. Diagonalizing Eq. (4.39) gives

$$E_\pm(p) = \pm\sqrt{(vp)^2 + m^2}, \tag{4.40}$$

so the mass term opens a bulk gap of size $2|m|$ at $p = 0$.

Comparing Eq. (4.38) and Eq. (4.39), we identify

$$v = \Delta, \qquad m = -\mu. \tag{4.41}$$

This is the main reason the Dirac viewpoint is helpful. The sign of the mass is controlled by the sign of μ. In Dirac-type models, changing the sign of the mass requires the bulk gap to close, and it separates phases that cannot be smoothly connected without a gap closing. Therefore, the weak-pairing regime ($\mu > 0$) is the topological phase, while the strong-pairing regime ($\mu < 0$) is trivial [50].

In this system, MZMs appear as bound-state zero-energy modes localized at the

edges of an open wire. To make this property more clear, we move from the momentum description to a lattice (site) representation. This allows us to explicitly describe a finite chain with boundaries.

We begin by discretizing the one-dimensional wire into N sites with lattice spacing a. In the continuum model, the kinetic energy is given by $p^2/2m$. On a lattice, this term is replaced by a nearest-neighbour hopping amplitude t, which describes the tunneling of fermions between adjacent sites. In the long-wavelength limit, we have

$$t \sim \frac{1}{2ma^2}, \tag{4.42}$$

so that the lattice model reproduces the continuum dispersion at small momenta.

Restricting ourselves to nearest-neighbour hopping, the Hamiltonian of the chain becomes

$$\hat{\mathcal{H}}_{\text{chain}} = -\mu \sum_{i=1}^{N} n_i - t \sum_{i=1}^{N-1} (c_i^\dagger c_{i+1} + c_{i+1}^\dagger c_i) + \Delta \sum_{i=1}^{N-1} (c_i c_{i+1} + c_{i+1}^\dagger c_i^\dagger), \tag{4.43}$$

where $n_i = c_i^\dagger c_i$ is the number operator at site i. We have chosen the superconducting phase to be zero, so that $\Delta = |\Delta|$ is real. The pairing term now couples fermions on neighbouring sites. This reflects the p-wave nature of the superconductivity. Because the fermions are spinless, each site can be either empty or occupied by a single fermion; double occupancy is forbidden by the Pauli exclusion principle. Therefore, the pairing is between different sites, leading to the nearest-neighbour term $c_i c_{i+1}$.

Equation (4.43) is the lattice model introduced by Kitaev [50]. From now on, we refer to this system as the Kitaev chain or the Kitaev model. To obtain the dispersion relation of the Kitaev chain, we first consider the system with periodic boundary conditions. In this case, the chain forms a closed ring. As a result, the wavevector k becomes a good quantum number, and the Hamiltonian can be diagonalized in momentum space. This allows us to define the bulk energy spectrum of the system. Once the bulk properties are understood, we can return to the open chain to study edge states.

With periodic boundary conditions, the fermionic operators can be expanded in plane waves through the Fourier transformation

$$c_j = \frac{1}{\sqrt{N}} \sum_k c_k \, e^{ikj}, \qquad c_j^\dagger = \frac{1}{\sqrt{N}} \sum_k c_k^\dagger \, e^{-ikj}, \tag{4.44}$$

where N is the number of lattice sites and $k = 2\pi n/N$ with $n = 0, 1, \ldots, N-1$. The

inverse transformation is

$$c_k = \frac{1}{\sqrt{N}} \sum_j c_j \, e^{-ikj}. \tag{4.45}$$

We now explicitly substitute the Fourier transform into the real-space Kitaev Hamiltonian with periodic boundary conditions.

First consider the chemical potential term. Substituting the Fourier expressions,

$$\sum_j c_j^\dagger c_j = \frac{1}{N} \sum_j \sum_{k,q} c_k^\dagger c_q e^{-ikj} e^{iqj} \tag{4.46}$$

$$= \frac{1}{N} \sum_{k,q} c_k^\dagger c_q \sum_j e^{i(q-k)j}. \tag{4.47}$$

Using the orthogonality relation

$$\sum_j e^{i(q-k)j} = N \, \delta_{k,q}, \tag{4.48}$$

we obtain

$$\sum_j c_j^\dagger c_j = \sum_k c_k^\dagger c_k. \tag{4.49}$$

Therefore,

$$-\mu \sum_j c_j^\dagger c_j = -\mu \sum_k c_k^\dagger c_k. \tag{4.50}$$

Next consider the hopping term. Substituting,

$$\sum_j c_j^\dagger c_{j+1} = \frac{1}{N} \sum_j \sum_{k,q} c_k^\dagger c_q e^{-ikj} e^{iq(j+1)} \tag{4.51}$$

$$= \frac{1}{N} \sum_{k,q} c_k^\dagger c_q e^{iq} \sum_j e^{i(q-k)j}. \tag{4.52}$$

Again using orthogonality,

$$\sum_j c_j^\dagger c_{j+1} = \sum_k e^{ik} c_k^\dagger c_k. \tag{4.53}$$

Including the Hermitian conjugate term gives

$$-t \sum_j \left(c_j^\dagger c_{j+1} + \text{h.c.} \right) = -t \sum_k \left(e^{ik} + e^{-ik} \right) c_k^\dagger c_k = -2t \sum_k \cos k \, c_k^\dagger c_k, \tag{4.54}$$

Which is also diagonal and can be combined with the chemical potential term to obtain

$$\xi_k = -\mu - 2t \cos k. \tag{4.55}$$

Now consider the pairing term

$$\sum_j c_j c_{j+1} = \frac{1}{N} \sum_j \sum_{k,q} c_k c_q e^{ikj} e^{iq(j+1)} \tag{4.56}$$

$$= \frac{1}{N} \sum_{k,q} c_k c_q e^{iq} \sum_j e^{i(k+q)j}. \tag{4.57}$$

The orthogonality condition now gives

$$\sum_j e^{i(k+q)j} = N\, \delta_{k,-q}, \tag{4.58}$$

so

$$\sum_j c_j c_{j+1} = \sum_k e^{-ik} c_k c_{-k}. \tag{4.59}$$

The sum runs over the full Brillouin zone, so we may relabel the dummy index $k \to -k$ without changing its value,

$$\sum_k e^{-ik} c_k c_{-k} = \sum_k e^{ik} c_{-k} c_k. \tag{4.60}$$

The fermion operators anticommute, so $c_{-k}c_k = -c_k c_{-k}$. Substituting this,

$$\sum_k e^{-ik} c_k c_{-k} = -\sum_k e^{ik} c_k c_{-k}. \tag{4.61}$$

We now have the same sum written in two ways. Adding them and dividing by two gives a manifestly antisymmetric form,

$$\sum_j c_j c_{j+1} = \frac{1}{2} \sum_k \left(e^{-ik} - e^{ik} \right) c_k c_{-k} = -\,i \sum_k \sin k\, c_k c_{-k}, \tag{4.62}$$

where $e^{-ik} - e^{ik} = -2i \sin k$.

Including the amplitude Δ and the Hermitian conjugate, and using the same anticommutation to order the operators symmetrically in the Nambu indices, the pairing term becomes

$$-\sum_j \left(\Delta\, c_j c_{j+1} + \text{h.c.} \right) = \frac{1}{2} \sum_k \left(\Delta_k\, c_k^\dagger c_{-k}^\dagger + \Delta_k^*\, c_{-k} c_k \right), \tag{4.63}$$

with

$$\Delta_k = 2i\, \Delta \sin k. \tag{4.64}$$

Collecting all terms, the Hamiltonian becomes

$$\hat{H}_{\text{chain}} = \sum_k \Big[\xi_k \, c_k^\dagger c_k + \frac{1}{2} \Big(\Delta_k \, c_k^\dagger c_{-k}^\dagger + \Delta_k^* \, c_{-k} c_k \Big) \Big] . \tag{4.65}$$

Since the pairing term creates two particles of k and $-k$, the Hamiltonian does not conserve particle number. As before, we introduce the Nambu spinor

$$\Psi_k = (c_k, \, c_{-k}^\dagger)^{\mathsf{T}}, \tag{4.66}$$

which allows us to write the Hamiltonian in BdG form,

$$\hat{H}_{\text{chain}} = \frac{1}{2} \sum_k \Psi_k^\dagger H_{\text{BdG}}(k) \Psi_k + \text{const}, \tag{4.67}$$

with

$$H_{\text{BdG}}(k) = \begin{pmatrix} \xi_k & \Delta_k \\ \Delta_k^* & -\xi_k \end{pmatrix} = \xi_k \, \sigma_z + 2\Delta \sin k \, \sigma_y. \tag{4.68}$$

Here σ_i are Pauli matrices acting in particle–hole (Nambu) space.

The quasiparticle energies are obtained by diagonalizing $H_{\text{BdG}}(k)$, which gives

$$E_\pm(k) = \pm \sqrt{\xi_k^2 + 4\Delta^2 \sin^2 k} \, = \pm \sqrt{(-\mu - 2t \cos k)^2 + 4\Delta^2 \sin^2 k} \, . \tag{4.69}$$

These two symmetric bands describe the bulk quasiparticle excitation spectrum of the Kitaev chain, as shown in Fig. 4.2. Because the square root is a sum of two nonnegative terms, the bulk gap can close only if both contributions vanish at the same momentum:

$$\xi_k = 0 \qquad \text{and} \qquad \sin k = 0. \tag{4.70}$$

The condition $\sin k = 0$ holds only at

$$k = 0 \quad \text{or} \quad k = \pi. \tag{4.71}$$

Evaluating ξ_k at these momenta gives

$$\xi_0 = -\mu - 2t \cos 0 = -\mu - 2t, \qquad \xi_\pi = -\mu - 2t \cos \pi = -\mu + 2t. \tag{4.72}$$

Imposing $\xi_0 = 0$ or $\xi_\pi = 0$ yields the two gap-closing (critical) points,

$$\xi_0 = 0 \;\Rightarrow\; \mu = -2t, \qquad \xi_\pi = 0 \;\Rightarrow\; \mu = +2t. \tag{4.73}$$

To understand the topological distinction between the phases, it is helpful to look at the BdG Hamiltonian in Pauli-matrix form in Eq. (4.68). This can be viewed as a two-level system with an effective pseudospin field

$$\mathbf{d}(k) = \Big(0,\ 2\Delta \sin k,\ \xi_k\Big), \qquad H_{\mathrm{BdG}}(k) = \mathbf{d}(k) \cdot \boldsymbol{\sigma}. \tag{4.74}$$

As k varies from $-\pi$ to π, the vector $\mathbf{d}(k)$ traces a curve in the (d_y, d_z) plane. A topological phase corresponds to a curve that winds around the origin, while a trivial phase does not. The only places where the curve can switch between these two behaviours are the points where it passes through the origin, i.e., where the bulk gap closes. This is the geometric reason why the gap closings in Eq. (4.73) mark topological phase transitions.

Since $\sin k = 0$ at $k = 0, \pi$, we have

$$\mathbf{d}(0) = (0, 0, \xi_0), \qquad \mathbf{d}(\pi) = (0, 0, \xi_\pi). \tag{4.75}$$

So at $k = 0$ and $k = \pi$ the vector $\mathbf{d}(k)$ lies purely on the d_z axis, pointing either "up" or "down" depending on the sign of ξ_k. In other words, the signs

$$\mathrm{sgn}[\xi_0] = \mathrm{sgn}[-\mu - 2t], \qquad \mathrm{sgn}[\xi_\pi] = \mathrm{sgn}[-\mu + 2t] \tag{4.76}$$

tell us whether $\mathbf{d}(k)$ points to $+d_z$ or to $-d_z$. A qualitative difference occurs depending on whether $\mathbf{d}(0)$ and $\mathbf{d}(\pi)$ point in the same direction or in opposite directions: If $\mathrm{sgn}[\xi_0] = \mathrm{sgn}[\xi_\pi]$, then $\mathbf{d}(k)$ starts and ends on the same side of the d_z axis. In this case the curve traced by $\mathbf{d}(k)$ can be continuously deformed away from the origin without crossing it, and the phase is topologically trivial.

If $\mathrm{sgn}[\xi_0] \neq \mathrm{sgn}[\xi_\pi]$, then $\mathbf{d}(k)$ points in opposite directions at $k = 0$ and $k = \pi$. Since $\mathbf{d}(k)$ varies continuously with k, it must rotate from one side of the d_z axis to the other as k goes from 0 to π. When $|\Delta| \neq 0$, this rotation is provided by the $d_y(k) = 2\Delta \sin k$ component. Geometrically, this means the curve winds around the origin, which is the signature of the nontrivial topological phase.

This criterion can be written compactly using the product $\xi_0 \xi_\pi$:

$$\xi_0 \xi_\pi = (-\mu - 2t)(-\mu + 2t) = \mu^2 - 4t^2. \tag{4.77}$$

Therefore,

$$\xi_0 \xi_\pi < 0 \quad \Longleftrightarrow \quad \mu^2 < 4t^2 \quad \Longleftrightarrow \quad |\mu| < 2t. \tag{4.78}$$

So the topological phase occurs precisely when ξ_0 and ξ_π have opposite signs, i.e., when $|\mu| < 2t$. Crossing $\mu = \pm 2t$ flips the sign of either ξ_0 or ξ_π, which forces the gap to close at $k = 0$ or $k = \pi$ and produces a topological phase transition.

The phrase band inversion refers to this sign flip. At the critical points, the pairing term vanishes, so the BdG energies reduce to $\pm|\xi_k|$. When the sign of ξ_k flips at one critical point, the ordering of the positive- and negative-energy BdG levels at that momentum is exchanged relative to the other critical point. This rearrangement cannot happen without a gap closing and is another way to see that the transition is topological.

The sign criterion in Eq. (4.78) also has an interpretation in the normal state ($\Delta = 0$). Then $E(k) = \xi_k$, and the band runs between

$$\xi_{\min} = -\mu - 2t, \qquad \xi_{\max} = -\mu + 2t, \tag{4.79}$$

corresponding to $k = 0$ and $k = \pi$. If $|\mu| > 2t$, then ξ_k does not cross zero anywhere: the chemical potential lies outside the normal-state band, and there are no Fermi points. Turning on pairing does not gap out any Fermi crossings; the resulting superconductor is topologically trivial, as shown in the left panel of Fig. 4.2.

At $|\mu| = 2t$, the normal band touches zero at $k = 0$ or $k = \pi$, and the superconducting gap closes there (critical case, middle panel). Finally, when $|\mu| < 2t$, ξ_k crosses zero at two momenta $\pm k_F$, so the normal state is metallic with two Fermi points. The p-wave pairing then opens a gap around these Fermi points, producing the topological superconducting phase (right panel). In an open chain, this is the regime where Majorana zero modes appear at the ends, as we show in the next section.

4.3 Majorana and Bond Transformations

A direct way to display the existence of Majorana zero modes (MZMs) in the Kitaev chain is to rewrite the Hamiltonian in terms of Majorana operators and diagonalize it explicitly [44, 50]. This procedure makes the zero-energy edge modes transparent.

We proceed in two steps. First, we rewrite the fermionic Hamiltonian in terms of Majorana operators (Majorana transformation). Second, we apply a bond transformation that pairs Majoranas on neighbouring sites. This ultimately yields a diagonal form of the Hamiltonian where the presence of unpaired Majoranas becomes explicit.

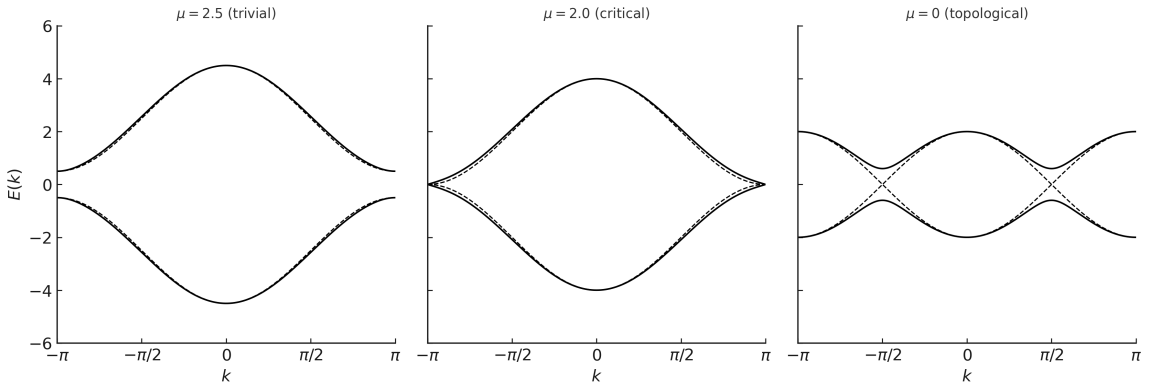

Figure 4.2: Dispersion of the Kitaev chain with $t = 1$ for (left) $\mu = 2.5$ (trivial), (middle) $\mu = 2.0$ (critical), and (right) $\mu = 0$ (topological). Solid lines show the superconducting quasiparticle bands, while dashed lines show the normal-state dispersion ($\Delta = 0$). The transition between trivial and topological phases occurs when $|\mu| = 2t$.

4.3.1 Majorana Operators

Consider a system with $2N$ spatially separated Majorana fermions (MFs), $\gamma_1, \ldots, \gamma_{2N}$. The number of Majoranas must be even, since one Majorana operator carries only half of the degrees of freedom of a fermion operator [50, 162].

A fermion operator can be decomposed into two Majorana operators as

$$c_i = \frac{1}{2}\left(\gamma_{2i-1} + i\gamma_{2i}\right). \tag{4.80}$$

The inverse relations are

$$\gamma_{2i-1} = c_i^\dagger + c_i, \tag{4.81}$$

$$\gamma_{2i} = i(c_i^\dagger - c_i). \tag{4.82}$$

The Majorana operators satisfy hermiticity

$$\gamma_j = \gamma_j^\dagger,$$

and anti-commutation relation

$$\{\gamma_i, \gamma_j\} = 2\delta_{ij}. \tag{4.83}$$

Setting $i = j$ in Eq. (4.83) gives

$$\gamma_i^2 = 1.$$

This differs from fermions, for which $c_i^2 = 0$. A single Majorana operator therefore does not define an occupation number in the usual sense. If we try to define a Majorana number operator as

$$n_i^M = \gamma_i^\dagger \gamma_i,$$

we find

$$n_i^M = \gamma_i^2 = 1.$$

Thus, a single Majorana cannot be occupied or empty. Only when two Majoranas are combined into a fermion does a meaningful number operator appear. The physical number states are therefore defined through fermions

$$n_i = c_i^\dagger c_i, \qquad n_i = 0, 1.$$

If two Majorana operators, say γ_{2i-1} and γ_{2i}, are spatially close, their wavefunctions can overlap. This overlap lifts the zero-energy degeneracy and generates a finite energy splitting [44, 50].

A Hermitian quadratic coupling between two distinct Majoranas γ_a and γ_b has the form $i\,\gamma_a\gamma_b$. The bare product $\gamma_a\gamma_b$ is anti-Hermitian, since $(\gamma_a\gamma_b)^\dagger = \gamma_b\gamma_a = -\gamma_a\gamma_b$, and the factor of i restores Hermiticity. Such a coupling can occur between any pair of Majoranas. The simplest case is the pair on the same site, γ_{2i-1} and γ_{2i}, which are the two halves of the fermion c_i. We treat this case first, because it shows most directly how an overlap between two Majoranas becomes an energy splitting. Couplings between Majoranas on different sites, such as $\gamma_{2i}\gamma_{2i+1}$, also occur. They appear when we write the full Kitaev Hamiltonian in the Majorana basis. For now we keep the same-site pair. Using Eqs. (4.81)–(4.82),

$$\gamma_{2i-1}\gamma_{2i} = (c_i^\dagger + c_i)\, i(c_i^\dagger - c_i) \tag{4.84}$$

$$= i\left[c_i^\dagger c_i^\dagger - c_i^\dagger c_i + c_i c_i^\dagger - c_i c_i\right]. \tag{4.85}$$

Using fermionic relations

$$c_i^2 = 0, \quad (c_i^\dagger)^2 = 0, \quad c_i c_i^\dagger = 1 - c_i^\dagger c_i,$$

this simplifies to

$$\gamma_{2i-1}\gamma_{2i} = i\left[-c_i^\dagger c_i + (1 - c_i^\dagger c_i)\right] \tag{4.86}$$

$$= i(1 - 2n_i). \tag{4.87}$$

Therefore,

$$\frac{i}{2}\gamma_{2i-1}\gamma_{2i} = \frac{i}{2}\cdot i(1-2n_i) = \frac{1}{2}(2n_i-1) = n_i - \frac{1}{2}. \tag{4.88}$$

Including an overlap amplitude t, we obtain

$$\frac{it}{2}\gamma_{2i-1}\gamma_{2i} = t\left(n_i - \frac{1}{2}\right). \tag{4.89}$$

This result shows that Majorana overlap is equivalent to introducing an energy splitting between the occupied and empty states of the corresponding fermions. If $n_i = 0$, the energy contribution is $-t/2$. If $n_i = 1$, the energy contribution is $+t/2$.

The experimentally measurable quantities are the occupation numbers n_i. Such a measurement can be done by bringing two MFs close together and measuring the energy splitting according to Eq. (4.89), which reveals the occupation through the coupling term [44]. Note that it does not make sense to talk about the "state of a MF" since a single MF contains only half a degree of freedom.

4.3.2 Kitaev Hamiltonian in Majorana Representation

We now express the Kitaev Hamiltonian in Eq. (4.43) in terms of Majorana Fermions. First, as schematically shown in fig. 4.3, we write each electron operator, c and $c^\dagger$, in terms of two Majorana Fermion operators, γ_1 and γ_2, as

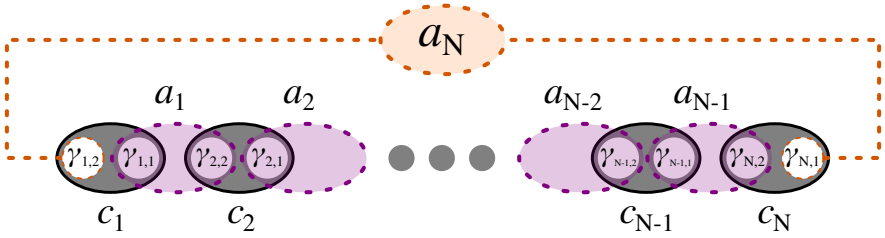

Figure 4.3: Schematic of Kitaev chain in the Majorana and bond representation, with non-zero bond Fermions in purple, and the nonlocal zero mode a_N living on the two ends of the chain. Adapted from [163]

.

$$c_j = \frac{1}{2}(\gamma_{j,1} + i\gamma_{j,2}), \qquad c_j^\dagger = \frac{1}{2}(\gamma_{j,1} - i\gamma_{j,2}), \tag{4.90}$$

where the γ's are Majorana Fermion operators with the anti-commutation relation $\{\gamma_{i,\alpha}, \gamma_{j,\beta}\} = 2\delta_{ij}\delta_{\alpha\beta}$.

Using (4.90) and Majorana anti-commutation relations, the Kitaev Hamiltonian in Eq. (4.43) can be written in terms of Majorana Fermions as

$$\hat{H}_{\text{chain}} = \frac{i}{2}\left((t+\Delta)\sum_{j=1}^{N-1}\gamma_{j,1}\gamma_{j+1,2} + (t-\Delta)\sum_{j=1}^{N-1}\gamma_{j+1,1}\gamma_{j,2} - \mu\sum_{j=1}^{N}(\gamma_{j,1}\gamma_{j,2} - i)\right). \tag{4.91}$$

The form in (4.91) shows the pairing between Majoranas of different types in adjacent sites. But it also shows that the Hamiltonian is not diagonal in Majorana Fermions, they are not quasiparticles of the Kitaev Hamiltonian. The form in Eq. (4.91) shows the pairing between Majoranas of different types on adjacent sites.

4.3.3 Bond Operators

To illustrate the zero modes explicitly in the Hamiltonian, we define a new transformation as "bond transformation". In this transformation, two Majoranas of different types from adjacent sites are combined as

$$a_j = \frac{1}{2}(\gamma_{j,1} + i\gamma_{j+1,2}) = \frac{1}{2}(c_j^\dagger + c_j + c_{j+1} - c_{j+1}^\dagger), \tag{4.92a}$$

$$a_N = \frac{1}{2}(\gamma_{N,1} + i\gamma_{1,2}) = \frac{1}{2}(c_N^\dagger + c_N + c_1 - c_1^\dagger), \tag{4.92b}$$

where we also defined a_N, to which we refer as the zero mode, from the two unpaired Majoranas at the two ends of the chain, as shown in Fig. 4.3. Then, the Hamiltonian in terms of bond operators is

$$\begin{aligned}\hat{H}_{\text{chain}} = \frac{1}{2}\Bigg((t+\Delta)\sum_{j=1}^{N-1}(2a_j^\dagger a_j - 1) + (t-\Delta)\sum_{j=1}^{N-1}(a_{j+1}^\dagger a_{j-1} + a_{j+1}a_{j-1} + h.c.) \\ -\mu\sum_{j=1}^{N}(1 + (a_j^\dagger a_{j-1} + a_j a_{j-1} + h.c.))\Bigg),\end{aligned} \tag{4.93}$$

where in the second and the third sum one should identify $a_0 \equiv a_N$. The Hamiltonian is still not diagonal, but we notice the diagonal term corresponding to the $t+\Delta$ term. We know that as long as $|\mu| < 2|t|$ the system remains in the topological phase. For a specific example, we take a special case of $t = \Delta$ and $\mu = 0$. This choice of parameters ensures the system to be within the topological phase. As a result, the bond Fermions

diagonalize the Hamiltonian in (4.93) and reduce it to

$$\hat{H}_{\text{chain}} = t \sum_{j=1}^{N-1} (2a_j^\dagger a_j - 1) + 0 \times a_N^\dagger a_N, \tag{4.94}$$

which implies a set of $N-1$ quasiparticles with energy $2t$, and one non-local quasiparticle a_N with zero energy, hence the name zero mode. In this case, since bond fermions are the quasiparticles of the Kitaev Hamiltonian, their configurations are the eigenstates of the system.

4.3.4 Energy Spectrum

In order to verify the validity of the bond transformation, we need to confirm energy spectra matching between normal and bond fermions. We use ED to calculate the energy spectrum of the Kitaev Hamiltonian. Beginning with normal fermions, for a chain of N sites, there are $\binom{N}{0} + \binom{N}{1} + ... + \binom{N}{N-1} + \binom{N}{N} = 2^N$ possible configurations for spinless fermions, which we construct as

$$|\alpha_1 \dots \alpha_N\rangle = \prod_{i=1}^{N} (c_i^\dagger)^{\alpha_i} |0\rangle , \tag{4.95}$$

where $|0\rangle$ is the vacuum of fermions, $\alpha_i = 1$ or 0, corresponds to having (1) or not having (0) fermions at site i.

For a given number of fermions M, there are p_M fermionic configurations. But since the superconducting term does not conserve particle number, the eigenstates of the Hamiltonian are coherent linear combinations of fermionic configurations with different fermion numbers. Based on this, the νth eigenstate is written as

$$|\psi^\nu\rangle = \sum_{M,p_M} C^\nu_{M,p_M} |M, p_M\rangle , \tag{4.96}$$

where we are populating N sites with $M = 0, 1, \dots, N$ fermions. To solve for coefficients C^ν_{M,p_M}, we apply the Hamiltonian on this state, and by using the orthogonality of the configurations we obtain the eigenvalue equation

$$\sum_{p_M,M} \langle q_{M'}, M'| \hat{H}_{\text{chain}} |p_M, M\rangle C^\nu_{M,p_M} = E^\nu C^\nu_{M',q_{M'}}. \tag{4.97}$$

However, since the Kitaev Hamiltonian only changes particle number in pairs, the matrix element $\langle q_{M'}, M'| \hat{H}_{\text{KC}} |p_M, M\rangle$ is non-zero only if M and M' have the same

parity, i.e. if they are both even or odd. This parity symmetry allows us to break the Hilbert space into two decoupled subspaces of even and odd configurations.

For bond fermions, we construct any bond fermion configurations just as in Eq. (4.95)

$$|\overline{\alpha_1 \dots \alpha_N}\rangle = \prod_{i=1}^{N} (a_i^\dagger)^{\alpha_i} |0_a\rangle \,, \tag{4.98}$$

where $|0_a\rangle$ is the vacuum of bond Fermions, and we used the overline to distinguish these configurations from the normal Fermion configurations. In the special case of $t = \Delta$ and $\mu = 0$, the Hamiltonian in bond fermions is diagonal, as expressed in Eq. (4.94). This is the usefulness of bond fermion basis that makes the energy spectrum calculations easier. We now describe the energy spectrum of a chain of $N = 3$ quantum dots, obtained both in the normal and bond fermion basis using ED.

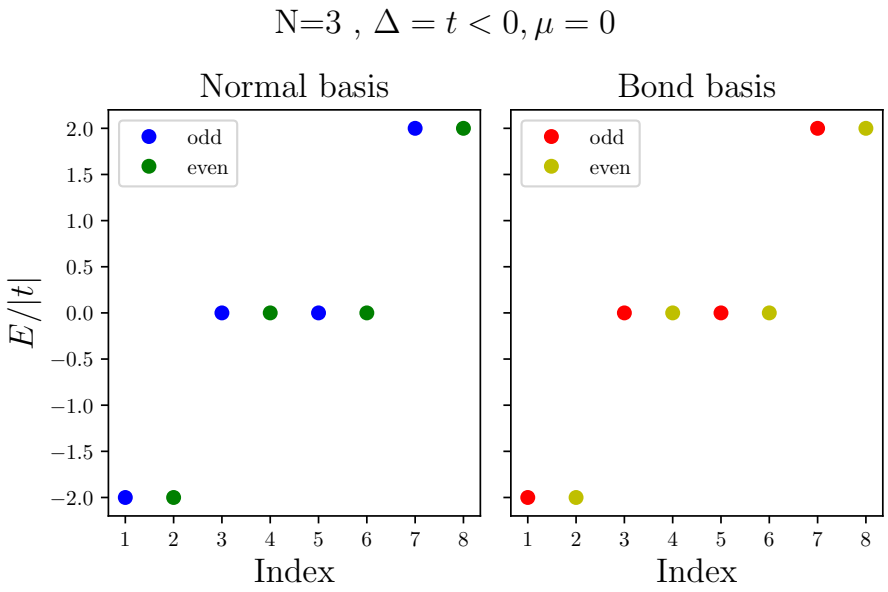

Figure 4.4: Energy spectra of Kitaev chain in normal (left) and bond (right) basis, where $\Delta = t = -1$ and $\mu = 0$. Energy is normalized to $|t|$. The energy spectrum in normal fermions matches the spectrum in bond fermions. As a result of being in the topological regime, the spectra of even and odd parity subspaces also match in both bases.

Figure 4.4 shows the energy spectrum for the case of $\Delta = t = -1$. As mentioned above, in this case, the configurations of bond fermions are also the eigenstates of the system since the Hamiltonian is diagonal. Being in the topological regime, the system has a doubly degenerate ground state, one in the odd subspace $|\mathrm{GS}\rangle = |\overline{111}\rangle$ with all bond fermions, and the other in the even subspace $|\overline{\mathrm{GS}}\rangle = |\overline{110}\rangle$, which is

missing the zero energy bond fermion $a_N \equiv a_3$. Next, we have the singly excited states, missing one non-zero bond Fermion, with excitation energy $2|t|$, from which we have two in each subspace, $|a_1\rangle = |\overline{011}\rangle$ and $|a_2\rangle = |\overline{101}\rangle$ in the even subspace, and $|\overline{a_1}\rangle = |\overline{010}\rangle$ and $|\overline{a_2}\rangle = |\overline{100}\rangle$ in the odd subspace. Finally, in each subspace, there is one doubly excited state, missing two non-zero bond fermions with excitation energy $4|t|$, $|\overline{a_1 a_2}\rangle = |000\rangle$ in the even subspace, and $|a_1 a_2\rangle = |001\rangle$ in the odd subspace. Table 4.1 summarizes the description of the spectrum in terms of bond Fermions.

Table 4.1: Describing the spectra plotted in Fig. 4.4. Configurations of bond fermions are the eigenstates of the Kitaev Hamiltonian when $\Delta = t$ and $\mu = 0$. The configuration labels are chosen to sort the corresponding energies from lower to higher.

index	1	2	3	4	5	6	7	8
configuration	$\|\overline{111}\rangle$	$\|\overline{110}\rangle$	$\|\overline{010}\rangle$	$\|\overline{011}\rangle$	$\|\overline{100}\rangle$	$\|\overline{101}\rangle$	$\|\overline{001}\rangle$	$\|\overline{000}\rangle$
label	$\|\mathrm{GS}\rangle$	$\|\overline{\mathrm{GS}}\rangle$	$\|\overline{a}_1\rangle$	$\|a_1\rangle$	$\|\overline{a}_2\rangle$	$\|a_2\rangle$	$\|a_1 a_2\rangle$	$\|\overline{a_1 a_2}\rangle$
parity	odd	even	odd	even	odd	even	odd	even
excitation energy	0	0	$2\|t\|$	$2\|t\|$	$2\|t\|$	$2\|t\|$	$4\|t\|$	$4\|t\|$

4.3.5 Probability Density Distribution

Once the eigenstates $|\psi^\nu\rangle$ of the Kitaev Hamiltonian are obtained by ED according to Eq. (4.97), we can compute the site-resolved probability density to visualize the localization properties of the quasiparticle states, in particular the Majorana edge modes.

The local fermionic occupation operator $\hat{n}_j = c_j^\dagger c_j$ at site j and its expectation value in an eigenstate $|\psi^\nu\rangle$ defines the probability density at site j

$$\rho_j^{(\nu)} = \langle\psi^\nu|\, \hat{n}_j\, |\psi^\nu\rangle\,. \tag{4.99}$$

Using the configuration basis introduced in Eq. (4.96), we write

$$|\psi^\nu\rangle = \sum_{M,p_M} C^\nu_{M,p_M}\, |M,p_M\rangle\,, \qquad \langle\psi^\nu| = \sum_{M',p_{M'}} (C^\nu_{M',p_{M'}})^*\, \langle M',p_{M'}|\,. \tag{4.100}$$

Substituting Eq. (4.100) into Eq. (4.99) gives

$$\begin{aligned}\rho_j^{(\nu)} &= \left(\sum_{M',p_{M'}} \left(C^{\nu}_{M',p_{M'}}\right)^* \langle M',p_{M'}|\right) \hat{n}_j \left(\sum_{M,p_M} C^{\nu}_{M,p_M} \,|M,p_M\rangle\right) \\ &= \sum_{M',p_{M'}} \sum_{M,p_M} \left(C^{\nu}_{M',p_{M'}}\right)^* C^{\nu}_{M,p_M} \,\langle M',p_{M'}|\,\hat{n}_j\,|M,p_M\rangle\,. \end{aligned} \tag{4.101}$$

A configuration state $|M,p_M\rangle$ is an eigenstate of every number operator $\hat{n}_j$ because it has a definite occupation (either 0 or 1) on each site. Therefore,

$$\hat{n}_j\,|M,p_M\rangle = n_j(M,p_M)\;|M,p_M\rangle\,, \tag{4.102}$$

where

$$n_j(M,p_M) = \begin{cases} 1, & \text{if site } j \text{ is occupied in the configuration } |M,p_M\rangle, \\ 0, & \text{if site } j \text{ is empty in the configuration } |M,p_M\rangle. \end{cases} \tag{4.103}$$

Taking the overlap with $\langle M',p_{M'}|$ and using orthonormality of the configuration basis,

$$\langle M',p_{M'}|\,|M,p_M\rangle = \delta_{M',M}\,\delta_{p_{M'},p_M}, \tag{4.104}$$

we obtain

$$\begin{aligned}\langle M',p_{M'}|\,\hat{n}_j\,|M,p_M\rangle &= n_j(M,p_M)\;\langle M',p_{M'}|\,|M,p_M\rangle \\ &= n_j(M,p_M)\,\delta_{M',M}\,\delta_{p_{M'},p_M}. \end{aligned} \tag{4.105}$$

Substituting Eq. (4.105) into Eq. (4.101) gives

$$\begin{aligned}\rho_j^{(\nu)} &= \sum_{M',p_{M'}} \sum_{M,p_M} \left(C^{\nu}_{M',p_{M'}}\right)^* C^{\nu}_{M,p_M}\, n_j(M,p_M)\,\delta_{M',M}\,\delta_{p_{M'},p_M} \\ &= \sum_{M,p_M} \left(C^{\nu}_{M,p_M}\right)^* C^{\nu}_{M,p_M}\, n_j(M,p_M) \\ &= \sum_{M,p_M} \left|C^{\nu}_{M,p_M}\right|^2 n_j(M,p_M). \end{aligned} \tag{4.106}$$

Since $\langle M,p_M|\,\hat{n}_j\,|M,p_M\rangle = n_j(M,p_M)$ equals 1 when site j is occupied and 0 otherwise, $\rho_j^{(\nu)}$ is simply the total probability of finding a fermion on site j in the eigenstate ν, obtained by summing the probabilities of all basis configurations that have site j occupied.

Plotting $\rho_j^{(\nu)}$ across the chain reveals the spatial structure of the eigenstate: for trivial superconducting phases ($|\mu| > 2t$) the lowest-energy eigenstate is extended throughout the bulk, while in the topological phase ($|\mu| < 2t$) the lowest-energy eigenstate shows localization at the chain ends, the Majorana zero modes as shown in Fig. 4.5.

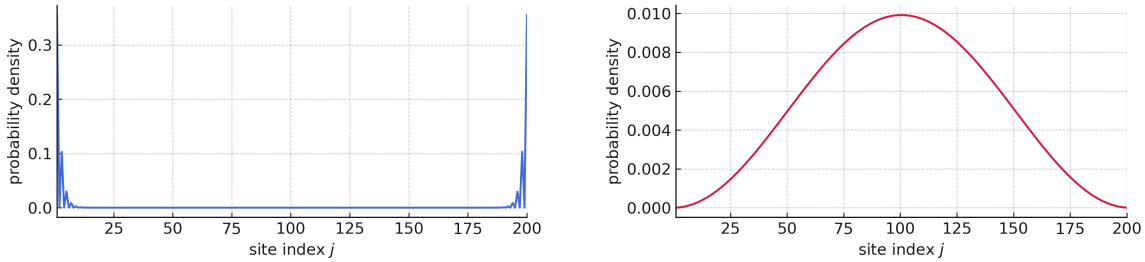

(a) Topological regime

(b) Trivial regime

Figure 4.5: Probability density $\rho_j^{(\nu)} = \langle\psi^\nu| c_j^\dagger c_j |\psi^\nu\rangle$ of the ground state along a Kitaev chain of 200 sites. In the trivial phase, ρ_j is delocalized, while in the topological phase, it is strongly localized at the two ends.

4.4 Experimental Realizations and Limitations of the Kitaev Chain

The Kitaev chain model provides one of the most elegant theoretical realizations of a topological superconductor, exhibiting localized MZMs at its ends [50]. Its minimal form, however, assumes a one-dimensional (1D) lattice of spinless fermions with intrinsic p-wave pairing [50]. Although this model captures the essential topological physics, its direct experimental realization in condensed matter systems is highly nontrivial.

Conventional superconductors found in nature are generally of the s-wave type, where Cooper pairs form between electrons of opposite spin and momentum, leading to a spin-singlet, isotropic pairing potential $\Delta_s(\mathbf{r}) \propto \langle c_\uparrow(\mathbf{r}) c_\downarrow(\mathbf{r})\rangle$ [154, 159]. In contrast, the Kitaev model assumes a p-wave, spinless, spin-triplet pairing of the form $\Delta_p(\mathbf{r}, \mathbf{r}') \propto \langle c(\mathbf{r}) c(\mathbf{r}')\rangle$, which is odd under exchange of spatial coordinates and corresponds to parallel-spin pairing [44, 162]. Such superconductors are extremely rare in nature and usually occur in strongly correlated materials such as Sr_2RuO_4, where the pairing symmetry remains under debate [59].

The absence of robust, intrinsic p-wave superconductors poses a fundamental

obstacle to implementing the Kitaev chain directly in the laboratory. This conceptual mapping between the idealized Kitaev model and real semiconductor–superconductor hybrid systems has guided many experimental efforts [44, 164, 165]. Signatures consistent with Majorana zero modes, such as zero-bias conductance peaks, have been reported in InSb and InAs nanowires proximitized by aluminum [52, 63]. While the unambiguous identification of topological superconductivity remains a subject of active investigation, these systems provide the most promising and controllable route toward realizing Majorana-based qubits.

While the Kitaev chain remains a powerful theoretical model for understanding topological superconductivity and Majorana modes [44, 50], its assumption of intrinsic p-wave pairing is experimentally unrealistic. The search for realizable platforms has thus shifted toward spin–orbit coupled semiconductor nanowires and related hybrid systems, where conventional s-wave superconductivity is transformed into effective p-wave pairing by spin–orbit interaction and Zeeman splitting [44, 164, 165]. This motivates the study of the Rashba nanowire Hamiltonian, which we introduce in the next chapter.

Chapter 5

Majorana Zero Modes in the Semiconducting-Superconducting Nanowire

In this chapter, we describe the semiconducting-superconducting (SM-SC) model that is shown to exhibit topological features and host MZMs [47, 50, 166–169]. The reason we turn to this system is the nature of its superconductivity which is a natural choice for experimental purposes [47, 168]. As we will see throughout the chapter, this model is theoretically more challenging compared to the 1D spinless chain described by the Kitaev Hamiltonian. Moreover, it is only an approximate topological system which shows MZMs under certain conditions. Despite that, it is much more experimentally friendly, so a comprehensive theoretical introduction is required. We will begin by introducing the s-wave superconductivity, which plays an essential role in this model, and the key differences of this type of superconductor compared to the p-wave one. We then proceed by presenting the 1D SM-SC system and its features. In doing so, we first study the semiconducting nanowire, and then we add the superconductor and see its effects. Finally, we discuss the superconductivity gap and how we derive the condition in which keeps the system in the topological phase.

5.1 S-wave Superconductivity

Following the discussion of superconductivity in sec. 4.1, starting from equations (4.14) and (4.15), we include the s-wave pairing to the BdG Hamiltonian. The s-wave pairing couples the spin up and down with opposite momenta [166, 167]. It has the following form

$$\hat{H}_{\Delta} = \Delta\, c^{\dagger}_{p\uparrow} c^{\dagger}_{-p\downarrow} + \Delta^{*} c_{-p\downarrow} c_{p\uparrow} \tag{5.1}$$

where Δ is the strength of superconductivity and is a complex number. To be able to add this term into our BdG form, we need to write it in an antisymmetrized form. Through using the anti-commutation relations [69]

$$\{c^\dagger_{p\uparrow}, c^\dagger_{-p\downarrow}\} = 0, \qquad \{c_{-p\downarrow}, c_{p\uparrow}\} = 0 \tag{5.2}$$

we obtain

$$c^\dagger_{p\uparrow}c^\dagger_{-p\downarrow} = -\,c^\dagger_{-p\downarrow}c^\dagger_{p\uparrow}, \qquad c_{-p\downarrow}c_{p\uparrow} = -\,c_{p\uparrow}c_{-p\downarrow}. \tag{5.3}$$

Using these identities, each term can be written in an explicitly antisymmetric form

$$c^\dagger_{p\uparrow}c^\dagger_{-p\downarrow} = \frac{1}{2}\Big(c^\dagger_{p\uparrow}c^\dagger_{-p\downarrow} - c^\dagger_{-p\downarrow}c^\dagger_{p\uparrow}\Big), \tag{5.4}$$

$$c_{-p\downarrow}c_{p\uparrow} = \frac{1}{2}\Big(c_{-p\downarrow}c_{p\uparrow} - c_{p\uparrow}c_{-p\downarrow}\Big). \tag{5.5}$$

Substituting these expressions back into $\hat{H}_\Delta$ gives

$$\hat{H}_\Delta = \frac{\Delta}{2}\Big(c^\dagger_{p\uparrow}c^\dagger_{-p\downarrow} - c^\dagger_{-p\downarrow}c^\dagger_{p\uparrow}\Big) + \frac{\Delta^*}{2}\Big(c_{-p\downarrow}c_{p\uparrow} - c_{p\uparrow}c_{-p\downarrow}\Big) \tag{5.6}$$

$$= \frac{1}{2}\Big[\Delta\Big(c^\dagger_{p\uparrow}c^\dagger_{-p\downarrow} - c^\dagger_{-p\downarrow}c^\dagger_{p\uparrow}\Big) + \Delta^*\Big(c_{-p\downarrow}c_{p\uparrow} - c_{p\uparrow}c_{-p\downarrow}\Big)\Big]. \tag{5.7}$$

The superconductivity term creates a Cooper pair by forming two electrons or two holes (absence of electrons) [159, 160, 168].

The total Hamiltonian (the BdG Hamiltonian in Eq. (4.14) plus the s-wave pairing term) is given by

$$\hat{H} + \hat{H}_\Delta = \sum_{\mathbf{p}} \Psi^\dagger_{\mathbf{p}} \hat{H}_{\mathrm{BdG}}(\mathbf{p}, \Delta)\Psi_{\mathbf{p}} \tag{5.8}$$

$$\hat{H}_{\mathrm{BdG}}(\mathbf{p}, \Delta) = \frac{1}{2}\begin{pmatrix} \epsilon(\mathbf{p}) & 0 & 0 & \Delta \\ 0 & \epsilon(\mathbf{p}) & -\Delta & 0 \\ 0 & -\Delta^* & -\epsilon(-\mathbf{p}) & 0 \\ \Delta^* & 0 & 0 & -\epsilon(-\mathbf{p}) \end{pmatrix}. \tag{5.9}$$

It can be rewritten in terms of Pauli matrices

$$\hat{H}_{\mathrm{BdG}}(\mathbf{p}, \Delta) = \epsilon(\mathbf{p})\,\tau^z \otimes I_{2\times 2} - (\mathrm{Re}\,\Delta)\,\tau^x \otimes \sigma^y - (\mathrm{Im}\,\Delta)\,\tau^y \otimes \sigma^y, \tag{5.10}$$

where τs are Pauli matrices in the particle-hole basis and σs are the Pauli matrices in the spin basis. τs take the same form of the Pauli matrices, but we are denoting them

with different notation to indicate that they act on particle and hole bases. To find the energy spectrum, we proceed as follows. We can write the Hamiltonian as

$$\hat{H}_{\mathrm{BdG}}(\mathbf{p}, \Delta) \equiv a\,\Gamma_1 + b\,\Gamma_2 + c\,\Gamma_3, \tag{5.11}$$

with

$$\Gamma_1 = \tau^z \otimes I_2, \qquad \Gamma_2 = \tau^x \otimes \sigma^y, \qquad \Gamma_3 = \tau^y \otimes \sigma^y,$$

$$a = \epsilon(\mathbf{p}), \qquad b = -\mathrm{Re}\,\Delta, \qquad c = -\mathrm{Im}\,\Delta.$$

Using the Pauli algebra $\{\tau^i, \tau^j\} = 2\delta_{ij} I_2$, $\{\sigma^i, \sigma^j\} = 2\delta_{ij} I_2$, and $(\tau^i)^2 = (\sigma^i)^2 = I_2$, we have

$$\Gamma_i^2 = I_{4\times 4}, \qquad \{\Gamma_i, \Gamma_j\} = 0 \quad (i \neq j).$$

Therefore,

$$\begin{aligned}(\hat{H}_{\mathrm{BdG}})^2 &= (a\,\Gamma_1 + b\,\Gamma_2 + c\,\Gamma_3)^2 \\ &= a^2\Gamma_1^2 + b^2\Gamma_2^2 + c^2\Gamma_3^2 + ab\{\Gamma_1, \Gamma_2\} + ac\{\Gamma_1, \Gamma_3\} + bc\{\Gamma_2, \Gamma_3\} \\ &= (a^2 + b^2 + c^2)\, I_{4\times 4} = \left(\epsilon(\mathbf{p})^2 + |\Delta|^2\right) I_{4\times 4}. \end{aligned} \tag{5.12}$$

Since the final form is diagonal, the eigenvalues are simply the diagonal elements. Hence the spectrum consists of two doubly degenerate bands with energies

$$E_{\pm}(\mathbf{p}) = \pm\sqrt{\epsilon(\mathbf{p})^2 + |\Delta|^2}, \tag{5.13}$$

where the twofold degeneracy is due to spin (the Hamiltonian squared is proportional to I_2 in spin space and I_2 in particle–hole space). If $\Delta \neq 0$, the spectrum has an energy gap which is called the superconducting gap, as shown in Fig. 5.1. This picture becomes important when we calculate the band structure of the SM-SC system.

5.2 SM-SC Model

The system we consider is a 1D semiconducting (SM) nanowire of length L with Rashba spin-orbit coupling of strength α and a Zeeman field V_z [47, 166–168]. The SM nanowire is placed in contact with a conventional s-wave superconductor. The nanowire is not superconducting on its own. Through the superconducting proximity effect, Cooper pairs from the adjacent superconductor tunnel into the nanowire across the interface, and this induces an effective s-wave pairing in the wire [166–168]. This

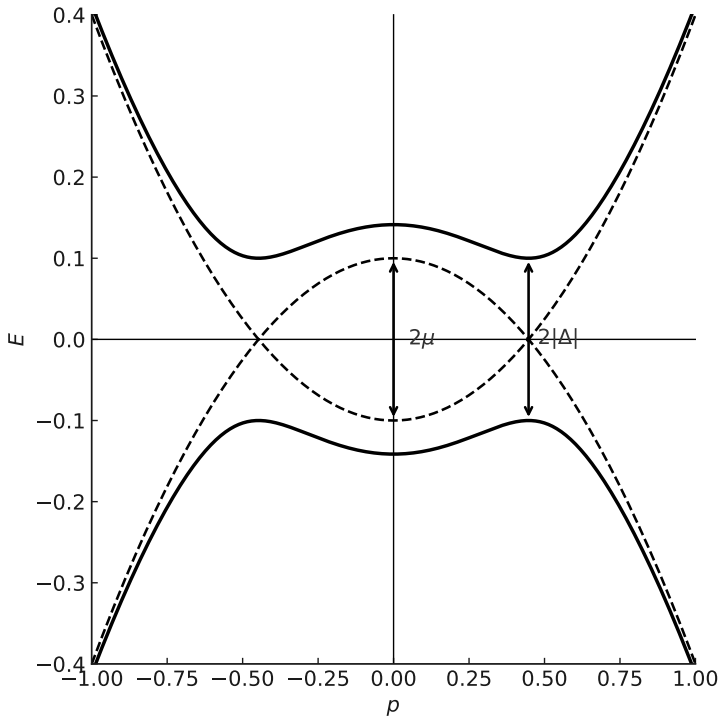

Figure 5.1: Energy dispersion of an s-wave superconductor ($m = 1$, $\mu = 0.1$, $|\Delta| = 0.1$). The solid curves represent $E_{\pm}(p) = \pm\sqrt{\epsilon(p)^2 + |\Delta|^2}$, while the dashed lines correspond to the normal-state dispersion $\pm\epsilon(p)$. The characteristic energy scales $2|\Delta|$ and 2μ are indicated.

induced pairing is the term $\hat{H}_{\rm SC}$ given below. Its amplitude $\Delta(x)$ is the induced gap, which is generally smaller than the gap of the parent superconductor. The Hamiltonian of the system is given by

$$\hat{H} = \hat{H}_{\rm SM} + \hat{H}_{\rm SC}, \tag{5.14}$$

$$\hat{H}_{\rm SM} = \int_0^L dx\, \psi^\dagger(x) \left[(-\frac{\hbar^2 \partial_x^2}{2m^*} - \mu) I + i\alpha\hbar\sigma_y \partial_x + V_x \sigma_x \right] \psi(x), \tag{5.15}$$

$$\hat{H}_{\rm SC} = \int_0^L dx \left[\Delta(x)\, \psi_\uparrow^\dagger(x) \psi_\downarrow^\dagger(x) + \text{h.c.} \right], \tag{5.16}$$

where we have taken the nanowire along the x-axis. Note that $\psi(x)$ here is not the wave function, but is a column spinor of annihilation field operators

$$\psi(x) = \begin{bmatrix} \psi_\uparrow(x) \\ \psi_\downarrow(x) \end{bmatrix}.$$

The first term of $\hat{H}_{SM}$ is the kinetic energy $\frac{p_x^2}{2m^\star}$ with $m^\star$ being the effective mass of the electron. μ is the chemical potential, α is the spin-orbit coupling, and V_x is the Zeeman field parallel to the nanowire (later we will show that one can take the Zeeman field perpendicular to the nanowire, but that will not change the physics of the problem). $\Delta(x)$ is the strength of the proximity-induced s-wave pairing in the nanowire, and I, σ_x, σ_y are the 2×2 identity, Pauli-x, and Pauli-y matrices, respectively.

The Zeeman term is in fact

$$-\boldsymbol{\mu} \cdot \mathbf{B} = \frac{g_{\mathrm{SM}} \mu_B B}{2} \sigma_x = V_z \, \sigma_x, \qquad V_z = \frac{g_{\mathrm{SM}} \mu_B B}{2}, \tag{5.17}$$

where $\boldsymbol{\mu}$ is the **magnetic moment** of the electron, defined as $\boldsymbol{\mu} = -g_{\mathrm{SM}} \mu_B \, \boldsymbol{\sigma}/2$, where the negative sign reflects the electron's negative charge [115, 122]. $\mathbf{B}$ is the externally applied **magnetic field** vector, and the letter Z denotes Zeeman. In this case, it is taken along the x-direction, i.e., $\mathbf{B} = B \, \hat{x}$, which couples to the spin through σ_x. g_{SM} is the dimensionless **Landé g-factor** (or effective g-factor) of the semiconductor material. It characterizes the strength of the spin coupling to the magnetic field and can be very large in narrow-gap semiconductors such as InSb or InAs (typically $|g_{\mathrm{SM}}| \sim 10$–$50$) [170, 171]. $\mu_B = e\hbar/(2m_e)$ is the **Bohr magneton**, the natural scale for the magnetic moment of an electron, where e is the elementary charge and m_e is the bare electron mass [122, 172]. B is the **magnitude** of the external magnetic field. V_z is the resulting Zeeman field, which quantifies the spin splitting between spin-up and spin-down states induced by the magnetic field [115, 122, 166, 167].

The spin–orbit coupling (SOC) term in the Hamiltonian is given by

$$\hat{H}_R = \alpha \, (\boldsymbol{\sigma} \times \mathbf{p}) \cdot \hat{\mathbf{z}}, \tag{5.18}$$

where $\boldsymbol{\sigma} = (\sigma_x, \sigma_y, \sigma_z)$ are the Pauli matrices acting on the electron spin, $\mathbf{p} = -i\hbar\nabla$ is the momentum operator, and $\hat{\mathbf{z}}$ is the unit vector perpendicular to the xy plane. This term arises due to the relativistic coupling between an electron's spin and its motion in an electric field $\mathbf{E}$, which in the electron's rest frame acts as an effective magnetic field $\mathbf{B}_{\text{eff}} \propto \mathbf{E} \times \mathbf{p}$ that couples to the spin through the Zeeman interaction [171, 173].

In semiconductor nanowires the electric field $\mathbf{E}$ originates from either the confining potential at the heterostructure interface or from an applied gate voltage [171, 173]. When $\mathbf{E}$ is along $\hat{z}$, the effective magnetic field points along $\hat{y}$ for motion along $\hat{x}$, and the Rashba Hamiltonian reduces to

$$\hat{H}_R = \alpha \, p_x \sigma_y. \tag{5.19}$$

This couples the electron's spin and momentum, and resulting in two helically spin-polarized bands displaced in momentum space [168, 171, 173, 174]. The Rashba effect is essential for realizing topological superconductivity when combined with Zeeman coupling and proximity-induced s-wave pairing [166–168], as will be explained later on.

5.2.1 BdG Formalism: Periodic Boundary Conditions

Diagonalizing the Hamiltonian in Eq. (5.14) is possible using Fourier transformation for periodic boundary conditions, where the field operators for each spin $\sigma = \uparrow, \downarrow$ are expanded as

$$\psi_\sigma(x) = \frac{1}{\sqrt{L}} \sum_k e^{ikx} c_{\sigma,k} \chi_z^\sigma, \tag{5.20}$$

with $k = 2\pi n/L$ ($n \in \mathbb{Z}$), and χ_z^σ are the eigenstates of Pauli z-matrix, i.e. $\sigma_z \chi_z^{\uparrow(\downarrow)} = +(-)\chi_z^{\uparrow(\downarrow)}$. We first focus on the SM nanowire. Through using

$$\int_0^L dx\, e^{ixq} = L\, \delta_{q,0}, \qquad q = \frac{2\pi n}{L},$$

we apply the Fourier transformation to the SM Hamiltonian from Eq. (5.14) to obtain the BdG form. The chemical potential term transforms as

$$-\mu \int_0^L dx\, \psi^\dagger(x)\psi(x) = -\mu \sum_\sigma \frac{1}{L} \sum_{k,k'} \int_0^L dx\, e^{i(k'-k)x} c^\dagger_{\sigma,k'} c_{\sigma,k} = -\mu \sum_\sigma \sum_k c^\dagger_{\sigma,k} c_{\sigma,k}.$$

The kinetic energy term gives

$$\int_0^L dx\, \psi^\dagger(x) \left(-\frac{\hbar^2 \partial_x^2}{2m^\star} \right) \psi(x) = -\frac{\hbar^2}{2m^\star} \sum_\sigma \frac{1}{L} \sum_{k,k'} \int_0^L dx\, e^{-ik'x}\, \partial_x^2 \big(e^{ikx} \big)\, c^\dagger_{\sigma,k'} c_{\sigma,k}.$$

Since $\partial_x^2 e^{ikx} = -k^2 e^{ikx}$,

$$\int_0^L dx\, \psi^\dagger(x) \left(-\frac{\hbar^2 \partial_x^2}{2m^\star} \right) \psi(x)$$

$$= \frac{\hbar^2}{2m^\star} \sum_\sigma \frac{1}{L} \sum_{k,k'} \int_0^L dx\, e^{i(k-k')x} k^2\, c^\dagger_{\sigma,k'} c_{\sigma,k} = \sum_\sigma \sum_k \frac{\hbar^2 k^2}{2m^\star}\, c^\dagger_{\sigma,k} c_{\sigma,k}.$$

The SOC term gives

$$i\alpha\hbar \int_0^L dx\, \psi^\dagger(x) \sigma_y \partial_x \psi(x) = i\alpha\hbar\, \frac{1}{L} \sum_{k,k'} \int_0^L dx\, e^{-ik'x} c^\dagger_{k'} \sigma_y \big(\partial_x e^{ikx} \big) c_k,$$

where $c_k = [c_{\uparrow,k}, c_{\downarrow,k}]^T$. Since $\partial_x e^{ikx} = ike^{ikx}$,

$$= i\alpha\hbar \frac{1}{L} \sum_{k,k'} \int_0^L dx\, e^{i(k-k')x} (ik)\, c_{k'}^\dagger \sigma_y c_k = i\alpha\hbar \sum_k (ik)\, c_k^\dagger \sigma_y c_k = -\alpha\hbar \sum_k k\, c_k^\dagger \sigma_y c_k.$$

The Zeeman term gives

$$V_z \int_0^L dx\, \psi^\dagger(x)\sigma_x\psi(x) = V_z \frac{1}{L} \sum_{k,k'} \int_0^L dx\, e^{i(k-k')x}\, c_{k'}^\dagger \sigma_x c_k = V_z \sum_k c_k^\dagger \sigma_x c_k.$$

Collecting all the terms, we obtain the SM Hamiltonian in k-space

$$\hat{H}_{\text{SM}} = \sum_k c_k^\dagger \left(\frac{\hbar^2 k^2}{2m^\star} - \mu - \alpha\hbar k\, \sigma_y + V_z\, \sigma_x \right) c_k, \tag{5.21}$$

with $c_k = [c_{\uparrow,k}, c_{\downarrow,k}]^T$ being the spinor of annihilation operators. The s-wave pairing term transforms as

$$\int_0^L dx\, \psi_\uparrow(x)\psi_\downarrow(x) = \frac{1}{L} \sum_{k,k'} \int_0^L dx\, e^{i(k+k')x}\, c_{\uparrow,k} c_{\downarrow,k'} = \sum_k c_{\uparrow,k} c_{\downarrow,-k}.$$

Therefore

$$\hat{H}_{\text{SC}} = \sum_k \Big(\Delta\, c_{\uparrow,k} c_{\downarrow,-k} + \text{h.c.} \Big). \tag{5.22}$$

We can write the $(\frac{\hbar^2 k^2}{2m^\star} - \mu - \alpha\hbar k\, \sigma_y + V_z\, \sigma_x)$ in the SM Hamiltonian as

$$\begin{bmatrix} \frac{\hbar^2 k^2}{2m} - \mu & \alpha i\hbar k + V_z \\ -\alpha i\hbar k + V_z & \frac{\hbar^2 k^2}{2m} - \mu \end{bmatrix}, \tag{5.23}$$

and the eigenvalues of this matrix are the two bands

$$\varepsilon_\pm(k) = \frac{\hbar^2 k^2}{2m} - \mu \pm \sqrt{(\alpha\hbar k)^2 + V_z^2}, \tag{5.24}$$

with $k = 2\pi n/L$ ($n \in \mathbb{Z}$).

5.2.2 Spin Texture of the Bands

It will be advantageous to study the SM nanowire itself and all its parameters to get a better sense of the system. Having the eigenvalues of the kernel of the Hamiltonian

in Eq. (5.23), we can easily find the corresponding eigenvectors, given by

$$v_+ = \frac{1}{\sqrt{2}} \begin{pmatrix} \frac{\alpha i\hbar k + V_z}{\sqrt{V_z^2 + (\alpha\hbar k)^2}} \\ 1 \end{pmatrix} \tag{5.25}$$

$$v_- = \frac{1}{\sqrt{2}} \begin{pmatrix} -\frac{\alpha i\hbar k + V_z}{\sqrt{V_z^2 + (\alpha\hbar k)^2}} \\ 1 \end{pmatrix}. \tag{5.26}$$

Firstly, we find the angle ϕ that each vector $v_\pm$ makes in the xy-plane

$$\tan_\pm(\phi) = \pm\frac{V_z}{\alpha\hbar k} \tag{5.27}$$

This angle determines the phase difference between each vector. To determine the number of electronic states available at each energy level, we compute the density of states (DOS). The DOS represents how many electron states exist per unit energy interval within the electronic bands [114, 115]. As electrons move through a lattice with different momenta k, they occupy distinct energy levels $\epsilon(k)$ given by the band structure Eq. (5.24). The DOS essentially "unfolds" this band structure from k-space to energy-space, providing a measure of the density of available states as a function of energy. In our system, the DOS is given by

$$\rho_{\text{PBC}}(\omega) = \frac{1}{L}\sum_k \delta(\omega - E_k) \tag{5.28}$$

where the wavevector k takes discrete values determined by the periodic boundary conditions

$$k = \frac{2\pi n}{L}, \quad n = 0, \pm1, \pm2, \ldots \tag{5.29}$$

and $\delta(\omega - E_k)$ is the Dirac delta function that picks out states at energy E_k, and L is the length of the system in one dimension. The DOS formula arises from converting the discrete k-space distribution to energy-space. With periodic boundary conditions, available wavevectors are quantized as $k = 2\pi n/L$, meaning states are discrete in k-space with spacing $\Delta k = 2\pi/L$. The density of k-states per length is therefore $\rho_k = L/(2\pi)$, meaning that there is one k-state per interval $2\pi/L$. To measure states in energy-space instead, we use the Dirac delta function $\delta(\omega - E_k)$ to "pick out" which discrete k-states contribute to a given energy ω. The sum $\sum_k \delta(\omega - E_k)$ counts all states at energy ω. The prefactor $1/L$ appears as the appropriate normalization: it converts the raw count of k-states into a density per unit system length. This ensures

the DOS has proper physical dimensions [1/energy/length] and that integrating over all energies recovers the total number of electronic states divided by system size. In the continuum limit ($L \to \infty$), this sum can be replaced by an integral using the density of states in k-space, which naturally produces the familiar forms $\rho(E) = \frac{g(k)}{2\pi}|dk/dE|$ for parabolic bands.

Another quantity that will help us to know the SM nanowire, is the **spin texture**. Spin texture refers to the spatial distribution and orientation of electron spins across the Brillouin zone in momentum space. The spin polarization varies with wavevector k, creating a texture of spin orientations.

The spin texture is quantified by computing the expectation values of the Pauli spin matrices σ_x, σ_y, and σ_z

$$\sigma_x = \begin{pmatrix} 0 & 1 \\ 1 & 0 \end{pmatrix}, \quad \sigma_y = \begin{pmatrix} 0 & -i \\ i & 0 \end{pmatrix}, \quad \sigma_z = \begin{pmatrix} 1 & 0 \\ 0 & -1 \end{pmatrix} \tag{5.30}$$

in each band. For v_+, the spin components are:

$$S_x^{(+)} = \langle v_+|\sigma_x|v_+\rangle, \quad S_y^{(+)} = \langle v_+|\sigma_y|v_+\rangle, \quad S_z^{(+)} = \langle v_+|\sigma_z|v_+\rangle \tag{5.31}$$

Evaluating the spin expectation values yield

$$\langle v_+|\sigma_x|v_+\rangle = \frac{1}{\sqrt{2}} \begin{pmatrix} \frac{V_z - i\alpha\hbar k}{\sqrt{V_z^2+(\alpha\hbar k)^2}} & 1 \end{pmatrix} \frac{1}{\sqrt{2}} \begin{pmatrix} 1 \\ \frac{V_z + i\alpha\hbar k}{\sqrt{V_z^2+(\alpha\hbar k)^2}} \end{pmatrix} \tag{5.32}$$

$$= \frac{1}{2}\left[\frac{V_z - i\alpha\hbar k}{\sqrt{V_z^2 + (\alpha\hbar k)^2}} \cdot 1 + 1 \cdot \frac{V_z + i\alpha\hbar k}{\sqrt{V_z^2 + (\alpha\hbar k)^2}}\right] \tag{5.33}$$

$$= \frac{1}{2}\left[\frac{V_z - i\alpha\hbar k + V_z + i\alpha\hbar k}{\sqrt{V_z^2 + (\alpha\hbar k)^2}}\right] \tag{5.34}$$

$$= \frac{1}{2} \cdot \frac{2V_z}{\sqrt{V_z^2 + (\alpha\hbar k)^2}} \tag{5.35}$$

$$= \frac{V_z}{\sqrt{V_z^2 + (\alpha\hbar k)^2}} \tag{5.36}$$

Therefore

$$S_x^{(+)}(k) = \frac{V_z}{\sqrt{V_z^2 + (\alpha\hbar k)^2}} \tag{5.37}$$

$$\langle v_+|\sigma_y|v_+\rangle = \frac{1}{\sqrt{2}}\begin{pmatrix}\frac{V_z-i\alpha\hbar k}{\sqrt{V_z^2+(\alpha\hbar k)^2}} & 1\end{pmatrix}\frac{1}{\sqrt{2}}\begin{pmatrix}-i\\ \frac{iV_z-\alpha\hbar k}{\sqrt{V_z^2+(\alpha\hbar k)^2}}\end{pmatrix} \tag{5.38}$$

$$= \frac{1}{2}\left[\frac{V_z-i\alpha\hbar k}{\sqrt{V_z^2+(\alpha\hbar k)^2}}\cdot(-i)+1\cdot\frac{iV_z-\alpha\hbar k}{\sqrt{V_z^2+(\alpha\hbar k)^2}}\right] \tag{5.39}$$

$$= \frac{1}{2\sqrt{V_z^2+(\alpha\hbar k)^2}}\left[-(V_z-i\alpha\hbar k)\cdot i+(iV_z-\alpha\hbar k)\right] \tag{5.40}$$

$$= \frac{1}{2}\left[-iV_z-\alpha\hbar k+iV_z-\alpha\hbar k\right] \tag{5.41}$$

$$= \frac{1}{2\sqrt{V_z^2+(\alpha\hbar k)^2}}\left[-2\alpha\hbar k\right] \tag{5.42}$$

$$= -\frac{\alpha\hbar k}{\sqrt{V_z^2+(\alpha\hbar k)^2}} \tag{5.43}$$

giving

$$S_y^{(+)}(k) = -\frac{\alpha\hbar k}{\sqrt{V_z^2+(\alpha\hbar k)^2}}. \tag{5.44}$$

And finally

$$\langle v_+|\sigma_z|v_+\rangle = \frac{1}{\sqrt{2}}\begin{pmatrix}\frac{V_z-i\alpha\hbar k}{\sqrt{V_z^2+(\alpha\hbar k)^2}} & 1\end{pmatrix}\frac{1}{\sqrt{2}}\begin{pmatrix}\frac{V_z+i\alpha\hbar k}{\sqrt{V_z^2+(\alpha\hbar k)^2}}\\ -1\end{pmatrix} \tag{5.45}$$

$$= \frac{1}{2}\left[\frac{V_z-i\alpha\hbar k}{\sqrt{V_z^2+(\alpha\hbar k)^2}}\cdot\frac{V_z+i\alpha\hbar k}{\sqrt{V_z^2+(\alpha\hbar k)^2}}+1\cdot(-1)\right] \tag{5.46}$$

$$= \frac{1}{2}\left[\frac{(V_z-i\alpha\hbar k)(V_z+i\alpha\hbar k)}{(\sqrt{V_z^2+(\alpha\hbar k)^2})^2}-1\right] \tag{5.47}$$

$$= \frac{1}{2}\left[\frac{V_z^2+(\alpha\hbar k)^2}{(\sqrt{V_z^2+(\alpha\hbar k)^2})^2}-1\right] \tag{5.48}$$

$$= \frac{1}{2}\left[\frac{(\sqrt{V_z^2+(\alpha\hbar k)^2})^2}{(\sqrt{V_z^2+(\alpha\hbar k)^2})^2}-1\right] \tag{5.49}$$

$$= \frac{1}{2}\left[1-1\right] \tag{5.50}$$

$$= 0 \tag{5.51}$$

leading to

$$S_z^{(+)}(k) = 0 \tag{5.52}$$

In the same fashion, we can compute the spin texture of v_-

$$S_x^{(-)}(k) = -\frac{V_z}{\sqrt{V_z^2 + (\alpha\hbar k)^2}} \tag{5.53}$$

$$S_y^{(-)}(k) = \frac{\alpha\hbar k}{\sqrt{V_z^2 + (\alpha\hbar k)^2}} \tag{5.54}$$

$$S_z^{(-)}(k) = 0 \tag{5.55}$$

The spin texture results do make physical sense. Since we have taken the magnetic field along x direction, and the SOC along y direction, the spin texture has no z component. Moreover, v_+ and v_- have opposite spin components, which was expected from their form.

For the numerical calculations, we take InAs or InP as our candidate materials for SM nanowire. InAs has an effective mass of $m^\star = 0.02m_e$, and SOC strength within the range $[0, 0.2]$ eV ÅInP has the same SOC strength range, but an effective mass of $m^\star = 0.08m_e$ [47, 170, 175, 176] . The length of SOC can be calculated from $\frac{\hbar}{\alpha m^\star}$. We take the length of the chain to be $L = 100\,\mu m$, which is considered to be a long nanowire chain.

5.2.3 SM Band Structure

We consider various cases of parameters of the nanowire, and compute the band structure, spin texture, and DOS. In all cases, we set $\mu = 0$ since it only shifts the energy, and we use InP for the nanowire. The first case is the Zeeman field, shown in figure 5.2 We can clearly see the π phase difference between the two parabolic bands. The spin texture also shows the spin orientation of the eigenvectors. Since the magnetic field is in the x direction, spins are polarized in the $\pm$ x directions, and they are not affected by the SOC as it is turned off. The DOS on the right shows the occupation of electronic states at each energy. There is no occupation for energies below -10 μeV, and the two peaks correspond to the energies -10 and 10 μeV for the ϵ_- and ϵ_+ bands, respectively. The occupation decreases as we go to higher energy values. The Zeeman field controls the gap between the two bands. As it can be seen in figure 5.3, with higher Zeeman field (30 μeV), the gap between the two bands opens up.

The next case is the SOC only, shown in figure 5.4. We set the Zeeman field to be zero, and take $\alpha\hbar = 5\mu$eV. μm. In the SOC only case, the bands change phase as they pass through the $k = 0$ point. It can be seen from the equation of the band structure

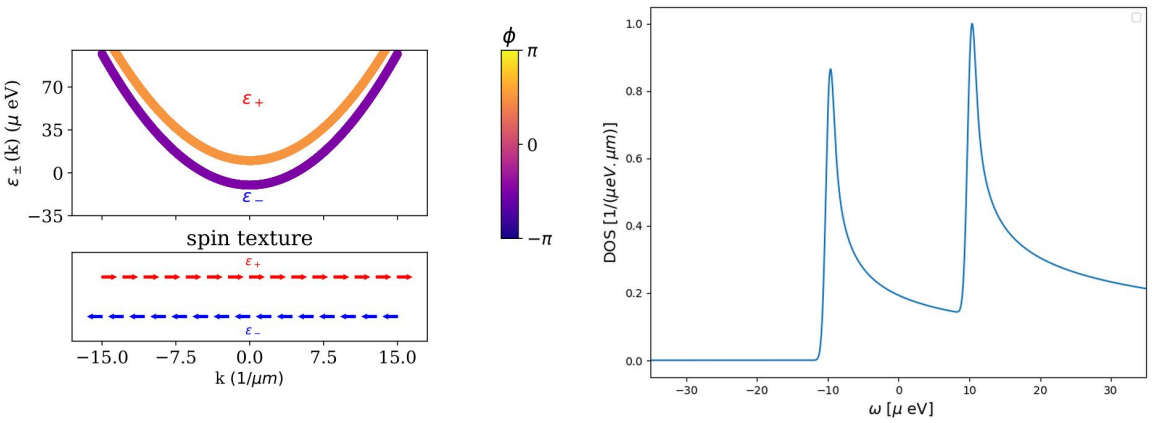

Figure 5.2: Band structure (left) as a function of k and the normalized density of states (right) and spin texture (bottom panel) for the SM nanowire with Zeeman field of strength 10 μeV. SOC and μ are set to 0. The energy is in units of μeV. The colour of the energy bands shows the angle ϕ in the xy-plane, calculated using Eq. (5.27).

Eq. (5.24), when $V_z = 0$ it is reduced to

$$\varepsilon_{\pm}(k) = \frac{k^2}{2m} - \mu \pm |\alpha k^2|, \tag{5.56}$$

and $k = 0$ is when the bands change phase. The highest occupation is localized around energy $-10\,\mu$eV, which is the two minima of ϵ_- band, and it shows a small bump at the point $k = 0$ due to the phase change of the band structures. As expected, the spins are polarized along $\pm y$ axis, changing directions at $k = 0$.

In the final case, we consider both the Zeeman field and SOC to see their sum effect on the band structure and spin texture. The result is shown in figure 5.5, where $\alpha\hbar = 5\,\mu$eV. μm and $V_z = 10\,\mu$eV. We can see that the phase of the bands change at every point k, going from 0 to $-\pi$ for the lower band ϵ_-, and π to 0 for the upper band ϵ_+. The highest DOS is located at the two minima of ϵ_- at energy around $-15\,\mu$eV. Then the next peak is at the maximum of ϵ_- at energy $-10\,\mu$eV, and the last peak is related to the minimum of ϵ_+ at energy $10\,\mu$eV. Moreover, spin texture now has components in both x and y directions, changing orientation at point $k = 0$. At the point $k = 0$ the spin is purely in the $\pm$ x direction, since it only depends on the Zeeman field, as it can be seen from the spin texture equations. If we take a higher Zeeman field, the gap between two bands will open up, resulting in a more flattened ϵ_- band. This effect is displayed in figure 5.6, where we are taking a Zeeman field of strength $V_z = 30\,\mu$eV.

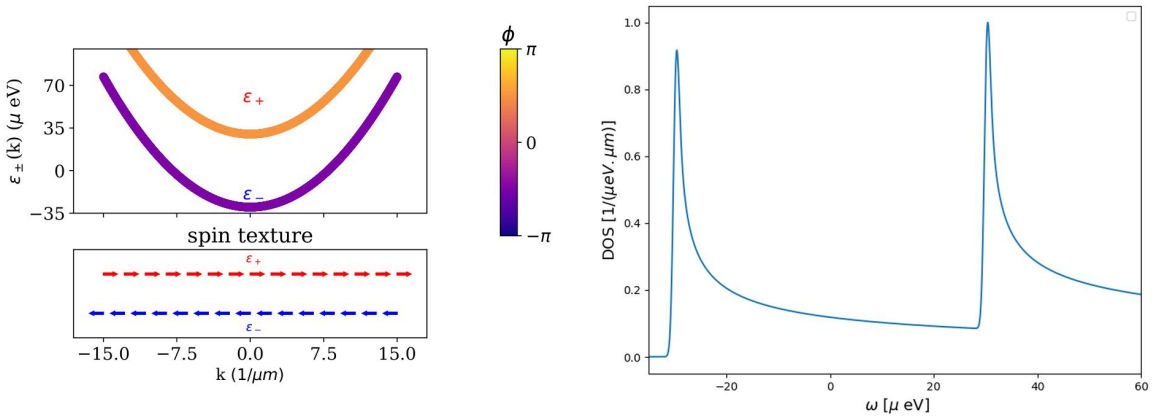

Figure 5.3: Band structure (left) as a function of k and normalized density of states (right) and spin texture (bottom panel) for the SM nanowire with Zeeman field of strength 30 μeV. The gap between the bands is larger compared to the case with the Zeeman field of strength 10 μeV

5.2.4 Comparison of the Magnetic Field Directions

As stated earlier, the direction of the magnetic field does not change the physics of the problem, and is rather a subtle choice for experimental purposes [166, 167]. So far, we have taken the magnetic field to be along the nanowire axis (the x-direction). Alternatively, one may consider a field applied perpendicular to the wire along the z-direction. In that case, the Zeeman term $V_z\sigma_x$ is replaced by $V_z\sigma_z$, and the semiconductor (SM) Hamiltonian in k-space becomes

$$\hat{H}_{\text{SM}} = \sum_k c_k^\dagger \left(\frac{k^2}{2m^\star} - \mu - \alpha k\, \sigma_y + V_z\, \sigma_z \right) c_k. \tag{5.57}$$

Following the same procedure in section 5.2.1, we rewrite the SM Hamiltonian as

$$\begin{bmatrix} \frac{\hbar^2 k^2}{2m^\star} - \mu + V_z & \alpha i\hbar k \\ -\alpha i\hbar k & \frac{\hbar^2 k^2}{2m^\star} - \mu - V_z \end{bmatrix}. \tag{5.58}$$

The eigenvalues of this matirx give the two energy bands

$$\varepsilon_\pm(k) = \frac{\hbar^2 k^2}{2m^\star} - \mu \pm \sqrt{(\alpha k)^2 + V_z^2}, \tag{5.59}$$

which is equal to Eq. (5.24) for a magnetic field along x direction. This equivalence arises because a global spin rotation about the y-axis by $\pi/2$ transforms $\sigma_x \to \sigma_z$ while leaving σ_y unchanged. Consequently, the energy spectrum is invariant under such a

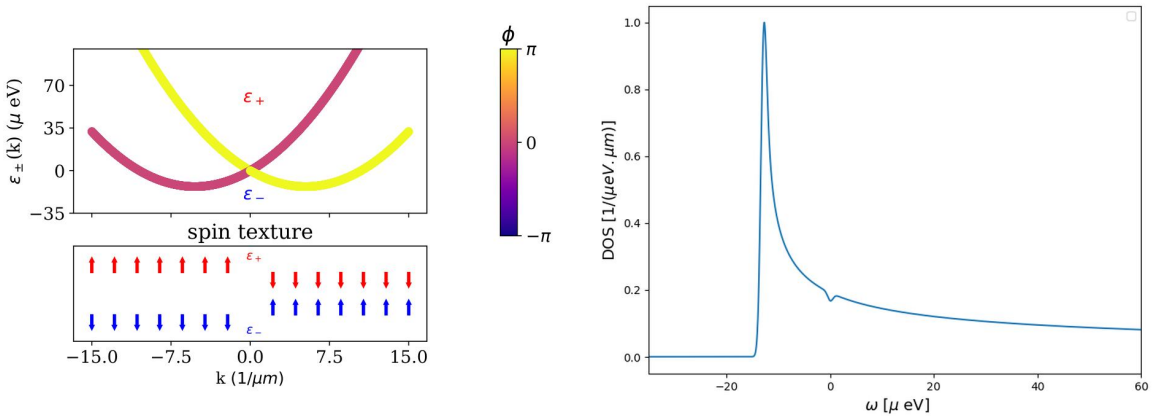

Figure 5.4: Band structure (left) as a function of k and normalized density of states (right) and spin texture (bottom panel) for the SM nanowire with spin-orbit coupling of strength $\alpha\hbar = 5\mu$eV. μm. Note that the ϵ_- band is the lower pink line for negative k, and continues as the yellow line for positive k, whereas the ϵ_+ band is the top yellow one for negative k, and pink for positive k.

unitary transformation. However, the spin texture changes: it now lies in the yz-plane instead of the xy-plane, acquiring no component along x. Hence, all spin-related interpretations previously made with respect to the x-axis will now correspond to the z-axis. Conclusively, the direction of the magnetic field (either along the x or z axis) does not alter the underlying physics of the system, but rather represents a convenient convention chosen for experimental or numerical purposes.

5.2.5 Complete band Structure with the S-wave Superconductor

Now that we have studied all the elements of the SM nanowire, we include the s-wave superconductivity and calculate the band structure. Starting from Eq. (5.22), we introduce the Nambu operator $\mathbf{c}_k = (c_{k\uparrow}, c_{k\downarrow})^\mathsf{T}$, which allows us to use the identity $c_{k,\uparrow}c_{-k,\downarrow} = \frac{1}{2}\,\mathbf{c}_k^\mathsf{T}(i\sigma_y)\mathbf{c}_{-k}$. The SC Hamiltonian can be expressed in matrix form as

$$\hat{H}_{\text{SC}} = \frac{1}{2}\sum_k \left[\mathbf{c}_k^\dagger\,(\Delta\, i\sigma_y)\,\mathbf{c}_{-k}^{\dagger\mathsf{T}} + \mathbf{c}_{-k}^\mathsf{T}\,(-\Delta\, i\sigma_y)\,\mathbf{c}_k\right]. \tag{5.60}$$

We now define the four-component Nambu spinor

$$C_k^\dagger = \left[c_{k\uparrow}^\dagger,\ c_{k\downarrow}^\dagger,\ c_{-k\uparrow},\ c_{-k\downarrow}\right], \tag{5.61}$$

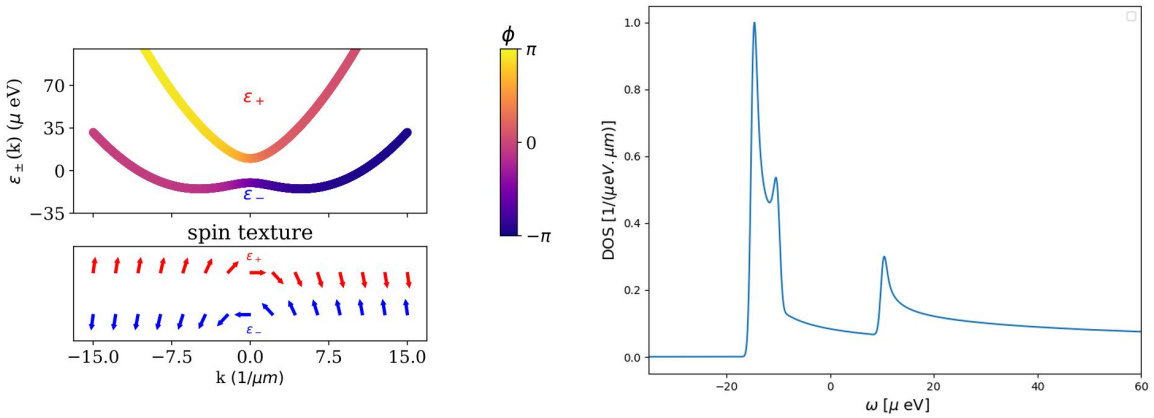

Figure 5.5: Band structure (left) as a function of k and normalized density of states (right) and spin texture (bottom panel) for the SM nanowire with Zeeman field of strength 10 μeV and $\alpha\hbar = 5\,\mu$eV. μm.

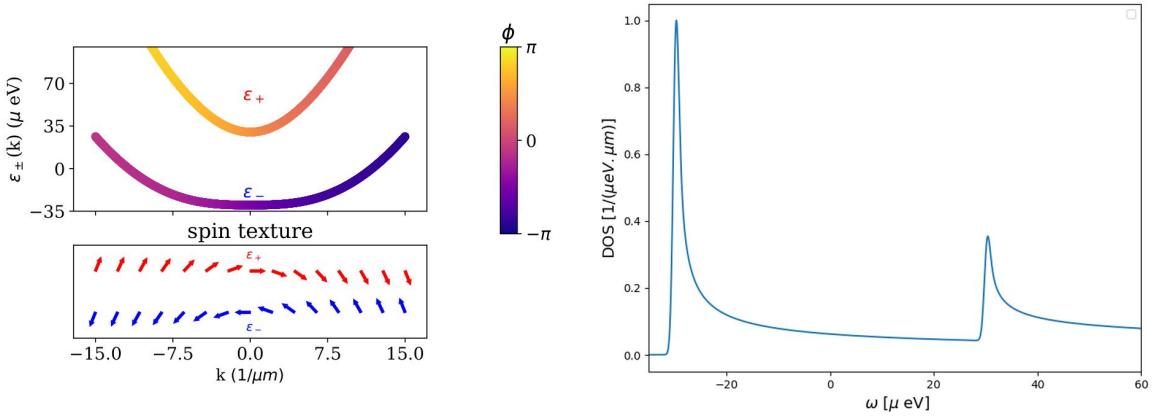

Figure 5.6: Band structure (left) as a function of k and normalized density of states (right) and spin texture (bottom panel) for the SM nanowire with Zeeman field of strength 30 μeV and $\alpha\hbar = 5\,\mu$eV. μm.

and write the semiconductor Hamiltonian kernel from Eq. (5.23) as

$$\hat{H}_{\mathrm{SM}}(k) = \left(\frac{\hbar^2 k^2}{2m^\star} - \mu\right)\mathbb{I}_2 - \alpha\hbar k\,\sigma_y + V_z\,\sigma_x. \tag{5.62}$$

Then the total Hamiltonian including both the semiconductor and superconductor contributions becomes

$$\hat{\mathcal{H}}_{\mathrm{BdG}}(k) = \frac{1}{2}\sum_k C_k^\dagger \begin{pmatrix} H_{\mathrm{SM}}(k) & -i\Delta^*\sigma_y \\ i\Delta\sigma_y & -H_{\mathrm{SM}}^*(-k) \end{pmatrix} C_k + T_k, \tag{5.63}$$

where $T_k = \frac{\hbar^2 k^2}{2m^\star} - \mu$ is the constant shift term arising from fermionic commutation

relations such as $c^{\dagger}_{\sigma,k}c_{\sigma,k} = \frac{1}{2}\big(1 + c^{\dagger}_{\sigma,k}c_{\sigma,k} - c_{\sigma,k}c^{\dagger}_{\sigma,k}\big)$. The explicit form of the 4×4 matrix is given by

$$\begin{pmatrix} T_k & V_z + i\alpha\hbar k & 0 & \Delta \\ V_z - i\alpha\hbar k & T_k & -\Delta & 0 \\ 0 & -\Delta^* & -T_k & -(V_z + i\alpha\hbar k) \\ \Delta^* & 0 & -(V_z - i\alpha\hbar k) & -T_k \end{pmatrix}. \tag{5.64}$$

We will now show that this Hamiltonian conserves the particle-hole symmetry. The particle–hole conjugation operator $\mathcal{C}$ is defined as an antiunitary operator acting on the Nambu spinor as

$$\mathcal{C}C_k\,\mathcal{C}^{-1} = \tau_x\,C^*_{-k}, \qquad \mathcal{C}C^{\dagger}_k\,\mathcal{C}^{-1} = C^{\mathsf{T}}_{-k}\tau_x, \tag{5.65}$$

where τ_x is the Pauli matrix acting in particle–hole (Nambu) space. If we show the complex conjugation of the coefficients by the operator $\mathcal{K}$, the particle–hole operator becomes

$$\mathcal{C} = \tau_x\,\mathcal{K}, \qquad \mathcal{C}^2 = +1. \tag{5.66}$$

Under this operation, the BdG kernel transforms as

$$\begin{aligned} \mathcal{C}\,\hat{\mathcal{H}}_{\mathrm{BdG}}(k)\,\mathcal{C}^{-1} &= \tau_x\hat{\mathcal{H}}^*_{\mathrm{BdG}}(k)\tau_x \\ &= \tau_x \begin{pmatrix} \hat{H}^*_{\mathrm{SM}}(k) & i\Delta\sigma_y \\ -i\Delta^*\sigma_y & -\hat{H}_{\mathrm{SM}}(-k) \end{pmatrix} \tau_x. \end{aligned} \tag{5.67}$$

Using the property $\tau_x\left(\begin{smallmatrix} A & B \\ C & D \end{smallmatrix}\right)\tau_x = \left(\begin{smallmatrix} D & C \\ B & A \end{smallmatrix}\right)$, one finds

$$\mathcal{C}\,\hat{\mathcal{H}}_{\mathrm{BdG}}(k)\,\mathcal{C}^{-1} = \begin{pmatrix} -\hat{H}_{\mathrm{SM}}(-k) & -i\Delta^*\sigma_y \\ i\Delta\sigma_y & \hat{H}^*_{\mathrm{SM}}(k) \end{pmatrix} = -\,\hat{\mathcal{H}}_{\mathrm{BdG}}(-k). \tag{5.68}$$

Equation (5.68) shows that the BdG Hamiltonian satisfies the fundamental particle–hole symmetry condition

$$\boxed{\mathcal{C}\,\mathcal{H}_{\mathrm{BdG}}(k)\,\mathcal{C}^{-1} = -\,\mathcal{H}_{\mathrm{BdG}}(-k)}. \tag{5.69}$$

Although the kernel changes sign, the full Hamiltonian

$$\hat{H} = \frac{1}{2}\sum_k C^{\dagger}_k\hat{\mathcal{H}}_{\mathrm{BdG}}(k)C_k + T_k$$

remains invariant under $\mathcal{C}$ because the spinor transforms as in Eq. (5.65):

$$\begin{aligned}\mathcal{C}\hat{H}\,\mathcal{C}^{-1} &= \frac{1}{2}\sum_k (\mathcal{C}C_k^\dagger\mathcal{C}^{-1})(\mathcal{C}\hat{\mathcal{H}}_{\mathrm{BdG}}(k)\mathcal{C}^{-1})(\mathcal{C}C_k\mathcal{C}^{-1}) + T_k \\ &= \frac{1}{2}\sum_k C_{-k}^{\mathsf{T}}\tau_x\Big[-\hat{\mathcal{H}}_{\mathrm{BdG}}(-k)\Big]\tau_x C_{-k}^* + T_k \\ &= \frac{1}{2}\sum_{-k} C_{-k}^\dagger\hat{\mathcal{H}}_{\mathrm{BdG}}(-k)C_{-k} + T_k = \hat{H}. \end{aligned} \tag{5.70}$$

Thus, despite the minus sign in Eq. (5.69), the total Hamiltonian is invariant under $\mathcal{C}$. Note that T_k remains the same under the transformation. This symmetry guarantees that the quasiparticle spectrum satisfies $E_n(k) = -E_n(-k)$, leading to eigenvalue pairs $\pm E_n(k)$. From the particle–hole symmetry condition in Eq. (5.69), every eigenstate Φ_k of $\hat{\mathcal{H}}_{\mathrm{BdG}}(k)$ with energy E_k has a corresponding conjugate state $\mathcal{C}\Phi_k$ that is an eigenstate of $-\hat{\mathcal{H}}_{\mathrm{BdG}}(-k)$ with energy $-E_k$:

$$\hat{\mathcal{H}}_{\mathrm{BdG}}(k)\,\Phi_k = E_k\,\Phi_k \quad\Longrightarrow\quad \hat{\mathcal{H}}_{\mathrm{BdG}}(-k)\,(\mathcal{C}\Phi_k) = -E_k\,(\mathcal{C}\Phi_k). \tag{5.71}$$

Thus, all quasiparticle excitations come in pairs at $\pm E_k$. However, when the system parameters (for instance the Zeeman field V_z) are tuned such that one of these energy pairs satisfies $E_k = 0$, the corresponding state is its own particle–hole conjugate. Indeed, for $E = 0$, the eigenvector Φ_0 satisfies

$$\hat{\mathcal{H}}_{\mathrm{BdG}}(k)\,\Phi_0 = 0. \tag{5.72}$$

Applying the $\mathcal{C}$ operator to both sides gives

$$\mathcal{C}\,\hat{\mathcal{H}}_{\mathrm{BdG}}(k)\,\Phi_0 = 0. \tag{5.73}$$

Using the commutation relation $\mathcal{C}\,\hat{\mathcal{H}}_{\mathrm{BdG}}(k) = -\hat{\mathcal{H}}_{\mathrm{BdG}}(-k)\,\mathcal{C}$ (from Eq. (5.68)), we obtain

$$-\hat{\mathcal{H}}_{\mathrm{BdG}}(-k)\,(\mathcal{C}\Phi_0) = 0 \quad\Rightarrow\quad \hat{\mathcal{H}}_{\mathrm{BdG}}(-k)\,(\mathcal{C}\Phi_0) = 0. \tag{5.74}$$

This means $\mathcal{C}\Phi_0$ is also a zero-energy eigenstate. Since the zero-energy eigenspace may be degenerate, we write

$$\mathcal{C}\Phi_0 = \lambda\,\Phi_0 \tag{5.75}$$

for some eigenvalue λ. Applying $\mathcal{C}$ again and using $\mathcal{C}^2 = +1$:

$$\Phi_0 = \mathcal{C}(\mathcal{C}\Phi_0) = \mathcal{C}(\lambda\,\Phi_0) = \lambda^*\,(\mathcal{C}\Phi_0) = \lambda^*\lambda\,\Phi_0. \tag{5.76}$$

Therefore $|\lambda|^2 = 1$, implying $\lambda = e^{i\varphi}$ for some real phase angle φ. This yields

$$\mathcal{C}\Phi_0 = e^{i\varphi}\Phi_0. \tag{5.77}$$

The zero-energy state is thus its own particle–hole conjugate (up to a phase). This is the same self-conjugacy we met in Chapter 2. There the Majorana condition $\psi = \psi_c$ in Eq. (5.72) states that a Majorana field equals its own charge conjugate, and the operator form $\gamma = \gamma^\dagger$ in Eq. (4.83) states that a Majorana mode is its own antiparticle. We obtained the same statement from the BdG formalism of the SM-SC Hamiltonian.

Physically, this symmetry reflects the fact that a quasiparticle excitation with energy E above the Fermi level is indistinguishable from a missing quasiparticle (a hole) with energy $-E$ below it [159]. The ground state of the superconductor—the condensate of Cooper pairs—defines the reference point $E = 0$, around which these excitations are symmetric. Consequently, the BdG Hamiltonian effectively "doubles" the number of modes compared to the normal-state Hamiltonian, but this redundancy is constrained by particle-hole symmetry: the particle and hole sectors are not independent [160].

In topological superconductors, this intrinsic particle–hole symmetry plays a central role: at certain parameter values the gap can close and reopen, yielding zero-energy modes that are their own particle–hole conjugates, as we saw earlier when we introduced the s-wave superconductivity [49, 50, 166–168] . We will see this explicitly in the band structure of the SM-SC system.

Because of particle-hole symmetry, the eigenvalues occur in $\pm E$ pairs. To find the band energies, we solve the eigenvalue problem $\hat{\mathcal{H}}_{\mathrm{BdG}}(k)\,\Phi_k = E\,\Phi_k$, whose eigenvalues are the roots of the secular equation $\det\!\left[\hat{\mathcal{H}}_{\mathrm{BdG}}(k) - E\,\mathbb{1}\right] = 0$. Using the compact form

$$\hat{\mathcal{H}}_{\mathrm{BdG}}(k) = T_k\,\tau_z + \alpha\hbar k\,\sigma_y\tau_z + V_z\,\sigma_x + \Delta\,\tau_x,$$

this gives the characteristic polynomial

$$E^4 - 2A_kE^2 + B_k = 0,$$

with

$$A_k = T_k^2 + (\alpha\hbar k)^2 + V_z^2 + |\Delta|^2, \tag{5.78}$$

$$B_k = A_k^2 - 4C_k, \tag{5.79}$$

$$C_k = T_k^2\Big((\alpha\hbar k)^2 + V_z^2\Big) + |\Delta|^2 V_z^2. \tag{5.80}$$

Only even powers of E appear, which is the particle-hole symmetry at work. The equation is therefore quadratic in E^2, and solving it gives the two positive branches

$$E_\pm^2(k) = A_k \pm \sqrt{A_k^2 - B_k} = A_k \pm 2\sqrt{C_k}.$$

Hence the band energies are

$$E_\pm(k) = \sqrt{T_k^2 + (\alpha\hbar k)^2 + V_z^2 + |\Delta|^2 \;\pm\; 2\sqrt{T_k^2\Big((\alpha\hbar k)^2 + V_z^2\Big) + |\Delta|^2 V_z^2}}\ , \tag{5.81}$$

and the remaining two are their particle-hole partners $-E_\pm(k)$.

We can check that when $\Delta \to 0$: $E_\pm(k) = \Big|\, T_k \pm \sqrt{(\alpha\hbar k)^2 + V_z^2}\,\Big|$ it gives the SM bands. Now we are in a position to show how adding the superconductivity term will open the superconducting gap, as was promised to show in figure 5.1.

5.2.6 Superconducting Gap and Topological Phase Transition

The three panels in Fig. 5.7 show the evolution of the quasiparticle band structure obtained from Eq. (5.81) as the Zeeman field V_z is varied. The key feature that distinguishes the trivial and topological superconducting phases is the behaviour of the energy gap at $k = 0$. At this point, the kinetic and spin–orbit terms vanish ($T_0 = -\mu$, $\alpha\hbar k = 0$), leading to

$$E_\pm(0) = \Big|\, V_z \pm \sqrt{\mu^2 + |\Delta|^2}\,\Big|. \tag{5.82}$$

The lower branch $E_-(0)$ thus closes when

$$V_z^{\mathrm{c}} = \sqrt{\mu^2 + |\Delta|^2}, \tag{5.83}$$

which marks the critical point of a **topological quantum phase transition**.

In case (a), we apply a Zeeman field smaller than the critical value $V_z < \sqrt{\mu^2 + |\Delta|^2}$. The system is in a conventional s-wave superconducting phase, characterized by a finite energy gap of size $2|\Delta|$ that separates the occupied and unoccupied quasiparticle states. Both spin subbands are degenerate, and the lowest positive-energy branch

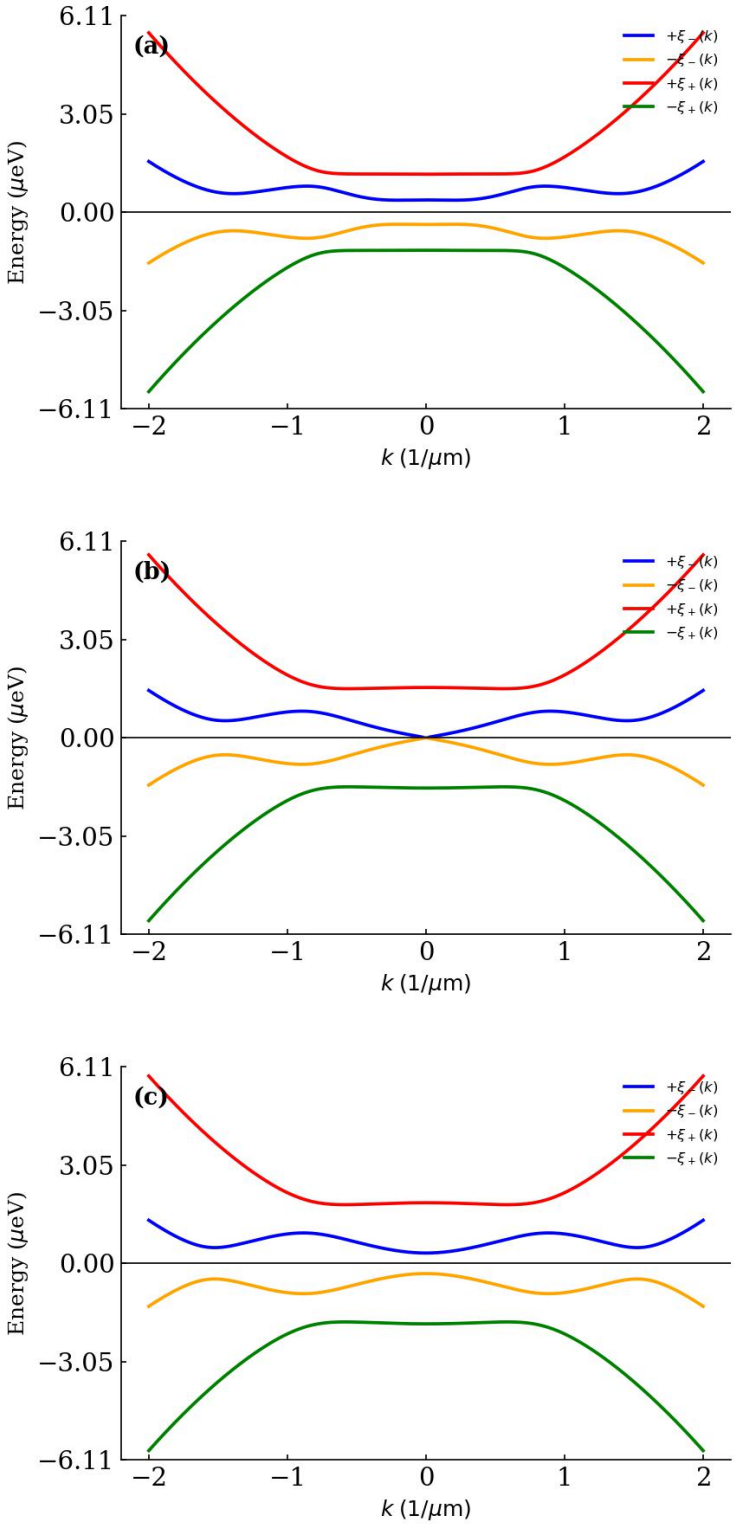

Figure 5.7: BdG band structure from Eq. (5.81) for $\mu = 0.5\,\mu$eV, $\alpha\hbar = 5\,\mu$eV. μm, and $\Delta = 0.6\,\mu$ eV. Top: gapped spectrum for $V_z < \sqrt{\mu^2 + \Delta^2}$. This system is in the trivial phase. Middle: gap closing at $V_z = \sqrt{\mu^2 + \Delta^2}$. This is where the topological phase transition occurs. Bottom: gapped spectrum for $V_z > \sqrt{\mu^2 + \Delta^2}$. This system is in the topological phase.

$\pm E_-(k)$ remains gapped for all k. Particle-hole symmetry is clearly preserved: the red and blue bands ($+E_\pm(k)$) are exact reflections of the yellow and green bands ($-E_+(k)$) about the zero energy line, respectively. Similarly, the blue band ($+E_-(k)$) mirrors the orange band ($-E_-(k)$). Although the spectrum is gapped, no topological order is present. For $V_z < V_z^c$ the Zeeman splitting is insufficient to invert the two spin-split parabolic bands at $k = 0$. The order of the occupied and unoccupied states remains the same as in the normal state: the lower band is predominantly spin-down and the upper band is predominantly spin-up (or vice versa, depending on convention). Thus, the energy gap visible in panel (a) is a conventional s-wave superconducting gap, not a topological one. We refer to this regime as the trivial regime or phase.

At the critical field, shown in Fig. 5.7 (b), the Zeeman energy exactly compensates the energy scale that maintains the separation between the two spin-split subbands. As a result, the two lowest quasiparticle branches $\pm E_-(k)$ touch each other at $k = 0$, and the bulk superconducting gap closes. This is the precise point where the superconducting spectrum switches from trivial to topological. Physically, the closing of the gap means that the lowest electron-like and hole-like states at $k = 0$ become degenerate in energy. The spin character of the bands begins to interchange: the state that used to belong to the lower band moves upward in energy, while the one that belonged to the upper band moves downward. This marks the onset of a band inversion. At this critical field the system is extremely sensitive to perturbations. A tiny increase or decrease of V_z immediately opens a new gap, but with a different character: for V_z slightly smaller than the critical value, the gap is still the ordinary s-wave gap of the trivial phase, whereas for V_z slightly larger, the gap reopens after the inversion, signaling the topological regime. Therefore, the gap-closing point represents the boundary between two qualitatively different superconducting states. In a finite nanowire, this is the parameter point where Majorana modes start to emerge at the ends of the system as the topological phase sets in.

In Fig. 5.7 (c), the Zeeman field exceeds the critical value, $V_z > \sqrt{\mu^2 + |\Delta|^2}$. The superconducting gap that had closed at the transition point now reopens, but with a completely different character. This reopened gap marks the onset of the topological superconducting phase. The most important change occurs in the structure of the bands near $k = 0$. After the transition, the order of the two lowest energy bands is reversed compared to the trivial phase (the previously two flat lines are now replaced by two symmetric parabolas): the state that was previously above the Fermi level now lies below it, and vice versa. This band inversion is the key signature that the system has changed its topological character [36, 177–180]. The quasiparticle wavefunctions

on either side of the inversion carry different spin textures, so the reopened gap does not simply correspond to the same s-wave pairing as before—it now has a built-in spin–momentum locking that mimics an effective spinless p-wave superconductor [56, 166]. Figure 5.8 makes this explicit. The colour gives the electron-sector spin of each band. The component $\langle\sigma_y\rangle$ is odd in k, which is the Rashba spin-momentum locking. Across the transition the lowest band at $k = 0$ flips its $\langle\sigma_x\rangle$ from negative to positive, the spin signature of the band inversion. Although the bulk remains gapped, the nature of this new gap is topologically distinct from the ordinary s-wave gap in panel (a). If the nanowire were cut open, the bulk–boundary correspondence ensures that a pair of localized zero-energy states would appear at its ends [44, 167]. These states are protected by the reopened bulk gap and cannot be removed by any local perturbation unless the bulk gap closes again [32, 168].

5.3 Discrete lattice Formulation with Open Boundary Conditions

To analyze finite-size effects and study the emergence of localized edge states, it is useful to move from the continuous k-space description of the SM-SC nanowire to a discrete real-space (tight-binding) representation [50, 166–168] . We will do this in two ways. First, through representing the continuous Hamiltonian in the orbital mode formalism, where we expand each field operator in the basis of a 1D quantum well. And second, the nanowire is modeled as a one-dimensional chain of sites indexed by $j = 1, \ldots, N$, hosting spinful electron operators $c_{j,\sigma}, c^\dagger_{j,\sigma}$, for $\sigma = \uparrow, \downarrow$. The continuous derivatives and momentum-dependent terms in the Hamiltonian are replaced by discrete hopping terms between neighbouring lattice sites. The second approach naturally allows the imposition of open boundary conditions (OBC), which are essential for capturing boundary physics such as the appearance of Majorana zero modes at the nanowire ends. Moreover, the lattice representation provides a convenient framework for numerical diagonalization and for connecting the continuum parameters (μ, α, V_z, Δ, $m^\star$) to experimentally relevant discrete energy scales such as hopping amplitudes and on-site potentials [50, 114, 166–168] . In the following, we construct the tight-binding version of the SM–SC Hamiltonian that faithfully reproduces the continuum model in the long-wavelength limit, and explicitly implement open boundary conditions to reveal the real-space structure of the topological superconducting phase.

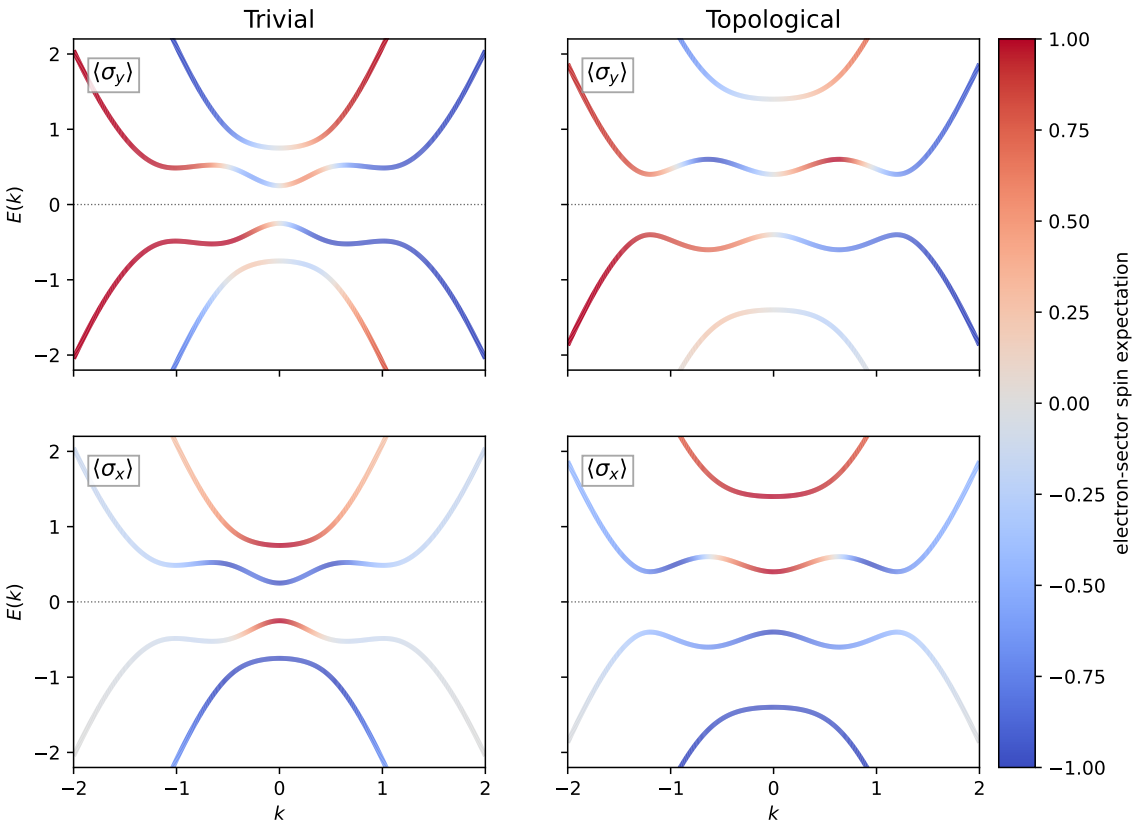

Figure 5.8: Electron-sector spin texture of the Bogoliubov-de Gennes bands of the SM-SC nanowire, in the trivial phase (left) and the topological phase (right). The top row colours each band by $\langle\sigma_y\rangle$ and the bottom row by $\langle\sigma_x\rangle$. The colour is the spin of the electron component of each quasiparticle, normalised by its electron weight. The odd-in-k pattern of $\langle\sigma_y\rangle$ is the Rashba spin-momentum locking. At $k = 0$ the lowest band flips its $\langle\sigma_x\rangle$ from negative in the trivial phase to positive in the topological phase, which is the spin signature of the band inversion. The parameters are $\alpha = 1$, $\Delta = 0.5$, and $\mu = 0$ in units $\hbar = 2m^* = 1$, with V_z below and above $V_z^c = \sqrt{\mu^2 + |\Delta|^2}$.

5.3.1 Orbital Mode Representation

We now rewrite the continuum SM-SC Hamiltonian in a basis suited to a finite nanowire. The wire has length L, so the electrons are confined to the interval $x \in [0, L]$. With open boundary conditions the wavefunction vanishes at both ends. This confinement is a one-dimensional quantum well, or particle in a box. Its single-particle eigenstates are the standing waves

$$\Phi_n(x) = \sqrt{\frac{2}{L}}\,\sin(k_n x), \qquad k_n = \frac{n\pi}{L}, \qquad n = 1, 2, \ldots, \tag{5.84}$$

satisfying

$$\int_0^L dx\,\Phi_n(x)\Phi_m(x) = \frac{2}{L}\int_0^L dx\,\sin(k_m x)\sin(k_n x)$$

$$= \frac{2}{L}\left(\frac{1}{2} - \frac{\sin(2\pi n)}{4\pi n}\right)L = 1, \quad m = n = 1, 2, \ldots \tag{5.85}$$

$$= \frac{2}{L}\cdot\frac{n\sin(m\pi)\cos(n\pi) - m\sin(n\pi)\cos(m\pi)}{\pi(m^2 - n^2)}\cdot L = 0, \quad m \neq n \tag{5.86}$$

which yields

$$\int_0^L dx\,\Phi_n\Phi_m = \delta_{nm} \tag{5.87}$$

We expand the field operators in this basis

$$\psi_\sigma(x) = \sum_{n\geq 1} c_{n,\sigma}\,\Phi_n(x)\chi_z^\sigma, \tag{5.88}$$

where $c_{n,\sigma}$ annihilates a fermion with spin $\sigma \in \{\uparrow, \downarrow\}$ in mode n, and χ_z^σ are the eigenstates of Pauli z-matrix, i.e. $\sigma_z\chi_z^{\uparrow(\downarrow)} = +(-)\chi_z^{\uparrow(\downarrow)}$.

We now rewrite the entire SM-SC Hamiltonian in the orbital mode basis

$$\hat{H}_{\text{SM}} = \int_0^L dx\,\psi^\dagger(x)\Big[-\frac{\hbar^2}{2m^\star}\partial_x^2 - \mu + i\alpha\hbar\,\sigma_y\,\partial_x + V_z\,\sigma_x\Big]\psi(x), \tag{5.89}$$

$$\hat{H}_{\text{SC}} = \int_0^L dx\,\Big(\Delta\,\psi_\uparrow(x)\psi_\downarrow(x) + \text{h.c.}\Big), \tag{5.90}$$

with $\psi = (\psi_\uparrow, \psi_\downarrow)^T$, and real, uniform Δ for clarity (phase may be reinstated as

needed). Using (5.84)–(5.88) one needs the overlap matrices

$$\int_0^L dx\,\Phi_n(x)\Phi_m(x) = \delta_{nm}, \tag{5.91}$$

$$\begin{aligned}\int_0^L dx\,\Phi_n(x)\,\partial_x\Phi_m(x) &= \frac{2}{L}\,k_m\int_0^L dx\,\sin(k_n x)\cos(k_m x)\\ &= \begin{cases} 0, & n = m \pmod 2,\\ \dfrac{4\,n\,k_m}{\pi\,(m^2-n^2)}, & n \neq m \pmod 2,\end{cases}\end{aligned} \tag{5.92}$$

so the second integral vanishes when n and m have the same parity and is nonzero otherwise, making a selection rule for Rashba SOC term.

Kinetic, chemical, and Zeeman terms. The kinetic operator is diagonal in n:

$$\int_0^L dx\,\Phi_n(x)\Big(-\frac{\hbar^2}{2m^\star}\partial_x^2\Big)\Phi_m(x) = \delta_{nm}\,\frac{\hbar^2 k_n^2}{2m^\star}. \tag{5.93}$$

Hence

$$\hat{H}_0 = \sum_{n\geq 1}\sum_{\sigma}\Big(\frac{\hbar^2 k_n^2}{2m^\star} - \mu\Big)c_{n,\sigma}^\dagger c_{n,\sigma}. \tag{5.94}$$

The Zeeman term $V_z\,\sigma_x$ is on–site in n and flips spin:

$$V_z\sum_{n\geq 1}\Big(c_{n,\uparrow}^\dagger c_{n,\downarrow} + c_{n,\downarrow}^\dagger c_{n,\uparrow}\Big). \tag{5.95}$$

Collecting these, the n–diagonal block in the spin basis $(c_{n,\uparrow}, c_{n,\downarrow})$ is

$$\begin{pmatrix} c_{n,\uparrow}^\dagger & c_{n,\downarrow}^\dagger\end{pmatrix}\begin{bmatrix}\dfrac{\hbar^2 k_n^2}{2m^\star} - \mu & V_z\\ V_z & \dfrac{\hbar^2 k_n^2}{2m^\star} - \mu\end{bmatrix}\begin{bmatrix} c_{n,\uparrow}\\ c_{n,\downarrow}\end{bmatrix}. \tag{5.96}$$

Rashba spin–orbit coupling. Using (5.92), the SOC matrix elements are

$$\begin{aligned}\hat{H}_{\mathrm{SO}} &= i\alpha\hbar\sum_{n,m}\sum_{\sigma,\sigma'} c_{n,\sigma}^\dagger\,(\sigma_y)_{\sigma\sigma'}\,c_{m,\sigma'}\int_0^L dx\,\Phi_n\,\partial_x\Phi_m\\ &= \sum_{\substack{n,m\geq 1\\ n\not\equiv m\,(\mathrm{mod}\,2)}}\frac{4\alpha\hbar\,m\,n}{(m^2-n^2)\,L}\Big(c_{n,\uparrow}^\dagger c_{m,\downarrow} - c_{n,\downarrow}^\dagger c_{m,\uparrow} + \mathrm{h.c.}\Big).\end{aligned} \tag{5.97}$$

The sign structure follows from $\sigma_y = \left(\begin{smallmatrix}0 & -i\\ i & 0\end{smallmatrix}\right)$. Equation (5.97) shows explicitly the inter–mode nature of SOC under OBC and its parity selection rule.

Superconducting Term And lastly, the superconducting term is written as

$$\hat{H}_{\mathrm{SC}} = \int_0^L dx \left(\Delta \, \psi_\uparrow \psi_\downarrow + \mathrm{h.c.} \right) = \sum_{n \geq 1} \left(\Delta \, c_{n,\uparrow} c_{n,\downarrow} + \Delta \, c_{n,\downarrow}^\dagger c_{n,\uparrow}^\dagger \right), \tag{5.98}$$

since $\int_0^L \Phi_n \Phi_m = \delta_{nm}$.

Putting everything together,

$$\begin{aligned} \hat{H}_{\mathrm{SM}} &= \sum_{n \geq 1} \begin{pmatrix} c_{n,\uparrow}^\dagger & c_{n,\downarrow}^\dagger \end{pmatrix} \begin{bmatrix} \varepsilon_n & h \\ h & \varepsilon_n \end{bmatrix} \begin{bmatrix} c_{n,\uparrow} \\ c_{n,\downarrow} \end{bmatrix} \\ &\quad + \sum_{\substack{n,m \geq 1 \\ n \not\equiv m \, (\mathrm{mod}\ 2)}} \frac{4\alpha\hbar \, m \, n}{(m^2 - n^2) \, L} \left(c_{n,\uparrow}^\dagger c_{m,\downarrow} - c_{n,\downarrow}^\dagger c_{m,\uparrow} + \mathrm{h.c.} \right), \end{aligned} \tag{5.99}$$

$$\hat{H}_{\mathrm{SC}} = \sum_{n \geq 1} \left(\Delta \, c_{n,\uparrow} c_{n,\downarrow} + \Delta \, c_{n,\downarrow}^\dagger c_{n,\uparrow}^\dagger \right), \tag{5.100}$$

with single–particle level energies

$$\varepsilon_n = \frac{\hbar^2 k_n^2}{2m^\star} - \mu = \frac{\hbar^2}{2m^\star} \left(\frac{n\pi}{L} \right)^2 - \mu. \tag{5.101}$$

Equations (5.99)–(5.100) are the desired orbital representation of the SM–SC Hamiltonian under OBC.

For numerical simulations it is convenient to scale energies by the Rydberg energy

$$E_{\mathrm{Ry}} = \frac{\hbar^2}{2m^\star a^2}, \tag{5.102}$$

where a is a chosen length in units of angstrom. We now introduce the dimensionless parameters represented by tildes

$$\tilde{L} = \frac{L}{a}, \quad \tilde{\mu} = \frac{\mu}{E_{\mathrm{Ry}}}, \quad \tilde{V}_z = \frac{V_z}{E_{\mathrm{Ry}}}, \quad \tilde{\Delta} = \frac{\Delta}{E_{\mathrm{Ry}}}, \quad \tilde{\alpha} = \frac{2m^\star a}{\hbar} \, \alpha, \tag{5.103}$$

so that

$$\frac{\hbar^2 k_n^2}{2m^\star} = E_{\mathrm{Ry}} \frac{(n\pi)^2}{\tilde{L}^2}, \qquad \frac{4\alpha\hbar \, m \, n}{(m^2 - n^2) \, L} = E_{\mathrm{Ry}} \frac{4 \, mn \, \tilde{\alpha}}{(m^2 - n^2) \, \tilde{L}}. \tag{5.104}$$

Dividing $H_{\rm SM}+H_{\rm SC}$ by $E_{\rm Ry}$, one obtains

$$\tilde{H}_{\rm SM}=\sum_{n\geq 1}\sum_{\sigma}\Big(\frac{(n\pi)^2}{\tilde{L}^2}-\tilde{\mu}\Big)c^{\dagger}_{n,\sigma}c_{n,\sigma}+\tilde{V}_z\sum_{n\geq 1}\Big(c^{\dagger}_{n,\uparrow}c_{n,\downarrow}+c^{\dagger}_{n,\downarrow}c_{n,\uparrow}\Big)$$
$$+\sum_{\substack{n,m\geq 1\\ n\not\equiv m\,(\mathrm{mod}\,2)}}\frac{4\,mn\,\tilde{\alpha}}{(m^2-n^2)\,\tilde{L}}\Big(c^{\dagger}_{n,\uparrow}c_{m,\downarrow}-c^{\dagger}_{n,\downarrow}c_{m,\uparrow}+\text{h.c.}\Big), \tag{5.105}$$

$$\tilde{H}_{\rm SC}=\sum_{n\geq 1}\Big(\tilde{\Delta}\,c_{n,\uparrow}c_{n,\downarrow}+\tilde{\Delta}\,c^{\dagger}_{n,\downarrow}c^{\dagger}_{n,\uparrow}\Big), \tag{5.106}$$

with $\tilde{H}_{\rm SM}=\frac{H_{\rm SM}}{E_{\rm Ry}}$ and $\tilde{H}_{\rm SC}=\frac{H_{\rm SC}}{E_{\rm Ry}}$. Equations (5.105)–(5.106) are the mode–space Hamiltonian in fully dimensionless form. Since each level can be occupied by up to two electrons with different spins, a system of n levels will have $2^{2N}=4^N$ configurations.

5.3.2 Lattice (site) Representation

Now we obtain a second-quantized lattice Hamiltonian in terms of fermionic operator $c_{i,\sigma}$ ($c^{\dagger}_{i,\sigma}$) that annihilates (creates) an electron with spin $\sigma=\uparrow,\downarrow$ on site (or dot) $i=1,\ldots,N$. We discretize the wire into N sites with lattice spacing a:

$$x_i=ia,\qquad i=1,\ldots,N,\qquad L=Na.$$

To preserve the fermionic anti-commutation relations, we define

$$\psi_\sigma(x_i)\;=\;\frac{1}{\sqrt{a}}\,c_{i\sigma},\qquad \psi^{\dagger}_\sigma(x_i)\;=\;\frac{1}{\sqrt{a}}\,c^{\dagger}_{i\sigma}, \tag{5.107}$$

so that $\{\psi_\sigma(x),\psi^{\dagger}_{\sigma'}(x')\}=\delta_{\sigma\sigma'}\delta(x-x')$ is mapped to $\{c_{i\sigma},c^{\dagger}_{j\sigma'}\}=\delta_{ij}\delta_{\sigma\sigma'}$.

The spatial integral is replaced by a sum,

$$\int_0^L dx\;f(x)\;\to\;a\sum_{i=1}^{N}f(x_i). \tag{5.108}$$

Spatial derivatives are approximated by finite differences:

$$\partial_x\psi_\sigma(x_i)\approx\frac{\psi_\sigma(x_{i+1})-\psi_\sigma(x_{i-1})}{2a}, \tag{5.109}$$

$$\partial_x^2\psi_\sigma(x_i)\approx\frac{\psi_\sigma(x_{i+1})-2\psi_\sigma(x_i)+\psi_\sigma(x_{i-1})}{a^2}. \tag{5.110}$$

We impose OBC: there are no sites beyond 1 and N, so terms involving $i=0$ or

$i = N + 1$ are simply omitted.

Kinetic energy and chemical potential

We first consider the kinetic plus chemical potential part, since they have the same functionality

$$H_0 = \int_0^L dx\ \psi^\dagger(x) \left(-\frac{\hbar^2}{2m^\star} \partial_x^2 - \mu \right) \psi(x). \tag{5.111}$$

Discretizing using Eq.(5.108)–(5.110) and Eq.(5.107):

$$\begin{aligned} H_0 &\approx a \sum_{i,\sigma} \frac{1}{a}\, c_{i\sigma}^\dagger \left[-\frac{\hbar^2}{2m^\star} \frac{\psi_\sigma(x_{i+1}) - 2\psi_\sigma(x_i) + \psi_\sigma(x_{i-1})}{a^2} - \mu \psi_\sigma(x_i) \right] \\ &= \sum_{i,\sigma} \left[-\frac{\hbar^2}{2m^\star a^2} \Big(c_{i\sigma}^\dagger c_{i+1\sigma} + c_{i\sigma}^\dagger c_{i-1\sigma} - 2 c_{i\sigma}^\dagger c_{i\sigma} \Big) - \mu\, c_{i\sigma}^\dagger c_{i\sigma} \right]. \end{aligned} \tag{5.112}$$

For the second term, relabel $i \to i - 1$ in $\sum_i c_{i\sigma}^\dagger c_{i-1\sigma}$ gives

$$\sum_i c_{i\sigma}^\dagger c_{i-1\sigma} = \sum_{i'} c_{i'-1\sigma}^\dagger c_{i',\sigma} = \sum_i c_{i-1\sigma}^\dagger c_{i\sigma} = \sum_i c_{i\sigma}^\dagger c_{i-1\sigma} + \text{h.c.} \tag{5.113}$$

Grouping the kinetic energy terms symmetrically gives

$$-\frac{\hbar^2}{2m^\star a^2} \Big(c_{i\sigma}^\dagger c_{i+1\sigma} + c_{i\sigma}^\dagger c_{i-1\sigma} \Big) = -t \Big(c_{i+1\sigma}^\dagger c_{i\sigma} + c_{i\sigma}^\dagger c_{i+1\sigma} \Big), \tag{5.114}$$

where we define the hopping amplitude as

$$t \equiv \frac{\hbar^2}{2m^\star a^2}. \tag{5.115}$$

The on-site diagonal term combines the kinetic energy contribution and chemical potential:

$$-\frac{\hbar^2}{2m^\star a^2} \cdot 2 c_{i\sigma}^\dagger c_{i\sigma} - \mu\, c_{i\sigma}^\dagger c_{i\sigma} = -\left(\frac{\hbar^2}{m^\star a^2} + \mu \right) c_{i\sigma}^\dagger c_{i\sigma} \equiv \varepsilon_0\, c_{i\sigma}^\dagger c_{i\sigma}, \tag{5.116}$$

with an on-site energy

$$\varepsilon_0 = 2t - \mu. \tag{5.117}$$

we can redefine the chemical potential to absorb the $2t$ shift $\mu_{\text{eff}} = \mu - 2t$, and write

$$H_0 = -t \sum_{i=1}^{N-1} \sum_\sigma \Big(c_{i+1\sigma}^\dagger c_{i\sigma} + \text{h.c.} \Big) - \mu_{\text{eff}} \sum_{i=1}^{N} \sum_\sigma c_{i\sigma}^\dagger c_{i\sigma}. \tag{5.118}$$

Zeeman term

The Zeeman contribution is

$$H_Z = \int_0^L dx\ \psi^\dagger(x)\, V_z \sigma_x\, \psi(x). \tag{5.119}$$

Using Eq.(5.108)–(5.107),

$$\begin{aligned} H_Z &\approx a \sum_i \frac{1}{a} \sum_{\sigma,\sigma'} c^\dagger_{i\sigma} (V_z \sigma_x)_{\sigma\sigma'} c_{i\sigma'} \\ &= V_z \sum_{i=1}^{N} \Big(c^\dagger_{i\uparrow} c_{i\downarrow} + c^\dagger_{i\downarrow} c_{i\uparrow} \Big), \end{aligned} \tag{5.120}$$

which also makes physical sense since σ_x is the spin-flip operator.

Rashba spin–orbit coupling

The Rashba term is

$$H_{\mathrm{SO}} = \int_0^L dx\ \psi^\dagger(x) \left(i\alpha\hbar\, \sigma_y \partial_x \right) \psi(x). \tag{5.121}$$

Discretizing the derivative as in Eq.(5.109),

$$\begin{aligned} H_{\mathrm{SO}} &\approx a \sum_i \frac{1}{a} \sum_{\sigma,\sigma'} c^\dagger_{i\sigma} \left[i\alpha\hbar\, (\sigma_y)_{\sigma\sigma'} \frac{\psi_{\sigma'}(x_{i+1}) - \psi_{\sigma'}(x_{i-1})}{2a} \right] \\ &= \frac{i\alpha\hbar}{2a} \sum_i \sum_{\sigma,\sigma'} c^\dagger_{i\sigma} (\sigma_y)_{\sigma\sigma'} \Big(c_{i+1\sigma'} - c_{i-1\sigma'} \Big). \end{aligned} \tag{5.122}$$

Separating the forward and backward terms gives

$$\frac{i\alpha\hbar}{2a} \sum_i \sum_{\sigma,\sigma'} c^\dagger_{i\sigma} (\sigma_y)_{\sigma\sigma'} c_{i+1\sigma'} - \frac{i\alpha\hbar}{2a} \sum_i \sum_{\sigma,\sigma'} c^\dagger_{i\sigma} (\sigma_y)_{\sigma\sigma'} c_{i-1\sigma'}. \tag{5.123}$$

For the second term, relabel the summation index $i \to i+1$ gives

$$\sum_i c^\dagger_{i\sigma} (\sigma_y)_{\sigma\sigma'} c_{i-1\sigma'} = \sum_{i'} c^\dagger_{i'+1\sigma} (\sigma_y)_{\sigma\sigma'} c_{i'\sigma'} = \sum_i c^\dagger_{i+1\sigma} (\sigma_y)_{\sigma\sigma'} c_{i\sigma'}. \tag{5.124}$$

Using the anticommutation relations for fermions we can write

$$c^\dagger_{i+1,\sigma} (\sigma_y)_{\sigma\sigma'} c_{i,\sigma'} = -c^\dagger_{i,\sigma'} (\sigma_y)_{\sigma'\sigma} c_{i+1,\sigma}. \tag{5.125}$$

Grouping the forward and backward hopping symmetrically gives

$$H_{\mathrm{SO}} = \frac{i\alpha\hbar}{2a} \sum_i \left[\sum_{\sigma,\sigma'} c^\dagger_{i\sigma} (\sigma_y)_{\sigma\sigma'} c_{i+1,\sigma'} - \sum_{\sigma,\sigma'} c^\dagger_{i+1,\sigma} (\sigma_y)_{\sigma\sigma'} c_{i,\sigma'} \right]. \tag{5.126}$$

Writing in spinor notation $c_i = (c_{i\uparrow}, c_{i\downarrow})^{\mathsf{T}}$, this becomes:

$$H_{\mathrm{SO}} = \frac{i\alpha\hbar}{2a} \sum_i \Big(c^\dagger_{i+1} \sigma_y c_i - c^\dagger_i \sigma_y c_{i+1} \Big). \tag{5.127}$$

By defining the lattice Rashba coupling strength

$$\alpha_{\mathrm{lat}} \equiv \frac{2\alpha\hbar}{a}, \tag{5.128}$$

we obtain the final form

$$H_{\mathrm{SO}} = \frac{i\alpha_{\mathrm{lat}}}{2} \sum_{i=1}^{N-1} \Big(c^\dagger_{i+1} \sigma_y c_i - c^\dagger_i \sigma_y c_{i+1} \Big). \tag{5.129}$$

Equivalently, in components,

$$H_{\mathrm{SO}} = \alpha_{\mathrm{SO}} \sum_{i=1}^{N-1} \Big(c^\dagger_{i+1,\uparrow} c_{i\downarrow} - c^\dagger_{i+1,\downarrow} c_{i\uparrow} + \mathrm{h.c.} \Big), \tag{5.130}$$

where $\alpha_{\mathrm{SO}} = \frac{i\alpha_{\mathrm{lat}}}{2}$ is an effective spin–orbit hopping amplitude.

s-wave pairing

The superconducting part becomes

$$\begin{aligned} H_{\mathrm{SC}} &= \int_0^L dx \, \Big(\Delta \, \psi_\uparrow(x) \psi_\downarrow(x) + \Delta^* \, \psi^\dagger_\downarrow(x) \psi^\dagger_\uparrow(x) \Big) \\ &\approx a \sum_i \frac{1}{a} \Big(\Delta \, c_{i\uparrow} c_{i\downarrow} + \Delta^* \, c^\dagger_{i\downarrow} c^\dagger_{i\uparrow} \Big). \end{aligned} \tag{5.131}$$

Thus

$$H_{\mathrm{SC}} = \sum_{i=1}^{N} \Big(\Delta \, c_{i\uparrow} c_{i\downarrow} + \Delta^* \, c^\dagger_{i\downarrow} c^\dagger_{i\uparrow} \Big). \tag{5.132}$$

This is an on-site (local) s-wave pairing between opposite spins on the same site.

Collecting Eq.(5.118), (5.120), (5.130), and Eq.(5.132), we obtain the second-

quantized lattice version of the SM–SC nanowire:

$$
\begin{aligned}
H = -t \sum_{i=1}^{N-1} \sum_{\sigma} \left(c_{i+1,\sigma}^{\dagger} c_{i\sigma} + \text{h.c.} \right) - \mu_{\text{eff}} \sum_{i=1}^{N} \sum_{\sigma} c_{i\sigma}^{\dagger} c_{i\sigma} \\
+ V_z \sum_{i=1}^{N} \left(c_{i\uparrow}^{\dagger} c_{i\downarrow} + c_{i\downarrow}^{\dagger} c_{i\uparrow} \right) \\
+ \alpha_{\text{SO}} \sum_{i=1}^{N-1} \left(c_{i+1,\uparrow}^{\dagger} c_{i\downarrow} - c_{i+1,\downarrow}^{\dagger} c_{i\uparrow} - \text{h.c.} \right) \\
+ \sum_{i=1}^{N} \left(\Delta \, c_{i\uparrow} c_{i\downarrow} + \Delta^{*} \, c_{i\downarrow}^{\dagger} c_{i\uparrow}^{\dagger} \right).
\end{aligned}
\tag{5.133}
$$

Here

- $t = \dfrac{\hbar^2}{2m^{\star}a^2}$ is the nearest-neighbour hopping amplitude,
- $\mu_{\text{eff}} = \mu - 2t$ is the effective chemical potential (after absorbing the discretization shift),
- V_z is the Zeeman energy coupling opposite spins on the same site,
- α_{SO} is the effective spin–orbit hopping between neighbouring sites (proportional to the continuum Rashba coefficient α),
- and Δ is the on-site induced s-wave pairing.

The sum over $i = 1, \ldots, N-1$ in the hopping and spin–orbit terms reflects *open boundary conditions*: there is no hopping or SOC between site N and site 1. This lattice Hamiltonian is the standard tight-binding SM–SC model used to study topological superconductivity and Majorana bound states in a chain of quantum dots or a discretized nanowire, and we will be using this model in the numerical simulations.

Chapter 6

Optical Absorption Signatures and Variational Quantum Simulation of Majorana Zero Modes in the Kitaev Chain

This chapter is based on Refs. [75, 77], with more derivations and detail shown. I have conducted all the calculations in this chapter.

In this chapter we use the methods from Chap. 3 on the nanowire chain of quantum dots in contact with a p-wave superconductor described by the Kitaev Hamiltonian, to better comprehend the topological phase and to find a non-transport signature of it, and in particular, MZMs. This is done in two ways. In the first section, we begin with a Kitaev chain of semiconductor quantum dots in a nanowire with proximity to a p-wave superconductor, and we introduce excitonic interactions. This is done through shining light (photon) to the nanowire, which causes the excitation of an electron from the conduction band, and a hole from the valence band. This creates an exciton which will interact with MZMs, and we analyze its behaviour in the absorption spectrum.

We then proceed to use VQE to reproduce the ground state and topological properties of the spinless Kitaev chain to serve as an illustration of a quantum algorithm for a topological many-body system to approximate the ground state energy. We study the performance of the hybrid classical-quantum algorithm with several variational wave functions. We also calculate the relative error for each variational wave function within the topological phase of the system.

6.1 Microscopic Framework for Optically Probing Majorana Excitons

In this section, we construct a microscopic theory of Majorana excitons, which are photoexcited conduction-band electrons and valence-band holes coupled to MZMs in a Kitaev chain. We further demonstrate how these composite excitations create distinct and experimentally measurable signatures in optical absorption spectra [75]. Through using analytical and numerical approaches with exact diagonalization, we will observe that MZMs can be identified through characteristic features in the electron–hole excitation spectrum. This provides an optical way for detecting MZMs in this system.

Semiconductor–superconductor nanowires, quantum-dot arrays, magnetic atomic chains, and vortex-bound states in two-dimensional materials are among some of the systems that have been used for better understanding Kitaev-like topological superconductors [64, 65, 163, 166, 169, 181, 182]. Tunneling spectroscopy and scanning tunneling microscopy measurements [51, 169, 183] are among zero-mode detection methods. These methods measure zero-bias conductance peaks, but these peaks can also arise from more conventional mechanisms, including disorder-induced Andreev bound states, smooth confinement, or mesoscopic effects [53, 184]. Among other approaches to better understand the nature of the trivial and topological phases, are transport through quantum dots, phase-sensitive ring geometries, or multiterminal devices [70, 185]. However, these are experimentally challenging due to sophisticated nanofabrication, fine control over disorder and coupling strengths, and low quasiparticle poisoning rates [53, 70, 184, 185]. All of these challenges motivate us to look for another practical approach to detect MZMs.

The system we consider is an array of InAsP quantum dots embedded in an InP nanowire and proximitized by a p-wave superconductor [75, 186, 187]. In such nanowire quantum-dot structures, modern growth techniques enable precise control over dot size, composition, and spacing, and optical experiments on single and coupled dots are routinely performed [188–193]. Optical excitation across the band gap then creates a conduction-band electron and a valence-band hole: the electron enters the superconducting many-body background, while the hole interacts with all quasiparticles of the chain, including the localized Majoranas at the edges of the chain. The resulting bound complexes—Majorana excitons—produce a structured, parameter-dependent absorption spectrum. In this section, we show how specific spectral peaks and their spatial dependence can be traced directly to the presence of MZMs and used as

optical fingerprints of the topological phase. In this way, we propose an experimentally realistic, spectroscopy-based probe that complements transport and scanning tunneling microscopy measurements, and is naturally suited to semiconductor quantum-dot nanowire platforms.

6.1.1 Interacting Kitaev Chain in a Semiconducting Nanowire

The physical system consists of a hexagonal InP nanowire with a sequence of InAsP quantum dots, placed in proximity to a p-wave superconductor and subjected to an external magnetic field [194–199], as is shown in Fig. 6.1 (a). These systems have been experimentally and theoretically studied [188–193].

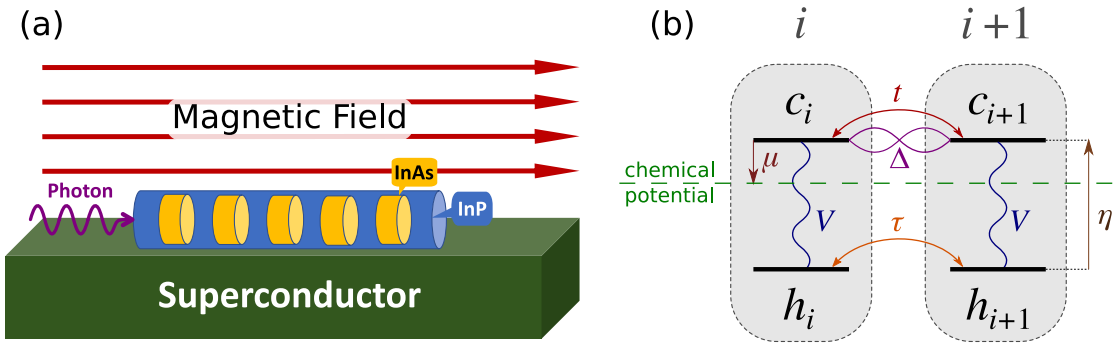

Figure 6.1: (a) Hexagonal InP nanowire with InAsP quantum dots in contact with a p-wave superconductor and an external magnetic field, used for the optical experiment. (b) Parameters of the Hamiltonian. Conduction(valence) levels are labeled by $c_i(h_i)$ operators. We use the conduction level as the reference of energy, so the downward arrow indicates negative μ. Reproduced from [75].

In our description, each quantum dot is modeled by retaining a single spin-resolved level from the lowest conduction band (CB) and a single spin-resolved level from the highest valence band (VB). Under the applied magnetic field, both levels are taken to be spin-polarized. Consequently, superconducting pairing is restricted to electrons on neighbouring dots, since each dot provides only one available spin-polarized conduction state. The field strength is chosen such that the Zeeman splitting exceeds the hopping and pairing energy scales, while remaining smaller than the single-dot level spacing [188, 189, 192, 200]. Although the magnetic field can in principle be applied in any direction, aligning it along the nanowire axis avoids additional effects such as Landau quantization and level repulsion between adjacent dots [188, 189, 191].

Optical spectroscopy is considered with light entering along the growth direction of the nanowire, as shown in Fig. 6.1(a). In equilibrium, the valence band is completely

filled, and the low-energy electronic behaviour is described by the Kitaev Hamiltonian. When light with energy close to the InAsP band gap is applied, it generates an electron–hole pair: an electron is excited to the conduction band, leaving a hole in the valence band [75, 201–203].

The Hamiltonian of the entire system can be decomposed into three parts

$$\hat{H} = \hat{H}_e + \hat{H}_h + \hat{H}_{\text{int}}, \tag{6.1}$$

where $\hat{H}_e$ describes the superconducting conduction electrons, $\hat{H}_h$ the valence-band hole, and $\hat{H}_{\text{int}}$ their mutual Coulomb attraction. Equation (6.1.1) is the matter Hamiltonian of the interacting electron-hole system. It carries no coupling to the light field, and this is deliberate. The light is a weak external probe, not part of the system we diagonalize. The eigenstates and energies obtained from $\hat{H}$ alone fix the positions of the absorption peaks. The optical coupling is treated separately, and only to first order in the field, within linear-response theory. It enters the absorption spectrum through the Fermi golden-rule matrix elements.

Explicitly,

$$\hat{H}_e = t \sum_{i=1}^{N-1} \left(c_{i+1}^\dagger c_i + \text{h.c.} \right) + \Delta \sum_{i=1}^{N-1} \left(c_{i+1}^\dagger c_i^\dagger + \text{h.c.} \right) - \mu \sum_{i=1}^{N} c_i^\dagger c_i, \tag{6.2}$$

$$\hat{H}_h = -\tau \sum_{i=1}^{N-1} \left(h_{i+1}^\dagger h_i + \text{h.c.} \right) + \eta \sum_{i=1}^{N} h_i^\dagger h_i, \tag{6.3}$$

$$\hat{H}_{\text{int}} = -V \sum_{i=1}^{N} n_i^e n_i^h. \tag{6.4}$$

Here, $c_i^\dagger$ ($h_i^\dagger$) creates a conduction-band electron (valence-band hole) on dot i. The parameter t denotes the hopping amplitude between neighbouring conduction levels, while Δ represents the induced p-wave pairing between electrons on adjacent dots. The chemical potential μ is measured relative to the conduction-band level and is tuned to bring the system close to half filling in the absence of superconductivity. The hole Hamiltonian $\hat{H}_h$ is described by a simple tight-binding model with hopping amplitude τ and an on-site energy η, corresponding to the CB–VB energy gap. Finally, $\hat{H}_{\text{int}}$ accounts for the local Coulomb attraction between an electron and a hole occupying the same quantum dot, with $n_i^e = c_i^\dagger c_i$ and $n_i^h = h_i^\dagger h_i$. The action of these parameters is schematically shown in Fig.6.1(b).

We normalize energies by units of $|t|$, which can be tuned experimentally over a range from μeV to meV [189]. In typical nanowire quantum-dot structures, the

electron–hole interaction strength V is significantly larger than $|t|$, while the hole hopping τ is much smaller due to the heavier effective mass of valence-band states [188, 189, 193]. The induced pairing Δ is also expected to lie in the μeV–meV range, and tuning t relative to Δ allows access to the topological regime of the Kitaev model.

6.1.2 Exact Diagonalization of the Interacting Kitaev Hamiltonian

Now we calculate the energy spectrum of the interacting Kitaev Hamiltonian using ED. Since we are looking for the interacting MZMS, we need to ensure that the system is in the topological phase. From chap. 4 we had seen that when $|\mu| < 2t$, the superconductivity gap opens up and the system hosts MZMs. Furthermore, the electronic part of the Kitaev Hamiltonian in bond fermion representation is diagonal when $t = \Delta$ and $\mu = 0$ and is given by Eq.(4.94). The ED for the non-interacting Kitaev Hamiltonian was described in Sec. 4.3.4. In the interacting case, for a chain of N quantum dots with up to N electrons and one hole, there are $2^N \times N$ possible configurations, which considers all the electronic and one hole configurations. In bond fermion configurations, we denote a basis state as $|M, p_M; m\rangle$, meaning the electrons occupy the bond-fermion configuration $|M, p_M\rangle$, and the hole sits on site m. To show this clearly, we take $N = 3$. In each parity sector (even/odd) there are 4 electronic bond-fermion configurations, and the hole can be at $m = 1, 2, 3$, giving 12 basis states per parity. Let

$$n_j \equiv a_j^\dagger a_j, \qquad n_j \left|\alpha_1 \cdots \alpha_N\right\rangle = \alpha_j \left|\alpha_1 \cdots \alpha_N\right\rangle . \tag{6.5}$$

Acting the Hamiltonian in Eq.(4.94) on a configuration state in Eq.(4.95) gives

$$t \sum_{j=1}^{N-1} (2\alpha_j - 1) \left|\alpha_1 \cdots \alpha_N\right\rangle = E(\{\alpha\}) \left|\alpha_1 \cdots \alpha_N\right\rangle , \tag{6.6}$$

$$E(\{\alpha\}) = t \sum_{j=1}^{N-1} (2\alpha_j - 1), \tag{6.7}$$

which is independent of α_N, the last bond fermion. We use $t < 0$ for the conduction bands hopping integrals. For each $j \leq N - 1$,

$$(2\alpha_j - 1) = \begin{cases} +1, & \alpha_j = 1, \\ -1, & \alpha_j = 0, \end{cases}$$

so the contribution of mode j to the energy is

$$t(2\alpha_j - 1) = \begin{cases} t \quad (<0), & \alpha_j = 1, \\ -t \quad (>0), & \alpha_j = 0. \end{cases}$$

Therefore, to minimize the energy when $t < 0$, we must choose

$$\alpha_j = 1, \qquad j = 1, \ldots, N-1, \tag{6.8}$$

i.e., all $N-1$ finite-energy bond fermions are occupied. Since $E(\{\alpha\})$ does not depend on α_N, the zero mode could be either empty or filled with no energy cost, producing a two-fold degenerate ground state, with each ground state corresponding to a parity sector. The odd-parity ground state (zero mode occupied, $\alpha_N = 1$) is given by

$$|\mathrm{GS}\rangle = \prod_{j=1}^{N} a_j^\dagger \, |0_a\rangle \,, \tag{6.9}$$

and the even-parity ground state (zero mode empty, $\alpha_N = 0$):

$$|\overline{\mathrm{GS}}\rangle = \prod_{j=1}^{N-1} a_j^\dagger \, |0_a\rangle \,. \tag{6.10}$$

Equations (6.9)–(6.10) are thus the two configurations that fill all $N-1$ modes appearing in $\hat{H}_e$, and differ only by the occupancy of the zero-energy bond fermion a_N, which is absent from $\hat{H}_e$ at $\Delta = t$ and $\mu = 0$. The rest of the configurations for $N = 3$ with one hole are shown in Table 6.1.

Table 6.1: Configurations of bond Fermions with one hole for $N = 3$ dots.

Even				Odd			
$\lvert\overline{\mathrm{GS}};1\rangle$	$\lvert a_1;1\rangle$	$\lvert a_2;1\rangle$	$\lvert\overline{a_1 a_2};1\rangle$	$\lvert\mathrm{GS};1\rangle$	$\lvert\overline{a}_1;1\rangle$	$\lvert\overline{a}_2;1\rangle$	$\lvert a_1 a_2;1\rangle$
$\lvert\overline{\mathrm{GS}};2\rangle$	$\lvert a_1;2\rangle$	$\lvert a_2;2\rangle$	$\lvert\overline{a_1 a_2};2\rangle$	$\lvert\mathrm{GS};2\rangle$	$\lvert\overline{a}_1;2\rangle$	$\lvert\overline{a}_2;2\rangle$	$\lvert a_1 a_2;2\rangle$
$\lvert\overline{\mathrm{GS}};3\rangle$	$\lvert a_1;3\rangle$	$\lvert a_2;3\rangle$	$\lvert\overline{a_1 a_2};3\rangle$	$\lvert\mathrm{GS};3\rangle$	$\lvert\overline{a}_1;3\rangle$	$\lvert\overline{a}_2;3\rangle$	$\lvert a_1 a_2;3\rangle$

A basis state is denoted by

$$|\Phi; m\rangle \equiv |\Phi\rangle \otimes |m\rangle \,, \tag{6.11}$$

where $|\Phi\rangle$ labels a bond-fermion configuration of the electronic Kitaev chain (e.g. $|\mathrm{GS}\rangle$, $|\overline{\mathrm{GS}}\rangle$, $|a_1\rangle$, $|a_1a_2\rangle$ for $N=3$), and $m=1,2,3$ denotes the position of the hole.

The action of the hole Hamiltonian in these configurations is as follows

$$\hat{H}_h^{\text{onsite}} = \eta \sum_m |m\rangle \langle m| \,, \tag{6.12}$$

which acts trivially on the hole configuration. Therefore, for any configuration $|\Phi\rangle$,

$$\hat{H}_h^{\text{onsite}} |\Phi; m\rangle = \eta \, |\Phi; m\rangle \,. \tag{6.13}$$

The hole hopping term is

$$\hat{H}_h^{\text{hop}} = -\tau \sum_m \Big(|m+1\rangle \langle m| + |m\rangle \langle m+1| \Big), \tag{6.14}$$

and again does not act on the electronic degrees of freedom. Its action on a configuration state is therefore

$$\hat{H}_h^{\text{hop}} |\Phi; m\rangle = -\tau \Big(|\Phi; m+1\rangle + |\Phi; m-1\rangle \Big), \tag{6.15}$$

provided the neighbouring site exists.

For example, for $N=3$,

$$\hat{H}_h^{\text{hop}} |\mathrm{GS}; 2\rangle = -\tau \Big(|\mathrm{GS}; 1\rangle + |\mathrm{GS}; 3\rangle \Big), \tag{6.16}$$

$$\hat{H}_h^{\text{hop}} |a_1a_2; 1\rangle = -\tau \, |a_1a_2; 2\rangle \,. \tag{6.17}$$

This demonstrates that hole hopping couples states with identical bond-fermion content but different hole positions.

To summarize, in this one-hole subspace, the hole Hamiltonian contributes (i) an overall onsite energy shift η and (ii) nearest-neighbour hopping with amplitude τ, which couples states with the same electronic configuration but different hole positions $m \to m \pm 1$. Therefore, if we order the basis by grouping states with fixed m (as in Table 6.1), the full Hamiltonian in a given parity sector acquires a 3×3 block structure, where each block is 4×4 (acting on the electronic configurations):

$$\hat{H} \;=\; \begin{pmatrix} H_1 & -\tau\, \mathbb{I}_4 & 0 \\ -\tau\, \mathbb{I}_4 & H_2 & -\tau\, \mathbb{I}_4 \\ 0 & -\tau\, \mathbb{I}_4 & H_3 \end{pmatrix} \;+\; \eta. \tag{6.18}$$

τ multiplies the 4×4 identity because hole hopping does not alter the electronic bond-fermion configuration, while each diagonal block H_j is the restriction of the electronic Hamiltonian plus interaction to the four bond-fermion configurations at fixed hole site $m = j$.

The interaction term $\hat{H}_{\text{int}}$ for each of the diagonal blocks H_j is $-Vn_j^e$ (for the hole located at site j), and it mixes up different bond Fermion configurations as we have

$$n_j^e = c_j^\dagger c_j = \frac{1}{2} + \frac{1}{2}(a_{j-1}^\dagger a_j + a_{j-1}^\dagger a_j^\dagger + h.c.), \qquad 1 < j \leq N, \tag{6.19a}$$

$$n_1^e = c_1^\dagger c_1 = \frac{1}{2} + \frac{1}{2}(a_N^\dagger a_1 + a_N^\dagger a_1^\dagger + h.c.), \qquad j = 1, \tag{6.19b}$$

where we have used the transformation between normal and bond fermions from Eq. (4.92). This shows that for interior sites ($1 < j \leq N$) the interaction mixes the two non-zero-energy bond fermions adjacent to site j, whereas at the edge ($j = 1$, and similarly $j = N$) the density couples the zero-mode a_N to a_1. This distinction is the microscopic origin of why an edge-localized hole couples directly to the MZM sector.

For $N = 3$, the diagonal block for a hole at site j has the form

$$H_j \;=\; H_e \;-\; V\, n_j^e, \tag{6.20}$$

where H_e is diagonal in the bond-fermion configuration basis at $t = \Delta$, $\mu = 0$, while $-Vn_j^e$ is the mixing term. To build H_j explicitly, we therefore need the 4×4 matrix of n_j^e in the chosen electronic basis. In the even configuration basis ordered as

$$\Big\{\, |\overline{\text{GS}}\rangle\,,\ |a_1\rangle\,,\ |a_2\rangle\,,\ |a_1 a_2\rangle \,\Big\}, \tag{6.21}$$

the following matrices for n_1^e and n_2^e are

$$n_1^e = \frac{1}{2}\begin{pmatrix} 1 & -1 & 0 & 0 \\ -1 & 1 & 0 & 0 \\ 0 & 0 & 1 & -1 \\ 0 & 0 & -1 & 1 \end{pmatrix}, \qquad n_2^e = \frac{1}{2}\begin{pmatrix} 1 & 0 & 0 & 1 \\ 0 & 1 & -1 & 0 \\ 0 & -1 & 1 & 0 \\ 1 & 0 & 0 & 1 \end{pmatrix}. \tag{6.22}$$

These follow directly from evaluating matrix elements $\langle\phi|\, n_j^e\, |\phi'\rangle$ between the four bond-fermion configurations: for $j = 1$, n_1^e mixes the pairs $(|\overline{\text{GS}}\rangle\,, |a_1\rangle)$ and $(|a_2\rangle\,, |a_1 a_2\rangle)$; for $j = 2$, n_2^e mixes $(|\overline{\text{GS}}\rangle\,, |a_1 a_2\rangle)$ and $(|a_1\rangle\,, |a_2\rangle)$. The operator n_3^e has the same structure as n_1^e (edge case) and similarly mixes $|\overline{\text{GS}}\rangle \leftrightarrow |a_2\rangle$ and $|a_1\rangle \leftrightarrow |a_1 a_2\rangle$.

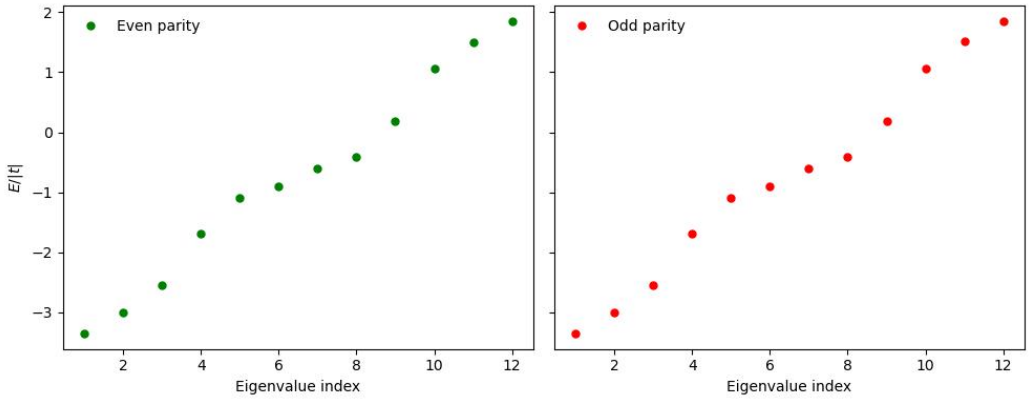

Figure 6.2: Energy spectrum of the interacting Kitaev chain with a single hole for $N = 3$ sites at $t = \Delta = -1$ and $\mu = \eta = 0$ and $\tau = 0.3|t|$ and $V = 1.5|t|$ in bond fermion representation using ED. The spectra are shown separately in the even-parity (left panel) and odd-parity (right panel) electronic sectors. Energies are normalized in units of $|t|$ as a function of the eigenvalue index.

This completes the usage of ED for $N = 3$ in each parity sector: one constructs the 12×12 Hamiltonian by (i) using the block structure in Eq. (6.18), (ii) setting $H_j = H_e - V n_j^e$ as in Eq. (6.20), with H_e diagonal in the bond basis at $t = \Delta$, $\mu = 0$, and (iii) diagonalizing H separately in the even and odd sectors to find the energy spectrum. The numerical analysis of the energy spectrum is shown in Fig. 6.2. Since we are in the topological regime, the spectra of the even and odd subspaces match. We also have 12 energy levels in each subspace, leading to a total of 24 energy levels for the entire system of 3 sites.

6.1.3 Absorption Spectrum

When a photon is absorbed, it creates an electron–hole pair in the system. As a result, the optically excited states belong to the subspace with exactly one hole. The extra electron disturbs the superconducting ground state and can excite its quasiparticles, while the hole couples to the electrons. These interactions can form bound states that appear as clear features in the optical absorption spectrum, including signatures related to Majorana zero modes localized at the ends of the chain [75].

In an absorption experiment, a photon probes the chain along the nanowire axis. Since InAsP quantum dots have a much smaller band gap than the surrounding InP nanowire material [204], the photon is absorbed only by the dots. The relevant light is in the near-infrared. Its photon energy is set by the interband transition of the InAsP dots, which is the conduction-band to valence-band gap η. In InAsP dots embedded

in InP nanowires this transition lies in the range from about 0.8 to 1.4 eV, that is, wavelengths from about 1550 to 880 nm [204]. We take the photon energy in this window. It lies above the InAsP dot gap, so an electron-hole pair is created on a dot. It lies below the InP host gap of about 1.4 to 1.5 eV, so the surrounding nanowire stays transparent and does not absorb [204]. The spectral features that carry the Majorana signatures are small shifts of order t, Δ, and V on top of this large gap energy. The photon is therefore tuned to η plus a small detuning of the same order. This fine structure, resolved on the scale of $|t|$, is what the absorption spectra in this chapter display. For calculating the absorption spectrum of the chain, we assume that the photon creates an electron–hole pair with uniform probability along the nanowire, and so define the polarization operator as

$$P = \frac{1}{\sqrt{N}} \sum_{i=1}^{N} c_i^\dagger h_i^\dagger = \frac{1}{\sqrt{N}} \sum_{i=1}^{N} P_i, \tag{6.23}$$

where we also introduced the local electron-hole pair operator $P_i = c_i^\dagger h_i^\dagger$. We assume that the system can be prepared so that the electron–hole pair is created on a selected quantum dot i, that is, by acting with the operator P_i on the chain instead of the global operator P. Creating the pair on a chosen dot is realistic in this platform. The dots are grown at deterministic positions with controllable spacing, so for the short chains studied here they can be set far enough apart to be addressed individually This local control is important for identifying the optical signature of the MZM. The polarization operator P_i connects the ground state of the system to an excited state containing one hole and one electron in the conduction band (CB). Since the ground state is degenerate in the topological phase (in particular at $\Delta = t$ and $\mu = 0$), the absorption spectrum separates into even and odd contributions, each associated with one of the degenerate ground states

$$\begin{aligned} A_{(i)}(E) &= |\beta_{\text{even}}|^2 \sum_{\phi_{\text{odd}}} |\langle \phi_{\text{odd}} | P_i \, | \text{GS}_{\text{even}} \rangle \, |^2 \delta(E - E_{\phi_{\text{odd}}} + E_{\text{GS}}) \\ &\quad + |\beta_{\text{odd}}|^2 \sum_{\phi_{\text{even}}} |\langle \phi_{\text{even}} | P_i \, | \text{GS}_{\text{odd}} \rangle \, |^2 \delta(E - E_{\phi_{\text{even}}} + E_{\text{GS}}) \\ &= |\beta_{\text{even}}|^2 A_{(i)}^{\text{even}}(E) + |\beta_{\text{odd}}|^2 A_{(i)}^{\text{odd}}(E), \end{aligned} \tag{6.24}$$

where $|\phi_{\text{even(odd)}}\rangle$ are the eigenstates of the one hole subspace and the corresponding electron parity.

Localized Hole In the case of $t = \Delta$ and $\mu = 0$, the Kitaev Hamiltonian is diagonal in bond fermions, and we have an analytical solution of the ground state energies of different parity sectors, given in Eq.(6.9) and Eq.(6.10). From Eq.(4.92) we have

$$c_j = \frac{1}{2}(a_j^\dagger + a_j + a_{j-1} - a_{j-1}^\dagger), \qquad 1 < j \leq N \tag{6.25a}$$

$$c_1 = \frac{1}{2}(a_1^\dagger + a_1 + a_N - a_N^\dagger), \qquad j = 1. \tag{6.25b}$$

and for $1 < j < N$ we have

$$P_j \left|\mathrm{GS}\right\rangle = c_j^\dagger h_j^\dagger \left|\mathrm{GS}\right\rangle = \frac{1}{2}(a_j - a_{j-1}) \left|\mathrm{GS}; j\right\rangle = \frac{1}{2}(\left|a_j; j\right\rangle - \left|a_{j-1}; j\right\rangle), \tag{6.26}$$

where we used the same notation as in Table 6.1 for the excited states. From Eq.(6.19a) we have

$$n_j^e \begin{pmatrix} \left|a_{j-1}\right\rangle \\ \left|a_j\right\rangle \end{pmatrix} = \frac{1}{2} \begin{pmatrix} 1 & -1 \\ -1 & 1 \end{pmatrix} \begin{pmatrix} \left|a_{j-1}\right\rangle \\ \left|a_j\right\rangle \end{pmatrix}. \tag{6.27}$$

Since both $\left|a_j\right\rangle$ and $\left|a_{j-1}\right\rangle$ are eigenstates of $\hat{H}_e$ with excitation energy $2|t|$, in the basis $\{\left|a_j; j\right\rangle, \left|a_{j-1}; j\right\rangle\}$, the full Hamiltonian for a localized hole ($\tau = 0$) $\hat{H} = \hat{H}_e + \eta - V n_j^e$ is

$$H = 2|t| + \eta - \frac{V}{2} \begin{pmatrix} 1 & -1 \\ -1 & 1 \end{pmatrix}, \tag{6.28}$$

with the following two eigenstates

$$\left|a_j^-; j\right\rangle = \frac{1}{\sqrt{2}} \left(\left|a_j; j\right\rangle - \left|a_{j-1}; j\right\rangle\right), \qquad E_0 = \eta + 2|t| - V \tag{6.29a}$$

$$\left|a_j^+; j\right\rangle = \frac{1}{\sqrt{2}} \left(\left|a_j; j\right\rangle + \left|a_{j-1}; j\right\rangle\right), \qquad E_1 = \eta + 2|t|. \tag{6.29b}$$

Through using Eq.(6.26) we have $\left|\left\langle a_j^-; j | P_j \left|\mathrm{GS}\right\rangle\right|^2 = \frac{1}{2}$, and $\left|\left\langle a_j^+; j | P_j \left|\mathrm{GS}\right\rangle\right|^2 = 0$. In the case of $j = 1$, by using Eq.(6.25b) we have

$$P_1 \left|\mathrm{GS}\right\rangle = c_1^\dagger h_1^\dagger \left|\mathrm{GS}\right\rangle = \frac{1}{2}(a_1 - a_N) \left|\mathrm{GS}; 1\right\rangle = \frac{1}{2}(\left|a_1; 1\right\rangle - \left|a_N; 1\right\rangle), \tag{6.30}$$

where $\left|a_N\right\rangle$ is identical to the other ground state $\left|\overline{\mathrm{GS}}\right\rangle$ up to a global phase, hence its excitation energy is zero. Then from Eq.(6.19b) we have

$$n_1^e \begin{pmatrix} \left|a_N\right\rangle \\ \left|a_1\right\rangle \end{pmatrix} = \frac{1}{2} \begin{pmatrix} 1 & -1 \\ -1 & 1 \end{pmatrix} \begin{pmatrix} \left|a_N\right\rangle \\ \left|a_1\right\rangle \end{pmatrix}. \tag{6.31}$$

Since $|a_1\rangle$ and $|a_N\rangle$ are eigenstates of $\hat{H}_e$ with excitation energy $2|t|$ and zero, respectively, the full Hamiltonian $\hat{H} = \hat{H}_e + \eta - Vn_1^e$ in the basis $\{|a_N;1\rangle, |a_1;1\rangle\}$ is

$$\hat{H} = \eta - \frac{V}{2} + \begin{pmatrix} 0 & \frac{V}{2} \\ \frac{V}{2} & 2|t| \end{pmatrix}, \tag{6.32}$$

with two eigenstates

$$|a_1^-;1\rangle = \cos(\theta)\,|a_1;1\rangle - \sin(\theta)\,|a_N;1\rangle\,, \quad E_- = \eta + |t| - \frac{V}{2} - \sqrt{t^2 + \left(\frac{V}{2}\right)^2}, \tag{6.33a}$$

$$|a_1^+;1\rangle = \sin(\theta)\,|a_1;1\rangle + \cos(\theta)\,|a_N;1\rangle\,, \quad E_+ = \eta + |t| - \frac{V}{2} + \sqrt{t^2 + \left(\frac{V}{2}\right)^2}, \tag{6.33b}$$

with

$$\cos(\theta) = \sqrt{\frac{1}{2} + \frac{t^2}{\sqrt{4t^2+V^2}}}, \qquad \sin(\theta) = \sqrt{\frac{1}{2} - \frac{t^2}{\sqrt{4t^2+V^2}}}. \tag{6.34}$$

Now using Eq.(6.30) we have $\left|\langle a_1^-;1|\,P_1\,|\mathrm{GS}\rangle\right|^2 = \frac{1}{2}(\cos(\theta)+\sin(\theta))^2 = \frac{1}{2}A_-$, and $\left|\langle a_1^+;1|\,P_1\,|\mathrm{GS}\rangle\right|^2 = \frac{1}{2}(\cos(\theta)-\sin(\theta))^2 = \frac{1}{2}A_+$. Altogether, the final result is

$$A_i(E) = \frac{1}{2}\begin{cases} \delta(E-E_0) & 1 < i < N \\ A_-\delta(E-E_-) + A_+\delta(E-E_+) & i = 1, N \end{cases}, \tag{6.35}$$

where

$$E_0 = \eta + 2|t| - V, \tag{6.36a}$$

$$E_\pm = \eta + |t| - \frac{V}{2} \pm \sqrt{t^2 + \left(\frac{V}{2}\right)^2}, \tag{6.36b}$$

$$A_\pm = \frac{1}{2}\left(1 \mp \frac{V}{\sqrt{4t^2+V^2}}\right), \tag{6.36c}$$

Therefore, if the electron is created at one of the two ends, one of the bond fermions is the zero mode a_N. On the other hand, when the hole is at site i, the interaction $-Vn_i^e n_i^h$ mixes the two bond fermions, as shown in Fig. 6.3, and expressed in Eq. (6.27) and Eq.(6.31). The evolution of the energies E_0 and $E_\pm$ as a function of the interaction V is shown in Fig. 6.4, where we are using ED to calculate the energy spectrum of a chain of 3 QDs.

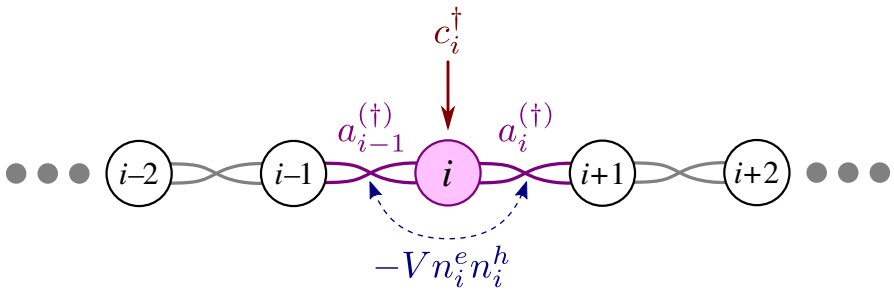

Figure 6.3: $c_i^\dagger$ is a superposition of creation and annihilation operators of two bond fermions $a_i^{(\dagger)}$ and $a_{i-1}^{(\dagger)}$, according to Eq.(6.25). The interaction $-Vn_i^e n_i^h$ mixes up the two bond fermions according to Eq.(6.27). Note that when i is one of the two ends, then one of the bond fermions is the zero mode a_N [75].

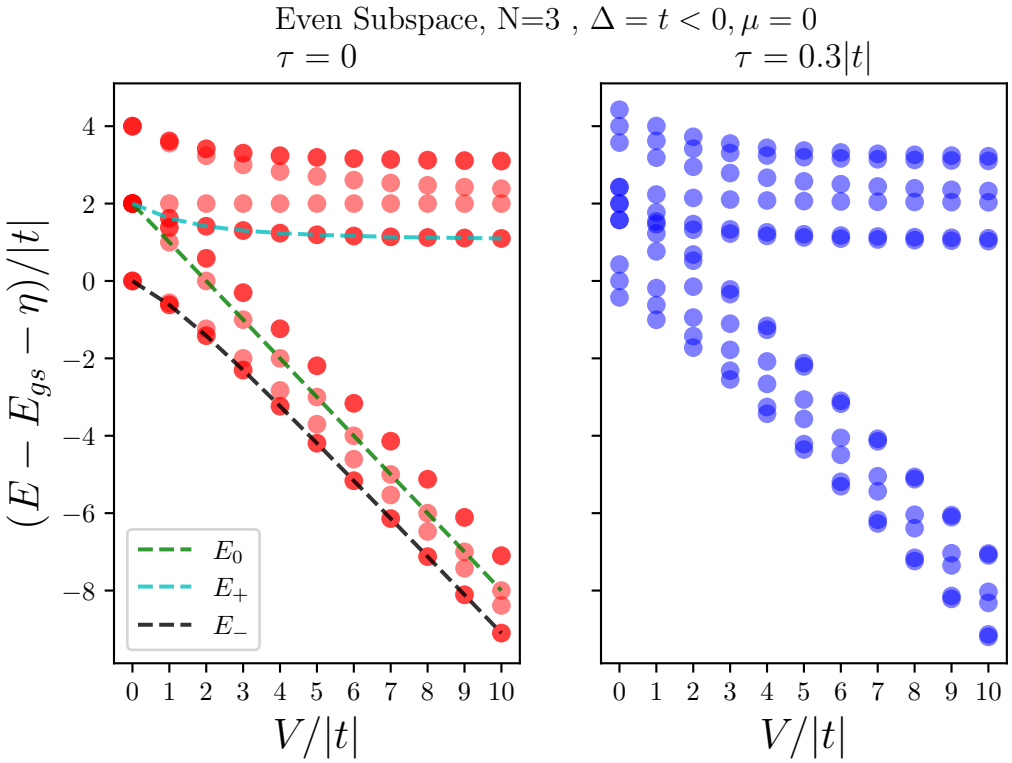

Figure 6.4: Energy spectra of the full Hamiltonian with one hole in the even subspace, as a function of electron-hole interaction V, for $N = 3$ dots, $\Delta = t$ and $\mu = 0$. (left) for the case of localized hole, $\tau = 0$, (right) for a mobile hole with $\tau = 0.3|t|$. The overlap of transparent markers makes the degenerate levels look darker. The peak energies E_0 and $E_\pm$ are also shown according to Eq.(6.36a) and Eq.(6.36b) [75].

Note that the full absorption spectrum is given by the sum in

$$A(E) = \frac{1}{N}\sum_{i=1}^{N} A_i(E). \tag{6.37}$$

The bottom row of Fig. 6.5 shows the results in Eq.(6.35) and Eq.(6.36) for the case of $N = 3$. The lines in each panel mark the positions of the absorption peaks, while the colour scale shows their intensity. The peak E_0 appears only when probing the non-edge interior dots, whereas the peaks $E_\pm$ are visible when probing the two end dots of the chain. The peaks $E_\pm$ contain a contribution from the zero mode, while E_0 is composed only of non-zero bond fermions.

At $V = 0$, the peak E_- comes entirely from the zero mode, while E_+ is made only of non-zero bond fermions. As V increases, E_+ gradually gains more zero-mode character, and E_- mixes more strongly with non-zero bond fermions. At the same time, the intensity of the E_+ peak decreases with increasing V, as follows from Eq.(6.36c).

If V is not too small, the E_+ peak provides a clearer optical signature of the MZM than E_-. This is because E_+ is separated from the rest of the spectrum by an energy scale set by V, and we typically expect $V \gg |t|$. In this sense, the optical approach offers an advantage compared to scanning tunnelling microscopy for detecting MZMs.

Furthermore, if spatially resolved absorption spectroscopy can be performed along the chain, the zero mode can be identified by the presence of a pronounced high-energy peak near E_+ when probing the end dots, and by its absence when probing the other dots.

Mobile Hole When the hole is allowed to move, there are N hole states that can spread along the chain, each with its own energy. One would therefore expect N possible transitions to a given electronic state. More importantly, as seen in Eq.(6.18), hole hopping mixes configurations where the hole sits on different dots. Because of this mixing, additional transitions become possible, and more peaks appear in the absorption spectrum.

In the top row of Fig. 6.5, we compare the absorption spectrum for a mobile hole with $\tau = 0.1|t|$ to the analytic result for a localized hole given in Eq.(6.35) (bottom row), for $N = 3$. It is clear that the mobile hole case shows more peaks, although the main features still lie close to the energies E_0 and $E_\pm$.

In the full spectrum $\overline{A}$ (top left panel of the figure), there is a single visible high-energy peak near E_+. The same peak is strong in $\overline{A}_1$ (top middle) and much weaker in $\overline{A}_2$ (top right), reflecting the fact that E_+ carries the localized Majorana

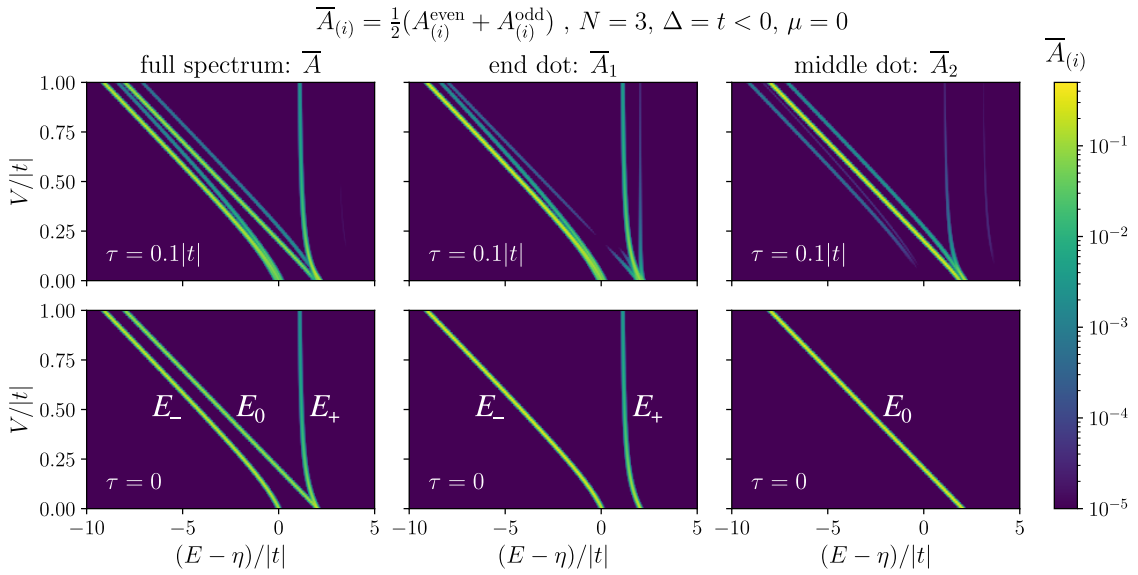

Figure 6.5: (left) The averaged absorption spectrum $\overline{A}(E)$, and (middle and right) spatially resolved absorption $\overline{A}_i(E)$, for $\Delta = t, \mu = 0$, and for $N = 3$ dots. (top) for a mobile hole with $\tau = 0.1|t|$, (bottom) for a localized hole, $\tau = 0$, according to the analytic results in Eqs. (6.35 and 6.36). The spectra are plotted against $(E - \eta)/|t|$ while changing $V/|t|$ on the y-axis. The bright curves show the location of the peaks as V changes, and the color scale shows their heights. Gaussian profile was used for the peaks with the width $\sigma = 0.025|t|$. The maximum value of each peak shows the magnitude of the corresponding matrix element [75].

character at the ends of the chain (see Fig. 6.5).

In plotting Fig. 6.5, we used the averaged spectrum

$$\overline{A}_{(i)} = \frac{1}{2}\left(A^{\text{even}}_{(i)} + A^{\text{odd}}_{(i)}\right),$$

since for a mobile hole the even and odd spectra are different. However, because the two ground states are degenerate and neither is favored, the measured signal is expected to correspond to their average.

The same reasoning applies to chains of arbitrary length, since the analytic result in Eq.(6.35) is for general N. Figure. 6.6 shows the absorption spectrum for a longer chain with $N = 9$, where we fix $V = 10|t|$ and vary τ. In the limit $\tau \to 0$, we recover the localized-hole case, in which the subspaces corresponding to the hole on different dots are effectively independent. As τ increases, hole hopping mixes these subspaces and the modes begin to hybridize. As a result, the zero mode gradually spreads away from the ends of the chain.

From the first panel of Fig. 6.6, we see that at high energy there remains only

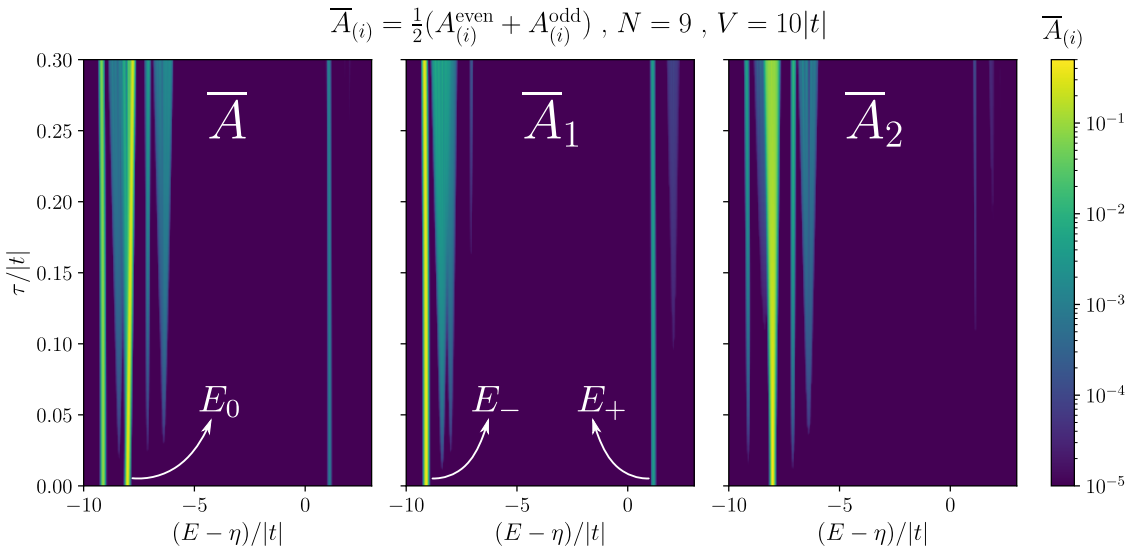

Figure 6.6: Absorption spectrum for a chain of length $N = 9$, and for $\Delta = t, \mu = 0, V = 10|t|$, and changing τ. (left) The full averaged spectrum $\overline{A}$, (middle) the spatially resolved spectrum for the first dot $\overline{A}_1$, and (right) the spatially resolved spectrum for the second dot $\overline{A}_2$. The bright curves show the location of the peaks as τ changes, and the colorscale shows their heights. Gaussian profile was used for the peaks with the width $\sigma = 0.025|t|$. The maximum value of each peak shows the magnitude of the corresponding matrix element [75].

one clear peak near E_+ over a wide range of τ. Only around $\tau \approx 0.3|t|$ does a faint additional peak appear to its right. This shows that the E_+ feature is quite stable against moderate hole hopping. With spatially resolved spectroscopy, one can further check that this peak originates from the chain ends. In the third panel, corresponding to $\overline{A}_2$, there is no visible high-energy peak on the site next to the end dot until about $\tau = 0.1|t|$. By contrast, the peak at E_-, which also contains a significant zero-mode contribution and is stronger in intensity, spreads away from the end much more quickly even for small τ.

It is worth estimating $V/|t|$ for this platform. The interaction V is the electron-hole interaction on a single dot, set by the dot confinement and essentially independent of the dot spacing. For InAsP dots in InP nanowires the on-dot energies are in the meV range, with bi-exciton binding energies near 2 meV and dot-to-dot energy fluctuations of about 5 meV, while the exciton binding is larger, of order tens of meV. The hopping t and the pairing Δ are instead inter-dot couplings. In a quantum-dot Kitaev chain they originate from elastic co-tunneling and crossed Andreev reflection through a proximitizing superconductor, and they are tuned to the $\Delta = t$. These couplings are far smaller than V, with reported Majorana scales of tens of μeV, for example a gap

above 70 μeV. The natural regime is therefore $V/|t| \gtrsim 10$.

The ratio is also broadly tunable. Since t falls off rapidly as the dots are moved apart while V stays fixed, $V/|t|$ can be raised from about 10 for strongly coupled dots to of order 10^3 for well separated dots. The value $V = 10|t|$ used here thus sits at the lower edge of the accessible range, and our localized-hole result, valid for any V and any chain length N, already covers the large $V/|t|$ limit. The practical upper end is set not by the ratio but by the absolute scale. The Majorana energy is $t = \Delta$, so reducing t to enlarge $V/|t|$ also shrinks the spectral features. Resolving them requires a broadening and a temperature well below t, which favors keeping $t = \Delta$ near tens of μeV.

Overall, the results for a mobile hole confirm that the main conclusions of the localized-hole case remain valid. Although finite τ introduces additional mixing and produces extra weak peaks, the absorption spectrum still shows a clear high-energy feature at the chain edge associated with the MZM content of the excited state near E_+. For the longer chain in Fig. 6.6, the averaged spectrum $\overline{A}$ continues to display a single dominant high-energy branch over a broad range of $\tau/|t|$. This peak remains strong at the end dot ($\overline{A}_1$) and strongly suppressed on nearby sites ($\overline{A}_2$) until τ becomes sufficiently large for the zero-mode weight to spread into the bulk. These observations indicate that E_+ provides a robust and practical optical signature of the MZM, even when the hole is mobile [75].

6.2 Majorana Zero Modes with Variational Quantum Eigenvalue Solver

We now apply the variational quantum eigensolver (VQE) to the Kitaev chain realized in InAsP quantum dots embedded in an InP semiconducting nanowire in contact with a p-wave superconductor.

We first explain why this is worth doing. The Kitaev chain is exactly solvable, both analytically and by exact diagonalization (ED), so VQE is not required to find its ground-state energy. That exact solvability is why the model is the right benchmark. The answer is known in advance, so any deviation of the VQE result measures the quality of the algorithm and the ansatz rather than an error in the model.

The demanding test is the topological ground state, not the energy alone. In the topological phase the Kitaev chain has a doubly-degenerate ground states of opposite fermion parity, related by the occupation of the nonlocal Majorana mode.

Representing this degenerate pair, and not collapsing onto a single parity sector, is hard for a near-term variational circuit. We therefore construct symmetry-adapted ansätze that respect the parity structure of the Hamiltonian, guided by the analytical solution [77], and we ask whether VQE can reproduce both the even and the odd ground state across the phase diagram.

Our aim is therefore twofold. First, we benchmark a hybrid quantum-classical algorithm on a model where the exact result is known, using analytical and numerical ED to compute the full spectrum [77] and comparing the VQE energies with ED at each point. Second, we establish that such algorithms can capture the topological ground-state degeneracy of the Kitaev Hamiltonian [205, 206]. This gives a validated route toward simulating topological matter on near-term quantum hardware, including regimes where exact methods become intractable, and it ties directly to the broader goal of using quantum computers to study the Majorana systems that could host topological qubits.

We consider the same Kitaev chain as we did in the previous section, a hexagonal InP nanowire with an array of embedded InAsP QDs in the proximity of a p-wave superconductor and in the presence of applied external magnetic field. The Hamiltonian of the system is the non-interactive Kitaev Hamiltonian

$$\hat{H} = t \sum_{i=1}^{N-1} (c_{i+1}^{\dagger} c_i + \text{h.c.}) + \Delta \sum_{i=1}^{N-1} (c_{i+1}^{\dagger} c_i^{\dagger} + \text{h.c.}) - \mu \sum_{i=1}^{N} c_i^{\dagger} c_i. \tag{6.38}$$

6.2.1 Variational Quantum Eigensolver for the Kitaev Chain

As was explained in Chap. 3, the VQE is a hybrid method that estimates the ground state energy of a given Hamiltonian through a quantum-classical computational approach [130, 207]. The quantum advantage comes from the capacity to manage and manipulate the variational states as quantum circuits [7, 208]. The variational state is generated by a unitary operation (quantum circuit) acting on an initial state. By using a classical optimizer to fine-tune the variational parameters of the quantum circuit, VQE could be a potential candidate to minimize the energy for large systems [138, 209, 210].

We follow the regular VQE workflow: The first step is to express the Hamiltonian $\hat{H}$ in terms of Pauli operators, through the Jordan-Wigner (JW) transformation. A quantum circuit with adjustable gates, parameterized by parameters $\boldsymbol{\theta}$, is then applied to generate the quantum state $|\psi(\boldsymbol{\theta})\rangle$, where $\boldsymbol{\theta}$ represents a set of parameters used in a quantum circuit, allowing the Hamiltonian to act on the state $|\psi(\boldsymbol{\theta})\rangle$. The expectation

value of the energy in the state $|\psi(\boldsymbol{\theta})\rangle$ is given by

$$E(\boldsymbol{\theta}) = \langle\psi(\boldsymbol{\theta})|\,\hat{H}\,|\psi(\boldsymbol{\theta})\rangle\,. \tag{6.39}$$

The measured energy $E(\boldsymbol{\theta})$ is fed into the classical optimizer, which adjusts the parameters $\boldsymbol{\theta}$ to minimize the energy. This process is iterated, repeating the quantum circuit execution and measurement, with the optimizer refining $\boldsymbol{\theta}$ until the minimum energy is found. Ultimately, the variational state with the optimized parameters corresponds to the approximate ground state of the Hamiltonian, providing a solution to the problem. We use a chain of five QDs to show the energy spectrum of ED and JW match, and w apply the VQE to a chain of ten QDs.

Jordan-Wigner (JW) Transformation We apply the JW transformation to the fermionic operators to transform them into spin operators represented by the Pauli matrices [211–213].

The JW transformation for spinless fermions was defined as

$$c_j^\dagger = e^{-i\Phi_j}\hat{S}_j^+, \tag{6.40a}$$
$$c_j = \hat{S}_j^- e^{i\Phi_j}, \tag{6.40b}$$

where $\hat{S}_j^\pm = \hat{S}_j^x \pm i\hat{S}_j^y$ are the raising and lowering spin operators for site j, and $\vec{\hat{S}} = \frac{\hbar}{2}\vec{\hat{\sigma}}$ are the spin-$\frac{1}{2}$ operators. The phase factor Φ_j can be expressed as

$$\Phi_j = \pi \sum_{m=1}^{j-1} \left(\frac{1}{2} + \hat{S}_m^z\right). \tag{6.41}$$

The fermionic products transform as

$$c_i^\dagger c_i = \hat{S}_i^+ \hat{S}_i^- \tag{6.42}$$
$$c_{i+1}^\dagger c_i = \hat{S}_{i+1}^+ \hat{S}_i^-, \tag{6.43}$$
$$c_{i+1}^\dagger c_i^\dagger = -\hat{S}_{i+1}^+ \hat{S}_i^+. \tag{6.44}$$

Any fermionic states $|0\rangle$ and $|1\rangle$, corresponding to the empty or occupied site, will now transform to spin-down $|\downarrow\rangle$ and spin-up $|\uparrow\rangle$, respectively. The transformed Hamiltonian in equation (6.38) is

$$\hat{H} = -\frac{\mu N}{2} - \mu \sum_{i=1}^{N} \hat{S}_i^z + 2\sum_{i=1}^{N-1} \left[(t+\Delta)\hat{S}_{i+1}^y \hat{S}_i^y + (t-\Delta)\hat{S}_{i+1}^x \hat{S}_i^x\right], \tag{6.45}$$

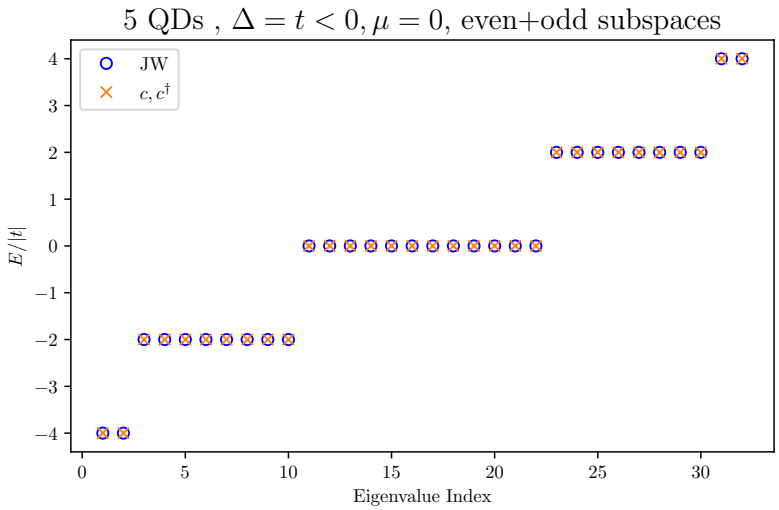

Figure 6.7: Energy spectrum of the fermionic and spin Hamiltonian in the analytical solution case. The even (odd) eigenvalue indices correspond to the even (odd) subspace eigenvalues [77].

We can see that this is similar to the XY model

$$\hat{H} = -h \sum_{i=1}^{N} \hat{S}_i^z + \sum_{i=1}^{N-1} [J_y \hat{S}_{i+1}^y \hat{S}_i^y + J_x \hat{S}_{i+1}^x \hat{S}_i^x], \tag{6.46}$$

with μ acting as the external magnetic field h along the z-direction, J_x as the $t - \Delta$ term, and J_y as the $t + \Delta$ term. The energy spectrum of the Hamiltonian in fermionic and JW representation using ED is shown in Fig. 6.7 to ensure the spectra matching within these two representations [77].

Variational Wave Function Next we define the variational wave function, called an ansatz. An ansatz is a trial state prepared by a quantum circuit whose gate parameters are the variational parameters. The VQE loop tunes these angles on a classical computer so as to minimize the energy expectation value. The choice of circuit fixes which states are reachable, so it controls how well the true ground state can be approximated.

We use four ansätze, namely Even, Odd, Efficient SU(2), and the Hamiltonian variational ansatz (HVA) [214, 215]. The Even and Odd ansätze target the two parity sectors of the Kitaev chain. The Efficient SU(2) ansatz is a hardware-efficient, while the HVA is built directly from the terms of the Hamiltonian.

The design of the Even and Odd ansätze follows from the structure of the topological ground state. In the topological regime the ground state is two-fold degenerate. The

two degenerate states have opposite fermion parity and are related by the occupation of the nonlocal Majorana mode. Within a single parity sector the ground state is not one basis state. It is spread over the configurations of that parity, and at $t = |\Delta|$, $\mu = 0$ it becomes an equal-weight superposition of them. This motivates an ansatz that can reach every configuration of one parity sector with independently tunable amplitudes. We build one such ansatz for the even sector and one for the odd sector.

The even ansatz is designed to variationally reach the even-parity ground state. For three qubits we start from the reference state $|000\rangle$, which has even parity. The circuit in Fig. 6.8 then applies a layer of single-qubit rotations, an entangling block of CNOT gates, and a final phase rotation. The variational state reads

$$|\psi_{\text{even}}(\boldsymbol{\theta})\rangle = R_z^{(0)}(\theta_4)\, U_{\text{ent}} \left[\prod_{j=0}^{2} R_x^{(j)}(\theta_{j+1})\right] |000\rangle\,, \tag{6.47}$$

where $R_x^{(j)}(\theta) = e^{-i\theta\sigma_x^{(j)}/2}$ and $R_z^{(0)}(\theta) = e^{-i\theta\sigma_z^{(0)}/2}$ act on qubit j, and the entangling unitary is

$$U_{\text{ent}} = \text{CNOT}_{0\to1}\,\text{CNOT}_{1\to2}\,\text{CNOT}_{2\to1}\,\text{CNOT}_{1\to0}. \tag{6.48}$$

The single-qubit rotations turn the reference state into a tunable product state,

$$\prod_{j=0}^{2} R_x^{(j)}(\theta_{j+1})\,|000\rangle = \bigotimes_{j=0}^{2} \left[\cos\!\left(\tfrac{\theta_{j+1}}{2}\right)|0\rangle - i\sin\!\left(\tfrac{\theta_{j+1}}{2}\right)|1\rangle\right]. \tag{6.49}$$

The CNOT block then entangles the three qubits and correlates their amplitudes, and the final $R_z^{(0)}(\theta_4)$ rotation sets a relative phase. The four even-parity states $|000\rangle$, $|011\rangle$, $|101\rangle$, $|110\rangle$ span the even-parity sector for three qubits. The ansatz is optimized to reproduce the even-parity ground state, which is a superposition of exactly these four states,

$$|\psi_{\text{even}}\rangle = \alpha_{000}\,|000\rangle + \alpha_{011}\,|011\rangle + \alpha_{101}\,|101\rangle + \alpha_{110}\,|110\rangle\,, \tag{6.50}$$

where the complex amplitudes $\alpha_{000}, \alpha_{011}, \alpha_{101}, \alpha_{110}$ are smooth functions of the variational parameters $\boldsymbol{\theta} = (\theta_1, \theta_2, \theta_3, \theta_4)$.

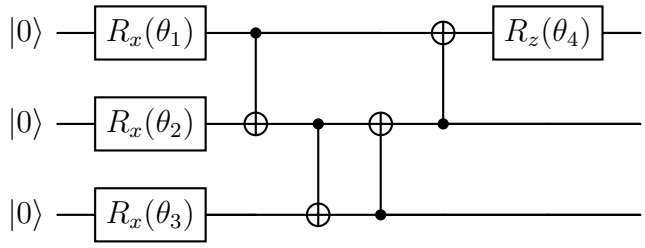

Figure 6.8: The quantum circuit for the even ansatz with 3 qubits [77].

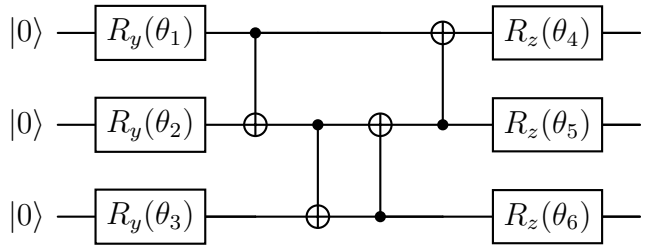

Figure 6.9: The quantum circuit for the odd ansatz with 3 qubits [77].

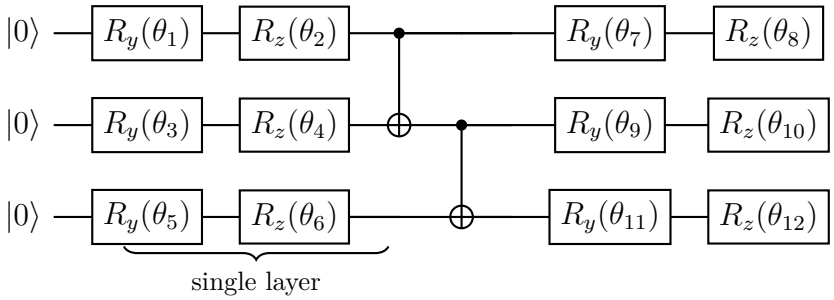

Figure 6.10: Quantum circuit of the efficient SU(2) ansatz with 3 qubits and 1 layer of linear entanglement [77].

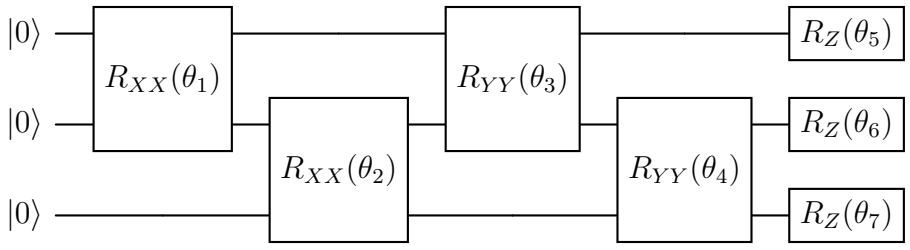

Figure 6.11: The quantum circuit for the HVA with 3 qubits [77].

The odd ansatz is constructed to variationally reach the odd-parity ground state. For three qubits the circuit in Fig. 6.9 prepares the variational state

$$|\psi_{\text{odd}}(\boldsymbol{\theta})\rangle = \left[\prod_{j=0}^{2} R_z^{(j)}(\theta_{4+j})\right] U_{\text{ent}} \left[\prod_{j=0}^{2} R_y^{(j)}(\theta_{1+j})\right] |\psi_0\rangle\,, \tag{6.51}$$

where $R_y^{(j)}(\theta) = e^{-i\theta\sigma_y^{(j)}/2}$ and $R_z^{(j)}(\theta) = e^{-i\theta\sigma_z^{(j)}/2}$ act on qubit j, and the entangling unitary is the same forward and reverse CNOT ladder as in the even ansatz,

$$U_{\text{ent}} = \text{CNOT}_{0\to1}\,\text{CNOT}_{1\to2}\,\text{CNOT}_{2\to1}\,\text{CNOT}_{1\to0}. \tag{6.52}$$

The reference state $|\psi_0\rangle$ is chosen to be an odd-parity computational basis state, for example $|001\rangle$, $|010\rangle$, or $|100\rangle$, so that the optimization is anchored in the odd-parity manifold. The R_y layer generates a real superposition of configurations, the entangling unitary U_{ent} correlates the amplitudes across qubits, and the final R_z rotations provide independent phase control. The four odd-parity states $|001\rangle$, $|010\rangle$, $|100\rangle$, $|111\rangle$ span the odd-parity sector for three qubits, and the ansatz is optimized to reproduce the odd-parity ground state as their superposition,

$$|\psi_{\text{odd}}\rangle = \beta_{001}\,|001\rangle + \beta_{010}\,|010\rangle + \beta_{100}\,|100\rangle + \beta_{111}\,|111\rangle\,, \tag{6.53}$$

where the complex amplitudes $\beta_{001}, \beta_{010}, \beta_{100}, \beta_{111}$ are smooth functions of the variational parameters $\boldsymbol{\theta} = (\theta_1, \theta_2, \theta_3, \theta_4, \theta_5, \theta_6)$.

The efficient SU(2) ansatz, shown in Fig. 6.10, is a hardware-efficient reference circuit. It uses no information about the Hamiltonian and is not tied to any parity sector. It alternates layers of single-qubit R_y and R_z rotations with a fixed pattern of CNOT entangling gates, which lets it explore a large part of the Hilbert space at the cost of more parameters. It therefore serves as a flexible baseline against which the physics-informed ansätze are measured. For N qubits and one layer of linear entanglement, the variational state prepared by Fig. 6.10 reads

$$\begin{aligned} |\psi_{\text{SU2}}(\boldsymbol{\theta})\rangle = &\left[\prod_{j=0}^{N-1} R_y^{(j)}(\theta_{2j+1})\, R_z^{(j)}(\theta_{2j+2})\right] U_{\text{lin}} \\ &\times \left[\prod_{j=0}^{N-1} R_y^{(j)}(\theta_{2N+2j+1})\, R_z^{(j)}(\theta_{2N+2j+2})\right] |\psi_0\rangle\,, \end{aligned} \tag{6.54}$$

where $R_{y,z}^{(j)}(\cdot)$ act on qubit j and the linear entangling unitary is

$$U_{\text{lin}} = \prod_{j=0}^{N-2} \text{CNOT}_{j\to j+1}, \tag{6.55}$$

with the product ordered from left to right as increasing j. For the three-qubit circuit in Fig. 6.10 with a single entangling layer, Eq. (6.54) reads

$$\begin{aligned}|\psi_{\text{SU2}}(\boldsymbol{\theta})\rangle = &\left[R_y^{(0)}(\theta_1)R_z^{(0)}(\theta_2)\ R_y^{(1)}(\theta_3)R_z^{(1)}(\theta_4)\ R_y^{(2)}(\theta_5)R_z^{(2)}(\theta_6)\right] \\ &\times \left[\text{CNOT}_{0\to1}\,\text{CNOT}_{1\to2}\right] \\ &\times \left[R_y^{(0)}(\theta_7)R_z^{(0)}(\theta_8)\ R_y^{(1)}(\theta_9)R_z^{(1)}(\theta_{10})\ R_y^{(2)}(\theta_{11})R_z^{(2)}(\theta_{12})\right]|\psi_0\rangle\,. \end{aligned} \tag{6.56}$$

The final ansatz is the HVA, shown in Fig. 6.11, which is built explicitly from the structure of the target Hamiltonian. The HVA generates the variational state through unitary evolutions associated with the individual terms of the Hamiltonian. This approach is well suited to lattice models with local interactions and converges efficiently for many-body systems [215]. Starting from the Jordan-Wigner transformed Kitaev Hamiltonian in Eq. (6.45), the spin representation reads

$$\hat{H} = 2(t-|\Delta|)\sum_{j=1}^{N-1}\hat{S}_{j+1}^x\hat{S}_j^x + 2(t+|\Delta|)\sum_{j=1}^{N-1}\hat{S}_{j+1}^y\hat{S}_j^y - \mu\sum_{j=1}^{N}\hat{S}_j^z - \frac{\mu N}{2}. \tag{6.57}$$

The constant shift $-\mu N/2$ can be dropped, since it plays no role in the optimization and only rigidly shifts the energy. Equation (6.57) splits naturally into three sets of mutually non-commuting terms,

$$\hat{H} = \hat{H}_{XX} + \hat{H}_{YY} + \hat{H}_Z, \tag{6.58}$$

with

$$\hat{H}_{XX} = \sum_{j=1}^{N-1}\hat{S}_{j+1}^x\hat{S}_j^x, \tag{6.59}$$

$$\hat{H}_{YY} = \sum_{j=1}^{N-1}\hat{S}_{j+1}^y\hat{S}_j^y, \tag{6.60}$$

$$\hat{H}_Z = \sum_{j=1}^{N}\hat{S}_j^z. \tag{6.61}$$

The physical coupling constants $2(t-|\Delta|)$, $2(t+|\Delta|)$, and μ are not fixed in the ansatz. They are absorbed into the variational angles, which are free to adjust each term independently. For a Hamiltonian written as a sum of terms $\hat{H} = \sum_j c_j \hat{H}^{(j)}$, the HVA assigns a variational unitary

$$\hat{U}_j(\theta_j) = \exp\Big(-i\theta_j \hat{H}^{(j)}\Big) \tag{6.62}$$

to each operator $\hat{H}^{(j)}$. The real parameters $\{\theta_j\}$ are optimized classically inside the VQE loop. Applying this to the Kitaev Hamiltonian gives the HVA unitary

$$\hat{U}(\boldsymbol{\theta}) = \prod_{k=1}^{R} \left[\prod_{j=1}^{N-1} \exp\Big(-i\theta^x_{j,k} \hat{S}^x_{j+1} \hat{S}^x_j\Big) \prod_{j=1}^{N-1} \exp\Big(-i\theta^y_{j,k} \hat{S}^y_{j+1} \hat{S}^y_j\Big) \prod_{j=1}^{N} \exp\Big(-i\theta^z_{j,k} \hat{S}^z_j\Big) \right], \tag{6.63}$$

where R is the number of HVA layers. Each layer applies the two-body XX and YY rotations followed by single-qubit Z rotations, which mirrors the operator content of the Kitaev Hamiltonian. A useful property follows from this structure. The gates R_{XX}, R_{YY}, and R_Z each flip an even number of qubits or are diagonal, so they conserve fermion parity. The HVA therefore stays in the parity sector of its reference state throughout the optimization, by construction rather than by tuning. Increasing R enlarges the variational manifold and lets the ansatz approach the exact ground state arbitrarily well at large depth. In practice the exponential of the full Hamiltonian within a layer is approximated by a second-order Trotter-Suzuki decomposition,

$$e^{-i(\hat{H}_{XX}+\hat{H}_{YY}+\hat{H}_Z)} \approx e^{-i\hat{H}_{XX}/2} e^{-i\hat{H}_{YY}/2} e^{-i\hat{H}_Z} e^{-i\hat{H}_{YY}/2} e^{-i\hat{H}_{XX}/2}, \tag{6.64}$$

which reduces the Trotter error while preserving locality. Each exponential in Eq. (6.63) is then realized with standard two-qubit R_{XX} and R_{YY} gates and single-qubit R_Z rotations, as shown in Fig. 6.11 for $N = 3$ qubits.

VQE Results First we investigate how each ansatz performs for a given number of layers (corresponding to the number of variational parameters) and the best number of layers that gives optimized results. To do so, we plot the relative error in the ground state energy vs. the number of layers of each ansatz, shown in Fig. 6.12. For a given number of layers, we take the minimum energy of 10 initial runs. The entire optimization is done using the **COBYLA** optimizer available in the **Qiskit** package, and 30000 trials. All the calculations are done using a quantum simulator on a classical computer. The relative error is basically the error in the VQE and ED

calculations

$$\text{Error} = \left|1 - \frac{E_{\text{VQE}}}{E_{\text{ED}}}\right|, \tag{6.65}$$

The number of parameters per layer for the even, odd, SU2, and HVA ansätze are 11, 20, 40, and 28, respectively.

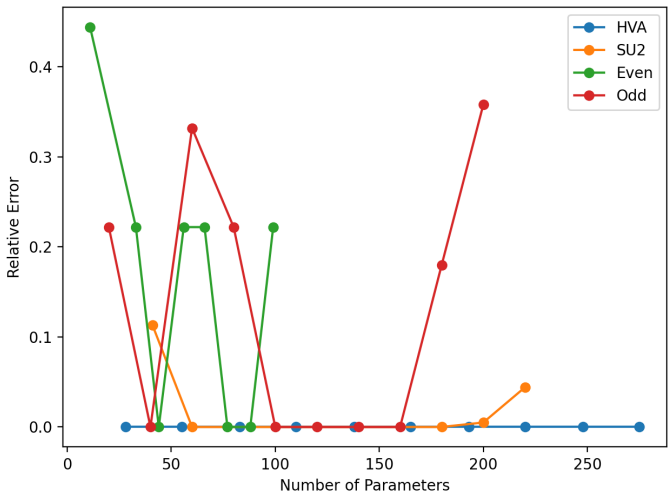

Figure 6.12: Relative error as a function of the number of parameters for different ansätze in the analytical solution regime, $\Delta = t$ and $\mu = 0$, for a chain of 10 QDs. The maximum number of layers is 10 [77].

From Fig. 6.12, we can see that HVA needs the least number of parameters to give a zero relative error. The even and odd ansätze show a fluctuating pattern, with the even ansatz eventually giving zero relative error for more than 100 parameters. The efficient SU(2) gives zero relative error for a number of parameters more than 50 and up to 200. Beyond about 200 parameters the SU(2) error rises again. This is not numerical round-off error. It is a loss of trainability. The relative error is defined as $|E_{\text{VQE}} - E_{\text{ED}}|/|E_{\text{ED}}|$, measured against the exact diagonalization ground-state energy. All four ansätze fall to the same floor near zero once they have enough parameters, because they all approximate the same ground state and the exact energy is a hard lower bound. The shared plateau is therefore the convergence of VQE to the exact result. The ansätze differ in how they reach it. The HVA attains zero error with the fewest parameters and remains there at all sizes. The Even and Odd ansätze reach zero but show spikes at intermediate sizes, where the optimizer is trapped in a local minimum. The Odd and SU(2) errors grow again at the largest parameter counts, reflecting the reduced trainability of deep circuits.

Next, to see how each ansatz performs in the ground state energy approximation,

we examine the loss function behaviour, which in this case is the ground state energy, as a function of iterations.

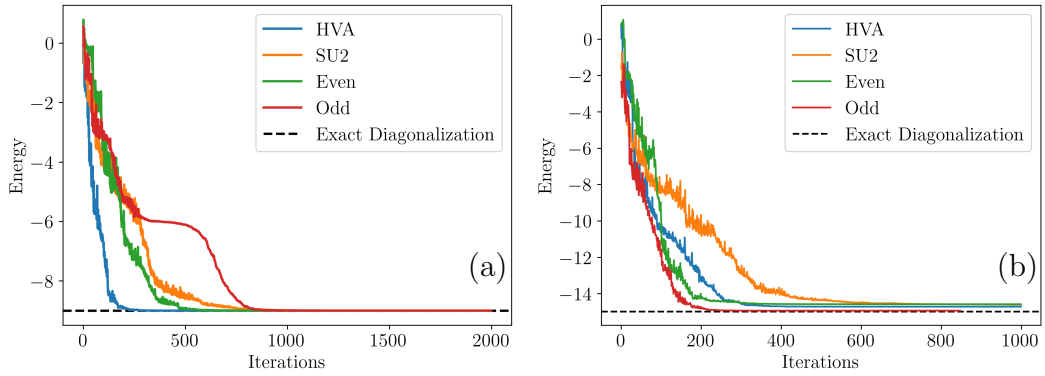

Figure 6.13: Ground state energy as a function of optimization steps for four ansätze: Even, Odd, SU2, and HVA, for a chain of 10 QDs. The comparison highlights the convergence pattern and efficiency of each ansatz in minimizing the ground state energy. (a) corresponds to the analytical case with $\Delta = t$ and $\mu = 0$, while (b) represents a case outside the analytical regime but still within the topological phase, with $\Delta = 2t$ and $\mu = -0.2t$. The optimal number of parameters is used in both cases from Fig. 6.12 [77].

By taking the best number of parameters from Fig. 6.12, in Fig. 6.13 (a), HVA is the fastest ansatz to converge to the ground state, followed by the even, SU2, and odd ansätze. Each ansatz stops at a particular optimization step once the classical optimizer decides it has converged. This happens when the loss function reaches a particular value of energy without changing any further.

In Fig. 6.13b, the system still lies in the topological phase, only there is no known analytical solution based on the choice of the parameters of the Hamiltonian. The odd ansatz gives the fastest convergence with the closest value to the actual ground state energy. The even ansatz converges faster than HVA, but they both give almost the same result for the ground state energy. And lastly the SU2 ansatz is the last ansatz to converge.

Based on these observations, in the analytical case, HVA is a more suitable candidate for representing the ground state. It converges faster than the other ansätze, and also requires less number of parameters. The reason is that by setting $t = \Delta$ and $\mu = 0$ in Eq. (6.57), we obtain

$$\hat{H} = 2t \sum_{j=1}^{N-1} \hat{S}^y_{j+1} \hat{S}^y_j. \tag{6.66}$$

With this simplified form, HVA is a more natural candidate to represent the ground state, since the only active part of the ansatz is the $\prod_{j=1}^{N-1} \exp\left(-i\theta_{j,k}^{y} \hat{S}_{j+1}^{y} \hat{S}_{j}^{y}\right)$, which is a rotation along y-axis.

In the non-analytical case, the odd ansatz proceeds to converge faster and gives a better approximation of the ground state energy comparede to the other ansätze. The system is still in the topological phase, so any wave function (including the ground state) is a linear superposition of all even or odd configurations. From Fig. 6.13b, it can be seen that the even ansatz is the next ansatz that converges to the ground state energy. Therefore, in the non-analytical case, these are the best candidates to display the ground state of the system.

Error Sensitivity within the Topological Phase The next step is to check the sensitivity of each ansatz within the topological phase. To do so, we analyze the relative error for each ansatz while we tune the parameters within the topological phase in the parameter space, which is shown in Fig. 6.14.

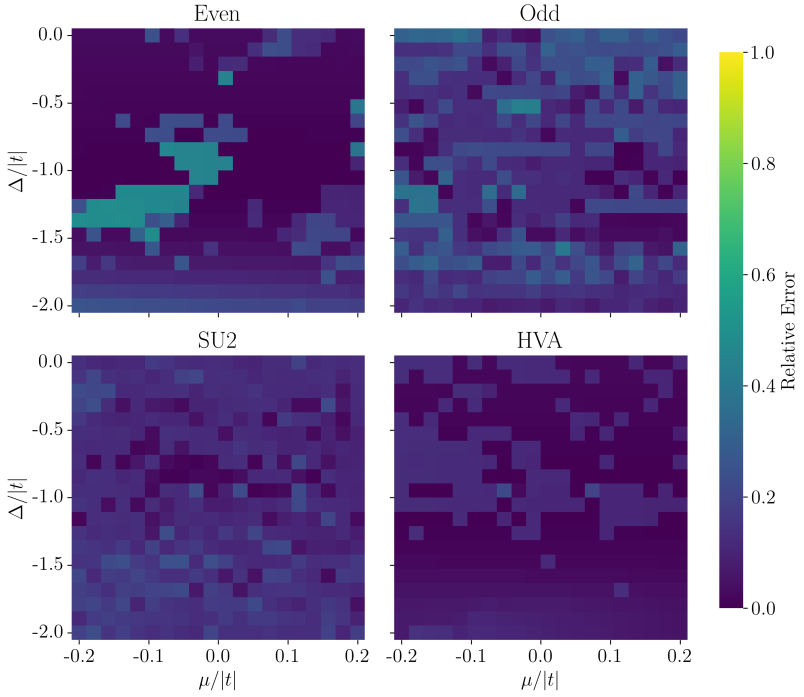

Figure 6.14: Relative error in the parameter space for all four ansätze, for a chain of 10 QDs. The choice of the parameters $\Delta/|t|$ and $\mu/|t|$ is such that the system remains in the topological phase, using 2000 iterations. The dark regions indicate areas of lower relative error, with the analytical solution located at the center of the plots ($t = \Delta$, $\mu = 0$) [77].

In general, as we move away from the centre of the topological phase, the relative

error increases. Once the values of the parameters (t, Δ, and μ) are chosen, Fig. 6.14 provides you with the relative error of each ansatz at that particular point in the parameter space. Therefore, when the choice of parameters of the Hamiltonian (in the topological phase) is given, we can make use of the error profiles to decide which ansatz could be a better representation of the ground state of the system. The error sensitivity, along with the loss function behaviour and the relative error vs. number of parameters are the main factors that affect the final decision of choosing an ansatz for approximating the ground state energy of the Kitaev chain.

This concludes the usage of VQE approach to estimate the ground state energy of the semiconducting QD nanowire in the proximity of a p-wave superconductor. Among the four chosen ansätze in this work, two of them, namely the Even and Odd ansatz are constructed directly from the topological features of the wave function in the topological phase. The HVA ansatz is built from the structure of the Hamiltonian. The final ansatz, efficient SU(2) is a built-in ansatz in the "Qiskit" package. We explored the performance of each ansatz within the topological phase, where the system hosts MZMs. This is an example of how we can design a quantum algorithm to estimate the ground state and the ground state energy of a topological system [77].

Chapter 7

Numerical Analysis of Majorana Zero Modes in the Semiconducting-Superconducting Nanowire

This chapter is based on Ref. [76], with more derivations and detail shown. I have collaborated in doing the calculations in this paper with the first author.

Finally, we study the semiconducting-superconducting nanowire in contact with s-wave superconductor. Our goal here is to introduce and show the application of numerical methods such as ED and DMRG in calculating the spectrum of the system based on the length of the chain, and how we can find the evidence of MZMs. For short chains, we make use of ED for numerical simulations. For longer chains, we use DMRG as a better alternative to calculate the ground state energy of the system. Then we show how this model is connected to the spinless Kitaev chain, and under what conditions they are equivalent. This is done through introducing a new transformation that transforms the spinful system into two coupled spinless chains, where each chain is associated with different spin sectors. Using this connection, we calculate the local spectral function to give us insights about the localized edge states that correspond to MZMs.

7.0.1 Exact Diagonalization in Fermionic Representation

We begin with a hexagonal InP nanowire of embedded InAsP quantum dots hosting spinful electrons. The system is in contact with an s-wave superconductor. We take the external magnetic field to be perpendicular to the nanowire, as is shown in Fig. 7.1.

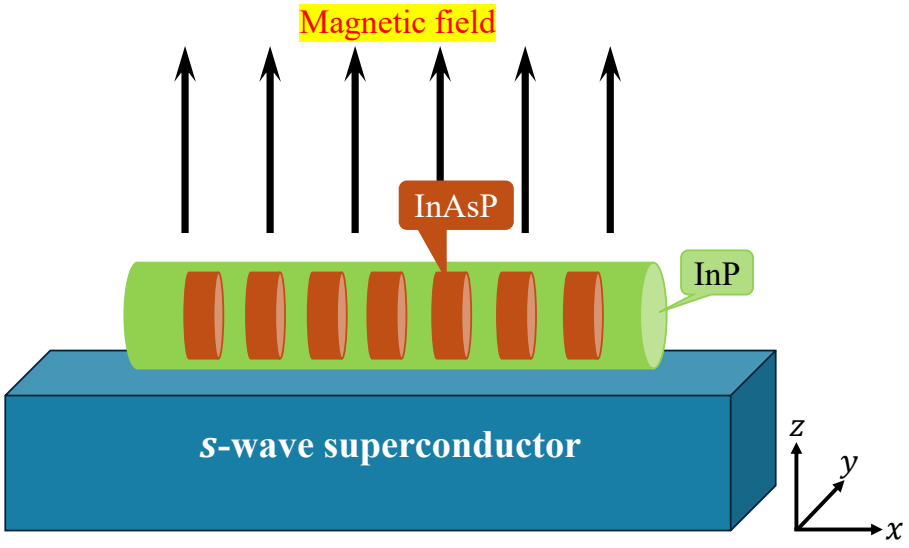

Figure 7.1: Schematic illustration of an InP nanowire hosting an array of embedded InAsP quantum dots, proximity coupled to an s-wave superconductor and subjected to a perpendicular magnetic field, chosen to be orthogonal to the effective Rashba spin orbit coupling and thereby inducing Zeeman splitting [76].

The system is described by the following Hamiltonian

$$
\begin{aligned}
H = t \sum_{i=1}^{N-1} \sum_{\sigma=\uparrow,\downarrow} \left(c^\dagger_{i+1,\sigma} c_{i\sigma} + \text{h.c.} \right) - \mu \sum_{i=1}^{N} \sum_{\sigma=\uparrow,\downarrow} c^\dagger_{i\sigma} c_{i\sigma} \\
+ V_z \sum_{i=1}^{N} \left(c^\dagger_{j\uparrow} c_{j\uparrow} - c^\dagger_{j\downarrow} c_{j\downarrow} \right) \\
+ \alpha \sum_{i=1}^{N-1} \left(c^\dagger_{i+1,\uparrow} c_{i\downarrow} - c^\dagger_{i+1,\downarrow} c_{i\uparrow} - \text{h.c.} \right) \\
+ \Delta \sum_{i=1}^{N} \left(c_{i\uparrow} c_{i\downarrow} + c^\dagger_{i\downarrow} c^\dagger_{i\uparrow} \right).
\end{aligned}
\tag{7.1}
$$

This is the same as the Hamiltonian given in Eq. (5.133), except that we are taking the Zeeman field along the z-axis, and we are using the letter μ instead of μ_{eff}.

We now use ED to obtain the energy spectrum of the system. We construct the Hilbert space in a configuration basis. If we have N orbitals occupied by spinful electrons, the dimension of the Hilbert space is $2^{2N} = 4^N$, as each orbital can be

occupied by two electrons with various spins. We then construct any basis as

$$|n_{1\downarrow}...n_{N\downarrow}\rangle \otimes |n_{1\uparrow}...n_{N\uparrow}\rangle = \prod_{j=1}^{N} (c_{j\downarrow}^{\dagger})^{n_{j\downarrow}} |0_{\downarrow}\rangle \otimes \prod_{j=1}^{N} (c_{j\uparrow}^{\dagger})^{n_{j\uparrow}} |0_{\uparrow}\rangle. \tag{7.2}$$

$|0\rangle$'s show the electron vacuum in each spin basis, $n_{j\sigma} \in \{0, 1\}$ specifies whether the orbital j with spin σ is unoccupied (0) or occupied (1). Each basis state is therefore generated by acting with creation operators on the vacuum according to its specified occupation numbers.

The superconducting term in the Hamiltonian creates or annihilates a pair of two electrons, thus breaking the conservation of particles, as we also saw in the case of a p-wave superconductor. However, the parity of the particles is conserved; i.e, if we begin with an even (odd) parity state, the Hamiltonian does not change it. The eigenstate of the Hamiltonian must therefore be a linear superposition of different particle number sections

$$|\psi^{\nu}\rangle = \sum_{M,p_M} C^{\nu}_{M,p_M} |M, p_M\rangle \tag{7.3}$$

where p_M enumerates all configurations with M electrons distributed among the $2N$ spin orbitals, thus giving the νth eigenstate. The superscript ν in Eq. (7.3) labels the different eigenstates of the Hamiltonian. In other words, for each ν there exists an eigenpair $(E^{\nu}, |\psi^{\nu}\rangle)$ satisfying

$$H|\psi^{\nu}\rangle = E^{\nu}|\psi^{\nu}\rangle. \tag{7.4}$$

Thus, ν plays the role of a spectral index, ordering the many-body eigenstates (for example, $\nu = 0$ for the ground state, $\nu = 1$ for the first excited state, etc.).

To determine the coefficients C^{ν}_{M,p_M}, we apply the Hamiltonian to this state and use the orthogonality of the configuration basis to obtain the eigenvalue equation

$$\sum_{p_M,M} \langle q_{M'}, M'|H_e|p_M, M\rangle C^{\nu}_{M,p_M} = E^{\nu} C^{\nu}_{M',q'_M}. \tag{7.5}$$

The matrix element $\langle q_{M'}, M'|H_e|p_M, M\rangle$ is non-zero only when M and M' have the same fermion parity, that is, both are even or both are odd. Using the parity symmetry, we calculate the energy spectrum in each parity subspace separately. From Eq. (5.83), we know that if $V_z^2 > \Delta^2 + \mu^2$, the system lies in the topological regime. In the topological regime, the energy spectrum of the even and odd parity subspaces must match, meaning that they give the same energy spectra. So, when we say that the

ground state of the system is doubly degenerate, we are referring to the fact that the ground state of the even and odd parity subspaces are the same, giving a doubly degenerate ground state to the total system (even+odd parity). An example of ED calculation is shown in Fig. 7.2 for a chain of 3 quantum dots.

7.0.2 Longer Chains

In the SM-SC Hamiltonian within the topological regime, short chains do not exhibit exact zero-energy Majorana edge states due to the finite-size hybridization of the edge modes [57, 58, 74, 168]. In a finite chain, the Majorana fermion wavefunctions localized at the two ends have a non-negligible spatial overlap that increases as the chain length decreases [74, 168]. This overlap allows the two edge modes to hybridize, lifting the exact zero-energy degeneracy and instead producing a bonding-antibonding pair of fermionic states separated by an energy splitting that decays exponentially with chain length [58, 79]. The term "hybridize" here refers to the fact that the two Majorana operators localized at the opposite ends of a finite chain are not strictly independent when their wavefunctions spatially overlap. The magnitude of this splitting is controlled by the localization length (or inverse bulk gap) ξ of the Majorana wavefunctions: when the chain length is comparable to or shorter than this characteristic length scale, hybridization effects dominate and preclude the observation of true topological protection [57]. The characteristic length scale ξ is the superconducting coherence length associated with the topological gap. In continuum models of one-dimensional topological superconductors, it can be estimated as

$$\xi \sim \frac{\hbar v_F}{\Delta_{\text{top}}}, \tag{7.6}$$

where v_F is the Fermi velocity and Δ_{top} is the bulk topological gap [57, 58, 168]. Equivalently, ξ is inversely proportional to the minimum excitation gap in the bulk spectrum.

For semiconductor nanowires with proximity-induced superconductivity, typical parameters ($\Delta_{\text{top}} \sim 0.1$–$0.5\,\text{meV}$, $v_F \sim 10^5$–$10^6\,\text{m/s}$) yield coherence lengths in the range

$$\xi \sim 100\,\text{nm to } 1\,\mu\text{m}. \tag{7.7}$$

Therefore, if the physical chain length L satisfies $L \lesssim \xi$, the Majorana edge wavefunctions overlap strongly and the energy splitting becomes significant. True topological protection is recovered only in the regime $L \gg \xi$, where the overlap—and hence the

splitting—decays exponentially as

$$\delta E \propto e^{-L/\xi}. \tag{7.8}$$

This requirement that $L \gg \xi$ (where L is chain length and ξ is the Majorana localization length) is thus essential for observing unambiguous signatures of topological protection in finite-size systems.

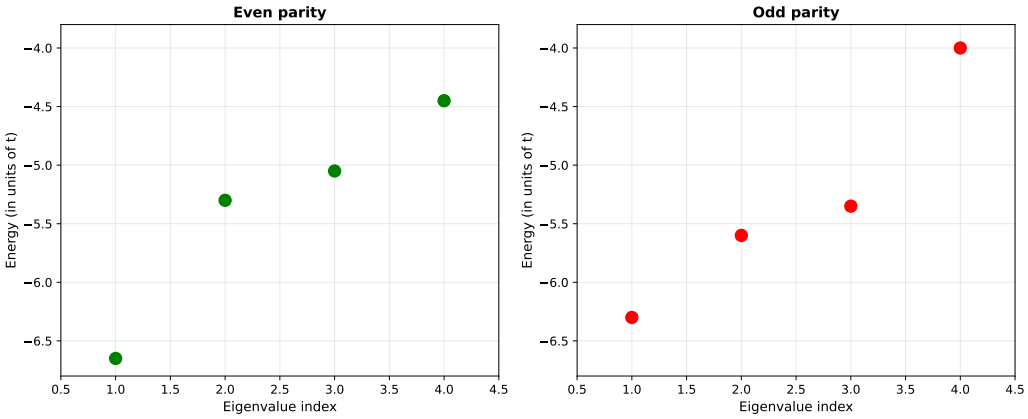

Figure 7.2: First four energy levels of the SM-SC Hamiltonian in the topological regime through using ED for a chain with 3 quantum dots, for $t = \Delta = -1$, $\mu = 0$, $\alpha = 0.8$, and $V_z = 1.7$, ensuring that the system is in the topological phase. All parameters and energy levels are normalized to the unit of t. Left panel shows even parity sector and right panel shows odd parity sector. The energy splitting between states reflects finite-size effects and hybridization of Majorana edge modes at the chain boundaries. Without the hybridization, we would have expected the ground states of the even and odd parity sectors to be the same (or a doubly-degenerate ground state energy of the entire system).

As an example, in Fig. 7.2 the first four energy levels of the even and odd parity subspaces for a chain of length $N = 3$ in the topological phase are shown. This is calculated using ED. Although energy levels of each subspace are very close to those of the other subspace, they are not exactly the same.

ED gives the entire spectrum in an exact fashion, but we can only use it for small system size. In our case, since the dimension of the full Hilbert space grows as 4^N for a chain of N quantum dots (each site hosting four local states), the computational cost increases exponentially with system size. For example,

$$4^{10} = 1,048,576, \tag{7.9}$$

so that already at $N = 10$ the Hamiltonian matrix has dimension of order 10^6. A dense

representation of such a matrix would require $\mathcal{O}(10^{12})$ complex entries, corresponding to multiple terabytes of memory, which is far beyond the capabilities of standard workstations.

Even when exploiting particle-number or parity conservation and using sparse-matrix iterative eigensolvers (e.g., Lanczos), the memory requirements and CPU time grow rapidly. On a typical multi-core desktop machine (32–128 GB RAM), exact diagonalization of the full Hilbert space becomes impractical beyond $N \approx 10$–12 sites. Larger system sizes require high-performance computing clusters and careful symmetry reduction. For chains longer than $N = 10$, we turn to the DMRG method. Being a variational approach, DMRG gives the ground state of the system with an error that can be controlled [68], and it works much more efficiently for longer chains. The downside is that it does not provide us with the entire spectrum. So, as long as one is interested only in the ground state energy for long chains, DMRG can serve as a fast and reliable method [68, 216, 217]. We use DMRG for each subspace separately to find its ground state, and then we find the sufficient system size for energy difference convergence (number of quantum dots) by calculating $\Delta E = |E_{\mathrm{GS}}^{\mathrm{Even}} - E_{\mathrm{GS}}^{\mathrm{Odd}}|$. We expect that in the topological regime, as we go to longer chains, ΔE goes to zero, as shown in Fig. 7.3.

7.0.3 Two Coupled Kitaev Chains

In this section, we illustrate how one can express the SM-SC Hamiltonian in terms of two coupled Kitaev chains, where each chain is for one spin species. The goal of this representation is to take advantage of the spinless Kitaev chain by imposing certain constraints on the parameters of the Hamiltonian that ensure Majorana zero modes to exist. This representation proves useful for spectral function calculations.

We begin with the lattice version of the Hamiltonian in Eq. (7.1). To isolate the on–site part (chemical potential, Zeeman, and pairing), we introduce a local electron–hole spinor built from the $\uparrow$ electrons and the $\downarrow$ holes:

$$\Phi_j^\dagger = \left(c_{j\uparrow}^\dagger,\ c_{j\downarrow}\right), \qquad \Phi_j = \begin{pmatrix} c_{j\uparrow} \\ c_{j\downarrow}^\dagger \end{pmatrix}. \tag{7.10}$$

Using $c_{j\downarrow}c_{j\downarrow}^\dagger = 1 - c_{j\downarrow}^\dagger c_{j\downarrow}$, one easily checks that

$$\left(c_{j\uparrow}^\dagger\ c_{j\downarrow}\right) \begin{pmatrix} 1 & 0 \\ 0 & 1 \end{pmatrix} \begin{pmatrix} c_{j\uparrow} \\ c_{j\downarrow}^\dagger \end{pmatrix} = c_{j\uparrow}^\dagger c_{j\uparrow} + c_{j\downarrow}c_{j\downarrow}^\dagger = 1 + c_{j\uparrow}^\dagger c_{j\uparrow} - c_{j\downarrow}^\dagger c_{j\downarrow}. \tag{7.11}$$

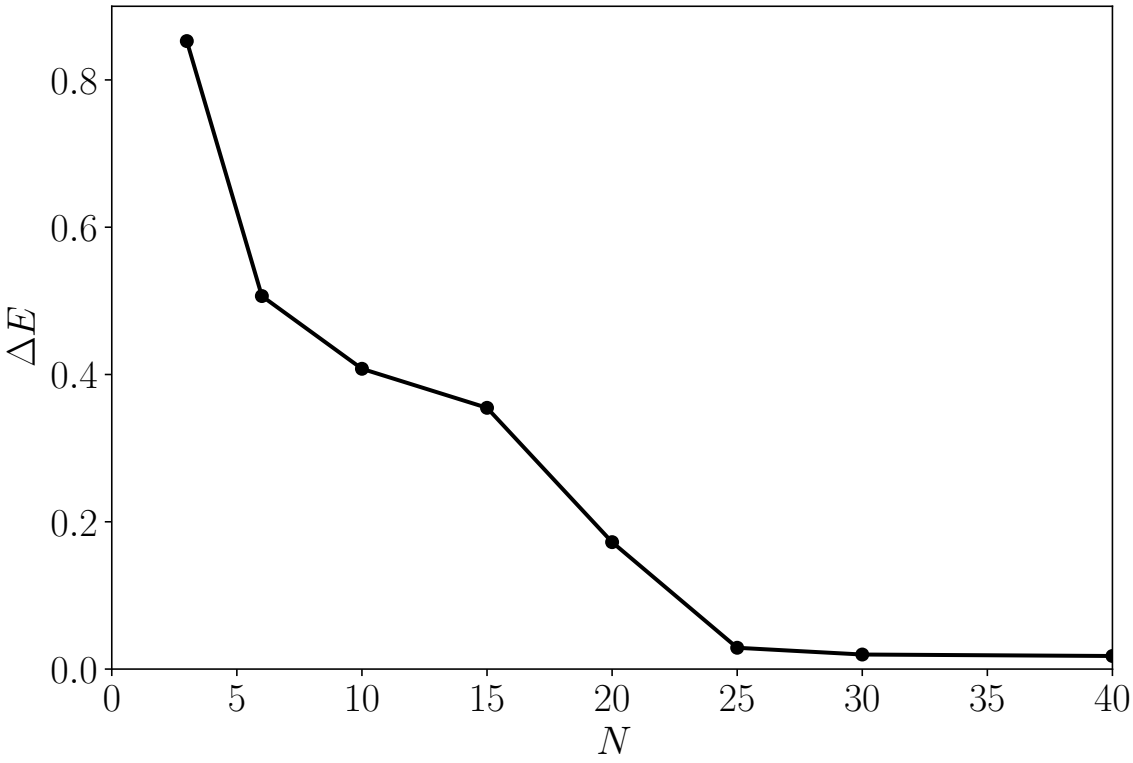

Figure 7.3: Finite size scaling of the even odd parity splitting $\Delta E = |E_{\mathrm{GS}}^{\mathrm{Even}} - E_{\mathrm{GS}}^{\mathrm{Odd}}|$ as a function of number of quantum dots in the chain using DMRG and the ITensor library [76, 218]. The parameters are chosen to be the same as in Fig. 7.2.

Collecting the chemical potential, Zeeman, and pairing terms, we obtain

$$\hat{H}_{\text{on-site}} = -\mu \sum_j \left(c_{j\uparrow}^\dagger c_{j\uparrow} + c_{j\downarrow}^\dagger c_{j\downarrow} \right) + V_z \sum_j \left(c_{j\uparrow}^\dagger c_{j\uparrow} - c_{j\downarrow}^\dagger c_{j\downarrow} \right) + \Delta \sum_j \left(c_{j\downarrow}^\dagger c_{j\uparrow}^\dagger + c_{j\uparrow} c_{j\downarrow} \right). \tag{7.12}$$

Using Eq. (7.11) to eliminate $c_{j\downarrow} c_{j\downarrow}^\dagger$ in favor of number operators and a constant, this can be rearranged as

$$\hat{H}_{\text{on-site}} = \sum_{j=1}^{N} \Phi_j^\dagger \, M \, \Phi_j - N \, (V_z + \mu), \tag{7.13}$$

where the 2×2 matrix M is

$$M = \begin{pmatrix} V_z - \mu & -\Delta \\ -\Delta & V_z + \mu \end{pmatrix}. \tag{7.14}$$

The constant $-N(V_z + \mu)$ only shifts the overall energy, with N being the total number of quantum dots in the system. The matrix M has two eigenvalues

$$\lambda_{1,2} = V_z \pm \sqrt{\mu^2 + \Delta^2}, \tag{7.15}$$

with corresponding normalized eigenvectors

$$X_1 = \ell \begin{pmatrix} -\xi \\ 1 \end{pmatrix}, \qquad X_2 = \ell \begin{pmatrix} 1 \\ \xi \end{pmatrix}, \tag{7.16}$$

where

$$\xi = \Delta \Big(\mu + \sqrt{\mu^2 + \Delta^2} \Big)^{-1}, \qquad \ell = (1 + \xi^2)^{-1/2}. \tag{7.17}$$

The vectors X_1 and X_2 form an orthonormal basis of the two–component electron–hole space at each site j.

We now define new fermionic operators $d_{j\sigma}$ by expanding the electron–hole spinor Φ_j in the eigenbasis of M:

$$\Phi_j = X_1 \, d_{j\uparrow} + X_2 \, d_{j\downarrow}, \tag{7.18}$$

or explicitly,

$$\begin{pmatrix} c_{j\uparrow}^{\dagger} \\ c_{j\downarrow}^{\dagger} \end{pmatrix} = \ell \begin{pmatrix} -\xi & 1 \\ 1 & \xi \end{pmatrix} \begin{pmatrix} d_{j\uparrow}^{\dagger} \\ d_{j\downarrow}^{\dagger} \end{pmatrix}, \qquad \text{equivalently} \qquad \begin{pmatrix} c_{j\uparrow} \\ c_{j\downarrow} \end{pmatrix} = \ell \begin{pmatrix} -\xi & 1 \\ 1 & \xi \end{pmatrix} \begin{pmatrix} d_{j\uparrow} \\ d_{j\downarrow} \end{pmatrix}. \tag{7.19}$$

Because the transformation matrix is unitary, the new operators $d_{j\sigma}, d_{j\sigma}^{\dagger}$ obey the usual fermionic anticommutation relations. The spin label $\sigma = \uparrow, \downarrow$ is now best regarded as a band index labelling the two eigenmodes of the local problem (rather than the original physical spin).

Using the transformation in Eq. (7.19), the chemical–potential, Zeeman and on–site s–wave pairing terms can be combined and rewritten as

$$\hat{H}_{\text{on-site}} = \widetilde{\mu} \sum_{j=1}^{N} \sum_{\sigma=\uparrow,\downarrow} d_{j\sigma}^{\dagger} d_{j\sigma} + V_z \sum_{j=1}^{N} d_{j\uparrow}^{\dagger} d_{j\uparrow} - V_z \sum_{j=1}^{N} d_{j\downarrow}^{\dagger} d_{j\downarrow} - N(\widetilde{\mu} + \mu), \tag{7.20}$$

where

$$\widetilde{\mu} = \sqrt{\mu^2 + \Delta^2}. \tag{7.21}$$

This form makes it clear that the new fermions $d_{j\sigma}$ still carry a spin label σ in the sense that the Zeeman term acts on them as $\pm V_z$ for $\sigma = \uparrow, \downarrow$, just as it did on the original operators $c_{j\sigma}$.

The nearest–neighbour hopping term $t \sum_{j\sigma} [c_{j+1,\sigma}^{\dagger} c_{j\sigma} + \text{h.c.}]$ transforms as

$$\begin{aligned} t \sum_{j=1}^{N-1} \sum_{\sigma=\uparrow,\downarrow} \left[c_{j+1,\sigma}^{\dagger} c_{j\sigma} + \text{h.c.} \right] = \widetilde{t} \sum_{j=1}^{N-1} \sum_{\sigma=\uparrow,\downarrow} \left[d_{j+1,\sigma}^{\dagger} d_{j\sigma} + \text{h.c.} \right] \\ + \Delta_t \sum_{j=1}^{N-1} \left[d_{j\uparrow}^{\dagger} d_{j+1,\downarrow}^{\dagger} + d_{j+1,\uparrow}^{\dagger} d_{j\downarrow}^{\dagger} + \text{h.c.} \right], \end{aligned} \tag{7.22}$$

with

$$\widetilde{t} = -\frac{2t\mu}{\Delta} \ell^2 \xi, \qquad \Delta_t = -2t \, \ell^2 \xi, \tag{7.23}$$

where ℓ and ξ are defined in Eq. (7.17). Thus a simple hopping term in the c-basis becomes, in the d-basis, a renormalized hopping $\widetilde{t}$ plus an intersite pairing term Δ_t, which has the structure of a p–wave pairing between adjacent sites.

Similarly, the spin–orbit term $-\alpha \sum_j [c^\dagger_{j\uparrow} c_{j+1,\downarrow} - c^\dagger_{j\downarrow} c_{j+1,\uparrow} + \text{h.c.}]$ transforms into

$$-\alpha \sum_{j=1}^{N-1} \Big[c^\dagger_{j\uparrow} c_{j+1,\downarrow} - c^\dagger_{j\downarrow} c_{j+1,\uparrow} + \text{h.c.}\Big] = -\widetilde{\alpha} \sum_{j=1}^{N-1} \Big[d^\dagger_{j\uparrow} d_{j+1,\downarrow} - d^\dagger_{j\downarrow} d_{j+1,\uparrow} + \text{h.c.}\Big] + \Delta_\alpha \sum_{j=1}^{N-1} \sum_{\sigma=\uparrow,\downarrow} \Big[d_{j+1,\sigma} d_{j\sigma} + \text{h.c.}\Big], \tag{7.24}$$

where

$$\widetilde{\alpha} = \frac{2\alpha\mu}{\Delta}\, \ell^2 \xi, \qquad \Delta_\alpha = 2\alpha\, \ell^2 \xi. \tag{7.25}$$

Again, we see that the original spin–orbit coupling produces both a renormalized spin–orbit term $\widetilde{\alpha}$ and an additional p–wave–like pairing term Δ_α between neighboring sites.

Putting together Eqs. (7.20), (7.22), and (7.24), the SM-SC Hamiltonian can be written as

$$\hat{H} = \hat{H}_1 + \hat{H}_2 + \hat{H}_{12} - N(\widetilde{\mu} + \mu), \tag{7.26}$$

where

$$\hat{H}_1 = \widetilde{t} \sum_{j=1}^{N-1} \Big[d^\dagger_{j+1,\downarrow} d_{j\downarrow} + \text{h.c.}\Big] + \Delta_\alpha \sum_{j=1}^{N-1} \Big[d_{j+1,\downarrow} d_{j\downarrow} + \text{h.c.}\Big] + (\widetilde{\mu} - V_z) \sum_{j=1}^{N} d^\dagger_{j\downarrow} d_{j\downarrow}, \tag{7.27}$$

$$\hat{H}_2 = \widetilde{t} \sum_{j=1}^{N-1} \Big[d^\dagger_{j+1,\uparrow} d_{j\uparrow} + \text{h.c.}\Big] + \Delta_\alpha \sum_{j=1}^{N-1} \Big[d_{j+1,\uparrow} d_{j\uparrow} + \text{h.c.}\Big] + (\widetilde{\mu} + V_z) \sum_{j=1}^{N} d^\dagger_{j\uparrow} d_{j\uparrow}, \tag{7.28}$$

$$\hat{H}_{12} = \Delta_t \sum_{j=1}^{N-1} \Big[d^\dagger_{j\uparrow} d^\dagger_{j+1,\downarrow} + d^\dagger_{j+1,\uparrow} d^\dagger_{j\downarrow} + \text{h.c.}\Big] - \frac{\widetilde{\alpha}}{2} \sum_{j=1}^{N-1} \Big[d^\dagger_{j\uparrow} d_{j+1,\downarrow} - d^\dagger_{j\downarrow} d_{j+1,\uparrow} + \text{h.c.}\Big]. \tag{7.29}$$

The terms H_1 and H_2 describe two independent Kitaev chains, built from the fermions $d_{j\downarrow}$ and $d_{j\uparrow}$, respectively. They have identical hopping $\widetilde{t}$ and p–wave pairing amplitude Δ_α, but different effective chemical potentials $\widetilde{\mu} - V_z$ and $\widetilde{\mu} + V_z$. The term H_{12} couples the two chains through both inter–chain pairing (Δ_t) and inter–chain

spin–orbit–induced hopping ($\widetilde{\alpha}$). This representation makes explicit that the original s–wave nanowire with Zeeman field and spin–orbit coupling can be viewed as two coupled Kitaev chains with different effective parameters.

Spinful Majorana and Bond Transformations Now we apply Majorana and bond transformations on spinful fermions of the SM-SC system, schematically shown in Fig. 7.4. Starting from the two coupled Kitaev chains written in terms of the $d_{j\sigma}$

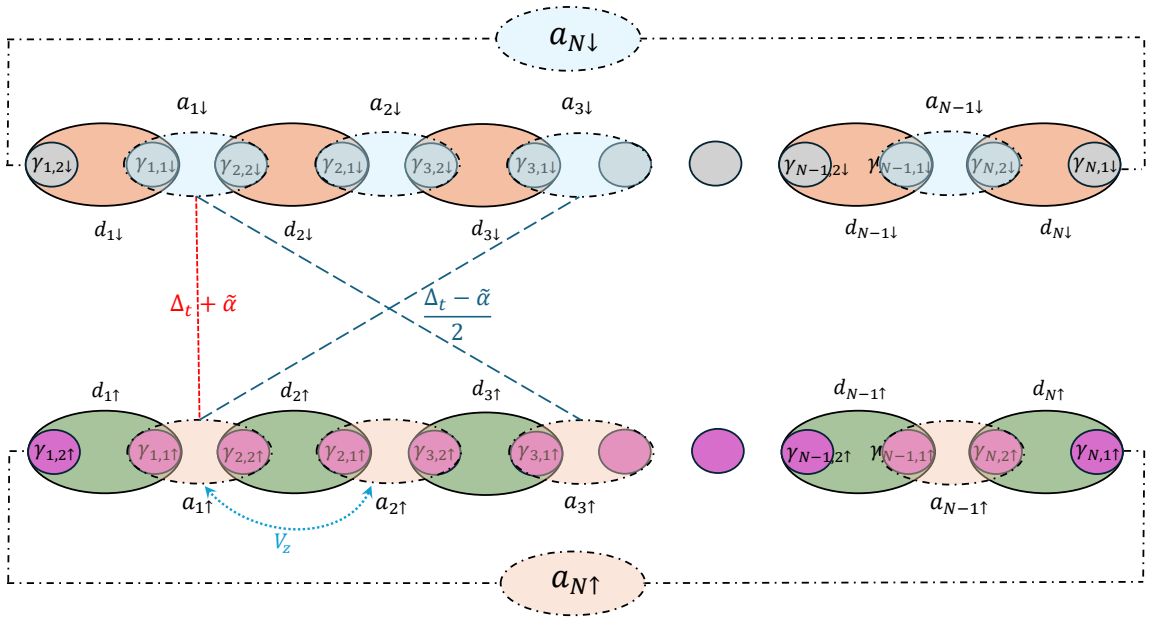

Figure 7.4: Schematic of the two coupled Kitaev chains (upper for spin down and lower for spin up) in the Majorana and bond Fermion representation, with non-zero bond Fermions $a_{j\downarrow}$ and $a_{j\uparrow}$ ($j \neq N$), and the non local zero mode positioned at the two ends of the two chains represented as $a_{N\downarrow}$ and $a_{N\uparrow}$. The couplings between the two chains are shown as red and blue dashed lines [76].

fermions, we first introduce on each site j and for each spin $\sigma =\uparrow,\downarrow$ a pair of Majorana operators. For the lower spin down chain we define

$$\gamma_{j\downarrow} = d_{j\downarrow} + d^{\dagger}_{j\downarrow}, \qquad \bar{\gamma}_{j\downarrow} = i\Big(d_{j\downarrow} - d^{\dagger}_{j\downarrow}\Big), \tag{7.30}$$

and for the upper spin up chain

$$\gamma_{j\uparrow} = d_{j\uparrow} + d^{\dagger}_{j\uparrow}, \qquad \bar{\gamma}_{j\uparrow} = i\Big(d_{j\uparrow} - d^{\dagger}_{j\uparrow}\Big). \tag{7.31}$$

Each Majorana operator is Hermitian, $\gamma^{\dagger}_{j\sigma} = \gamma_{j\sigma}$ and $\bar{\gamma}^{\dagger}_{j\sigma} = \bar{\gamma}_{j\sigma}$, and they satisfy the standard anticommutation relations $\{\gamma_{j\sigma}, \gamma_{l\sigma'}\} = \{\bar{\gamma}_{j\sigma}, \bar{\gamma}_{l\sigma'}\} = 2\delta_{jl}\delta_{\sigma\sigma'}$ and

$\{\gamma_{j\sigma}, \bar{\gamma}_{l\sigma'}\} = 0$.

From chapter 4, we know that the spinless Kitaev Hamiltonian is diagonal for the choice of $t = \Delta$ and $\mu = 0$. We choose the same point here in terms of our parameters

$$\tilde{t} = \Delta_\alpha, \qquad V_z = \tilde{\mu}. \tag{7.32}$$

The two Kitaev chains and their coupling can be rewritten in the Majorana basis as

$$\hat{H}_1 = \tilde{t} \sum_{j=1}^{N-1} i\, \bar{\gamma}_{j\downarrow}\, \gamma_{j+1,\downarrow}, \tag{7.33}$$

$$\hat{H}_2 = \tilde{t} \sum_{j=1}^{N-1} i\, \bar{\gamma}_{j\uparrow}\, \gamma_{j+1,\uparrow} + V_z \sum_{j=1}^{N} \Big(1 + i\, \bar{\gamma}_{j\uparrow}\gamma_{j\uparrow}\Big), \tag{7.34}$$

$$\begin{aligned}\hat{H}_{12} = {} & \frac{i(2\Delta_t + \tilde{\alpha})}{4} \sum_{j=1}^{N-1} \Big[\gamma_{j\uparrow}\, \bar{\gamma}_{j+1,\downarrow} + \bar{\gamma}_{j+1\uparrow}\, \gamma_{j,\downarrow}\Big] \\ & + \frac{i(2\Delta_t - \tilde{\alpha})}{4} \sum_{j=1}^{N-1} \Big[\gamma_{j+1,\uparrow}\, \bar{\gamma}_{j\downarrow} + \bar{\gamma}_{j,\uparrow}\, \gamma_{j+1\downarrow}\Big].\end{aligned} \tag{7.35}$$

The first two terms, H_1 and H_2, now clearly describe Majoranas coupled on neighbouring sites of each chain. The inter-chain coupling H_{12} contains Majorana bilinears that connect the two chains and mix the $\uparrow$ and $\downarrow$ sectors.

Now we recombine neighbouring Majoranas into bond fermions. For the $\downarrow$ chain we define, for $j = 1, \ldots, N-1$,

$$a_{j\downarrow} = \frac{1}{2}\Big(\gamma_{j+1,\downarrow} - i\bar{\gamma}_{j\downarrow}\Big), \qquad a^\dagger_{j\downarrow} = \frac{1}{2}\Big(\gamma_{j+1,\downarrow} + i\bar{\gamma}_{j\downarrow}\Big), \tag{7.36}$$

and the last bond fermion of the $\downarrow$ chain we set

$$a_{N\downarrow} = \frac{1}{2}\Big(\gamma_{1\downarrow} - i\bar{\gamma}_{N\downarrow}\Big). \tag{7.37}$$

Similarly, for the $\uparrow$ chain we introduce

$$a_{j\uparrow} = \frac{1}{2}\Big(\gamma_{j+1,\uparrow} - i\bar{\gamma}_{j\uparrow}\Big), \qquad a^\dagger_{j\uparrow} = \frac{1}{2}\Big(\gamma_{j+1,\uparrow} + i\bar{\gamma}_{j\uparrow}\Big), \tag{7.38}$$

with

$$a_{N\uparrow} = \frac{1}{2}\Big(\gamma_{1\uparrow} - i\bar{\gamma}_{N\uparrow}\Big). \tag{7.39}$$

In terms of these bond fermions, the Hamiltonian $\hat{H}_1$ simplifies to

$$\hat{H}_1 = 2\tilde{t} \sum_{j=1}^{N-1} \left(a_{j\downarrow}^\dagger a_{j\downarrow} - \frac{1}{2} \right) + 0 \left(a_{N\downarrow}^\dagger a_{N\downarrow} - \frac{1}{2} \right). \tag{7.40}$$

Thus, in this representation H_1 is a sum over independent bond fermion number operators (up to a constant), and the boundary mode $a_{N\downarrow}$ completely drops out, similar to the diagonal form of the original spinless Kitaev Hamiltonian.

For the upper chain, $\hat{H}_2$ in the bond–fermion basis becomes

$$\begin{aligned} \hat{H}_2 = {} & 2\tilde{t} \sum_{j=1}^{N-1} \left(a_{j\uparrow}^\dagger a_{j\uparrow} - \frac{1}{2} \right) + 0 \left(a_{N\uparrow}^\dagger a_{N\uparrow} - \frac{1}{2} \right) \\ & + V_z \Big[a_{1\uparrow}^\dagger a_{N\uparrow}^\dagger + a_{N\uparrow} a_{1\uparrow} + a_{N\uparrow}^\dagger a_{1\uparrow} + a_{1\uparrow}^\dagger a_{N\uparrow} \Big] \\ & + V_z \sum_{j=1}^{N-1} \Big[a_{j+1,\uparrow}^\dagger a_{j\uparrow}^\dagger + a_{j\uparrow} a_{j+1,\uparrow} + a_{j+1,\uparrow}^\dagger a_{j\uparrow} + a_{j\uparrow}^\dagger a_{j+1,\uparrow} \Big] + N V_z. \end{aligned} \tag{7.41}$$

The first line mirrors the structure of $\hat{H}_1$, while the second and third lines show that the Zeeman term V_z induces on-site and nearest-neighbour pairing and hopping of the bond fermions, as well as couplings between the two boundary modes $a_{1\uparrow}$ and $a_{N\uparrow}$.

The second term of $\hat{H}_{12}$ in Eq. (7.35) simplifies to a pure s–wave pairing between bond fermions on the same bond:

$$\frac{i(2\Delta_t - \tilde{\alpha})}{4} \sum_{j=1}^{N-1} \Big[\gamma_{j+1,\uparrow}\, \bar{\gamma}_{j\downarrow} + \bar{\gamma}_{j,\uparrow}\, \gamma_{j+1\downarrow} \Big] = - \frac{2\Delta_t - \tilde{\alpha}}{2} \sum_{j=1}^{N-1} \Big(a_{j\downarrow}^\dagger a_{j\uparrow}^\dagger + a_{j\uparrow} a_{j\downarrow} \Big). \tag{7.42}$$

Note that the boundary bond fermions $a_{N\uparrow}$ and $a_{N\downarrow}$ do not appear in this term.

The other term in H_{12} generates longer-range pairing and spin-orbit-like couplings

between bond fermions on different links

$$\frac{i(2\Delta_t+\tilde{\alpha})}{4}\sum_{j=1}^{N-1}\Big[\gamma_{j\uparrow}\,\bar{\gamma}_{j+1,\downarrow}+\bar{\gamma}_{j+1\uparrow}\,\gamma_{j,\downarrow}\Big]=$$

$$-\frac{2\Delta_t+\tilde{\alpha}}{4}(\sum_{j=1}^{N-2}\Big[a^{\dagger}_{j+2,\downarrow}a^{\dagger}_{j\uparrow}+a_{j\uparrow}a_{j+2,\downarrow}$$

$$+a^{\dagger}_{j+2,\downarrow}a_{j\uparrow}+a^{\dagger}_{j\uparrow}a_{j+2,\downarrow}$$

$$+\;a^{\dagger}_{j\downarrow}a^{\dagger}_{j+2,\uparrow}+a_{j+2,\uparrow}a_{j\downarrow}$$

$$+a^{\dagger}_{j+2,\uparrow}a_{j\downarrow}+a^{\dagger}_{j\downarrow}a_{j+2,\uparrow}\Big]$$

$$+\Big[a^{\dagger}_{2\downarrow}a^{\dagger}_{N\uparrow}+a_{N\uparrow}a_{2\downarrow}$$

$$+a^{\dagger}_{2\downarrow}a_{N\uparrow}+a^{\dagger}_{N\uparrow}a_{2\downarrow}$$

$$+\;a^{\dagger}_{N\downarrow}a^{\dagger}_{2\uparrow}+a_{2\uparrow}a_{N\downarrow}$$

$$+a_{2\uparrow}a^{\dagger}_{N\downarrow}+a_{N\downarrow}a^{\dagger}_{2\uparrow}\Big]). \tag{7.43}$$

This structure shows explicitly that $\hat{H}_{12}$ contains s–wave pairing and spin-orbit-induced couplings between even-even and odd-odd numbered bond fermions (or auxiliary sites). The boundary bond fermions again appear only through the last line, coupling the sites near one end of the chain to those at the opposite end.

In the ideal situation where the two effective Kitaev chains are decoupled (i.e. $\hat{H}_{12}=0$), the spin–down chain $\hat{H}_1$ is a perfect Kitaev chain in the topological regime. In that case it is easy to show that the creation operator of the right–end bond fermion, $a^{\dagger}_{N\downarrow}$, commutes with the full Hamiltonian,

$$[\hat{H},a^{\dagger}_{N\downarrow}]=0, \tag{7.44}$$

since the Hamiltonian does not contain any of the bond operators regarding the last site N. So that $a^{\dagger}_{N\downarrow}$ creates an exact zero–energy edge mode.

Once the two chains are coupled by $\hat{H}_{12}$, this commutator is no longer exactly zero. A straightforward calculation using the bond fermion representation shows that

$$[H_0,a^{\dagger}_{N\downarrow}]=-\frac{2\Delta_t+\tilde{\alpha}}{4}\Big(a_{2\uparrow}-a^{\dagger}_{2\uparrow}+a_{N-2,\uparrow}+a^{\dagger}_{N-2,\uparrow}\Big), \tag{7.45}$$

so the right–end spin–down bond fermion couples only to two spin–up bond fermions, namely $a^{\dagger}_{2\uparrow}$ and $a^{\dagger}_{N-2,\uparrow}$. Equation (7.45) shows that the commutator can be made

small and in the thermodynamic limit essentially zero, by imposing the constraint

$$2\Delta_t + \tilde{\alpha} \approx 0. \tag{7.46}$$

This leads to the so-called "maximal constraints". From the Majorana and bond–fermion analysis, we found that, in order for $\hat{H}_1$ to describe a topological Kitaev chain (with a well localized edge Majorana) we must choose the renormalized parameters as

$$\tilde{t} = \Delta_\alpha, \qquad \tilde{\mu} = V_z, \tag{7.47}$$

where V_z is the Zeeman energy associated with the magnetic field along the z-direction in our convention, and Δ_α is the effective p-wave pairing amplitude within each chain.

For the second chain H_2 we obtain analogous conditions,

$$\tilde{t} = \Delta_\alpha, \qquad \tilde{\mu} = -V_z. \tag{7.48}$$

Equations (7.47) and (7.48), together with the requirement in Eq.(7.46), define a set of maximal constraints: they make $\hat{H}_1$ diagonally solvable in terms of bond fermions, while $\hat{H}_2 + \hat{H}_{12}$ still supports a gapped spectrum. In the thermodynamic limit the even and odd ground states of the full Hamiltonian $\hat{H} = \hat{H}_1 + \hat{H}_2 + \hat{H}_{12}$ form a two–fold degenerate ground space.

With a magnetic field $+V_z$, the spin-down Majorana fermion is localized at the end of the chain; reversing the field to $-V_z$ localizes the spin-up Majorana at the end of the chain. Thus the sign of the Zeeman field selects which spin sector hosts the edge Majorana mode.

We now express the constraints on the renormalized parameters $\tilde{t}, \tilde{\mu}, \Delta_t, \Delta_\alpha$ and $\tilde{\alpha}$ in terms of the original parameters of the proximitized nanowire: nearest–neighbour hopping t, spin–orbit strength α, chemical potential μ, s–wave pairing Δ, and Zeeman field V_z.

From the two–chain mapping we had

$$\tilde{\mu} = \sqrt{\mu^2 + \Delta^2}, \tag{7.49}$$

$$\tilde{t} = -\frac{2t\mu}{\Delta}\frac{\xi}{1+\xi^2}, \qquad \Delta_\alpha = \frac{2\alpha\,\xi}{1+\xi^2}, \tag{7.50}$$

where

$$\xi = \Delta\Big(\mu + \sqrt{\mu^2 + \Delta^2}\Big)^{-1}. \tag{7.51}$$

The condition $\tilde{\mu} = \pm V_z$ immediately yields

$$V_z = \pm\sqrt{\mu^2 + \Delta^2}, \tag{7.52}$$

which is precisely the same criterion for gap closing and reopening that we found from the bulk spectrum: tuning V_z through $\sqrt{\mu^2 + \Delta^2}$ drives the system through the topological phase transition. It marks the phase boundary, not the topological phase itself. Exactly at $V_z = \sqrt{\mu^2 + \Delta^2}$ the bulk gap vanishes, the spectrum is gapless, and there is no protecting gap, so the system is not topologically protected at this single point. This is expected rather than a problem. The bulk gap must close for the topological index to change, so the closing is the fingerprint of the transition and not a feature of the topological phase.

Next we impose $\tilde{t} = \Delta_\alpha$. Using Eq. (7.50), we obtain

$$-\frac{2t\mu}{\Delta}\frac{\xi}{1+\xi^2} = \frac{2\alpha\,\xi}{1+\xi^2} \quad \Longrightarrow \quad t\mu = -\alpha\Delta. \tag{7.53}$$

Up to an overall sign convention for α (which can be absorbed by a gauge transformation), this is usually written as

$$t\,\mu = \Delta\,\alpha. \tag{7.54}$$

Equations (7.52) and (7.54) summarize the maximal constraints in terms of the original parameters:

$$t\,\mu = \Delta\,\alpha, \qquad V_z = \pm\sqrt{\mu^2 + \Delta^2}. \tag{7.55}$$

They provide a concrete recipe for engineering Majorana zero modes in a given device. For instance, in the case of InAsP quantum dots embedded in an InP nanowire, one can first determine the effective hopping amplitudes t, spin–orbit strength α, and induced pairing Δ from microscopic calculations. The relations above then specify which combinations of chemical potential μ and magnetic field V_z optimally realize the Kitaev–chain limit and hence maximize the localization and robustness of the Majorana edge states. This model exhibits MZMs as we approach the thermodynamic limit, i.e. we take a long enough chain so that the interaction term between the two spin bands becomes negligible, and then through choosing the right set of parameters, one of the spin bands is in the trivial phase, while the other one is in the topological phase, in the exact diagonal form in bond fermion representation that shows the zero mode as the last missing bond fermion.

To show these results numerically, we calculate the energy spectrum of the two

coupled Kitaev chains using ED. We take a chain of $N = 3$ quantum dots, and we choose $t = \Delta = 1$, $\alpha = 0.8$, $\mu = \alpha\frac{\Delta}{t}$, and $V_z = \sqrt{\mu^2 + \Delta^2}$. This way $\tilde{t} = \Delta_\alpha$ and $V_z = \tilde{\mu}$ are satisfied, and the system remains in the topological phase. We show the first four energy levels in each parity subspace. In Fig. 7.5 we see that the spectrum of $\hat{H}_1$ shows a perfect matching of the even and odd parity subspaces, since the spin down band is in the topological phase. As this case corresponds to the diagonal representation of the original spinless Kiteav Hamiltonian, we see a perfect matching in the energy spectra of the even and odd subspaces despite the small size of the chain. Fig. 7.6 shows the spin up band spectrum, which is in the trivial phase, thus the spectra of even and odd subspaces do not match. The spectrum of the entire system with the spin coupling term is shown in Fig. 7.7. There is a quite small difference in the even and odd parity energy levels. This is due to the finite system size effect as we include the coupling between the two spin bands. As was shown in Fig. 7.3, we need a chain with at least 30 quantum dots to be able to see the topological behaviour of the system.

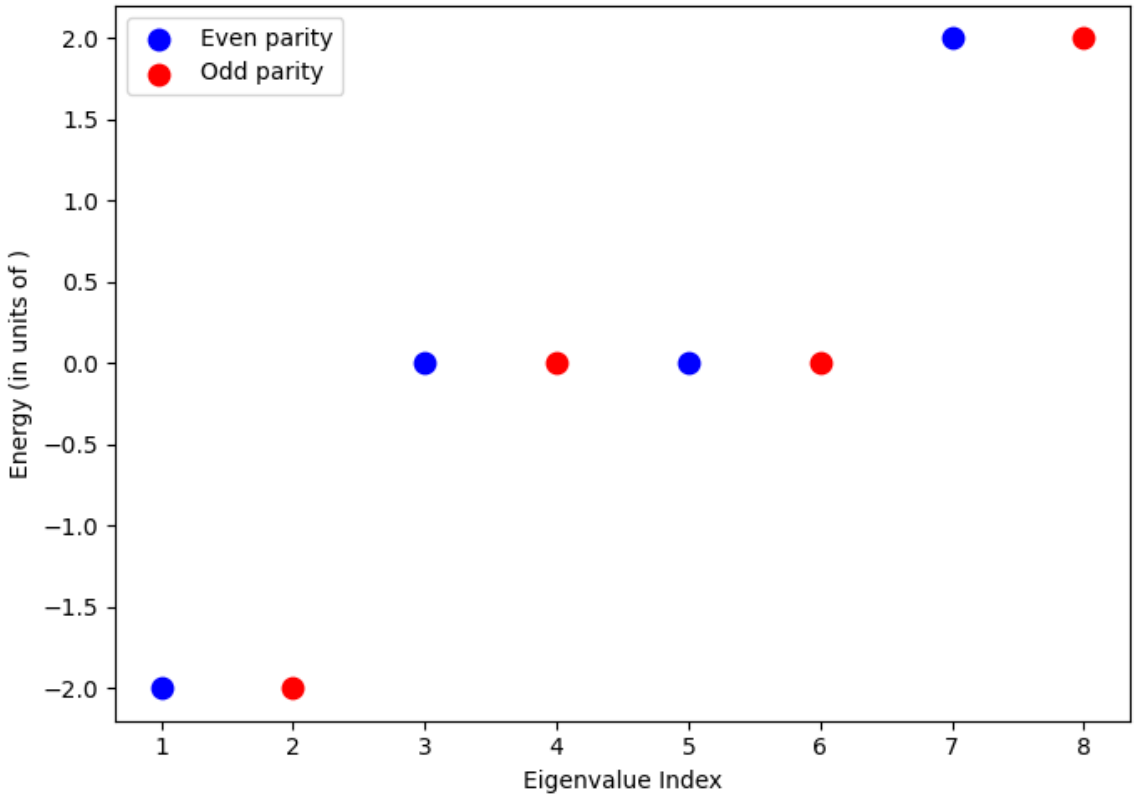

Figure 7.5: First four energy levels of $\hat{H}_1$ showing even (blue) and odd (red) parity states for the three-site spin down chain. There is perfect matching of the even and odd energy spectra as $\hat{H}_1$ represents the diagonal form of the Kitaev Hamiltonian in the topological phase.

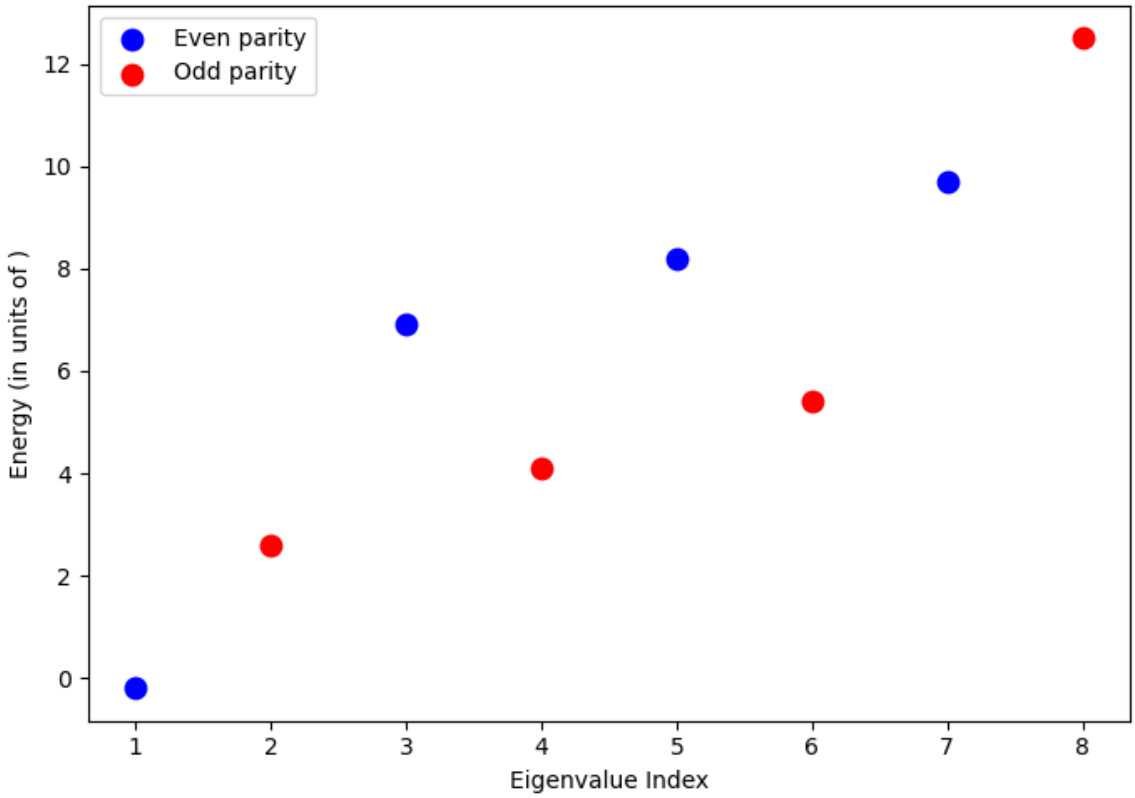

Figure 7.6: First four energy levels of $\hat{H}_2$ showing even (blue) and odd (red) parity states for the three-site spin up chain. Since $\hat{H}_2$ is in the trivial regime, the corresponding energy spectra of the even and odd parity subspaces do not match.

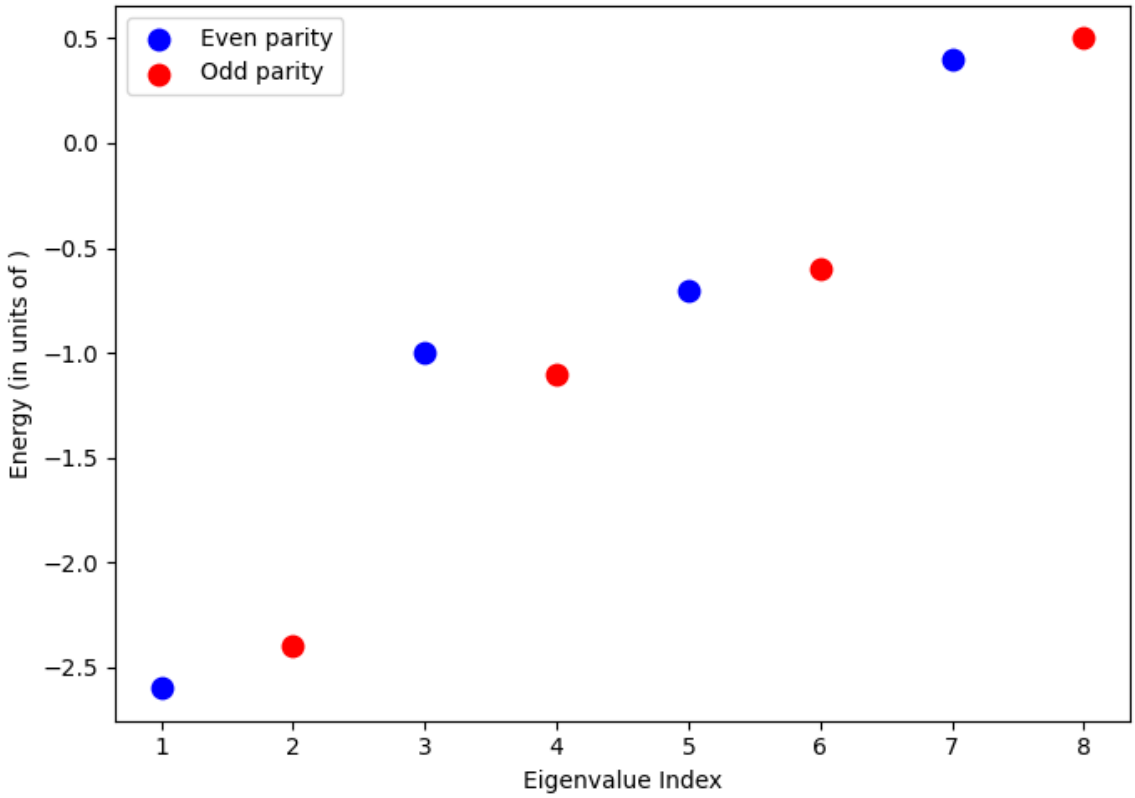

Figure 7.7: First four energy levels of the entire Hamiltonian $\hat{H} = \hat{H}_1 + \hat{H}_2 + \hat{H}_{12}$ showing even (blue) and odd (red) parity energies for the three-site spinful chain. There is a small difference in the even and odd parity energy levels due to the finite system size effect as we include the coupling between the two spin bands.

7.0.4 Spectral Function

Another beneficial quantity in observing MZMs is the electronic spectral function. It is particularly useful because it provides direct access to the energy-resolved quasiparticle spectrum together with spatial information [219, 220]. MZMs appear as a zero-energy excitation localized at the boundaries [44, 50]. As a consequence, they produce pronounced spectral weights near the ends of the system. In contrast, trivial bulk states typically appear at finite energies and are spatially extended [44, 46]. The spectral function therefore allows one to distinguish between localized zero-energy edge modes and ordinary bulk excitations.

We focus on the spin-down band, since for our choice of parameters it is diagonal in the topological phase. The spectral function measures the probability of adding a spin-down fermion at site (or bond) j_0 to the many-body ground state of the system and is directly related to the single-particle Green's function [69, 113]. The spectral

function is energy resolved. At each energy it measures how strongly the ground state couples to the true eigenstates of the system when a single spin-down electron is added at a chosen site or bond. Its value at a given energy is large when adding the electron there produces a genuine eigenstate of the many-body system at that energy, and it is small otherwise. Added over all energies it gives the total probability that the spin-down orbital at that site is empty and can accept an electron. The spectral function spreads this probability across energy. It therefore plays the role of a site-resolved density of states for adding a spin-down electron, and it is the electron-addition part of the single-particle Green's function. It is given by

$$A_j(\omega) = \sum_f |\langle \Psi_f | a_{j\downarrow}^\dagger | \Psi_{GS} \rangle|^2 \delta(\omega - (E_f - E_{GS})), \tag{7.56}$$

where the sum runs over the entire many-body eigenstates $|\Psi_f\rangle$, including the ground state and all excited states, with corresponding energies E_f, and the delta function enforces energy conservation during the particle addition process.

The procedure is closely related to that used for calculating absorption spectra, except that here we add a single electron rather than creating an electron–hole pair. We evaluate the spectral function in the full Hilbert space of the spin-down band rather than restricting to a specific parity sector.

Any many-body wave function can be written as a linear superposition of basis configurations with definite fermionic parity,

$$|\Psi\rangle = \sum_i D_i^p |i\rangle^{\text{even}} + \sum_j C_j^q |j\rangle^{\text{odd}}, \tag{7.57}$$

where $|i\rangle^{\text{even}}$ and $|j\rangle^{\text{odd}}$ denote basis states with even and odd fermion parity, respectively, and D_i^p and C_j^q are the corresponding expansion coefficients. Since the creation operator $a_{j\downarrow}^\dagger$ changes the fermion number by one, it flips the fermion parity. Therefore, only those matrix elements contribute in which the final state has opposite parity to the ground state. The spectral function can thus be written explicitly as

$$\begin{aligned} A_j(\omega) = &\sum_f |\langle \Psi_f^{\text{odd}} | a_{j\downarrow}^\dagger | \Psi_{GS}^{\text{even}} \rangle|^2 \delta(\omega - (E_f - E_{GS})) \\ &+ \sum_f |\langle \Psi_f^{\text{even}} | a_{j\downarrow}^\dagger | \Psi_{GS}^{\text{odd}} \rangle|^2 \delta(\omega - (E_f - E_{GS})). \end{aligned} \tag{7.58}$$

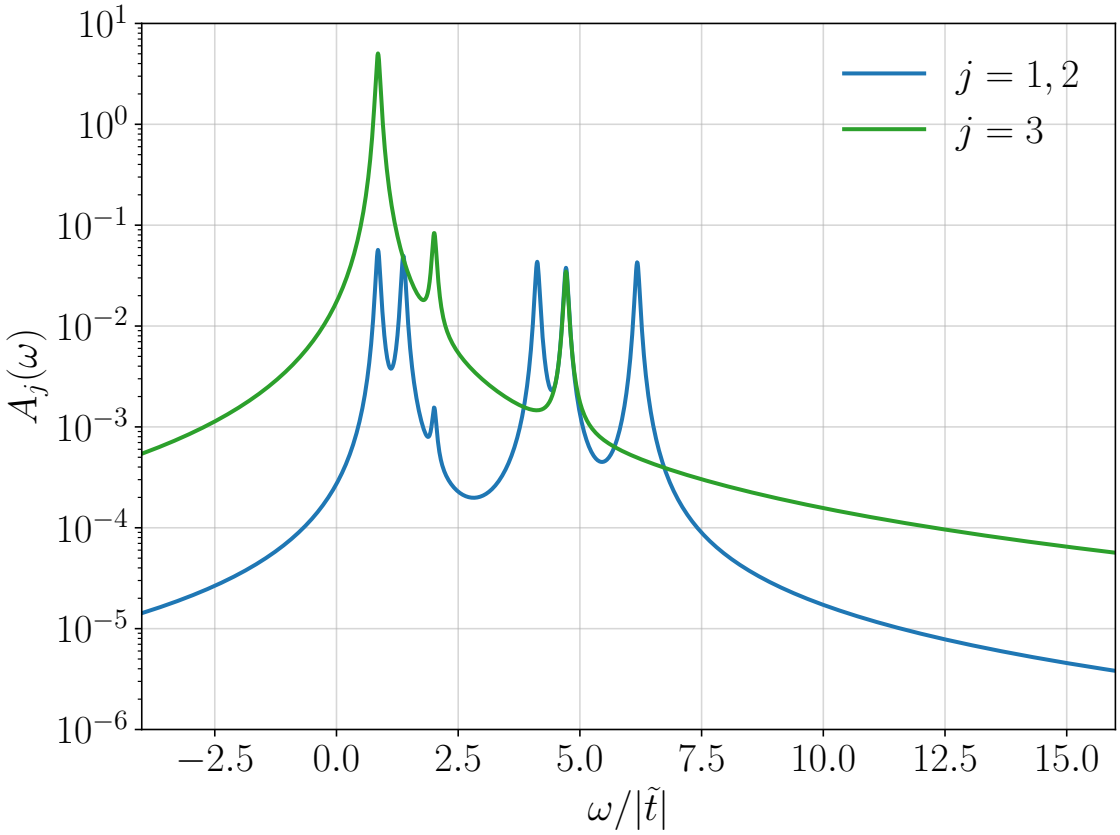

Figure 7.8: Site resolved spectral functions $A_j(\omega)$ of the down-spin bond Fermions for chain of $N = 3$ quantum dots, evaluated at the chain ends and in the bulk. Low-energy spectral weight is strongly localized at the chain ends [76].

If we observe a zero energy peak in the spectral function, that means a low-energy quasiparticle excitation exists. In our case, this feature is associated with the zero energy bond fermion $a_{N\downarrow}$, which plays the role of a MZM. Therefore, we expect a sharp peak around frequency zero in the spectral function.

Figure 7.8 shows the bond resolved spectral function $A_j(\omega)$ of the down-spin chain for a chain of 3 quantum dot system, evaluated at bonds $j = 1, 2, 3$. It is calculated using ED and for $t = \Delta = 1$, $\alpha = 0.8$, $\mu = \alpha\frac{\Delta}{t}$, and $V_z = \sqrt{\mu^2 + \Delta^2}$. The dominant low-energy resonance appears exclusively at the terminal bond $j = 3$, while the interior bonds $j = 1$ and $j = 2$ exhibit strongly suppressed spectral weight in the low-frequency window and are instead dominated by higher-energy excitations [76]. Although the dominant peak at $j = 3$ is shifted away from exactly zero frequency, reflecting finite-size effects, it remains clearly separated from the bulk excitation continuum. In contrast, the interior bonds show only weak low-energy response, with spectral weight redistributed toward higher energies, signaling enhanced mixing between edge and

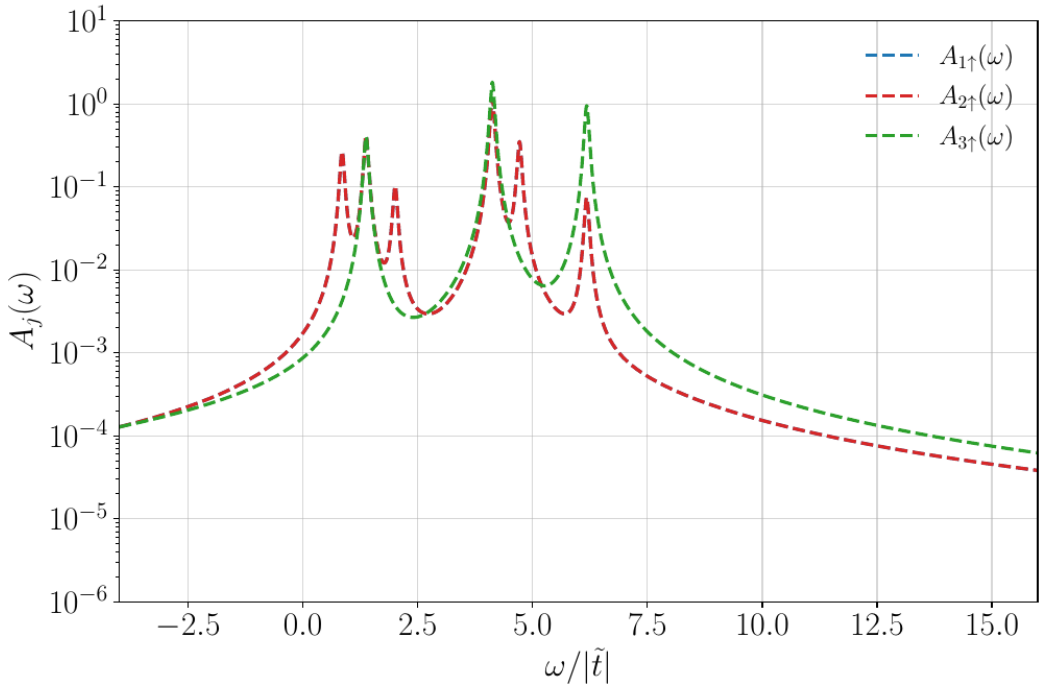

Figure 7.9: Site-resolved spectral functions $A_j(\omega)$ of the up-spin bond fermions for a chain of $N = 3$ quantum dots, evaluated at the end bond and in the bulk. The low-energy spectral weight here comes mainly from the interior bonds, while the end bond contributes only at higher energy. The overall magnitude is also about two orders smaller. This is the response of a trivial chain with no edge-localized zero mode [76].

bulk sectors.

For comparison, Fig. 7.9 shows the site-resolved spectral function of the up-spin sector, which is the trivial partner chain. The contrast with the topological down-spin sector is clear. In the down-spin chain the low-energy spectral weight is sharply concentrated on the end bond, which is the fingerprint of the edge-localized Majorana mode. In the up-spin chain the low-energy weight instead comes from the interior bonds, and the end bond contributes only at higher energy. The peak magnitudes are also about two orders of magnitude smaller than in the down-spin sector. The absence of an edge-localized low-energy resonance confirms that the up-spin chain is trivial. This side-by-side comparison isolates the edge-localized zero-energy peak as the distinguishing feature of the topological sector.

In summary, the bond-resolved spectral function provides a direct signature of the spatial localization of low-energy excitations in the finite Kitaev chain. The low-frequency peak observed at bond $j = 3$ (Fig. 7.8) demonstrates that the dominant

quasiparticle excitation is localized at the edge of the system, consistent with the presence of a Majorana zero mode. Despite the peak being slightly shifted away from exactly zero energy, its clear separation from the bulk excitation continuum confirms its edge character. The strong suppression of low-energy spectral weight in the interior bonds further supports this interpretation, indicating that the zero-mode is located at the boundary. Thus, even for a short three-dot chain, the spectral function shows the emergence of boundary-localized Majorana excitations.

Chapter 8

Conclusions and perspectives

In this thesis, we have established a systematic analytical and numerical framework for synthetic topological quantum matter, with the goal of advancing fault-tolerant quantum computing [32, 50, 74, 168]. The central object of study was Majorana zero modes (MZMs), exotic zero-energy quasiparticle excitations that are prime candidates for encoding topologically protected qubits. By combining exact diagonalization, bond-fermion analytics, excitonic spectroscopy, hybrid quantum-classical algorithms, and tensor-network methods, we addressed two platforms for hosting MZMs, characterized their topological phases, and proposed concrete detection and simulation strategies. Our results clarify the choice of the numerical method when there are certain conditions applied to the system, and also lower the barrier between theoretical models of topological matter and experimental protocols.

The first challenge of solving the many-body problem is the exponential scaling of the Hilbert space dimension. Despite the topological phase transition, our systems are still regular many-body systems, so a thorough understanding of their methodology is vital. In Chapter 3 we introduced some of the standard methods of solving a many-body problem, in which we included exact diagonalization (ED) and mean-field approximations. We also explored the variational quantum eigensolver (VQE) approach as a hybrid method of approximating the ground state energy of a many-body system, and the density matrix renormalization group (DMRG), which is generally used for larger systems.

In Chapter 4 we studied the Kitaev chain, our first topological system, which is a one-dimensional nanowire in contact with a p-wave superconductor. After studying its band structure, we showed that a bond-fermion transformation diagonalizes the Hamiltonian exactly in the topological regime, making the spatial non-locality of the MZMs transparent and providing an analytic benchmark for all subsequent numerical work. This exact solution is a powerful tool, it unambiguously separates the topological from the trivial phase and explains, at a fundamental level, why MZMs are immune to local perturbations.

Our second topological system, a semiconducting nanowire in contact with an s-wave superconductor was described in Chapter 5. This system is one of the experimental frameworks for detecting MZMs. Through using BdG formalism, we examined the behaviour of the band structure, and showed that when the parameters of the Hamiltonian obey a certain condition such that the system lies in the topological phase, the band structure displays a p-wave superconductor pattern. This suggests that the semiconducting-superconducting with s-wave superconductivity is an approximate system that shows MZMs only when the chain is long enough.

The second challenge in the engineering of the topological matter is the detection of MZMs. In the first part of Chapter 6, we provided an optical path by adding the excitonic (electron+hole) interaction to the system. Through analytical and numerical calculations using ED, we showed how to track zero modes in the absorption spectrum. We identified clear spectroscopic signatures of zero modes, including characteristic peak splittings and edge-localized intensity patterns. This is a powerful experimental technique that provides a recipe to detect MZMs, since our results are directly comparable to optical measurements on InAsP quantum dot nanowires. We also showed that for a localized hole, there is an analytical solution for the absorption spectrum, regardless of the system size. Therefore, we can generalize the procedure to longer chains without having to consider extra calculations.

In the second part of Chapter 6, we demonstrated that MZMs can be probed and simulated on quantum hardware. By designing symmetry-adapted variational ansätze that respect the parity structure of the Kitaev Hamiltonian, we showed that a hybrid variational quantum eigensolver (VQE) reliably reproduces the ground-state energy in the topological regime. Although the process was done on a simulator, but our method provides a framework for quantum simulation of topological matter on a quantum computer.

In Chapter 7 we provided practical solutions to the two challenges (exponential scaling of the Hilbert space dimension and MZM detection) for the semiconducting-superconducting (SM-SC) nanowire with s-wave superconductivity. We began with the short chain case, and demonstrated ED in calculating the many-body spectrum. For long chains, we showed that DMRG could be a useful method in providing the ground state energy of the system. Through using DMRG, we also demonstrated the sufficient length of the chain (number of quantum dots) to ensure the system shows MZMs explicitly. We also established an explicit mapping between the SM-SC model and a pair of coupled Kitaev chains, demonstrating that both systems realize the same topological phase. Through using this mapping, we then calculated the local spectral

function of the spin-down band. The local spectral function shows sharp zero-energy edge peaks, a direct numerical counterpart of the zero-bias conductance peaks sought in tunneling experiments.

In summary, these results make several contributions that should be of broad interest to the concept of topological quantum matter, from numerical and experimental perspective. The excitonic detection scheme introduces optical spectroscopy in the MZM detection toolkit. The symmetry-preserving VQE protocol offers a practical path to quantum simulation of topological phases using a quantum computer. The DMRG treatment of the SM-SC nanowire demonstrates that tensor-network methods are applicable but well-suited for device-scale simulations. In our future work, we intend to concentrate on interactive topological systems with Hubbard, extended Hubbard, and excitonic interactions. This is inspiring in a way that we could explore the reaction of MZMs to various types of interaction, and examine their detection methods. It would also enable us to study the impacts of interactions on measurable quantities such as energy spectrum and entanglement entropy. We also aim to generalize the quantum algorithmic method to semiconducting-superconducting nanowire. Since this model is the ideal type for experimental means, the quantum algorithm approach could pave the way of simulating the model on a quantum computer.

Bibliography

[1] Richard P. Feynman. “Simulating Physics with Computers”. In: *International Journal of Theoretical Physics* 21.6–7 (1982), pp. 467–488.

[2] Michael A. Nielsen and Isaac L. Chuang. *Quantum Computation and Quantum Information*. 10th Anniversary Edition. Cambridge, UK: Cambridge University Press, 2010.

[3] Laszlo Gyongyosi and Sandor Imre. “A survey on quantum computing technology”. In: *Computer Science Review* 31 (2019), pp. 51–71.

[4] Peter W. Shor. “Algorithms for Quantum Computation: Discrete Logarithms and Factoring”. In: *SIAM Journal on Computing* 26.5 (1997), pp. 1484–1509.

[5] Lov K. Grover. “A Fast Quantum Mechanical Algorithm for Database Search”. In: *Proceedings of the 28th Annual ACM Symposium on Theory of Computing*. 1996, pp. 212–219.

[6] K. Head-Marsden, S. Sun, P. Campuzano-Jost, and D. A. Mazziotti. “Quantum algorithms for quantum chemistry and quantum materials science”. In: *Chemical Reviews* 121 (2021), pp. 3061–3120.

[7] Vincent E Elfving, Benno W Broer, Mark Webber, Jacob Gavartin, Mathew D Halls, K Patrick Lorton, and A Bochevarov. “How will quantum computers provide an industrially relevant computational advantage in quantum chemistry?” In: *arXiv preprint arXiv:2009.12472* (2020).

[8] Jens Koch, Terri M. Yu, Jay Gambetta, A. A. Houck, D. I. Schuster, J. Majer, Alexandre Blais, M. H. Devoret, S. M. Girvin, and R. J. Schoelkopf. “Charge-insensitive qubit design derived from the Cooper pair box”. In: *Physical Review A* 76 (2007), p. 042319.

[9] J. Ignacio Cirac and Peter Zoller. “Quantum Computations with Cold Trapped Ions”. In: *Physical Review Letters* 74.20 (1995), pp. 4091–4094.

[10] E. Knill, R. Laflamme, and G. J. Milburn. “A scheme for efficient quantum computation with linear optics”. In: *Nature* 409 (2001), pp. 46–52.

[11] Daniel Loss and David P. DiVincenzo. “Quantum computation with quantum dots”. In: *Physical Review A* 57.1 (1998), pp. 120–126.

[12] M. Saffman, T. G. Walker, and K. Mølmer. “Quantum information with Rydberg atoms”. In: *Reviews of Modern Physics* 82 (2010), pp. 2313–2363.

[13] John Preskill. “Quantum Computing in the NISQ era and beyond”. In: *Quantum* 2 (2018), p. 79.

[14] Maximilian Schlosshauer. “Quantum Decoherence”. In: *Physics Reports* 831 (2019), pp. 1–57.

[15] Wojciech H. Zurek. “Decoherence, einselection, and the quantum origins of the classical”. In: *Reviews of Modern Physics* 75.3 (2003), pp. 715–775.

[16] E. Knill. “Quantum computing with realistically noisy devices”. In: *Nature* 434 (2005), pp. 39–44.

[17] Joel J. Wallman, Marie Barnhill, and Joseph Emerson. “Characterization of Leakage Errors via Randomized Benchmarking”. In: *New Journal of Physics* 16.10 (2014), p. 103032.

[18] Mohan Sarovar, David L. Zhou, Jens R. M. de Lima, and Michael A. Nielsen. “Detecting crosstalk errors in quantum information processors”. In: *Quantum* 4 (2020), p. 321.

[19] John Preskill. “Fault-tolerant quantum computation”. In: *Introduction to quantum computation and information* 213 (1998).

[20] ET Campbell, BM Terhal, and C Vuillot. “The steep road towards robust and universal quantum computation”. In: *arXiv preprint arXiv:1612.07330* (2016).

[21] Austin G. Fowler, Matteo Martinis, Gilles Duclos-Cianci, and David Poulin. “Surface codes: Towards practical large-scale quantum computation”. In: *Physical Review A* 86 (2012), p. 032324.

[22] Dorit Aharonov and Michael Ben-Or. “Fault-tolerant quantum computation with constant error rate”. In: *SIAM Journal on Computing* 38.4 (2008). Preliminary version in STOC 1997, pp. 1207–1282.

[23] Claude E. Shannon. “A Mathematical Theory of Communication”. In: *Bell System Technical Journal* 27.3 (1948), pp. 379–423.

[24] William K. Wootters and Wojciech H. Zurek. “A single quantum cannot be cloned”. In: *Nature* 299 (1982), pp. 802–803.

[25] Daniel Gottesman. “Stabilizer Codes and Quantum Error Correction”. arXiv:quant-ph/9705052. PhD thesis. California Institute of Technology, 1997.

[26] Alexei Y. Kitaev. “Fault-tolerant quantum computation by anyons”. In: *Annals of Physics* 303.1 (2003). arXiv:quant-ph/9707021, pp. 2–30.

[27] Daniel Gottesman. “The Heisenberg Representation of Quantum Computers”. In: *arXiv preprint quant-ph/9807006* (1998). arXiv: `quant-ph/9807006 [quant-ph]`.

[28] Sergey Bravyi and Alexei Kitaev. “Universal quantum computation with ideal Clifford gates and noisy ancillas”. In: *Physical Review A* 71.2 (2005), p. 022316.

[29] Sergey Bravyi and Alexei Kitaev. “Universal quantum computation with ideal Clifford gates and noisy ancillas”. In: *Physical Review A* 71.2 (2005), p. 022316.

[30] Craig Gidney and Martin Ekerå. “How to Factor 2048 Bit RSA Integers in 8 Hours Using 20 Million Noisy Qubits”. In: *Quantum* 5 (2021), p. 433.

[31] Craig Gidney. “How to Factor 2048 Bit RSA Integers with Less than a Million Noisy Qubits”. In: *arXiv preprint arXiv:2505.15917* (2025). arXiv: `2505.15917 [quant-ph]`.

[32] Chetan Nayak, Steven H. Simon, Ady Stern, Michael Freedman, and Sankar Das Sarma. “Non-Abelian anyons and topological quantum computation”. In: *Reviews of Modern Physics* 80 (2008), pp. 1083–1159.

[33] Sankar Das Sarma, Michael Freedman, and Chetan Nayak. “Majorana zero modes and topological quantum computation”. In: *npj Quantum Information* 1 (2015), p. 15001.

[34] Michael Freedman, Alexei Kitaev, Michael Larsen, and Zhenghan Wang. “Topological quantum computation”. In: *Bulletin of the American Mathematical Society* 40.1 (2003), pp. 31–38.

[35] Xiao-Gang Wen. “Zoo of Quantum-Topological Phases of Matter”. In: *Reviews of Modern Physics* 89.4 (2017), p. 041004.

[36] X.-L. Qi and S.-C. Zhang. “Topological Insulators and Superconductors”. In: *Reviews of Modern Physics* 83 (2011), pp. 1057–1110.

[37] Jon M. Leinaas and Jan Myrheim. “On the theory of identical particles”. In: *Il Nuovo Cimento B* 37.1 (1977), pp. 1–23.

[38] Frank Wilczek. “Quantum Mechanics of Fractional-Spin Particles”. In: *Physical Review Letters* 49.14 (1982), pp. 957–959.

[39] P. Zanardi and M. Rasetti. "Topological protection and quantum noiseless subsystems". In: *Physical Review Letters* 90.6 (2003), p. 067902.

[40] Ville Lahtinen and Jiannis K. Pachos. "A Short Introduction to Topological Quantum Computation". In: *SciPost Physics* 3 (2017), p. 021.

[41] Gregory Moore and Nicholas Read. "Nonabelions in the fractional quantum Hall effect". In: *Nuclear Physics B* 360.2–3 (1991), pp. 362–396.

[42] Alexei Yu. Kitaev. "Anyons in an exactly solved model and beyond". In: *Annals of Physics* 321.1 (2006), pp. 2–111.

[43] Dmitri A. Ivanov. "Non-Abelian statistics of half-quantum vortices in p-wave superconductors". In: *Physical Review Letters* 86.2 (2001), pp. 268–271.

[44] Jason Alicea. "New directions in the pursuit of Majorana fermions in solid state systems". In: *Reports on Progress in Physics* 75.7 (2012), p. 076501.

[45] Martin Leijnse and Karsten Flensberg. "Introduction to topological superconductivity and Majorana fermions". In: *Semiconductor Science and Technology* 27.12 (2012), p. 124003.

[46] R. Aguado. "Majorana quasiparticles in condensed matter". In: *Riv. Nuovo Cim.* 40 (2017), pp. 523–593.

[47] Roman M. Lutchyn, Erik P. A. M. Bakkers, et al. "Majorana zero modes in superconductor–semiconductor heterostructures". In: *Nature Reviews Materials* 3 (2018), pp. 52–68.

[48] Ettore Majorana. "Teoria simmetrica dell'elettrone e del positrone". In: *Il Nuovo Cimento* 14.4 (1937). English translation: *Symmetrical theory of the electron and positron*, pp. 171–184.

[49] N. Read and Dmitry Green. "Paired states of fermions in two dimensions with breaking of parity and time-reversal symmetries and the fractional quantum Hall effect". In: *Physical Review B* 61 (2000), pp. 10267–10297.

[50] A Yu Kitaev. "Unpaired Majorana fermions in quantum wires". In: *Physics-uspekhi* 44.10S (2001), pp. 131–136.

[51] K. T. Law, Patrick A. Lee, and T. K. Ng. "Majorana Fermion Induced Resonant Andreev Reflection". In: *Physical Review Letters* 103 (2009), p. 237001.

[52] Vincent Mourik, Kun Zuo, Sergey M. Frolov, S. R. Plissard, Erik P. A. M. Bakkers, and Leo P. Kouwenhoven. "Signatures of Majorana fermions in hybrid superconductor–semiconductor nanowire devices". In: *Science* 336.6084 (2012), pp. 1003–1007.

[53] B. Jäck, Y. Xie, and A. Yazdani. "Detecting and distinguishing Majorana zero modes with the scanning tunnelling microscope". In: *Nature Reviews Physics* 3 (2021), pp. 541–554.

[54] Hao Zhang, Dong E. Liu, Michael Wimmer, and Leo P. Kouwenhoven. "Quantum information and computation with Majorana qubits". In: *Nature Reviews Physics* 2 (2020), pp. 213–226.

[55] Masatoshi Sato and Yoichi Ando. "Topological superconductors: a review". In: *Reports on Progress in Physics* 80.7 (2017), p. 076501. eprint: `arXiv:1608.03395`.

[56] Liang Fu and Charles L. Kane. "Superconducting Proximity Effect and Majorana Fermions at the Surface of a Topological Insulator". In: *Physical Review Letters* 100 (2008), p. 096407.

[57] Roman M. Lutchyn, Jay D. Sau, and S. Das Sarma. "Majorana Fermions and a Topological Phase Transition in Semiconductor-Superconductor Heterostructures". In: *Physical Review Letters* 105.7 (2010), p. 077001.

[58] Yuval Oreg, Gil Refael, and Felix von Oppen. "Helical Liquids and Majorana Bound States in Quantum Wires". In: *Physical Review Letters* 105.17 (2010), p. 177002.

[59] Catherine Kallin. "Chiral p-wave order in Sr2RuO4". In: *Reports on Progress in Physics* 75.4 (2012), p. 042501.

[60] A. Pustogow, Yongkang Luo, A. Chronister, Y.-S. Su, D. A. Sokolov, F. Jerzembeck, A. P. Mackenzie, C. W. Hicks, N. Kikugawa, S. Raghu, E. D. Bauer, and S. E. Brown. "Constraints on the Superconducting Order Parameter in Sr_2RuO_4 from Oxygen-17 Nuclear Magnetic Resonance". In: *Nature* 574.7776 (2019), pp. 72–75.

[61] Aaron Chronister, Andrej Pustogow, Naoki Kikugawa, Dmitry A. Sokolov, Fabian Jerzembeck, Clifford W. Hicks, Andrew P. Mackenzie, Eric D. Bauer, and Stuart E. Brown. "Evidence for Even Parity Unconventional Superconductivity in Sr_2RuO_4". In: *Proceedings of the National Academy of Sciences* 118.25 (2021), e2025313118.

[62] John Bardeen, Leon N. Cooper, and J. Robert Schrieffer. “Theory of Superconductivity”. In: *Physical Review* 108.5 (1957), pp. 1175–1204.

[63] M. T. Deng, S. Vaitiekenas, E. B. Hansen, J. Danon, M. Leijnse, K. Flensberg, T. S. Jespersen, J. Nygård, P. Krogstrup, and C. M. Marcus. “Majorana bound state in a coupled quantum-dot hybrid-nanowire system”. In: *Science* 354.6319 (2016), pp. 1557–1562.

[64] T. Dvir, G. Wang, N. van Loo, C.-X. Liu, G. P. Mazur, A. Bordin, et al. “Realization of a Minimal Kitaev Chain in Coupled Quantum Dots”. In: *Nature* 614 (2023), pp. 445–450.

[65] Jay D. Sau and S. Das Sarma. “Realizing a Robust Practical Majorana Chain in a Quantum-Dot-Superconductor Linear Array”. In: *Nature Communications* 3 (2012), p. 964.

[66] Hao Zhang, Chun-Xiao Liu, Sasa Gazibegovic, et al. “Retraction Note: Quantized Majorana Conductance”. In: *Nature* 591.7851 (2021), E30.

[67] Elbio Dagotto. “Correlated electrons in high-temperature superconductors”. In: *Reviews of Modern Physics* 66 (1994), pp. 763–840.

[68] Ulrich Schollwöck. “The density-matrix renormalization group”. In: *Reviews of Modern Physics* 77 (2005), pp. 259–315.

[69] A. L. Fetter and J. D. Walecka. *Quantum Theory of Many-Particle Systems*. New York: McGraw-Hill, 1971.

[70] D. I. Pikulin, B. van Heck, T. Karzig, E. A. Martinez, B. Nijholt, T. Laeven, G. W. Winkler, et al. “Protocol to identify a topological superconducting phase in a three-terminal device”. In: *arXiv* (2021). eprint: `2103.12217`.

[71] John W. Negele and Henri Orland. *Quantum Many-Particle Systems*. Redwood City: Addison-Wesley, 1988.

[72] H. Q. Lin and J. E. Gubernatis. “Exact diagonalization studies of two-dimensional Hubbard models”. In: *Computers in Physics* 7 (1993), pp. 400–407.

[73] Gene H. Golub and Charles F. Van Loan. *Matrix Computations*. 4th ed. Baltimore: Johns Hopkins University Press, 2013.

[74] C. W. J. Beenakker. “Search for Majorana Fermions in Superconductors”. In: *Annual Review of Condensed Matter Physics* 4 (2013), pp. 113–136.

[75] Mahan Mohseni, Hassan Allami, Daniel Miravet, David J. Gayowsky, Marek Korkusinski, and Pawel Hawrylak. "Majorana Excitons in a Kitaev Chain of Semiconductor Quantum Dots in a Nanowire". In: *Nanomaterials* 13.16 (2023), p. 2293.

[76] Mijanur Islam, Mahan Mohseni, Ibsal Assi, Daniel Miravet, and Pawel Hawrylak. "Majorana Fermions in spin up and down electronic complexes in spin-orbit coupled array of semiconductor quantum dots in proximity to *s*-type superconductor and in magnetic field". In: *arXiv preprint arXiv:2601.14527* (2026).

[77] Mahan Mohseni, Iann Cunha, Daniel Miravet, Alina Wania Rodrigues, Hassan Allami, Ibsal Assi, Marek Korkusinski, and Pawel Hawrylak. "Designing Majorana Quasiparticles in InAsP Quantum Dots in InP Nanowires with Variational Quantum Eigenvalue Solver". In: *physica status solidi (b)* 262.7 (2025), p. 2400552.

[78] Biao Lian, Xiao-Qi Sun, Abolhassan Vaezi, Xiao-Liang Qi, and Shou-Cheng Zhang. "Topological quantum computation based on chiral Majorana fermions". In: *Proceedings of the National Academy of Sciences* 115.43 (2018), pp. 10938–10942.

[79] Jay D Sau, Roman M Lutchyn, Sumanta Tewari, and Sankar Das Sarma. "Generic new platform for topological quantum computation using semiconductor heterostructures". In: *Physical review letters* 104.4 (2010), p. 040502.

[80] John Preskill. *Lecture Notes on Topological Quantum Computation*. Available at http://www.theory.caltech.edu/~preskill/ph219/topological.pdf. 2004.

[81] John M. Martinis, K. B. Cooper, R. McDermott, M. Steffen, M. Ansmann, K. Osborn, K. Cicak, S. Oh, D. P. Pappas, R. W. Simmonds, and C. C. Yu. "Decoherence in Josephson Qubits from Dielectric Loss". In: *arXiv* (2005). eprint: `cond-mat/0507622`.

[82] Erich Joos, H. Dieter Zeh, Claus Kiefer, Domenico Giulini, Joachim Kupsch, and Ion-Olimpiu Stamatescu. "Decoherence and the Appearance of a Classical World in Quantum Theory". In: *Springer* (2003). 2nd ed.

[83] Michael A. Nielsen and Isaac L. Chuang. *Quantum Computation and Quantum Information*. 10th Anniversary Edition. See Chapters 2–4 for qubits, quantum gates, and circuit model; Chapter 9 for quantum algorithms. Cambridge University Press, 2010.

[84] Daniel A. Lidar and Todd A. Brun. “Introduction to decoherence and noise in open quantum systems”. In: *Quantum Error Correction*. Cambridge University Press, 2013, pp. 3–40.

[85] Daniel Greenbaum and Zachary Dutton. “Modeling coherent errors in quantum error correction”. In: *Quantum Science and Technology* 3.1 (2018), p. 015007.

[86] Roger S. K. Mong, David J. Clarke, Jason Alicea, Netanel H. Lindner, Paul Fendley, Chetan Nayak, Yuval Oreg, Ady Stern, Ehud Berg, Kirill Shtengel, and Sankar Das Sarma. “Universal topological quantum computation from a superconductor–Abelian quantum Hall heterostructure”. In: *Physical Review X* 4.1 (2014), p. 011036.

[87] R Walter Ogburn and John Preskill. “Topological quantum computation”. In: *NASA International Conference on Quantum Computing and Quantum Communications*. Springer. 1998, pp. 341–356.

[88] Simone De Liberato. “Open quantum systems with local and collective incoherent processes: theory and applications”. In: *Physical Review A* 98.6 (2018), p. 063815.

[89] Anthony J. Leggett. *Quantum Liquids: Bose Condensation and Cooper Pairing in Condensed-Matter Systems*. See pp. 90–140 for BCS theory and superconducting coherence length. Oxford University Press, 2006.

[90] Janusz E. Jacak et al. “Application of path-integral quantization to indistinguishable particle systems topologically confined by a magnetic field”. In: *Physical Review A* 97.1 (2018), p. 012108.

[91] Christian Kassel. *Quantum Groups*. Graduate Texts in Mathematics. Springer, 2008.

[92] Daniel C. Tsui, Horst L. Störmer, and Arthur C. Gossard. “Two-Dimensional Magnetotransport in the Extreme Quantum Limit”. In: *Physical Review Letters* 48.22 (1982), pp. 1559–1562.

[93] Nicholas Read and Dmitry Green. “Paired states of fermions in two dimensions with breaking of parity and time-reversal symmetries and the fractional quantum Hall effect”. In: *Physical Review B* 61.15 (2000), pp. 10267–10297.

[94] Parsa Bonderson, Michael Freedman, and Chetan Nayak. “Measurement-only topological quantum computation via anyonic interferometry”. In: *Annals of Physics* 323.11 (2008), pp. 2709–2755.

[95] Jiannis K. Pachos. *Introduction to Topological Quantum Computation*. Cambridge University Press, 2012.

[96] David Aasen, Michael Hell, Ryan V. Mishmash, Andrew Higginbotham, Jesper Danon, Mark Leijnse, Thomas S. Jespersen, Joshua A. Folk, Charles M. Marcus, Karsten Flensberg, and Jason Alicea. "Milestones Toward Majorana-Based Quantum Computing". In: *Physical Review X* 6 (2016), p. 031016.

[97] Michael H. Freedman, Alexei Kitaev, Michael J. Larsen, and Zhenghan Wang. "Topological quantum computation". In: *Bulletin of the American Mathematical Society* 40.1 (2002), pp. 31–38.

[98] Scott Aaronson and Daniel Gottesman. "Improved Simulation of Stabilizer Circuits". In: *Physical Review A* 70.5 (2004), p. 052328.

[99] C. N. Yang. "Some exact results for the many-body problem in one dimension with repulsive delta-function interaction". In: *Physical Review Letters* 19.23 (1967), pp. 1312–1315.

[100] R. J. Baxter. "Partition function of the eight-vertex lattice model". In: *Annals of Physics* 70.1 (1972), pp. 193–228.

[101] N. E. Bonesteel, L. Hormozi, G. Zikos, and S. H. Simon. "Braid Topologies for Quantum Computation". In: *Physical Review Letters* 95.14 (2005), p. 140503.

[102] N. Read and E. Rezayi. "Beyond Paired Quantum Hall States: Parafermions and Incompressible States in the First Excited Landau Level". In: *Physical Review B* 59.12 (1999), pp. 8084–8092.

[103] Roger S. K. Mong, Michael P. Zaletel, Frank Pollmann, and Zlatko Papić. "Fibonacci Anyons and Charge Density Order in the 12/5 and 13/5 Quantum Hall Plateaus". In: *Physical Review B* 95.11 (2017), p. 115136.

[104] Shibo Xu et al. "Non-Abelian Braiding of Fibonacci Anyons with a Superconducting Processor". In: *Nature Physics* 20 (2024), pp. 1469–1475.

[105] Michael H. Freedman, Michael J. Larsen, and Zhenghan Wang. "A modular functor which is universal for quantum computation". In: *Communications in Mathematical Physics* 227.3 (2002), pp. 605–622.

[106] P. A. M. Dirac. "The Quantum Theory of the Electron". In: *Proceedings of the Royal Society A* 117 (1928), pp. 610–624.

[107] J. D. Bjorken and S. D. Drell. *Relativistic Quantum Mechanics*. McGraw-Hill, 1964.

[108] Walter Greiner. *Relativistic Quantum Mechanics: Wave Equations*. Springer, 1990.

[109] Michael E. Peskin and Daniel V. Schroeder. *An Introduction to Quantum Field Theory*. Addison-Wesley, 1995.

[110] David Aasen, Michael Hell, Roman M. Lutchyn, Jason Alicea, and Charles Nayak. "Milestones toward Majorana-based quantum computing". In: *Physical Review X* 6.3 (2016), p. 031016.

[111] Torsten Karzig, Christina Knapp, Roman M. Lutchyn, Parsa Bonderson, Matthew B. Hastings, Chetan Nayak, Jason Alicea, Karsten Flensberg, Stephan Plugge, Yuval Oreg, Charles M. Marcus, and Michael H. Freedman. "Scalable Designs for Quasiparticle-Poisoning-Protected Topological Quantum Computation with Majorana Zero Modes". In: *Physical Review B* 95.23 (2017), p. 235305.

[112] Ramon Aguado. "Majorana quasiparticles in condensed matter". In: *La Rivista del Nuovo Cimento* 40.11 (2017), pp. 523–593.

[113] Henrik Bruus and Karsten Flensberg. *Many-Body Quantum Theory in Condensed Matter Physics: An Introduction*. Oxford: Oxford University Press, 2004.

[114] Neil W. Ashcroft and N. David Mermin. *Solid State Physics*. Holt, Rinehart and Winston, 1976.

[115] Charles Kittel. *Introduction to Solid State Physics*. 8th ed. Wiley, 2005.

[116] Nicola Marzari and David Vanderbilt. "Maximally localized generalized Wannier functions for composite energy bands". In: *Physical Review B* 56.20 (1997), pp. 12847–12865.

[117] Nicola Marzari, Arash A. Mostofi, Jonathan R. Yates, Ivo Souza, and David Vanderbilt. "Maximally localized Wannier functions: Theory and applications". In: *Reviews of Modern Physics* 84.4 (2012), pp. 1419–1475.

[118] Giovanni Pizzi et al. "Wannier90 as a community code: new features and applications". In: *Journal of Physics: Condensed Matter* 32.16 (2020), p. 165902.

[119] Attila Szabo and Neil S. Ostlund. *Modern Quantum Chemistry: Introduction to Advanced Electronic Structure Theory*. Mineola, NY: Dover, 1996.

[120] Trygve Helgaker, Poul Jørgensen, and Jeppe Olsen. *Molecular Electronic-Structure Theory*. Chichester: Wiley, 2000.

[121] Isaiah Shavitt and Rodney J. Bartlett. *Many-Body Methods in Chemistry and Physics: MBPT and Coupled-Cluster Theory*. Cambridge: Cambridge University Press, 2009.

[122] J. J. Sakurai and Jim Napolitano. *Modern Quantum Mechanics*. 2nd ed. Addison-Wesley, 1994.

[123] Lloyd N. Trefethen and III Bau David. *Numerical Linear Algebra*. Philadelphia: SIAM, 1997.

[124] E. Anderson, Z. Bai, C. Bischof, S. Blackford, J. Demmel, J. Dongarra, J. Du Croz, A. Greenbaum, S. Hammarling, A. McKenney, and D. Sorensen. "LAPACK Users' Guide". In: *LAPACK Users' Guide*. 3rd ed. Philadelphia: SIAM, 1999.

[125] J. Jaklič and P. Prelovšek. "Lanczos method for the calculation of finite-temperature quantities in correlated systems". In: *Advances in Physics* 49 (2000), pp. 1–92.

[126] P. Prelovšek and J. Bonča. "Ground State and Finite Temperature Lanczos Methods". In: *Strongly Correlated Systems: Numerical Methods*. Ed. by A. Avella and F. Mancini. Berlin: Springer, 2013, pp. 1–30.

[127] Jean-Paul Blaizot and Georges Ripka. *Quantum Theory of Finite Systems*. Cambridge, MA: MIT Press, 1986.

[128] A. Peruzzo, J. McClean, P. Shadbolt, M.-H. Yung, X.-Q. Zhou, P. J. Love, A. Aspuru-Guzik, and J. L. O'Brien. "A variational eigenvalue solver on a photonic quantum processor". In: *Nature Communications* 5 (2014), p. 4213.

[129] M. Cerezo, A. Arrasmith, R. Babbush, S. C. Benjamin, S. Endo, K. Fujii, J. R. McClean, K. Mitarai, X. Yuan, L. Cincio, and P. J. Coles. "Variational quantum algorithms". In: *Nature Reviews Physics* 3 (2021), pp. 625–644.

[130] J. Tilly, H. Chen, S. Cao, D. Picozzi, K. Setia, Y. Li, E. Grant, L. Wossnig, I. Rungger, G. H. Booth, and J. Tennyson. "The variational quantum eigensolver: a review of methods and best practices". In: *Reports on Progress in Physics* 85 (2022), p. 076001.

[131] J. R. McClean, J. Romero, R. Babbush, and A. Aspuru-Guzik. "The theory of variational hybrid quantum-classical algorithms". In: *New Journal of Physics* 18 (2016), p. 023023.

[132] Sukin Sim, Peter D. Johnson, and Alán Aspuru-Guzik. "Expressibility and entangling capability of parameterized quantum circuits for hybrid quantum-classical algorithms". In: *Advanced Quantum Technologies* 2 (2019), p. 1900070.

[133] J. R. McClean, S. Boixo, V. N. Smelyanskiy, R. Babbush, and H. Neven. "Barren plateaus in quantum neural network training landscapes". In: *Nature Communications* 9 (2018), p. 4812.

[134] J. A. Nelder and R. Mead. "A simplex method for function minimization". In: *The Computer Journal* 7 (1965), pp. 308–313.

[135] M. J. D. Powell. "A direct search optimization method that models the objective and constraint functions by linear interpolation". In: *Advances in Optimization and Numerical Analysis*. Ed. by S. Gomez and J.-P. Hennart. Dordrecht: Springer, 1994, pp. 51–67.

[136] J. C. Spall. "Multivariate stochastic approximation using a simultaneous perturbation gradient approximation". In: *IEEE Transactions on Automatic Control* 37 (1992), pp. 332–341.

[137] Jorge Nocedal and Stephen J. Wright. *Numerical Optimization*. 2nd ed. New York: Springer, 2006.

[138] Aidan Pellow-Jarman, Ilya Sinayskiy, Anban Pillay, and Francesco Petruccione. "A comparison of various classical optimizers for a variational quantum linear solver". In: *Quantum Information Processing* 20.6 (2021), p. 202.

[139] A. Kandala, A. Mezzacapo, K. Temme, M. Takita, M. Brink, J. M. Chow, and J. M. Gambetta. "Hardware-efficient variational quantum eigensolver for small molecules and quantum magnets". In: *Nature* 549 (2017), pp. 242–246.

[140] S. Endo, S. C. Benjamin, and Y. Li. "Hybrid quantum–classical algorithms and quantum error mitigation". In: *Journal of the Physical Society of Japan* 90 (2021), p. 032001.

[141] J. Lee, W. J. Huggins, J. Head-Marsden, N. C. Rubin, R. Babbush, and J. R. McClean. "Evaluating the evidence for quantum computational advantage in chemistry". In: *Nature Chemistry* 14 (2022), pp. 115–119.

[142] A. Anand, S. Schulgasser, V. von Burg, R. Sweke, J. J. Meyer, M. Cerezo, and P. J. Coles. "A quantum natural gradient". In: *Quantum* 6 (2022), p. 841.

[143] J. Romero, R. Babbush, J. R. McClean, C. Hempel, P. J. Love, and A. Aspuru-Guzik. "Strategies for quantum computing molecular energies using the unitary coupled cluster ansatz". In: *Quantum Science and Technology* 4 (2018), p. 014008.

[144] H. R. Grimsley, S. E. Economou, E. Barnes, and N. J. Mayhall. "An adaptive variational algorithm for exact molecular simulations on a quantum computer". In: *Nature Communications* 10 (2019), p. 3007.

[145] Michael A Nielsen et al. "The Fermionic canonical commutation relations and the Jordan-Wigner transform". In: *School of Physical Sciences The University of Queensland* 59 (2005), p. 75.

[146] E. Lieb, T. Schultz, and D. Mattis. "Two soluble models of an antiferromagnetic chain". In: *Annals of Physics* 16 (1961), pp. 407–466.

[147] Subir Sachdev. *Quantum Phase Transitions*. 2nd ed. Cambridge: Cambridge University Press, 2011.

[148] Steven R. White. "Density matrix formulation for quantum renormalization groups". In: *Physical Review Letters* 69 (1992), pp. 2863–2866.

[149] Steven R. White. "Density-matrix algorithms for quantum renormalization groups". In: *Physical Review B* 48 (1993), pp. 10345–10356.

[150] Ulrich Schollwöck. "The density-matrix renormalization group in the age of matrix product states". In: *Annals of Physics* 326 (2011), pp. 96–192.

[151] Román Orús. "A practical introduction to tensor networks: Matrix product states and projected entangled pair states". In: *Annals of Physics* 349 (2014), pp. 117–158.

[152] F. Verstraete, V. Murg, and J. I. Cirac. "Matrix product states, projected entangled pair states, and variational renormalization group methods for quantum spin systems". In: *Advances in Physics* 57 (2008), pp. 143–224.

[153] D. Pérez-García, F. Verstraete, M. M. Wolf, and J. I. Cirac. "Matrix product state representations". In: *Quantum Information and Computation* 7 (2007), pp. 401–430.

[154] Michael Tinkham. *Introduction to Superconductivity*. 2nd. Covers fundamental properties of superconductors including zero resistance and the Meissner effect. New York: Dover Publications, 2004.

[155] Neil W. Ashcroft and N. David Mermin. *Solid State Physics*. Classic introduction to condensed matter physics, including superconductivity and the Meissner effect. Philadelphia: Saunders College Publishing, 1976.

[156] Manfred Sigrist and Kazuo Ueda. "Phenomenological theory of unconventional superconductivity". In: *Reviews of Modern Physics* 63.2 (1991). Comprehensive review on superconducting order parameter symmetries (s-, p-, d-wave, etc.) and their physical implications., pp. 239–311.

[157] Xiao-Liang Qi and Shou-Cheng Zhang. "Topological insulators and superconductors". In: *Reviews of Modern Physics* 83.4 (2011), pp. 1057–1110. eprint: `arXiv:1008.2026`.

[158] Andreas P. Schnyder, Shinsei Ryu, Akira Furusaki, and Andreas W. W. Ludwig. "Classification of topological insulators and superconductors in three spatial dimensions". In: *Physical Review B* 78.19 (2008), p. 195125. eprint: `arXiv:0803.2786`.

[159] Pierre-Gilles De Gennes. *Superconductivity of metals and alloys*. CRC press, 2018.

[160] Michael Tinkham. *Introduction to Superconductivity*. 2nd ed. Dover Publications, 2004.

[161] N. N. Bogoliubov. "A New Method in the Theory of Superconductivity". In: *Soviet Physics JETP* 7 (1958), pp. 41–46.

[162] N. Read and Dmitry Green. "Paired states of fermions in two dimensions with breaking of parity and time-reversal symmetries and the fractional quantum Hall effect". In: *Physical Review B* 61.15 (2000), pp. 10267–10297.

[163] M. Leijnse and K. Flensberg. "Introduction to topological superconductivity and Majorana fermions". In: *Semiconductor Science and Technology* 27 (2012), p. 124003.

[164] Roman M. Lutchyn, Jay D. Sau, and S. Das Sarma. "Majorana fermions and a topological phase transition in semiconductor–superconductor heterostructures". In: *Physical Review Letters* 105.7 (2010), p. 077001.

[165] Yuval Oreg, Gil Refael, and Felix von Oppen. "Helical liquids and Majorana bound states in quantum wires". In: *Physical Review Letters* 105.17 (2010), p. 177002.

[166] Roman M. Lutchyn, Jay D. Sau, and S. Das Sarma. “Majorana Fermions and a Topological Phase Transition in Semiconductor–Superconductor Heterostructures”. In: *Physical Review Letters* 105 (2010), p. 077001.

[167] Yuval Oreg, Gil Refael, and Felix von Oppen. “Helical Liquids and Majorana Bound States in Quantum Wires”. In: *Physical Review Letters* 105 (2010), p. 177002.

[168] Jason Alicea. “New directions in the pursuit of Majorana fermions in solid state systems”. In: *Reports on Progress in Physics* 75.7 (2012), p. 076501.

[169] V. Mourik, K. Zuo, S. M. Frolov, S. R. Plissard, E. P. A. M. Bakkers, and L. P. Kouwenhoven. “Signatures of Majorana Fermions in Hybrid Superconductor-Semiconductor Nanowire Devices”. In: *Science* 336.6084 (2012), pp. 1003–1007.

[170] Igor Vurgaftman, Jerry R. Meyer, and L. R. Ram-Mohan. “Band parameters for III–V compound semiconductors and their alloys”. In: *Journal of Applied Physics* 89.11 (2001), pp. 5815–5875.

[171] Roland Winkler. *Spin-Orbit Coupling Effects in Two-Dimensional Electron and Hole Systems*. Springer, 2003.

[172] Claude Cohen-Tannoudji, Bernard Diu, and Franck Laloë. *Quantum Mechanics*. Vol. 1. Wiley, 1977.

[173] Y. A. Bychkov and E. I. Rashba. “Oscillatory effects and the magnetic susceptibility of carriers in inversion layers”. In: *Journal of Physics C: Solid State Physics* 17 (1984), p. 6039.

[174] Supriyo Datta and Biswajit Das. “Electronic analog of the electro-optic modulator”. In: *Applied Physics Letters* 56.7 (1990), pp. 665–667.

[175] Peter Y. Yu and Manuel Cardona. *Fundamentals of Semiconductors: Physics and Materials Properties*. 4th ed. Springer, 2010.

[176] A. Manchon, H. C. Koo, J. Nitta, S. M. Frolov, and R. A. Duine. “New perspectives for Rashba spin–orbit coupling”. In: *Nature Materials* 14 (2015), pp. 871–882.

[177] C. L. Kane and E. J. Mele. “Quantum Spin Hall Effect in Graphene”. In: *Physical Review Letters* 95 (2005), p. 226801.

[178] B. A. Bernevig, T. L. Hughes, and S. C. Zhang. “Quantum Spin Hall Effect and Topological Phase Transition in HgTe Quantum Wells”. In: *Science* 314 (2006), pp. 1757–1761.

[179] M. Z. Hasan and C. L. Kane. “Colloquium: Topological Insulators”. In: *Reviews of Modern Physics* 82 (2010), pp. 3045–3067.

[180] L. Fu, C. L. Kane, and E. J. Mele. “Topological Insulators in Three Dimensions”. In: *Physical Review Letters* 98 (2007), p. 106803.

[181] S. Nadj-Perge, I. K. Drozdov, J. Li, H. Chen, S. Jeon, J. Seo, A. H. MacDonald, B. A. Bernevig, and A. Yazdani. “Observation of Majorana Fermions in Ferromagnetic Atomic Chains on a Superconductor”. In: *Science* 346 (2014), pp. 602–607.

[182] H.-H. Sun and J.-F. Jia. “Detection of Majorana Zero Mode in the Vortex”. In: *npj Quantum Materials* 2 (2017), p. 34.

[183] S. Nadj-Perge, I. K. Drozdov, J. Li, H. Chen, S. Jeon, J. Seo, A. H. MacDonald, B. A. Bernevig, and A. Yazdani. “Observation of Majorana fermions in ferromagnetic atomic chains on a superconductor”. In: *Science* 346 (2014), pp. 602–607.

[184] D. E. Liu and H. U. Baranger. “Detecting a Majorana-fermion zero mode using a quantum dot”. In: *Phys. Rev. B* 84 (2011), p. 201308.

[185] F. Pientka, A. Romito, M. Duckheim, Y. Oreg, and F. von Oppen. “Signatures of topological phase transitions in mesoscopic superconducting rings”. In: *New Journal of Physics* 15 (2013), p. 025001.

[186] B. Jaworowski, N. Rogers, M. Grabowski, and P. Hawrylak. “Macroscopic Singlet-Triplet Qubit in Synthetic Spin-One Chain in Semiconductor Nanowires”. In: *Scientific Reports* 7 (2017), p. 5529.

[187] David B. Northeast, Dan Dalacu, John F. Weber, Jason Phoenix, Jean Lapointe, Geof C. Aers, Philip J. Poole, and Robin L. Williams. “Optical fibre-based single photon source using InAsP quantum dot nanowires and gradient-index lens collection”. In: *Scientific Reports* 11 (2021), p. 22878.

[188] Moritz Cygorek, Marek Korkusinski, and Pawel Hawrylak. “Atomistic theory of electronic and optical properties of InAsP/InP nanowire quantum dots”. In: *Physical Review B* 101.7 (2020), p. 075307.

[189] J. Manalo, M. Cygorek, A. Altintas, and P. Hawrylak. "Electronic and magnetic properties of many-electron complexes in charged $InAs_xP_{1-x}$ quantum dots in InP nanowires". In: *Phys. Rev. B* 104 (2021), p. 125402.

[190] Z.X. Koong, G. Ballesteros-Garcia, R. Proux, D. Dalacu, P.J. Poole, and B.D. Gerardot. "Multiplexed single photons from deterministically positioned nanowire quantum dots". In: *Phys. Rev. Appl.* 14 (2020), p. 034011.

[191] D. Dalacu, K. Mnaymneh, J. Lapointe, X. Wu, P.J. Poole, G. Bulgarini, V. Zwiller, and M.E. Reimer. "Ultraclean emission from InAsP quantum dots in defect-free wurtzite InP nanowires". In: *Nano Lett.* 12 (2012), pp. 5919–5923.

[192] J. Phoenix, M. Korkusinski, D. Dalacu, P.J. Poole, P. Zawadzki, S. Studenikin, R.L. Williams, A.S. Sachrajda, and L. Gaudreau. "Magnetic tuning of tunnel coupling between InAsP double quantum dots in InP nanowires". In: *Sci. Rep.* 12 (2022), p. 5100.

[193] P. Laferrière, E. Yeung, M. Korkusinski, P.J. Poole, R.L. Williams, D. Dalacu, J. Manalo, M. Cygorek, A. Altintas, and P. Hawrylak. "Systematic study of the emission spectra of nanowire quantum dots". In: *Appl. Phys. Lett.* 118 (2021), p. 161107.

[194] E. F. Talantsev, K. Iida, T. Ohmura, T. Matsumoto, W. P. Crump, N. M. Strickland, S. C. Wimbush, and H. Ikuta. "p-wave superconductivity in iron-based superconductors". In: *Scientific Reports* 9 (2019), p. 14245.

[195] W. S. Wang, C. C. Zhang, F. C. Zhang, and Q. H. Wang. "Theory of chiral p-wave superconductivity with near nodes for Sr_2RuO_4". In: *Physical Review Letters* 122 (2019), p. 027002.

[196] N. F. Q. Yuan, K. F. Mak, and K. T. Law. "Possible topological superconducting phases of MoS_2". In: *Physical Review Letters* 113 (2014), p. 097001.

[197] P. Frigeri, D. F. Agterberg, A. Koga, and M. Sigrist. "Superconductivity without Inversion Symmetry: MnSi versus $CePt_3Si$". In: *Physical Review Letters* 92 (2004), p. 097001.

[198] F. Hardy and A. Huxley. "p-wave superconductivity in the ferromagnetic superconductor URhGe". In: *Physical Review Letters* 94 (2005), p. 247006.

[199] K. Ishida, H. Mukuda, Y. Kitaoka, K. Asayama, Z. Q. Mao, Y. Mori, and Y. Maeno. "Spin-triplet superconductivity in Sr_2RuO_4 identified by ^{17}O Knight shift". In: *Nature* 396 (1998), pp. 658–660.

[200] Jacob Manalo, Daniel Miravet, and Pawel Hawrylak. “Microscopic design of a synthetic spin-1 chain in an InAsP quantum dot array”. In: *Phys. Rev. B* 109 (8 Feb. 2024), p. 085112.

[201] Yasser Saleem, Katarzyna Sadecka, Marek Korkusinski, Daniel Miravet, Amintor Dusko, and Pawel Hawrylak. “Theory of excitons in gated bilayer graphene quantum dots”. In: *Nano Letters* 23.7 (2023), pp. 2998–3004.

[202] Daniel Miravet, Ludmiła Szulakowska, Maciej Bieniek, Katarzyna Sadecka, Marek Korkusi ński, and Paweł Hawrylak. “Theory of excitonic complexes in gated WSe_2 quantum dots”. In: *Phys. Rev. B* 110 (23 Dec. 2024), p. 235404.

[203] Matthew Albert, Daniel Miravet, Yasser Saleem, Katarzyna Sadecka, Marek Korkusinski, Gabriel Bester, and Pawel Hawrylak. “Optical properties of gated bilayer graphene quantum dots with trigonal warping”. In: *Phys. Rev. B* 110 (15 Oct. 2024), p. 155421.

[204] Sadao Adachi. “Energy-Band Structure: Energy-Band Gaps”. In: *Properties of Group-IV, III-V and II-VI Semiconductors*. John Wiley & Sons, Ltd, 2005. Chap. 6, p. 116.

[205] Manisha Thakurathi, K Sengupta, and Diptiman Sen. “Majorana edge modes in the Kitaev model”. In: *Physical Review B* 89.23 (2014), p. 235434.

[206] Lei Chen, W LiMing, Jia-Hui Huang, Chengping Yin, and Zheng-Yuan Xue. “Majorana zero modes on a one-dimensional chain for quantum computation”. In: *Physical Review A* 90.1 (2014), p. 012323.

[207] Dmitry A Fedorov, Bo Peng, Niranjan Govind, and Yuri Alexeev. “VQE method: a short survey and recent developments”. In: *Materials Theory* 6.1 (2022), p. 2.

[208] Jérôme F Gonthier, Maxwell D Radin, Corneliu Buda, Eric J Doskocil, Clena M Abuan, and Jhonathan Romero. “Identifying challenges towards practical quantum advantage through resource estimation: the measurement roadblock in the variational quantum eigensolver”. In: *arXiv preprint arXiv:2012.04001* 7 (2020).

[209] Gokul Subramanian Ravi, Pranav Gokhale, Yi Ding, William Kirby, Kaitlin Smith, Jonathan M Baker, Peter J Love, Henry Hoffmann, Kenneth R Brown, and Frederic T Chong. “CAFQA: A classical simulation bootstrap for variational quantum algorithms”. In: *Proceedings of the 28th ACM International Conference on Architectural Support for Programming Languages and Operating Systems, Volume 1*. 2022, pp. 15–29.

[210] David Wierichs, Christian Gogolin, and Michael Kastoryano. “Avoiding local minima in variational quantum eigensolvers with the natural gradient optimizer”. In: *Physical Review Research* 2.4 (2020), p. 043246.

[211] CD Batista and Gerardo Ortiz. “Generalized jordan-wigner transformations”. In: *Physical review letters* 86.6 (2001), p. 1082.

[212] Eduardo Fradkin. “Jordan-Wigner transformation for quantum-spin systems in two dimensions and fractional statistics”. In: *Physical review letters* 63.3 (1989), p. 322.

[213] Michael A Nielsen et al. “The Fermionic canonical commutation relations and the Jordan-Wigner transform”. In: *School of Physical Sciences The University of Queensland* 59 (2005), p. 75.

[214] Roeland Wiersema, Cunlu Zhou, Yvette de Sereville, Juan Felipe Carrasquilla, Yong Baek Kim, and Henry Yuen. “Exploring entanglement and optimization within the hamiltonian variational ansatz”. In: *PRX quantum* 1.2 (2020), p. 020319.

[215] Dave Wecker, Matthew B Hastings, and Matthias Troyer. “Progress towards practical quantum variational algorithms”. In: *Physical Review A* 92.4 (2015), p. 042303.

[216] Alexei Kitaev and John Preskill. “Topological Entanglement Entropy”. In: *Physical Review Letters* 96 (2006), p. 110404.

[217] Michael Levin and Xiao-Gang Wen. “Detecting Topological Order in a Ground State Wave Function”. In: *Physical Review Letters* 96 (2006), p. 110405.

[218] Matthew Fishman, Steven R. White, and E. Miles Stoudenmire. “The ITensor Software Library for Tensor Network Calculations”. In: *SciPost Phys. Codebases* (2022), p. 4.

[219] Gerald D. Mahan. *Many-Particle Physics*. 3rd. Springer, 2000.

[220] E. N. Economou. *Green’s Functions in Quantum Physics*. 3rd. Springer, 2006.